

# **Experimental and theoretical investigation of chiral separation by crystallisation**

**Miguel Ardid Candel**

**A thesis submitted to University College London in partial fulfilment of  
the requirements for the degree of Doctor of Philosophy**

**University College London**

**2013**

**Department of Chemical Engineering**

**University College London**

**Torrington Place**

**London, WC1E 7JE**

**United Kingdom**

## **Declaration**

I, Miguel Ardid Candel, confirm that the work presented in this thesis is my own. Where information has been derived from other sources, I confirm that this has been indicated in the thesis.

## Acknowledgements

I would like to sincerely thank my supervisors Professor Alan Jones and Professor Sally Price for all their help, encouragement and continued support throughout my research studies. Sally's help and encouragement over the last year has been invaluable. She has always had time to discuss my work with me and to help me clarify my thoughts and has kept me going with the writing up. Without her help arriving to this point would not have been possible.

I am very grateful to everyone in Sally's group who I had the chance to meet and work with for they are an incredible group of scientists and everyone has at some point had some useful advice that has helped develop this work. I am especially indebted to Dr Doris Braun, for her guidance and assistance with experimental work, and for the numerous discussions we had during lunch breaks that helped me find my way so often during my studies. I am also extremely grateful to Dr Louise Price for helping me with the diastereomeric salt searches presented in Chapter 6 and for having so much patience with me, helping to figure out mistakes in the input files. I was lucky to meet Dr's Sharmarke Mohamed and Nizar Issa before they were done with their PhD's and must thank them for their invaluable advice at the start of my research studies and for showing me how to use the X-ray diffractometer. Dr Emiliana D'Oria first taught me how to use the programmes used in Chapter 6 and Dr Matthew Habgood was there at the end to assist me with my problems and for that I thank them too. I am grateful to Martin Vickers for teaching me how to use the powder X-ray diffractometer and assisting me whenever I had problems with it. Thanks also to Ogaga Uzoh, Jean-Baptiste Arlin, Rajni Miglani, Sarah Barnett, Professor Derek Tocher and Bob Lancaster.

I am also really grateful to Dr.Simon Gaisford at the London School of Pharmacy for letting me use his solution and differential scanning calorimeters, without which I would not have been able to complete this work. I would also like to thank his group, especially Ms (probably Dr by now) Asma Buanz, for being so welcoming and making work in their lab so enjoyable.

In the Chemical Engineering Department I am very thankful to Dr Han Wu and Olga Narducci. Although not for academic matters, I am also grateful to other friends and colleagues at the department of Chemical Engineering with whom I used to pop down for a beer and a chat on a Friday evening for much needed unwinding: Alberto Cantu Perez, Melanie Ramirez Jaramillo, Eleftheria Polykarpou, Alberto Hernandez and Shane Morrin. Dr Luca Mazzei, Damiano Rossi and Luigi Gargiulo, with whom I've been working with over the last year, have also been incredibly helpful and encouraging. Luigi also proved to be amazing with all matters Word.

Last but not least I must thank Adamma for putting up with my grumpiness over some difficult times and helping me get through this tough experience.

## Abstract

Chiral molecules often show different pharmacological and toxicological properties, making their separation crucial for pharmaceutical companies. The resolution of racemic mixtures is often achieved via crystallisation methods. The lack of experimental data has been a major constraint in validating proposed computational methods for aiding the design of crystallisation processes for chiral resolution. This thesis provides both structural and thermodynamic data, and uses it to assess the limitations of current computer modelling methods. Progress in computational methods might eventually result in the design of resolving agents and hence reduce production costs of drugs and fine chemicals.

Previous studies of naproxen have concentrated on the marketed enantiopure form of this anti-inflammatory drug. A crystallisation screen was conducted to identify all possible crystal phases of racemic and enantiopure naproxen. No polymorphs were detected and the crystal structure of the racemic compound was solved from powder X-ray diffraction data. The nature of the racemic species was confirmed with thermal methods, and differential scanning calorimetric and solubility measurements were used to estimate the enthalpy difference between the crystals at 156 °C and in the range of 10 to 40 °C. These data were used to test the different approximations involved in determining the energy differences between the racemic and enantiopure crystals.

An extensive crystallisation screen was also performed for (1R,2S)-ephedrine 2-phenylpropionate salts. The crystal structure of the least soluble salt and three polymorphs of the most soluble salt were determined by low temperature single crystal X-ray diffraction or powder X-ray diffraction. Solubility measurements and differential scanning calorimetry were used to determine the relative stability of the salt pairs and polymorphs. These results showed the inadequacies of lattice energy calculations of the diastereomeric salt pair and their polymorphs. Experimental work on related diastereomeric salt pairs emphasised the difficulty in fully structurally and thermodynamically characterising these systems.

## Table of Contents

|  |    |
|--|----|
| EXPERIMENTAL AND THEORETICAL INVESTIGATION OF CHIRAL SEPARATION BY CRYSTALLISATION ..... | 1  |
| DECLARATION.....   | 2  |
| ACKNOWLEDGEMENTS .....   | 3  |
| ABSTRACT .....   | 4  |
| Table of Contents .....  | 5  |
| List of Figures .....  | 8  |
| List of Tables.....  | 15 |
| CHAPTER 1 INTRODUCTION TO CHIRALITY AND RESOLUTIONS .....                                | 17 |
| 1.1 Background to Stereochemistry and Research motivation.....                           | 17 |
| 1.2 Classification of Enantiomers: the Cahn-Ingold-Prelog rule .....                     | 19 |
| 1.3 Biological activity of enantiomers .....   | 21 |
| 1.4 Production of Enantiomerically Pure Compounds .....                                  | 23 |
| 1.5 The search for Conglomerates.....  | 33 |
| 1.6 Efficiency of Classical Resolution .....   | 36 |
| 1.7 Thesis Outline .....   | 65 |
| CHAPTER 2 CRYSTALLISATION FROM SOLUTION .....  | 67 |
| 2.1 Introduction.....  | 67 |
| 2.2 Supersaturation .....  | 67 |
| 2.3 Nucleation .....   | 69 |
| 2.4 Crystal Growth.....  | 74 |
| 2.5 Polymorphism.....  | 77 |

|   |            |
|---|------------|
| 2.6 Crystallisation of Racemic Mixtures.....  | 80         |
| <b>CHAPTER 3 EXPERIMENTAL AND COMPUTATIONAL METHODS .....</b>   | <b>85</b>  |
| 3.1 Introduction.....   | 85         |
| 3.2 Crystallisation Screening Method.....   | 85         |
| 3.3 Crystal Form Analysis.....  | 87         |
| 3.4 Computational Methodology .....   | 91         |
| <b>CHAPTER 4 RACEMIC NAPROXEN: A MULTIDISCIPLINARY STRUCTURAL AND<br/>THERMODYNAMIC COMPARISON WITH THE ENANTIOPURE FORM.....</b> | <b>94</b>  |
| 4.1 Introduction.....   | 94         |
| 4.2 Objectives.....   | 98         |
| 4.3 Summary of the Crystallisation screen .....   | 98         |
| 4.4 Results and Discussion .....  | 99         |
| 4.5 Discussion.....   | 111        |
| 4.6 Conclusions .....   | 113        |
| <b>CHAPTER 5 EPHEDRINE AND PSEUDOEPHEDRINE DIASTEREOMERIC SALTS: A<br/>STUDY OF CLASSICAL RESOLUTION.....</b>                     | <b>114</b> |
| 5.1 Introduction.....   | 114        |
| 5.2 Objectives.....   | 115        |
| 5.3 Experimental .....  | 115        |
| 5.4 Results.....  | 122        |
| 5.5 Conclusions .....   | 155        |
| 5.6 Appendix .....  | 159        |
| <b>CHAPTER 6 COMPUTATIONAL INVESTIGATION OF THE RESOLUTION EFFICIENCY OF<br/>EPHEDRINE WITH (R/S)2-PHENYLPROPIONIC ACID .....</b> | <b>164</b> |

|   |            |
|---|------------|
| <b>6.1 Introduction.....</b>  | <b>164</b> |
| <b>6.2 Molecular Conformation Analysis .....</b>  | <b>165</b> |
| <b>6.3 Intermolecular Energy.....</b>   | <b>173</b> |
| <b>6.4 Calculation of the Lattice Energies using CrystalOptimizer .....</b>   | <b>179</b> |
| <b>6.5 “Crystal structure prediction” to generate crystal structures .....</b>  | <b>182</b> |
| <b>6.6 Conclusions .....</b>  | <b>189</b> |
| <b>6.7 Appendix .....</b>   | <b>191</b> |
| <br>  |            |
| <b>CHAPTER 7 OVERALL CONCLUSIONS AND RECOMMENDATIONS FOR FUTURE WORK .....</b>  | <b>196</b> |
| <br>  |            |
| <b>7.1 Crystallisation behaviour of (1R,2S)-Ephedrine-2-phenylpropionate salts and other closely related diastereomeric salt pairs .....</b>  | <b>197</b> |
| <b>7.2 Opportunities for the design of resolution processes .....</b>   | <b>198</b> |
| <b>7.3 Computing the Relative Stabilities of Racemic and Enantiopure Naproxen and Ephedrine-2-phenylpropionate Diastereomeric salts .....</b> | <b>198</b> |
| <b>7.4 Will Lattice Energy Minimisations ever be reliable for the prediction of resolution efficiency? .....</b>                              | <b>199</b> |
| <b>7.5 Summary .....</b>  | <b>200</b> |
| <br>  |            |
| <b>REFERENCE LIST.....</b>  | <b>201</b> |
| <br>  |            |
| <b>CIF FILES .....</b>  | <b>CD</b>  |

## List of Figures

|   |    |
|---|----|
| Figure 1.1 Prelog's <i>ex libris</i> by Hans Erni "Rassi-maid".   | 17 |
| Figure 1.2 Classification of isomers [1].   | 18 |
| Figure 1.3 (a) (1R, 2S) Ephedrine – the two stereocentres are marked 1 and 2. (b) View of the first stereocentre as seen when the hydrogen is pointing away (into the paper) and (c) view of the second stereo-centre.  | 21 |
| Figure 1.4 Examples of chiral drugs and the effects of their different enantiomers.   | 22 |
| Figure 1.5 Overview of the routes towards enantiopure compounds. This thesis will concentrate on the resolution of chiral molecules by crystallisation of diastereomeric salts.   | 23 |
| Figure 1.6 The principle of simulated moving bed chromatography (a) The chromatographic columns are run in a loop by connecting the exit of one to the inlet of the next (b) The inlet (eluent and feed mixture) and exit (extract and raffinate) positions are moved in the direction of the liquid flow to create a moving resin effect [26]. | 26 |
| Figure 1.7 Schematic diagram of the apparatus used in simultaneous crystallisation of enantiomers [18].   | 28 |
| Figure 1.8 Representation of diastereomeric salt formation between a chiral resolving agent (RA) and the two enantiomers (R or S) [37]. From the diagram, it is evident that upon formation of a salt, the two compounds are not mirror image of one another.   | 30 |
| Figure 1.9 Common basic resolving agents (taken from [36]).   | 31 |
| Figure 1.10 Common acidic resolving agents.   | 31 |
| Figure 1.11 Typical ternary Phase Diagram for a Diastereomeric salt mixture in solution.  | 38 |
| Figure 1.12 (a) Partial solid solution of salt p in the pure salt n (b) total miscibility between the two salts.  | 40 |
| Figure 1.13 Ternary phase diagram for the solvates (n' and p'), of n and p diastereomeric salts [65].   | 41 |
| Figure 1.14 Ternary phase diagram of 1:1 double salts with (a) congruent solubility (b) non-congruent solubility [62].  | 42 |
| Figure 1.15 Construction of a ternary phase diagram by the method of wet residues.  | 43 |
| Figure 1.16 If the composition of the eutectic is not affected by temperature, the composition of the eutectic in a ternary and a binary phase diagram should be the same [63].   | 44 |
| Figure 1.17 Example of the construction of a binary phase diagram from DSC data [68].   | 45 |
| Figure 1.18 (a) Packing of hydrogen bonded columns forming an efficient planar hydrophobic surface (b) Inefficient packing of hydrogen bonding columns in which substituents at the para position project out of the plane [58].  | 48 |
| Figure 1.19 Systems studied by Kinbara <i>et al</i> for the design of an acidic resolving agent [77] (a) (2-naphthyl)glycolic acid, (b) 1-arylalkylamine R can be Me, Et, Pr, OMe, c-Hex, Cl, Br, NO <sub>2</sub> or Phe.   | 49 |



|  |    |
|--|----|
| Figure 1.20 Systems studied by Kinbara <i>et al</i> for the design of a basic resolving agent [79] (a) cis-1-aminobenz[f]inan-2-ol (ABI) (b) arylalkanoic acids where R <sub>1</sub> = Me, Et or Pr and R <sub>2</sub> = H, o-Me, m-Me, p-Me, p-Cl, p-Bu, Phe, or Phe-p-OMe. ....  | 50 |
| Figure 1.21 Thermodynamic cycle used to describe the link between the resolution of diastereomeric salts, n and p, and the solid state properties of the diastereomeric salts. The outer cycle corresponds to the resolution process. The inner cycle is used to approximate the difference in Gibbs free energy to the lattice enthalpy of the salts [56]. ....   | 53 |
| Figure 1.22 Intermolecular energy U <sub>(R)</sub> as a function of the intermolecular separation (R) between two spherical molecules. The energy minimum at the equilibrium distance of separation (R <sub>e</sub> ) [88]. ....   | 56 |
| Figure 2.1 A typical solubility diagram [137]. ....  | 67 |
| Figure 2.2 Schematic representation of the primary nucleation process. ....  | 69 |
| Figure 2.3 Free energy diagram for nucleation [137]. ....  | 70 |
| Figure 2.4 Nucleation rate as a function of supersaturation [139]. ....  | 72 |
| Figure 2.5 Gibbs free energy change as a function of r for (a) low supersaturation concentration and (b) high supersaturation [146]. ....  | 73 |
| Figure 2.6 Kossel's model of a growing crystal surface [151]. ....   | 75 |
| Figure 2.7 Crystal growth at a screw dislocation as proposed by Burton-Cabrera-Frank [152]. ....   | 76 |
| Figure 2.8 Free energy relationship of a dimorphic monotropic system [164]. ....   | 78 |
| Figure 2.9 Free energy relationship of a dimorphic enantiotropic system [164]. ....  | 78 |
| Figure 2.10 Reaction pathways for the crystallisation of a dimorphic system [165]. ....  | 80 |
| Figure 2.11 Melting Point Phase diagram of (a) conglomerate (b) racemic crystal and (c) pseudoracemates [47]. ....   | 81 |
| Figure 2.12 Thermodynamic cycle showing the entropy changes between stages [169]. ....   | 83 |
| Figure 4.1 Molecular diagram of naproxen (C <sub>14</sub> H <sub>14</sub> O <sub>3</sub> , Mr = 230.26), with the three main torsion angles considered during computational modelling studies defined as Φ <sub>1</sub> = C <sub>14</sub> -O <sub>1</sub> -C <sub>7</sub> -C <sub>8</sub> , Φ <sub>2</sub> = C <sub>12</sub> -C <sub>11</sub> -C <sub>2</sub> -C <sub>1</sub> and Φ <sub>3</sub> = O <sub>2</sub> -C <sub>12</sub> -C <sub>11</sub> -C <sub>2</sub> ....   | 95 |
| Figure 4.2 Lattice energy landscape for naproxen ( $E_{latt}=U_{inter}+\Delta E_{intra}$ ) after relaxation of the conformation within the crystal structure and considering molecular polarization in the crystal (PCM, ε=3), classified by the hydrogen-bonding motif. Each symbol denotes a crystal structure which is a lattice energy minimum. The empty triangle corresponds to the lower symmetry version of the experimental racemic crystal structure [202]. .... | 96 |
| Figure 4.3 Structure similarities (building blocks) observed between the experimental NPX crystal structures and all predicted low energy structures. The two hands ((R) and (S)) are coloured differently [202]. ....   | 97 |
| Figure 4.4 Structure overlays of experimental (black) and calculated (grey) NPX structures: (a) (S)-NPX viewed along c, (b) modelling of the bending observed in (S)-NPX. The braces indicate the layers in Figure 4.3. ....   | 97 |

|   |     |
|---|-----|
| Figure 4.5 FT-IR spectra of (S)- and (RS)-naproxen. Highlighted are the regions of the C=O stretching vibrations. ....  | 99  |
| Figure 4.6 X-ray powder diffraction patterns of (S)- and (RS)-naproxen. The experimental diffractograms are contrasted with the calculated powder patterns (S: single crystal data, COYRUD11 [192], RS: own structure solution). ....   | 100 |
| Figure 4.7 Example of a multilayered (SR)-naproxen crystal (size 0.6mm x 0.3mm x 0.07mm). This was the largest crystal grown in the attempts to obtain single crystals over a period of a few months. ....  | 100 |
| Figure 4.8 Packing diagrams of (a) racemic and (b) enantiopure naproxen (COYRUD11). ....  | 102 |
| Figure 4.9 DSC curves of (S)- and (RS)-Naproxen (heating rate 10 K/min). ....   | 104 |
| Figure 4.10 Binary (melting point) phase diagram of naproxen showing racemic compound formation. Black circles represent the eutectic temperature and grey circles the liquidus or melting temperatures measured with DSC. The dotted line represents the eutectic temperature as measured by hot-stage microscopy (147.0 – 147.5 °C). The dashed line represents equation (4.1) and the solid line equation (4.2) calculated using DSC thermal data from Table 4.1. .... | 105 |
| Figure 4.11 Temperature dependence for solubility of (S)- and (RS)-NPX in EtOH:water (4:1, v/v) expressed in mole fraction. The gradient is $-\Delta H_{\text{sol}}^{\circ}/R$ and the intercept is $-\Delta G_{\text{sol}}^{\circ}/RT_{\text{hm}}$ . ....  | 106 |
| Figure 4.12 Diagrammatic summary of the measured thermodynamic quantities (thick lines) and other enthalpic contributions relating the solid forms to the gas phase. Contributions that are probably negligible for naproxen but could be significant for other chiral systems with a more distinctive shape difference are indicated by yellow boxes. ....   | 113 |
| Figure 5.1 FT-IR Spectra of the different forms of PRP. One stable hydrate and one anhydrous phase were identified in the crystallisation experiments. ....   | 123 |
| Figure 5.2 FT-IR Spectra of the different forms of PSP. One stable hydrate and one anhydrous phase were identified in the crystallisation experiments. ....   | 123 |
| Figure 5.3 FT-IR Spectra of the different forms of PRB identified in the limited crystallisation screen of (1R,2R) pseodephedrine-2-phenylbutyrate salts. ....  | 124 |
| Figure 5.4 FT-IR Spectra of the different forms of PSB identified in the limited crystallisation screen of (1R,2R) pseodephedrine-2-phenylbutyrate salts. ....  | 125 |
| Figure 5.5 FT-IR Spectra of the different forms of ERB. Two anhydrous phases were identified together with six solvates. ....   | 126 |
| Figure 5.6 FT-IR Spectra of the different forms of ESB. Two anhydrous phases were identified together with one solvate. ....  | 127 |
| <b>Figure 5.7</b> Powder diffraction patterns for the two different polymorphs of ERP found in the crystallisation screen. ERP I <sup>o</sup> (diffraction pattern in red) is the most stable phase at room temperature, whereas ERP II (diffraction pattern in blue) is a metastable phase. ....   | 128 |
| Figure 5.8 FT-IR Spectra of the two polymorphs of ERP found in the screen (ERP I <sup>o</sup> in red and ERP II in blue) and the dichloromethane solvate (S <sub>DCM</sub> in green). ....  | 129 |

|  |     |
|--|-----|
| Figure 5.9 DSC curve showing the transformation of ERP II to ERP I° (II → I°) and melting of ERP I°.....   | 130 |
| Figure 5.10 Schematic energy/temperature diagram of ERP polymorphs. $T_{fus}$ : melting point, $G$ : Gibbs free energy, $H$ : enthalpy, $\Delta_{fus}H$ : enthalpy of fusion, $\Delta_{trs}H$ : transition enthalpy and liq: liquid phase (melt), RT: room temperature (~25°C).....  | 131 |
| Figure 5.11 Transition pathways of the different ESP forms under different conditions. $\Delta T$ represents heating and * denotes removing from the mother liquor.....  | 132 |
| Figure 5.12 Powder diffraction patterns for the three different polymorphs of ESP and the hydrate form found in the crystallisation screen. ESP I (diffraction pattern in red) and ESP II (diffraction pattern in green) are metastable phases at room temperature. ESP III (diffraction pattern in dark blue green) is the most stable phase at room temperature. The hydrate form is shown in light blue. ....   | 134 |
| Figure 5.13 FT-IR spectra of the different polymorphs of ESP found during the crystallisation screen plus the Hydrate phase. ESP I (shown in red) and ESP II (green) are metastable forms. ESP III° (dark blue) is the thermodynamically stable phase. The hydrate is shown in light blue. ....  | 134 |
| Figure 5.14 FT-IR spectra of the solvate forms of ESP found during the screen from dioxane ( $S_{Dioxane}$ in red), dichloromethane ( $S_{DCM}$ in dark blue), tetrahydrofurane ( $S_{THF}$ in pink) and acetonitrile ( $S_{MeCN}$ in light blue). The thermodynamically stable phase (III° in orange) is shown for comparison. Bands in the high energy region due to hydrogen bonding characteristics show that all the phases are very similar. Differences in the IR patterns are mainly in the low region and are highlighted in yellow. .... | 135 |
| Figure 5.15 DSC traces of the three forms of ESP, ESPI and ESP II and ESP III°. The melting is represented by the endothermic peaks around 95°C and 105°C. Melting of ESP III° is followed by a crystallisation exotherm and the melting of either ESP II or ESP I. All DSC traces were measured at a heating rate of 10 °C/min.....   | 136 |
| Figure 5.16 Schematic energy/temperature diagram of ESP polymorphs. $T_{fus}$ : melting point, $G$ : Gibbs free energy, $H$ : enthalpy, $\Delta_{fus}H$ : enthalpy of fusion, $\Delta_{trs}H$ : transition enthalpy and liq: liquid phase (melt).....  | 136 |
| Figure 5.17 Temperature dependence of the solubility of ERP I° and ESP III° in ethanol between 5°C and 30°C expressed in mol fraction. ....  | 137 |
| Figure 5.18 van't Hoff plot for the temperature dependence of the solubility of ERP I° and ESP III° in ethanol. The gradient is $-\Delta H_{sol}/R$ and the intercept is $-\Delta G_{sol}/RT_{hm}$ .....   | 138 |
| Figure 5.19 Asymmetric unit of ERP I°. Displacement ellipsoids are drawn at the 50% probability level and hydrogen atoms are displayed as spheres of arbitrary radii.....  | 140 |
| Figure 5.20 Extended conformation of ephedrine in ERP I°. The view along O3-C11 in (a) shows the position of the hydroxyl hydrogen pointing away from the amine group. The view in (b) is along the N1-C10 bond. The value of the torsion angle defined by C19-N1-C10-C11 is marked in green.....  | 141 |

|   |     |
|---|-----|
| Figure 5.21 (a) Packing diagram of (1R,2S)-ephedrinium-(R)-2-phenylpropionate (ERP I°) viewed along b. (b) $2_1$ Columnar hydrogen bonding network viewed along a with the $R_4^3(13)$ hydrogen bond motif highlighted with the dotted line (only the atoms involved in the hydrogen bonding are showed for clarity). .....   | 141 |
| Figure 5.22 Asymmetric unit of ESP I. Displacement ellipsoids are drawn at the 50% probability level and hydrogen atoms are displayed as spheres of arbitrary radii. ....   | 142 |
| Figure 5.23 Folded conformation of ephedrine in ESP I. The view along O3-C11 in (a) shows the position of the hydroxyl hydrogen pointing towards the amine group. The view in (b) is along the N1-C10 bond. The value of the torsion angle defined by C19-N1-C10-C11 is marked in green. ....   | 143 |
| Figure 5.24 (a) Packing diagram of (1R,2S)-ephedrinium-(S)-2-phenylpropionate form I (ESPI). (b) Hydrogen bonded network.....   | 144 |
| Figure 5.25 (a) Packing diagram of (1R,2S)-ephedrinium-(S)-2-phenylpropanoate (ESP form II) (b) Hydrogen bonding network. ....  | 145 |
| Figure 5.26 (a) Packing diagram of (1R,2S)-ephedrinium-(S)-2-phenylpropanoate (ESP form III) (b) Hydrogen bonding network. ....   | 146 |
| Figure 5.27 (a) Crystal structure of ESB I viewed down axis b. (b) $2_1$ Columnar Hydrogen bonding network viewed along a with the $R_4^3(13)$ hydrogen bond motif highlighted with the dotted line (only the atoms involved in the hydrogen bonding are showed for clarity). .....   | 147 |
| Figure 5.28 (a) Packing diagram of PRP Hydrate. The hydrogen bonding pattern is shown in (b). .....   | 148 |
| Figure 5.29 (a) Packing diagram of PSP Hydrate. The hydrogen bonding pattern is shown in (b). The hydrogen bonding pattern can be represented using graph set notation as $R_4^3(13)$ . .....   | 150 |
| Figure 5.30 (a) Packing diagram of PRB. The hydrogen bonding pattern is shown in (b) and is the same as that seen in the disordered structure PSP.....  | 150 |
| Figure 5.31 (a) Packing diagram of PSB. The hydrogen bonding pattern is shown in (b). .   | 151 |
| Figure 5.32 Melting behaviour of the hydrate of PSB where the blue line represents the DSC thermogram and the green line shows the thermogravimetric data. Only one endotherm is seen and no mass loss upon heating, showing that the water is not lost before melting. ...   | 152 |
| Figure 5.33 Isothermal ternary phase diagram of ERP I° and ESP III° in ethanol measured at 10 °C. The dashed line represents the liquidus line and is included as a guide to the eye. Only the dots were measured experimentally. The tie lines are presented by the dotted lines and join the liquid phase composition with the solid phase composition. Tie lines have only been included for a few representative samples for clarity. Compositions are given in mass fractions..... | 154 |
| Figure 5.34 Isothermal ternary phase diagram of ERP I° and ESP III° in ethanol measured at 30°C. The dashed line represents the liquidus line and is included as a guide to the eye. Only the dots were measured experimentally. The tie lines are displayed by the dotted lines  |     |

and join the liquid phase composition with the solid phase composition. Tie lines have only been included for a few representative samples for clarity. Compositions are given in mass fractions..... 155

Figure 6.1. Flexible torsion angles considered in the search for (a) (1R,2S)-Ephedrine and (b) 2-phenylpropionic acid. The torsion angles in ephedrine were defined as  $\theta_1 = \text{C1-C2-C3-C4}$ ,  $\theta_2 = \text{H-O12-C2-C1}$ ,  $\theta_3 = \text{N9-C1-C2-C3}$  and  $\theta_4 = \text{C11-N9-C1-C2}$ . For 2-phenylpropionic acid the torsion angles in were defined as  $\Phi_1 = \text{C9-C2-C3-C4}$  and  $\Phi_2 = \text{O11-C1-C2-C3}$ . 165

Figure 6.2 CSD searches and 1D potential energy surface scans for ephedrine with respect to (a)  $\theta_1$  (b)  $\theta_2$  (extended conformation in pink and folded conformation in blue) (c)  $\theta_3$  (d)  $\theta_4$ , at the HF level of theory with the 6-31G(d,p) basis set. The values of the torsion angles found in the experimental crystal structures of ephedrine-2-phenylpropionate salts are indicated in the graphs by the squares and crosses. The extended conformations of ephedrine are represented by the squares ( - ERP - ESP III°) whereas the crosses represent the folded conformation (X – ESP I + - ESP II)..... 168

Figure 6.3 Potential energy surface scan for 2-phenylpropionate ion with respect to  $\theta_1$  and  $\theta_2$  at the HF level of theory with the 6-31G(d,p) basis set. The experimental conformation found in the diastereomeric salts are represented by for ERP for ESP III for ESPI and ...for ESP II. .... 171

Figure 6.4 CSD searches for 2-phenylpropionic acid for (a)  $\theta_1$  and (b)  $\theta_2$ . The values of the dihedral angles in the experimental structures are represented by for ERP for ESP I ....for ESP II and for ESP III°. .... 172

Figure 6.5 The intermolecular distances used to guide the choice of intermolecular potential. The specific illustration is for the ExminExp structure of ERP I°, showing the extended conformation. .... 175

Figure 6.6. Overlay of the constrained optimised (ConOpt) conformations of ephedrine and 2-phenylpropionic acid for (a) ERP I° and (b) ESP I. The ions were overlaid by optimising atoms C2, C3, and C4 in ephedrine and in 2-phenylpropionic acid molecules (see Figure 6.1). The minimum RMSD<sub>15</sub> overlays of the unit cells of ERP I° (ConOpt in blue) and ESP I (ConOpt in green) with the experimental crystal structures are shown in (c). .... 177

Figure 6.7 Overlay of the fully optimised “gas-phase” conformations of ephedrine and 2-phenylpropionic acid with the (a) extended ephedrine conformation in ERP I° and (b) the folded conformation ESP I. (c) shows the poor reproduction of the crystal structures when these conformations are used (“Opt” in Table 6.2) for ERP I° (in blue) and ESP I (green). 178

Figure 6.8 Superposition of the experimental structure and the CrystalOptimizer minimised structures of (a) ERP I° (minimised structure in blue) and (b) ESP III° (minimised structure in green). .... 180

Figure 6.9 Molecular clusters used for the charge density calculations of (a) Ephedrine and (b) 2-phenylpropionate ions. The distributed multipoles up to the hexadecapole were calculated only for the central molecule. .... 181

Figure 6.10 Energy landscapes of the search for hypothetical crystal structures of (a) ephedrine-(R)-2-phenylpropionate and (b) ephedrine-(S)-2-phenylpropionate salts. Each search was split into a sub search for structures with the extended conformation of ephedrine (blue) and a search for structures with the folded conformation (orange). Each point on the graph represents a hypothetical crystal structure. The experimental crystal structures were minimised using the same intra and intermolecular energy models as the search and are shown in red..... 184

Figure 6.11 Overlay of the experimental and predicted hypothetical (in green) structure for ERP I°..... 185

Figure 6.12 Overlay of the experimental and predicted hypothetical (in green) structure for ESP I..... 186

Figure 6.13 Overlay of the experimental and predicted hypothetical (in green) structure for ESP II..... 186

Figure 6.14 Overlay of the experimental and predicted hypothetical (in green) structure for ESP III°..... 187

Figure 6.15 Hydrogen bonding patterns found in the low energy hypothetical structures of ephedrine-2-phenylpropionate salts in which ephedrine is in a high energy conformation. (a) Chain of  $R_2^1(7)$  hydrogen bonded motifs, found in majority of low energy structures (b) chain of  $R_2^2(9)$  found in ESPI and ESP II..... 188

Figure 6.16 Hydrogen bonding patterns found in the low energy hypothetical structures of ephedrine-2-phenylpropionate salts in which ephedrine is in a low energy conformation. Both (a) and (b) can be described as  $R_4^3(13)$  hydrogen bonded motifs. (b) is found in the thermodynamically stable ERP I° and ESP III°..... 189

## List of Tables

|   |     |
|---|-----|
| Table 4.1 Values of the Thermodynamic Parameters of Enantiomer, Racemic compound and Eutectic of Naproxen. Parameters were obtained from Differential Scanning Calorimetry and van't Hoff plots. The experimentally determined values are contrasted to literature values and lattice energies calculated by DE Braun. ....   | 103 |
| Table 4.2 Experimental solubility of (S)- and (RS)-NPX in EtOH/water (4:1, v/v) expressed in molarity and mole fraction at several temperatures. ....   | 107 |
| Table 5.1 2x4 grid of the diastereomeric salt systems studied. The objective is to obtain crystal structures of all experimentally observed phases as well as thermodynamic and stability data. ....  | 116 |
| Table 5.2 Summary of the crystallisation experiments performed for the different diastereomeric salt pairs for the crystallisation screen. An X indicates that the experiment was performed at least three times, whereas – indicates that this crystallisation experiment was not set up. ....   | 119 |
| Table 5.3 Summary of the solvent diffusion experiments performed for the ERP/ESP diastereomeric salt pair system. ....  | 120 |
| Table 5.4 Composition of the initial mixtures in the determination of the ternary phase diagram of ERP I° and ESP III° in ethanol at 30 °C. ....  | 121 |
| Table 5.5 Composition of the initial mixtures in the determination of the ternary phase diagram of ERP I° and ESP III° in ethanol at 10 °C. ....  | 121 |
| Table 5.6 DSC data collected for ERP I° and ERP II. $T_{fus}$ = melting temperature; $\Delta H_{fus}$ = enthalpy of fusion; $\Delta S_{fus}$ = entropy of fusion calculated from $\Delta H_{fus}/T_{fus}$ ; $T_{trs}$ II - I° = transition temperature and $\Delta H_{trs}$ II - I° = transition enthalpy. ....   | 130 |
| Table 5.7 Thermal data for the different polymorphs of ESP at high temperature (DSC measurements) and at room temperature (solution calorimeter). Melting points and heats of fusion of the different polymorphs of ESP were measured with a DSC and the entropies of fusion were calculated by $\Delta H_{fus}/T_{fus}$ . The enthalpy of solution data was obtained with a solution calorimeter. .... | 135 |
| Table 5.8 Solubility data for the two thermodynamically stable phases of the diastereomeric salt pair, ERP I° and ESP III°, in ethanol at different temperatures. ....  | 138 |
| Table 5.9 Standard enthalpy and free energy of solution for ERP I° and ESP III° obtained by fitting the solubility data to the van't Hoff plot using Krug's approach as well as enthalpies of solution obtained from solution calorimetric measurements. ....   | 139 |
| Table 5.10 2x4 grid summarising the crystallisation outcome for a set of closely related diastereomeric salts. The hydrogen bonding patterns found in the experimentally determined structures are shown. ....  | 156 |

|  |     |
|--|-----|
| Table 5.11 Rough assessment of the solubility of the diastereomeric salt pair in the 20 solvents used in the crystallisation screen. The different categories were defines as either very soluble (>100mg/ml), soluble (20 > x > 4mg/ml) or hardly soluble (<3 mg/ml).....   | 159 |
| Table 5.12 Summary of the evaporation and cooling crystallisations.....  | 160 |
| Table 5.13 Summary of the solvent diffusion experiments performed with ESP.....  | 161 |
| Table 5.14 Crystallographic data for ERP I° and ESP I.....   | 162 |
| Table 5.15 Crystallographic Data for ESB, PRP <sub>Hydrate</sub> , PSP, PRB and PSB <sub>Hydrate</sub> .....   | 163 |
| Table 6.1 Summary of the lattice energy minimisations with the ion conformations held rigid at the experimental structures (ExminExp), using different repulsion-dispersion models FIT and WILL performed using DMACRYS. The charge distribution was calculated using the MP2/6-31G(d,p) level of theory and represented by distributed multipoles.....  | 191 |
| Table 6.2 Summary of the lattice energy minimisations performed to test sensitivity to rigid ion conformations using DMACRYS[182]. ConOpt refers to minimisations in which the molecular conformations had been optimised with $\theta$ and $\Phi$ , the flexible torsion angles identified in Figure 6.1, fixed at the experimental values, and all other degrees of freedom optimised. Opt refers to minimisations in which the molecular conformations had been fully optimised for the molecule in isolation. Constrained and full optimisations of the molecular conformations were performed using the HF/6-31G(d,p) level of theory whilst the distributed multipoles were calculated using the MP2/6-31G(d,p) level of theory..... | 192 |
| Table 6.3 CrystalOptimizer Lattice Energy minimisations of the experimental structures of ephedrine 2-phenylpropionate. HF_MP2 refers to calculations in which the intra-molecular energy penalty, $\Delta E_{intra}$ , was calculated using HF/6-31G(d,p) level of theory and the intermolecular energy, $U_{inter}$ , was calculated using the charge density from the distributed multipole from the wavefunction calculated at the MP2/6-31G(d,p) level of theory. PBE_PBE refers to calculation in which $\Delta E_{intra}$ and $U_{inter}$ were calculated at the PBE1/6-31G(d,p) level of theory. ....  | 193 |
| Table 6.4 CrystalOptimizer Lattice Energy minimisations of the experimental structures of ephedrine 2-phenylpropionate. Aug-cc-pVTZ refers to calculations in which, following the PBE_PBE minimisation, a further rigid-body lattice energy minimisation using the multipoles from a PBE aug-cc-pVTZ electron density calculation was performed. PCMe3 refers to calculations in which, following the PBE_PBE minimisation, a further lattice energy minimisation was performed using the multipoles obtained from the electron density calculated in a dielectric continuum, with $\epsilon=3$ . ....  | 194 |
| Table 6.5 CrystalOptimizer Lattice Energy minimisations of the experimental structures of ephedrine 2-phenylpropionate using the charge density distribution calculated for the central ion in a hydrogen bonded cluster.....  | 195 |



# Chapter 1 Introduction to Chirality and Resolutions

## 1.1 Background to Stereochemistry and Research motivation

Chirality, from the Greek *kheir* or hand, is the geometric property whereby, like one's hands, a given object cannot be superimposed on its mirror image (Figure 1.1). Chiral objects lack inversion symmetry elements and exist as two different forms, mirror images of one another. For macroscopic chiral objects these are termed enantiomorphs. It follows that if an object has inversion symmetry elements and is superimposable on its mirror image, it is said to be achiral.



**Figure 1.1** Prelog's *ex libris* by Hans Erni "Rassi-maid".

In chemistry the two different forms of chiral molecules are known as enantiomers. Enantiomers belong to the class of configurational stereoisomers known as optical isomers (isomers are compounds that share molecular formula but have different structural formula – a classification of isomers is given in Figure 1.2). Unlike other stereoisomers, enantiomers share physical (e.g. melting and boiling points, densities) and chemical properties under achiral environments, and only show differences in the direction they rotate plane-polarised light. A solution that rotates plane-polarised light clockwise (dextrorotatory) will be designated (+) or d, whereas a solution of the opposite enantiomer will be designated (-) or l (from levorotatory) since it will rotate plane-polarised light by the same degree but in the opposite direction. A mixture containing equal amounts of opposing enantiomers is a racemate. Racemic solutions show no rotation of plane-polarised light.

Conventional separation methods, which normally work based on differences in physical properties – distillation, chromatography with achiral stationary phases - cannot be used in

the separation of enantiomers since enantiomers have identical physical properties. Enantiomers are therefore very difficult to separate.

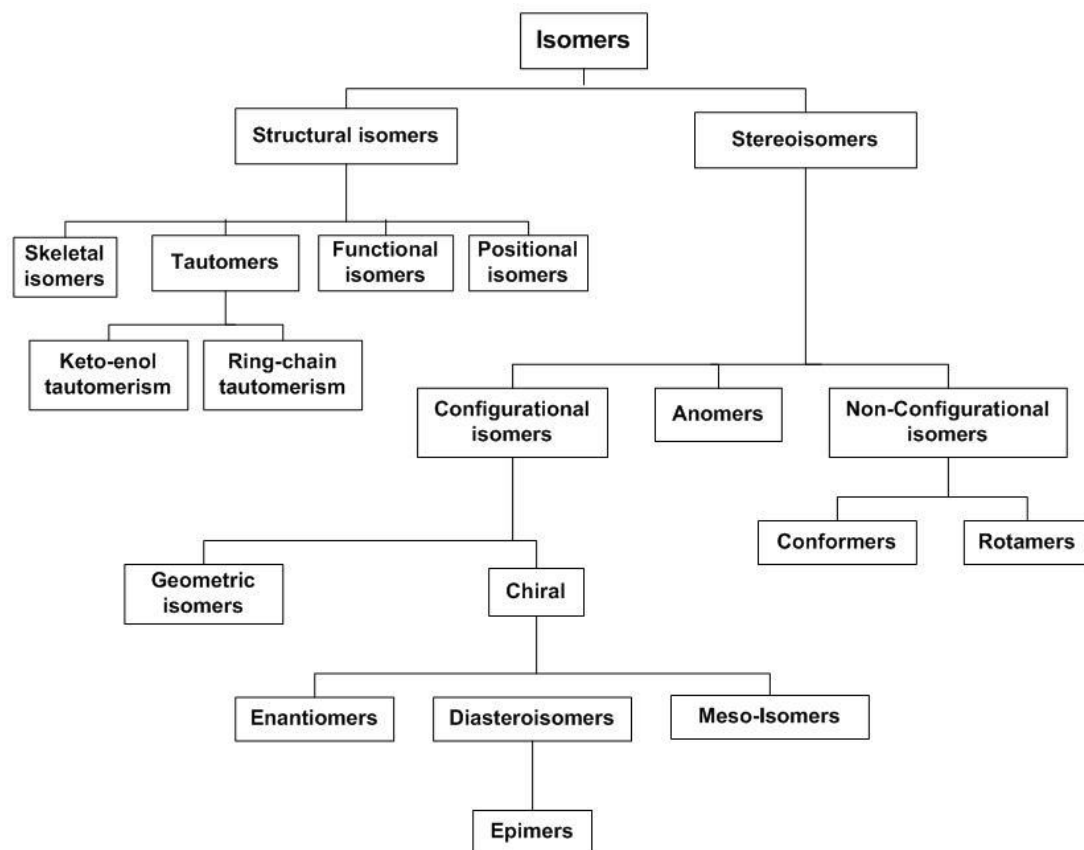


**Figure 1.2** Classification of isomers [1]

Furthermore chirality is a basic ingredient of life. In the course of evolution, organisms adopted one of the mirror images for chiral molecules they are built from; for example amino acids of all living organisms have the same chiral configuration. This explains why the pharmacological or toxicological properties of drugs introduced to an organism can be very different depending on the enantiomer used. Pharmaceutical regulatory authorities have set strict guidelines for the use of chiral drugs. Other industries are becoming increasingly cautious. For example, enantiomerically pure insecticides are generally preferred over racemic ones.

Despite progress in synthetic chemistry, we are still far from the perfection of nature which produces chiral products by using enzymes whose action is highly optimised to discriminate between enantiomers. Frequently, the end product of a chemical synthesis is a racemic mixture which needs to be resolved into its chiral components via a suitable separation method, such as crystallisation. Unfortunately, crystallisation from a racemic melt or solution

rarely leads to spontaneous resolution (mechanical mixture of homochiral crystals). When this does not occur, separation can be achieved by exploiting the fact that the two enantiomers interact differently with enantiomerically pure resolving agents, forming a pair of salts or molecular complexes (diastereomers) with different physical properties. By carefully choosing the resolving agent, the solubility of the two diastereomers will be substantially different and their separation will be possible by crystallising out the less soluble one. Despite the widespread use of this method, the choice of the resolving agent and process conditions is still based on trial-and-error experimentation.

Therefore, the objective of this project is to gain understanding of the crystallisation behaviour of enantiomers and diastereomer salts to progress in the challenge of predicting the separation of enantiomers by crystallisation. This will be done as part of a multidisciplinary project using experimental and computational chemistry resources. This project exploits the increased availability of highly accurate methods to model the interactions of molecules at the atomic level which allow the prediction of crystal structures, thermodynamic stability and properties of enantiomers and diastereomers from first principles. A range of experimental data, from crystal structures to resolution efficiencies, is however also needed to develop and validate the computational models used in the prediction of resolutions by crystallisation (whether spontaneous or through the formation of diastereomeric salts). This project aims to obtain such data for a number of closely related systems. This data is currently only available for few systems. This research is of significant industrial importance, as one hopes that outcomes will eventually help reduce resource-consuming trial-and-error experimentation, and contribute to the development of specialised chemical products.

## **1.2 Classification of Enantiomers: the Cahn-Ingold-Prelog rule**

Enantiomers can be classified according to various conventions, some of the most common being +/-, d/l, or D/L nomenclatures [2]. As it was mentioned earlier, the prefixes +/- and d/l are assigned depending on the enantiomers' optical activity, i.e. on the direction that they rotate plane polarised light. On the other hand, the D/L convention, which is generally used to designate amino acids and carbohydrates, uses glyceraldehyde as a reference molecule in order to assign the appropriate prefix [2, 3], and is unrelated to the direction that the enantiomers rotate plane polarised light. These conventions are not ideal since prefixes cannot be assigned independently from structural information.

In order to establish a system that would help specify the absolute configuration of enantiomers based on a self-contained set of general rules, the Cahn-Ingold-Prelog (CIP) or

sequence rule method was first introduced in 1951 [4] by Robert Sidney Cahn, Sir Christopher Ingold and Valdimir Prelog and refined in subsequent studies [5, 6]. The usefulness of the method comes from its simplicity and from the fact that it provides information on the spatial arrangements of atoms in the model.

The first step in designating enantiomers according to CIP rules is to assign priorities to each group attached to the stereo-centre. In order to assign priorities, the groups are compared by the atomic number of the atoms directly bonded to the chiral centre, with higher atomic number receiving a higher priority. Where atoms directly attached to the chiral centre are the same, the next atoms in sequence are compared and priority assigned again based on atomic number. Where atoms are double or triple bonded their atomic number is doubled or triplicated. Once the priorities have been assigned, the molecule is oriented so as the group with the lowest priority is pointing away from the observer. If the other three groups are numbered 1 to 3, 1 being the highest priority, the sense of rotation joining 1, 2 and 3 defines the stereo-centre. A centre with a clockwise sense of rotation is designated R (from rectus) whereas an anticlockwise sense of rotation is designated S (from sinister).

For example, Ephedrine, shown in Figure 1.3, has two stereo-centres of opposite configuration. If we take the first stereo-centre, labelled 1 on Figure 1.3 (a), and look at it so that the group with lowest priority (i.e. the hydrogen) is pointing away, the atoms attached to the chiral centre are oxygen and two carbons. Oxygen has the largest atomic number and therefore the hydroxyl group has the highest priority. To assign the priority of the carbons it is necessary to look at the atoms attached to them. One of the carbons is bonded to nitrogen whereas the second is part of a phenyl ring. Because nitrogen has a higher atomic number than carbon, the carbon attached to nitrogen gets higher priority. The sequence connecting the groups in order of priority is clockwise (see Figure 1.3 (b)). Hence, the first stereo-centre has an R configuration.

The same is done for the second stereo-centre (Figure 1.3 (c)). In this case, the groups attached to the chiral carbon are nitrogen, which gets the highest priority, and two carbons. The carbon attached to the hydroxyl group gets a higher priority to the carbon from the methyl group, and since the direction joining the groups in order of priority is anticlockwise, as can be seen from Figure 1.3 (c), the configuration of the second centre is S. Ephedrine is therefore labelled (1R, 2S)-Ephedrine.

As far as possible the R and S nomenclature will be used throughout this thesis. Only in certain situations will other nomenclatures be used, such as when naming amino acids and other biological molecules in which the D/L convention has stuck for historical reasons.

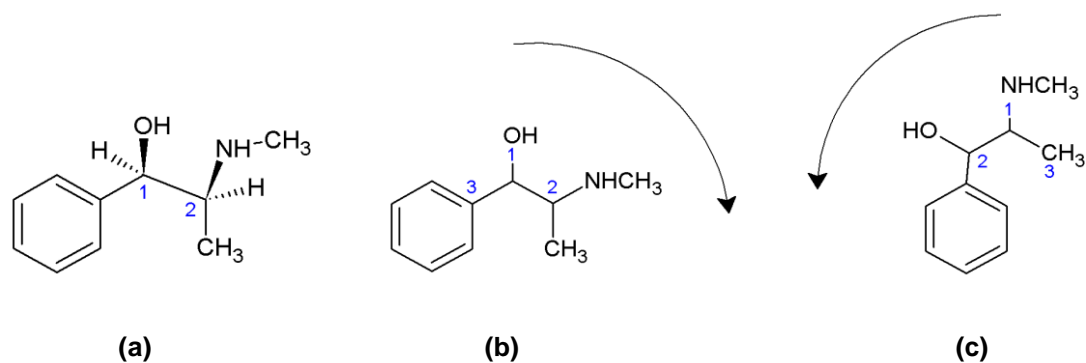


**Figure 1.3 (a)** (1R, 2S) Ephedrine – the two stereocentres are marked 1 and 2. **(b)** View of the first stereocentre as seen when the hydrogen is pointing away (into the paper) and **(c)** view of the second stereo-centre.

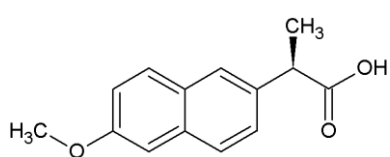
### 1.3 Biological activity of enantiomers

Unlike the behaviour in achiral environments, enantiomers have different physical and chemical properties in chiral environments. This has significant implications in biology and medicine since most macromolecules in living organisms are made up of chiral molecules. All amino acids except achiral glycine are L- enantiomers, and most carbohydrates have a D-configuration. Hence, the interaction between proteins and carbohydrates with drug compounds will tend to be stereospecific.

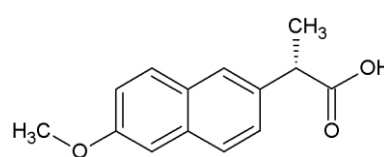
Indeed, in many cases enantiomeric pairs of chiral drugs display differences in their biological effects. Differences may range from reduced or no activity, such as in Naproxen (shown in Figure 1.4), where the ability to inhibit the enzyme cyclo-oxygenase, necessary to have anti-inflammatory and analgesic effect, resides exclusively on the (S)-enantiomers [7]; to antagonism, such as with the  $\beta_2$  agonist salbutamol in which the R and S enantiomers cause bronchodilation or bronchoconstriction respectively; or they may even present completely distinct pharmacological activities [8, 9]. It is perhaps the latter that raises most concerns, especially when the changes in activity lead to differences in toxicological properties. One can't help but remember the thalidomide tragedy of the 1960's. Thalidomide, a mild sedative, was given to pregnant women to reduce morning sickness symptoms only to discover later that at least one of the enantiomers had teratogenic effects.<sup>1</sup>

<sup>1</sup> The teratogenic effect of thalidomide has generally been thought to reside solely on the (S) enantiomer [10], after studies done on mice [11]. However, it had been shown earlier that, in fact, both enantiomers have teratogenic

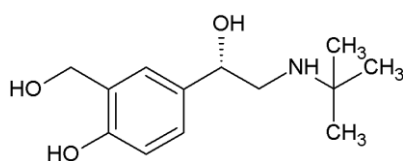
The realisation of the importance of stereochemistry in the pharmacological and toxicological properties of drugs therefore led to the introduction in 1992 of regulatory guidelines for chiral drugs by the Food and Drug Administration (FDA) in the USA, and two years later by the European Medicines Agency (EMA) [14]. This resulted in a drastic surge in the preparation and production of chemical entities as enantiomerically pure compounds in the pharmaceutical industry. The worldwide market for single-enantiomer drugs increased from \$30 billion to \$123 billion between 1992 and 2001 [9]. This, consequently, led also to an emergence of new techniques for asymmetric synthesis and enantiomeric separation [9, 15, 16].



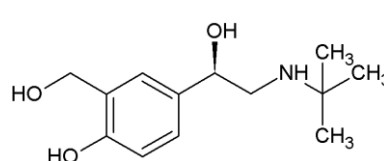
(R)Naproxen – no activity



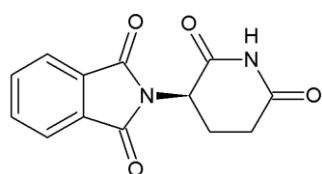
(S)Naproxen – common non-steroidal anti-inflammatory drug



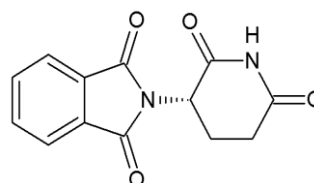
(R)Salbutamol – bronchodilator



(S)Salbutamol – causes bronchoconstriction



(R)Thalidomide – used as sedative



(S)Thalidomide – has teratogenic effects in humans

**Figure 1.4** Examples of chiral drugs and the effects of their different enantiomers

---

effects on rabbits [12]. Furthermore, it has also been shown that an interconversion between the (R) and (S) forms occurs *in vivo* [13].

## 1.4 Production of Enantiomerically Pure Compounds

In the pharmaceutical industry chiral compounds are normally obtained in their enantiomerically pure form through one of three main routes: they can either be isolated directly from a natural product; they can be synthesised, either by using an enantiopure starting material from the chiral pool (generally natural products such as amino acids, carbohydrates, hydroxy acids, etc.) or by asymmetric synthesis; or finally they can be obtained by resolution from a racemate [17-20]. The different routes to obtain enantiopure compounds are summarised in Figure 1.5.

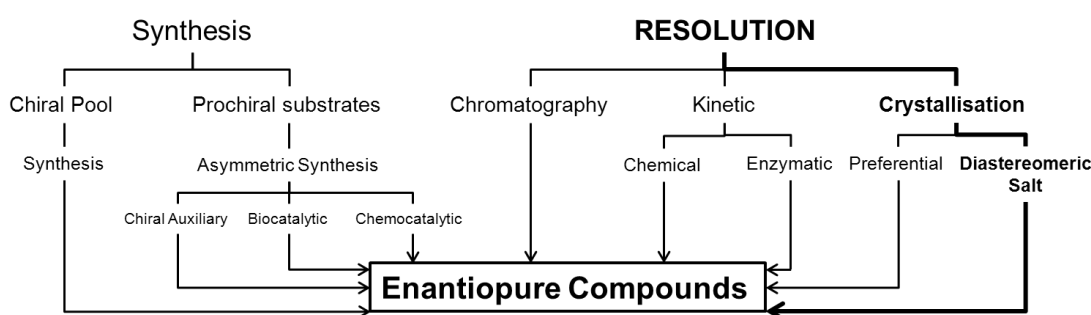


**Figure 1.5** Overview of the routes towards enantiopure compounds. This thesis will concentrate on the resolution of chiral molecules by crystallisation of diastereomeric salts.

### 1.4.1 Isolation from a Natural Product

Natural products have been, and arguably still are, the source of most of the active ingredients in medicines, as recent reviews comparing the sources of new drugs show [21, 22]. Although not all compounds isolated from natural compounds are necessarily enantiopure [23], many of them are. A good example of the importance of natural products in the production of enantiopure medicines is paclitaxel, a mitotic inhibitor used in cancer chemotherapy and sold under the trademark Taxol® by Bristol-Myers Squibb (BMS). Paclitaxel's production over the years exemplifies just how much effort the pharmaceutical industry has put in the production of enantiopure compounds as different approaches (direct isolation, total synthesis and synthesis starting from an enantiopure starting molecule) have been developed.

Paclitaxel was discovered in 1965, as part of an anticancer compound screening program set up by the National Cancer Institute in the United States, after having been isolated from the bark of the Pacific yew tree. Until 1995, the production of Taxol® was mainly based on its

isolation from the bark of the pacific yew tree. This process was, however, far from ideal as the harvesting of the bark led to the death of the tree. Therefore much effort was put into finding ways of obtaining it by total synthesis. Finally, a semisynthetic process was developed based on an initial compound isolated from the needles of a related yew tree thus sparing the life of thousands of trees that would have otherwise been killed. Currently, all paclitaxel production for BMS uses plant cell fermentation technology, in which a specific *Taxus* cell line is propagated in aqueous medium in large fermentation tanks. Paclitaxel is then extracted directly, purified by chromatography and isolated by crystallisation. Compared to the semisynthetic synthesis, plant cell fermentation eliminates the need for many hazardous chemicals and saves a considerable amount of energy.

## 1.4.2 Synthesis

Synthetic routes to the production of enantiopure compounds can be broadly divided into two methods: asymmetric synthesis or synthesis based on the chiral pool.

### 1.4.2.1 Chiral Pool

Taxol's example, where a semisynthetic route based on an initial similar chiral compound was developed, illustrates clearly the usefulness of the chiral pool, i.e. a range of enantiopure compounds that can be used in the synthesis of useful pharmaceutical ingredients. If available, the synthesis from enantiomerically rich or pure starting materials from the chiral pool is often the most effective way of introducing asymmetry into the end product [19]. Some other examples of common enantiopure pharmaceutical compounds synthesised from amino acids are ampicillin (from D-phenylglycine), lisinopril (an angiotensin converting enzyme – ACE - inhibitor derived from L-proline) and aspartame (a synthetic sweetener containing L-phenylalanine) [18].

### 1.4.2.2 Asymmetric Synthesis from Prochiral Substrates

Achiral compounds that lead to the formation of a stereogenic centre after a reaction step (e.g. creation of a chiral centre upon addition to a double bond) are called prochiral substrates. Three strategies are commonly used in the asymmetric synthesis from prochiral substrates: use of chiral auxiliaries, chemocatalysis and biocatalysis.

The use of chiral auxiliaries involves the addition of a chiral group to a prochiral substrate in order to increase the diastereoselectivity of the reaction step that leads to a new stereogenic



centre. Once the reaction has taken place the auxiliary is removed and recycled. An example of a widely used chiral auxiliary is the oxazolidinones [20] introduced by Evans to control the stereochemistry of the aldol reaction.

The synthesis of optically pure compounds from prochiral substrates may also be achieved by enzyme or chemical catalysed reactions. A good example of the success of chemocatalysis in the production of enantiomerically pure compounds is the production of the herbicide (S)-Metolachlor, in which an asymmetric hydrogenation of imine is catalysed using a ligand known as Josiphos (iridium complexed to a ferrocenyl diphosphate). This process has a capacity of more than 10000 tons a year and is one of the largest in industry [24].

The use of biocatalysts is also a feasible process used in industry, although the throughput can be much lower than chemocatalytic routes, since in order to achieve high enantiomeric excess the process must run with dilute solutions leading to a reduction in throughput [24].

### **1.4.3 Resolution of Racemates**

Though asymmetric synthesis has seen great progress in recent years, resolution methods are often still preferred for the preparation of optically pure compounds in the pharmaceutical industry [15, 25]. This is because yields are generally higher and also because the development of enantiospecific syntheses are often time consuming and economically less viable than the manufacture of racemates [19]. Furthermore, resolutions provide the availability of both enantiomers needed for studies on their properties, essential in order to satisfy FDA requirements even if the drug is developed as a single enantiomer.

The most common resolution methods in industry can be broadly separated into three major categories: chromatographic methods, kinetic resolutions and crystallisation methods [15, 18].

#### **1.4.3.1 Chromatographic Methods**

Separations using high-pressure liquid chromatography (HPLC) work on the basis of differences in the interactions between enantiomers and the chiral stationary phases within the chromatographic columns. HPLC is generally used as a preparative method only, since it requires significant amounts of solvents, and stationary phases and high pressure equipment are expensive.

In recent years however, the development of simulated moving bed chromatography (SMBC) has enabled the production of enantiomers within the gram to kilogram scale [26-28]. The SMBC process is a practical approach to the true moving bed chromatography theory. In the theoretical true moving bed chromatography approach, the chromatographic eluent and the resin circulate in opposite directions. When a binary mixture is injected, the component that is more readily adsorbed by the resin (known as the extract) will flow in opposite direction to the less readily adsorbed component (known as the raffinate), which will move in the direction of the eluent. If the flow rates of eluent and resin are carefully controlled the two components in the mixture could in theory be continuously separated and recovered. True moving bed chromatography is a very difficult process to put into practice and therefore is approximated using a simulated moving bed approach.

SMBC is a continuous chromatography separation process in which a number of columns are run in a loop by connecting the exit of one column to the feed of the next column as illustrated in Figure 1.6 (a). The liquid eluent is easily made to flow in one direction along the loop by placing pumps between the columns. However, it is impossible to create a flow of resin because it is stationary within the columns. The movement of resin in the opposite direction to the liquid flow is simulated in the SMB approach by moving the position of the inlet and exit positions in the direction of the liquid flow.

(R)-Miconazole, a drug used in the treatment of skin diseases and tuberculosis, is a prime example of a successful SMB chromatographic process operating at commercial scale [24].

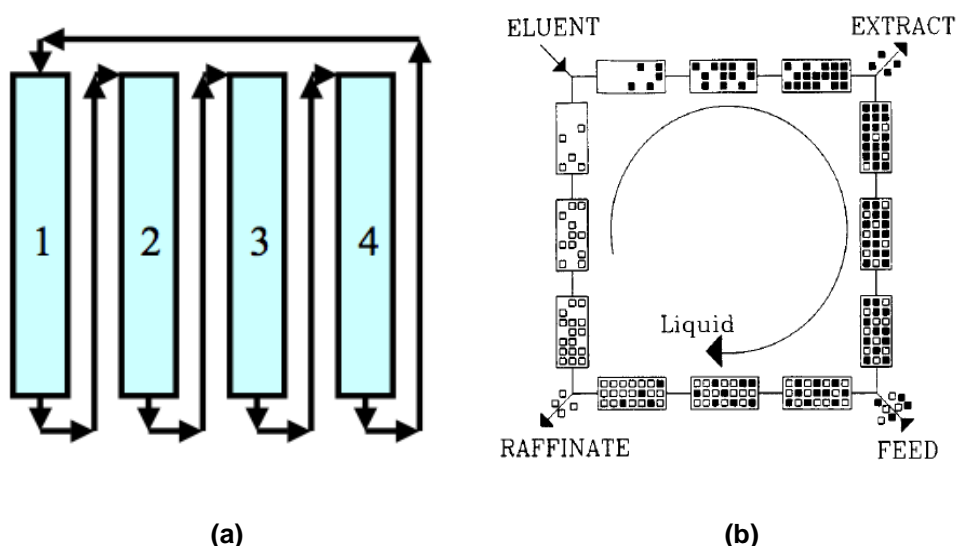


**Figure 1.6** The principle of simulated moving bed chromatography (a) The chromatographic columns are run in a loop by connecting the exit of one to the inlet of the next (b) The inlet (eluent and feed mixture) and exit (extract and raffinate) positions are moved in the direction of the liquid flow to create a moving resin effect [26].

### 1.4.3.2 Kinetic Resolution

Kinetic resolutions normally involve a step in which one of the enantiomers can be converted into product more readily than the other. This is normally achieved by using either an enzyme or an inorganic catalyst. If the unwanted enantiomer can be racemised *in situ* then the process is known as dynamic kinetic resolution. During a dynamic kinetic resolution it is theoretically possible to achieve 100% yields.

The production of Benazepril, an ACE (angiotensin converting enzyme) inhibitor used to treat hypertension, is an example of a process in which enzymatic kinetic resolution is used. L-homophenylalanine (L-HPA), one of the intermediate compounds in the production of Benazepril can be kinetically resolved from (R/S)-N-acetyl-HPA by using kidney acetone powder isolated from beef kidneys [29]. This enzymatic resolution gives 41% yield and >99% enantiomeric excess (ee).

### 1.4.4 Resolution by Crystallisation Methods

The resolution of enantiomers by crystallisation has a special place in the history of chemistry. Pasteur was the first to realise that enantiomers could be separated by crystallisation as early as 1847. After slow crystallisation of a solution of the sodium ammonium salt of tartaric acid Pasteur noticed the formation of colourless mirror image crystals, which, tradition holds, he managed to separate with help of a magnifying glass and a pair of tweezers. This resolution was only possible because sodium ammonium tartrate tetrahydrate spontaneously resolves into its constituent enantiomers<sup>2</sup> (i.e. it is a conglomerate, an equimolar mechanical mixture of crystals each one of which contains only one of the two enantiomers present in a racemate - this is discussed fully in section 2.6).

Though often seen as not technologically advanced, the separation of chiral compounds by crystallisation has been, and still is, one of the preferred techniques in industry, especially the so called classical resolution where a resolving agent is used to form diastereomeric pairs and the least soluble diastereomer is precipitated out [18].

---

<sup>2</sup> Had Pasteur carried out his experiments on a warm Parisian summer day history of science might have turned out slightly different. Sodium ammonium tartrate forms racemic crystals above 28°C [30].

#### 1.4.4.1 Resolution by Direct Crystallisation

Conglomerate forming racemates can be resolved by direct crystallisation provided that they spontaneously resolve into their constituent enantiomers. Two different techniques may be applied, simultaneous crystallisation and resolution by entrainment, both of which use seeding with enantiopure crystals to enhance the rate of crystallisation of the desired enantiomer.

In the first example, a supersaturated solution of a racemic conglomerate is allowed to crystallise in two different crystallisers simultaneously, which are seeded with the respective enantiomer and filtered before the other enantiomer begins to crystallise. The process is then repeated by mixing in a make-up vessel which is at a higher temperature in order to re-dissolve any particles that might have passed through the filter as exemplified in Figure 1.7.

The second slightly different method is resolution by entrainment, also known as resolution by preferential crystallisation [31, 32]. Gernez first described the resolution by entrainment in 1866. In this process, seeds of R are added to an initial supersaturated enriched solution of R (i.e. a solution in which the concentration of R is slightly higher than the other). On addition of the seeds, crystals of R form, thus depleting the solution of the R enantiomer and creating an enriched solution of the S enantiomer. If now seeds of S are added a cyclic process can be created in which the formation of R and S crystals could in theory be formed *ad infinitum*. In practice build-up of impurities, either from the synthetic process leading to the racemate or introduced with the seeds, limits the number of cycles that can be performed. There are many examples of the use of entrainment in industry, such as the successful resolution of the ethylamine salt of Naproxen [33]. This method has been perfected over the years as exemplified by the process known as auto seeded polythermic programmed preferential crystallisation (or AS3PC) [34].

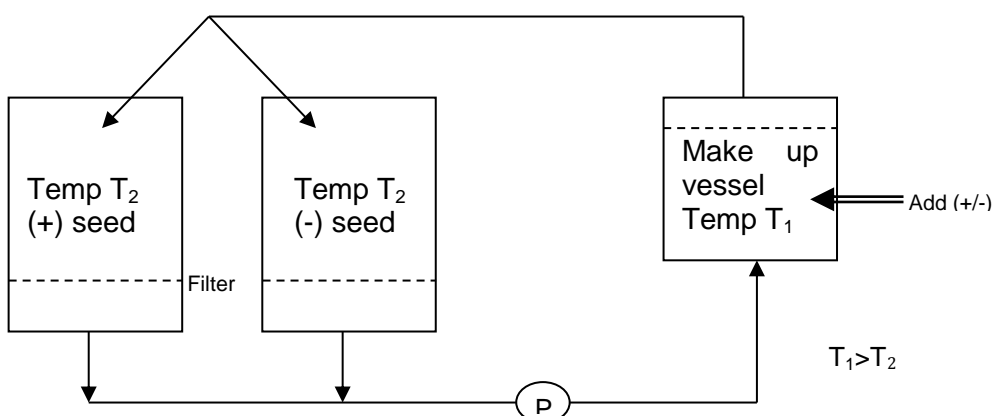


**Figure 1.7** Schematic diagram of the apparatus used in simultaneous crystallisation of enantiomers [18].

#### 1.4.4.2 Classical Resolution: Resolution by Diastereomeric salt formation

Given that only 10% of racemates crystallise as conglomerates, a more practical approach to resolutions by crystallisation is needed in order for crystallisation to be used in industry as method to resolve chiral chemical products. The most widely used technique in industry is classical resolution in which diastereomeric salt pairs with different solubilities are produced after an acid base reaction between a racemate and a resolving agent (see Figure 1.8). Again, we owe the development of this method to Pasteur, who in 1853 carried out the first classical resolution [35]. He noticed that the crystallisation of the salts of cinchotoxine with racemic tartaric acid produced crystals of salts that were enriched with D-tartaric acid.

Diastereoisomerism occurs when stereoisomers of a compound differ in one or more equivalent stereocentres, but not in all as it occurs with enantiomeric pairs. Diastereomeric pairs are therefore not mirror images of one another, as exemplified in Figure 1.8, and have different physicochemical properties. Hence, provided that the difference in solubility between the two salts is sufficient so that one remains in solution and the other can be filtered off, the diastereomeric salt pairs can be easily separated.

The designation of diastereomers in the literature is somewhat confusing. The combination of two chiral compounds may lead to four diastereomers: RR, SS, RS and SR according to CIP rules. The convention used by Jacques *et al*, and which has generally been adopted in the literature, uses the letter *p* to designate diastereomers that result from the combination of constituents which rotate plane polarised light in the same direction (i.e. +/+ or -/-) and *n* for diastereomers resulting from the combination of constituents which rotate polarised light in the opposite direction (i.e. +/- or -/+) [36]. This convention therefore takes no account of the absolute configuration of the chiral centres of the constituents.

The last step in the resolution process by diastereomeric salt formation is the recovery of the enantiomers from the salt. This is normally achieved by a simple hydrolysis step, by treating the salts with an acid or a base.

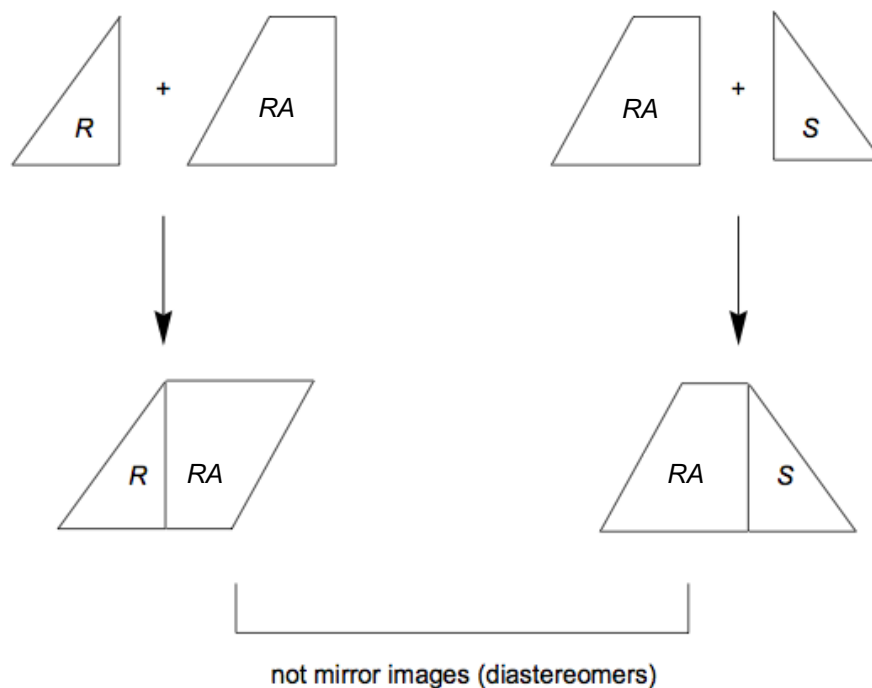


**Figure 1.8** Representation of diastereomeric salt formation between a chiral resolving agent (RA) and the two enantiomers (R or S) [37]. From the diagram, it is evident that upon formation of a salt, the two compounds are not mirror image of one another.

#### 1.4.4.2.1 Commonly Used Resolving Agents<sup>3</sup>

Some of the most widely used basic resolving agents for the resolution of racemic acids are shown in Figure 1.9. Most are naturally occurring alkaloids, such as quinine and quinidine (obtained from the cinchona bark). (1R,2S)-Ephedrine, used in the work described in Chapter 5 for the resolution of (RS)-2-phenylpropionic acid and (RS)-2-phenylbutyric, is another example of a naturally occurring alkaloid. (1R,2S)-Ephedrine is normally found in plants of the ephedra genus and is the main component in the Chinese Ma Huang, a remedy for amongst other things, a common cold.

A major drawback in using naturally occurring resolving agents is that usually only one of the enantiomers is available, since nature is extremely good at producing highly enantiopure compounds. Hence, the opposite enantiomer would have to be synthesised in order to be able to use it. Synthetic amines, such as phenylethylamine, are therefore now generally preferred, as both enantiomers are widely available.

<sup>3</sup> For a more extensive list of possible resolving agents please refer to reference [37].

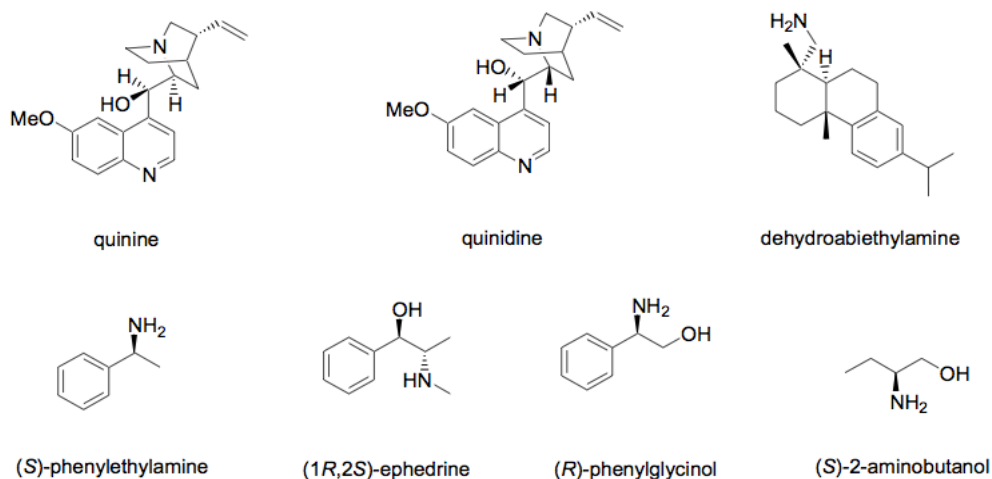


**Figure 1.9** Common basic resolving agents (taken from [36])

Acidic resolving agents for the resolution of racemic amines are somewhat more limited than basic resolving agents. The most common are tartaric acid and its derivatives, mandelic acid, the camphor sulphonic acids and N-acetylated amino acids (structures of which are shown in Figure 1.10).

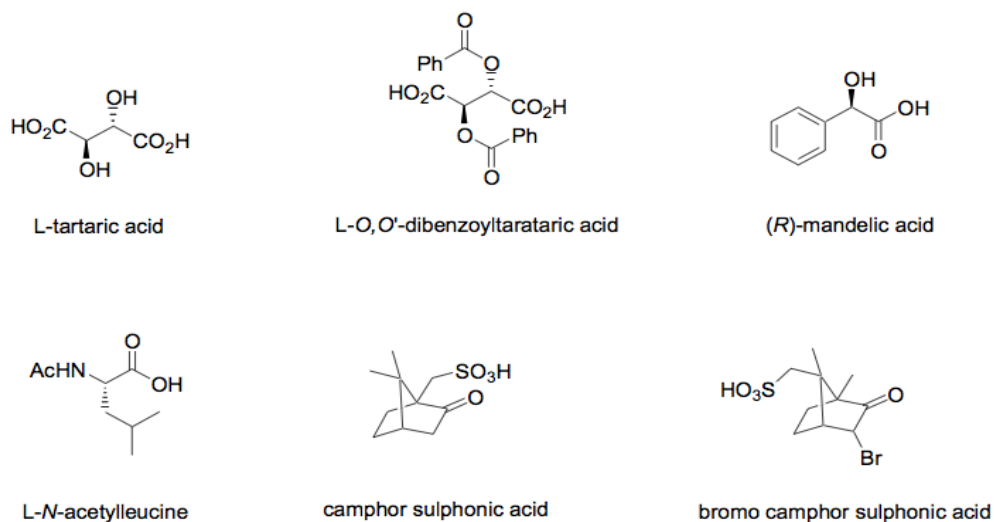


**Figure 1.10** Common acidic resolving agents.

Though quite a lot of emphasis has been put in rationalising the choice of resolving agents in classical resolution, at present this choice is mostly made based on prior experience, and then tested and developed on a trial and error basis [18].

### 1.4.4.3 Other crystallisation methods

#### 1.4.4.3.1 Dutch Resolution

This new approach to classical resolution, first described in 1998, involves the addition of a mixture of structurally related resolving agents (known as families of resolving agents) to a racemic mixture [38, 39]. Examples of families of acidic and basic resolving agents that have been used include families based on chalcone sulphonic acids, mandelic acids, cyclic phosphoric acids, phenylethylamines, and 1,2-amino alcohols, in which the resolving agents differ on the nature and position of a substituent.

In the first examples of Dutch resolution, resolutions carried out by adding three of these related compounds in a 1:1:1 ratio to a racemic mixture, resulted in isolated salts containing mixtures of the resolving agents in non-stoichiometric ratios. In ten of the forty-six cases reported in the study, at least one of the resolving agents added was not found in the first isolated salts [38]. Further experiments have shown that resolutions carried out in the presence of these poorly incorporated resolving agents lead to higher resolvabilities. It has been suggested that these poorly incorporated resolving agents act as nucleation inhibitors of the diastereomeric salts [40, 41] and by inhibiting the nucleation of the most soluble of the salts, higher resolvability can be obtained.

#### 1.4.4.3.2 Non-stoichiometric Resolutions: Method of Half-quantities and the Pope and Peachey method

In the method of half quantities, only half of the resolving agent necessary for the formation of one mole of the salt pair from one mole of racemate is used [36]. This resolution is therefore based on the separation of one of the diastereomers and one of the enantiomers as opposed to the more common method in which the two diastereomers are formed in equal quantities and are separated.

Similarly, the Pope and Peachey method [36] uses only half equivalence of resolving agent, but involves the addition of an achiral acid (or base) in order to neutralise the excess unreacted substrate<sup>4</sup>.

#### 1.4.4.3.3 Dielectrically Controlled resolution

During resolution studies by diastereomeric salt formation of (RS)- $\alpha$ -amino- $\epsilon$ -caprolactam with N-tosyl-(S)phenylalanine as resolving agent, it was observed that the crystallisation outcome, i.e. which of the two diastereomeric salts precipitated out first, depended on the solvent used [42, 43]. Further investigations looking into the physicochemical properties of

---

<sup>4</sup> For a rationalisation of these methods please refer to ref [36] and [37].



the solvents showed that there was a strong correlation between the dielectric constant of the solvent and the diastereomeric excess of the crystal product.

## 1.5 The search for Conglomerates

The choice of resolution process depends mainly on the nature of the solid state behaviour of racemic mixtures, as it has been highlighted in section 1.4.4. If a racemic mixture crystallises as a conglomerate a resolution based on preferential crystallisation principles can be designed, whereas if the mixture crystallises as racemic crystals another resolution technique has to be employed (normally resolution by the formation a diastereomeric adduct). Fast screening methods to determine whether a racemic system spontaneously resolves are of great industrial importance. The different methods that can be used to determine whether a racemic mixture has crystallised as a conglomerate, i.e. a physical mixture of both enantiomers, are described in the following sections.

### 1.5.1 Shape recognition

Due to hemihedrism, it is possible to detect a conglomerate by the morphology of the crystals formed [44]. In fact, it was in this way that Pasteur discovered and resolved the first conglomerate, by separating the crystals of sodium ammonium tartrate tetrahydrate using a pair of tweezers [45]. This method is perhaps not ideal if one intends to obtain an answer as quickly as possible, as the process of obtaining good quality crystals can be quite time consuming. Furthermore, when carrying out a crystallisation starting from a racemic solution, the presence of the opposite enantiomer often acts as a growth inhibitor, rendering smaller crystals with ill-defined hemihedral faces, and so making this method even more difficult.

### 1.5.2 Examination of the binary phase diagram

The construction of a binary phase diagram will provide the answer to the solid state nature of the racemate at temperatures close to their melting point, as discussed in Chapter 2, section 2.6, and successfully applied in Chapter 4 for Naproxen. In this method, the melting points of enantiomeric mixtures of known composition are measured, usually using a differential scanning calorimeter (DSC) or a hot stage microscope. Since conglomerates, racemates and pseudoracemates exhibit distinct differences in their melting behaviours over a composition range (see Figure 2.11 in section 2.6), this method can distinguish between the different crystal forms.

Furthermore, in situations where the enantiomers display polymorphism, a careful investigation of the melting behaviour of a binary system of two enantiomers might provide additional alternatives for the use of preferential crystallisation through the crystallisation of metastable polymorphs. A comprehensive review of the heterogeneous equilibria of binary systems of enantiomers describing all the different equilibria has been written by Coquerel [46]. Obtaining this data can however also be rather time consuming. Methods based on measuring the melting point and heat of fusion of the enantiopure and racemic mixtures have been described [63, 67]. These methods have shown to be relatively efficient for conglomerate forming systems by allowing identification of the solid state nature based on two measurements only. However these methods are further limited by being restricted to systems whose components can undergo fusion without chemical decomposition.

### **1.5.3 Examination of the Ternary Phase Diagram**

As with binary phase diagrams, the examination of the ternary phase diagram for a mixture of the R and S forms of a compound in a solvent will unequivocally provide the answer to the solid state nature of the racemate. Furthermore, careful determination of the ternary phase diagram will provide useful information for the design of a separation process. As with a binary phase diagram, obtaining a ternary phase diagram is very time consuming, and can be quite tricky when possible metastable phases exist. Recently a relatively quick method to establish the phase diagram of chiral compounds has been described [47], in which the saturation temperature for solutions of known composition is determined as opposed to the usual method, in which the saturation composition at a given temperature is determined.

### **1.5.4 PXRD, IR, Raman, solid state NMR.**

Any analytical technique used for the analysis of the solid state, can in principle be used to determine whether a racemate crystallises as a conglomerate or not. If one has an enantiopure sample and a racemic mixture, the IR, Raman or ssNMR spectra, or PXRD diffraction pattern should be exactly the same if the racemate is a conglomerate, since, apart from the chirality of the constituent molecules, the crystals are identical and these methods cannot distinguish between the chirality of the two. In the case that the patterns are not identical, this gives strong indications that the racemates must be racemic crystals or pseudoracemates. The obvious limitation of this method is that one needs to have obtained an enantiopure sample against to which a comparison can be made.

### 1.5.5 Second Harmonic Generation (SHG) [48]

Under irradiation with a light beam of wavelength  $\lambda$ , crystals with non-centrosymmetric space groups generate a beam of  $\lambda/2$  whose intensity depends on  $\chi^{(2)}$ , the second order non-linear susceptibility of the material [48]. This property provides a relatively easy and quick way of screening for conglomerates, since conglomerate forming systems will crystallise in non-centrosymmetric chiral space groups (mainly  $P2_12_12_1$ ,  $P2_1$ ,  $C2$  and  $P1$ ) while racemic forming crystals will generally not. However, there is still a small probability that racemic crystals crystallise in a non-centrosymmetric achiral space group that would hence lead to a false result. It is thought that about 4.5-5% of racemic compounds crystallise in non-centrosymmetric space groups predominantly in space groups  $Pna2_1$ ,  $Pca2_1$ ,  $Cc$ , and  $Pc$  [49, 50].

### 1.5.6 Computational Structure Prediction: can it help in the search for Conglomerates?

In recent years the use of Crystal Structure Prediction (CSP) methods has been applied to rationalise the spontaneous resolution phenomena observed for certain chiral compounds. The use of CSP methods can, in theory, also be employed to rationalise the crystallisation behaviour of chiral compounds, by calculating whether the lowest energy crystal is in a chiral space group (i.e. enantiopure) or whether in a centrosymmetric space group (i.e. racemic). In order for spontaneous resolution to occur, provided the crystallisation process is thermodynamically controlled, racemic crystals must be less stable and hence have a higher Gibbs free energy than homochiral crystals. In other words, the Gibbs free energy difference for the formation of racemic crystals must be positive.

Since entropy differences are generally small between low energy crystal structures [51], lattice energy calculations can provide insights into spontaneous resolution by estimating the lattice energy differences between homochiral and racemic crystals although, as shown by different studies, highly accurate models of intermolecular forces are needed [52-54]. Although great advance in computational prediction methods have been made in recent years, their application to the predict spontaneous resolution is still not feasible as a standalone method but rather as a tool to help rationalise why this process might be happening for some compounds but not others.

## 1.6 Efficiency of Classical Resolution

It is clear that a method for the prediction of the resolution efficiency by diastereomeric salt formation would have a major impact on the design of processes to manufacture optically pure compounds. Up to date the choice of resolving agent is mostly based on a trial and error basis, searching through a large range of resolving agents to find the best for the particular system under investigation [18, 55]. Even the development of the Dutch resolution was serendipitously made while trying to speed up the trial and error process for the choice of resolving agent, hoping that by adding more than one resolving agent to the experiment would obviate the need for multiple experiments to decide on the best resolving agent [38].

Though many studies have addressed the problem of predicting resolution, there is not a clear theory one can use to design a resolution process. The different approaches that have been used to predict resolution efficiency include computer assisted modelling [56, 57], crystal structure analysis [58, 59], investigation of the energy differences between diastereomeric salts [60], and empirical correlations [61].

### 1.6.1 Parameters for the evaluation of Resolutions

The first parameter that must be calculated in order to evaluate how well a resolution has proceeded is the enantiomeric or diastereomeric purity of the enantiomer or diastereomeric salt mixtures. These are normally expressed as the enantiomeric excess (*ee*) or diastereomeric excess (*de*). If the relative quantities of enantiomers R and S or of diastereomers RA-R and RA-S are known, it is possible to quantify *ee* or *de*:

$$ee = \frac{[R] - [S]}{[R] + [S]} \times 100 \quad 1.1$$

$$de = \frac{[RA - R] - [RA - S]}{[RA - R] + [RA - S]} \times 100 \quad 1.2$$

The relative quantities of enantiomers can be measured by chiral HPLC, by integrating the area under the peaks of the chromatogram of a particular enantiomer mixture or diastereomeric salt. Another available method that is commonly used to calculate the

enantiomeric excess of a sample is the use of a polarimeter to measure its optical rotation. The optical purity of the sample, equal to the enantiomeric excess, is then defined as:

$$\text{Optical purity (\%)} = 100 \times \frac{[\alpha]_{\text{mixture}}}{[\alpha]_{\text{puresample}}} \quad 1.3$$

Where  $[\alpha]$  is the specific rotation and is zero for a racemic mixture. The specific rotation can be calculated by:

$$[\alpha]_{\lambda}^T = \frac{\alpha}{c \times l} \quad 1.4$$

$\alpha$  being the observed rotation (in degrees),  $l$  the length of the cell (in decimetres and usually equal to 1) and  $c$  the concentration of the sample (in g/ml).

In order to compare the efficiency of resolution processes a resolvability (S) term can be calculated. The S term or S-factor, first introduced by Fogassy *et al* is calculated by multiplying the yield by the diastereomeric excess (de) of the first salt produced [61]. To avoid confusion with the supersaturation ratio (defined later in section 2.2 of this thesis) the resolution factor will be defined as the efficiency. Note, however, that in the literature S will be commonly used.

$$\text{Efficiency} = 2 \times \text{yield} \times \text{de} \quad 1.5$$

where the yield is the amount of salt precipitated divided by the initial concentration of the racemate. Given that the theoretical yield in a resolution cannot be higher than 0.5 (unless racemisation occurs in the process), the efficiency of a resolution ranges from 0 to 1 where 1 corresponds to complete separation.

## 1.6.2 Calculating resolution efficiency from phase diagrams

### 1.6.2.1 Ternary Phase Diagrams of Un-solvated Salts [62]

The thermodynamic behaviour of mixtures of two components in solution at constant temperature can be understood through ternary phase diagrams. A typical ternary phase diagram for a mixture of two un-solvated diastereomeric salts in solution is depicted in Figure 1.11. Ternary phase diagrams are usually built based on mole fractions or mole percentages. Each apex on the triangle (normally equilateral, although in some cases right hand triangles are also used) represents a pure component, in this case solvent, n and p salts. The sides of the triangle represent mixtures of the components that lie at the end of the

line. For instance, points N and P on Figure 1.11 represent the solubility of the n and p salt respectively in solvent S at a given temperature.

The information that can be obtained from an isothermal ternary phase diagram such as the one shown in Figure 1.11 is essential to understand and be able to run an efficient resolution. If one starts from M, an equimolar mixture of p and n salts, the overall composition of the system moves along line joining M and the solvent apex, as solvent is added. At any point between M and B the solid recovered by filtration will be a mixture of n and p salts in a mother liquor of overall composition  $E_u$  (whose enantiomeric composition is given by  $E_s$ ). The composition of the solid recovered at point A, for example, is  $A_s$ . Therefore, a resolution carried out with too little solvent would be inefficient as the solid recovered would be a mixture of the two salts. In order to obtain salt p only, the overall composition of the system would have to be between that represented by points B and D. This would correspond for example to a ternary system with composition C in Figure 1.11.

Line  $NE_uP$  in Figure 1.11 represents the line above which only liquid phase is present. Therefore, if more solvent were added to the system, eventually all solids would dissolve. A resolution carried out above point D would be pointless since there would be no solid phase left to recover.

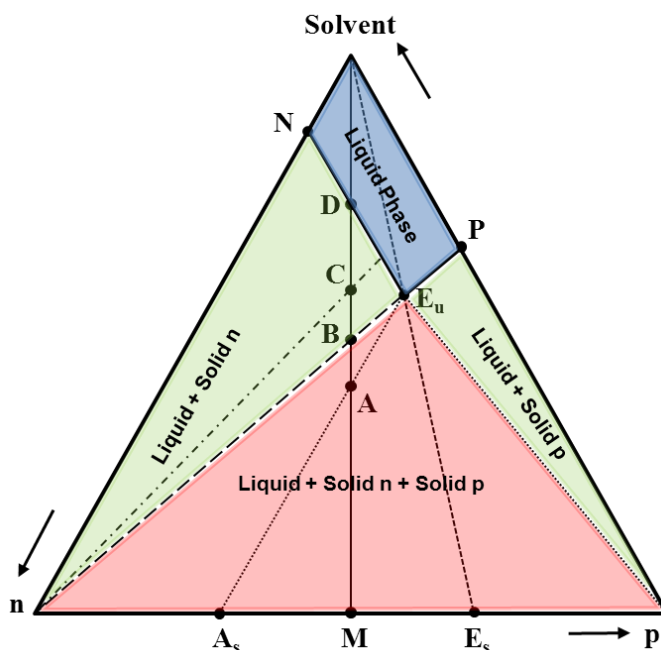


**Figure 1.11** Typical ternary Phase Diagram for a Diastereomeric salt mixture in solution.

If the resolution is carried out at equilibrium the optimum conditions for the resolution process are achieved when the overall composition of the mixture is given by B. At this point the productivity of the resolution, i.e. the mass of salt n collected compared to the total mass of the system, including the solvent, is given by:

$$Productivity = \frac{E_u B}{E_u n} \quad 1.6$$

Where  $E_u B$  and  $E_u n$  are the lengths of the corresponding segments.

The efficiency of the resolution, i.e. the mass of salt n collected by filtration compared to the total mass of salt n in the system is given by:

$$Efficiency = \frac{E_s M}{E_s n} \times 2 \quad 1.7$$

Where  $E_s M$  and  $E_s n$  are the lengths of the corresponding segments on Figure 1.11.

The efficiency can also be expressed in terms of the eutectic composition:

$$Efficiency = \frac{1 - 2x_{eut}}{1 - x_{eut}} = \frac{ee(\%)_{eut}}{50 - ee(\%)_{eut}} \quad 1.8$$

where  $x_{eut}$  is the composition of salt n of the dry residue of the eutectic solution.

Therefore, for an efficient resolution the eutectic composition should be as close to diastereomeric purity as possible [37, 63, 64]. Knowing what the maximum resolution efficiency that can be obtained for a particular system is very useful because, if not reached experimentally it might indicate that equilibrium has not been attained. It is also possible to calculate the maximum yield from eutectic composition:

$$Y_{max} = \frac{0.5 - x_{eut}}{1 - x_{eut}} \times 100 \quad 1.9$$

### 1.6.2.2 Possible problems towards an efficient resolution: solid solutions, solvates and intermediate compounds [36].

One of the problems that might be encountered when carrying out a resolution is partial or total miscibility in the solid state. In this situation the salts in equilibrium with the solution contain both enantiomers as can be seen from the tie lines joining the solid and liquid phase compositions in Figure 1.12. This therefore results in a decrease in the quality of the resolution, as the solids recovered are no longer enantiopure.

If a resolution process were run at an overall composition corresponding to A on Figure 1.12 (a), the solid collected by filtration would be a single solid phase, mixture of the two diastereomeric salts with composition given by  $A_s$ . In order to increase the purity of salt n recovered, several re-crystallisations would be required. However, as purity increases yield tends to 0% and therefore a balance between the purity obtained and yield must be met.

Where total miscibility in the solid state occurs, a resolution will always lead to poor efficiencies since the salt recovered will always be a mixture of both salts (Figure 1.12 (b)). Several crystallisations may lead to the increase of one of the salts in the solid phase but will never reach 100% ee. Furthermore, as the ee approaches 100% yield tends to 0%.

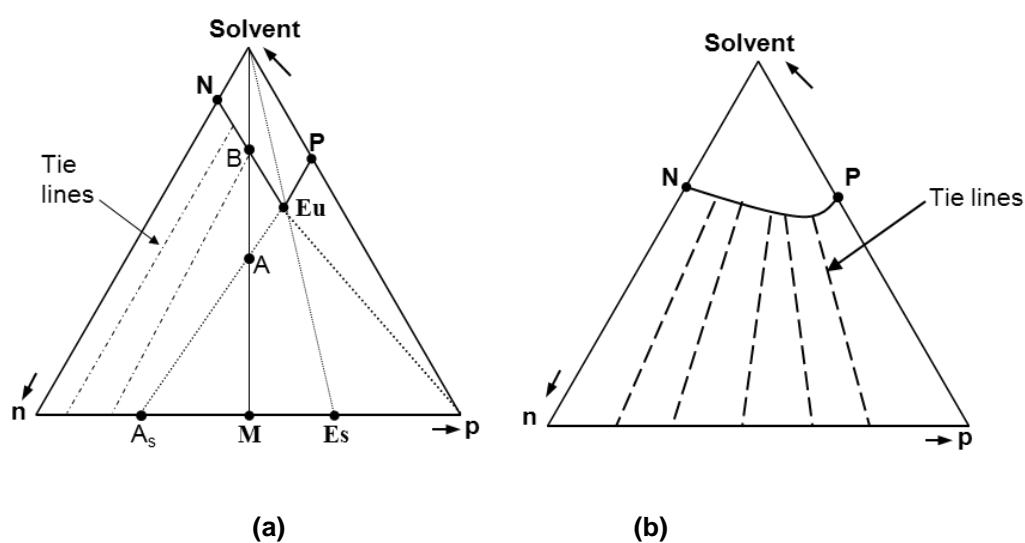


**Figure 1.12 (a)** Partial solid solution of salt p in the pure salt n **(b)** total miscibility between the two salts.

Another slight problem that might be encountered during the resolution process is the appearance of solvates or intermediate compounds. The phase diagrams associated with these are represented by Figure 1.13 and Figure 1.14 respectively.



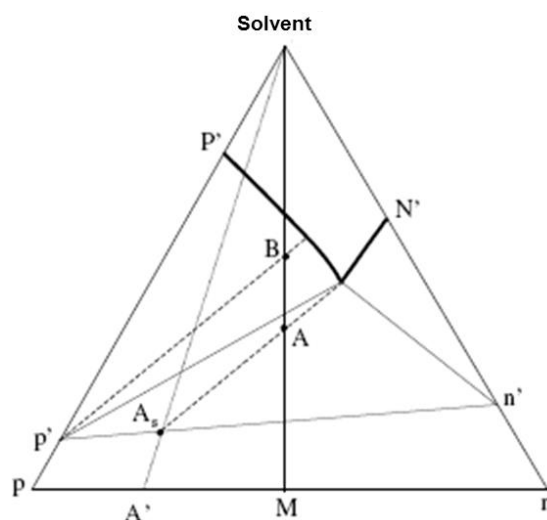


**Figure 1.13** Ternary phase diagram for the solvates ( $n'$  and  $p'$ ), of  $n$  and  $p$  diastereomeric salts [65].

The interpretation of a phase diagram for the solvated phases of the diastereomeric salts is analogous to that of the classic case of un-solvated salts. In this case, however, the composition of the recovered salt contains some solvent, represented by  $p'$  and  $n'$  on Figure 1.13. The presence of a solvate does not necessarily have an effect on the purity of the salt recovered in a resolution process, since a resolution carried in the right composition range (e.g. point  $B$  on Figure 1.13) will contain no unwanted salt in the end product. The only consequence on the process design will be the need for a de-solvation step in order to be able to recover pure salt  $p$ . The consequences that the appearance of solvates might have on the resolution efficiency will depend on whether both salts are solvated and the effect the solvation has on the solubility difference of the salt pairs, since this will affect the position of the eutectic. Since solvation usually increases the solubility, solvation of the more soluble salt only might increase the efficiency of the resolution since the difference in solubility between the solvated pair and unsolvated pair will be increased and hence the position of the eutectic shifted closer to the edge of the least stable salt.

A further potential complication to a resolution process is the crystallisation at equilibrium of intermediate compounds, such as 1:1 double salts. In the case where the double salt shows a congruent solubility, as shown in Figure 1.14 (a), the resolution process cannot be run at equilibrium, and is only possible if the nucleation of the stable double salt is avoided, under metastable conditions. This situation would correspond to the area delimited by the dashed lines on Figure 1.14 (a), with  $Eu'$ ,  $A'$  and  $B'$  as the characteristic compositions. In the case where the double salt exhibits a non-congruent solubility, as in Figure 1.14 (b), the resolution process could be run in the composition range between  $A$  and  $B$ . However, the efficiency of this resolution is much decreased compared to that obtained under metastable conditions,

as can be seen by the displacement of  $Eu'$  (associated with the polysaturated point in the metastable equilibrium) compared to  $Cs$ .

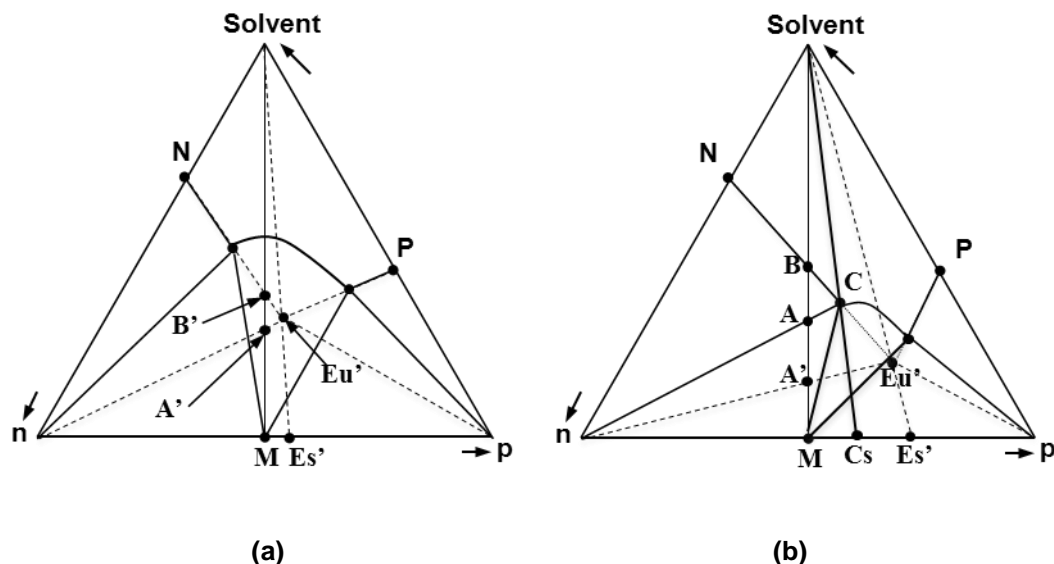


**Figure 1.14** Ternary phase diagram of 1:1 double salts with (a) congruent solubility (b) non-congruent solubility [62].

### 1.6.2.3 Construction of Ternary Phase Diagrams

The construction of a ternary phase diagram is normally achieved by the method of wet residues [36]. In this method, one begins with a known mixture of salts in a known amount of solvent, represented by  $s$  on Figure 1.15. The mixture is left under constant stirring in a sealed flask at a fixed temperature until thermodynamic equilibrium has been reached (normally a few days). Once equilibrium has been reached, the mixture is vacuum filtered. The amount of solvent in the mother liquor can be determined by distillation. The composition of the solute after evaporation of all the solvent can be determined by chiral HPLC. From the data obtained one can then plot point  $m$  on the ternary phase diagram represented on Figure 1.15.

Once the composition of the saturated solution is known, one determines that of the wet solids recovered by filtration. The amount of solvent in the wet filter cake is determined by evaporation, and the composition of the solids is again determined by chiral HPLC. These values provide the composition of point  $w$ . By extrapolating the tie line joining  $m$ ,  $s$  and  $w$  one obtains the composition of the solid phase i.e.  $n$ .

An alternative method to quickly determine the composition of **n** would be to wash the solids after filtration with cold solvent to then determine the enantiomeric excess by HPLC. This method however could lead to errors due to unwanted dissolution of the material, and could potentially miss the formation of solvates.

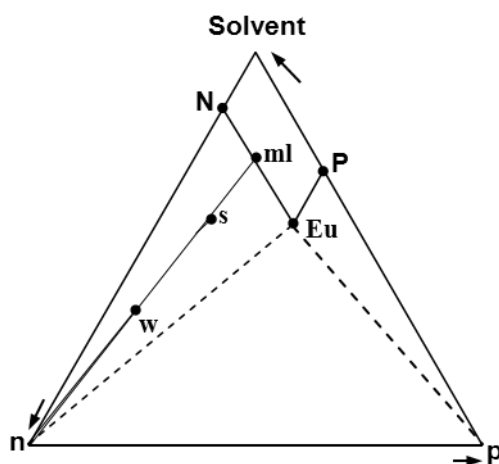


**Figure 1.15** Construction of a ternary phase diagram by the method of wet residues.

A faster method, and one employed in Chapter 5 of this thesis, is that of Hill and Ricci [66] also known as the method of algebraic extrapolation. This method requires one to measure the composition of the liquid phase, point **ml** on Figure 1.15, and to know what the starting composition is, point **s**. A mass balance on the whole system leads to the composition of the solid phase.

Although ternary phase diagrams are very useful to design resolution processes, their calculation is a very laborious and time-consuming process and therefore is not always measured. Furthermore, in order to be able to construct the ternary phase diagrams, large amounts of both diastereomers are required and these are not generally widely available. Therefore, a quicker and more practical approach to obtain information on the optimal resolution efficiency is required.

#### 1.6.2.4 Binary Phase Diagram

Based on work by Leclercq and Jacques [67] in which they found that the position of the eutectic does not depend much on temperature, and assuming that the solubility ratio between the salts is constant, if the temperature in a ternary phase system is increased to

the point where no solvent is required, the eutectic composition is the same in the ternary and binary phase diagrams, as seen in Figure 1.16. If one refers back to equation 1.8 it can be seen that now the maximum efficiency does not depend on the solubility relation but only on the location of the eutectic. This therefore allows an estimation of the resolution efficiency through a binary melting point phase diagram, which is more easily obtainable than ternary phase diagrams.

Melting point phase diagrams describe the behaviour of two components on melting (in this case either the different enantiomers or the different diastereomeric salts), and are represented by plotting the beginning and termination melting temperatures as a function of composition, which is usually expressed in mole fractions (see Figure 1.17). The construction of melting point phase diagrams is now usually done from melting point temperatures collected by differential scanning calorimetry (DSC). Differential calorimeters work by heating (or cooling) a sample and a reference cell simultaneously at constant rate, and measuring the energy required to keep the two cells at the same temperature. Another slightly different widely used technique is differential thermal analysis or DTA. In DTA, the supply of energy per unit time is kept constant for the two cells and the difference in temperature between the cells is measured.

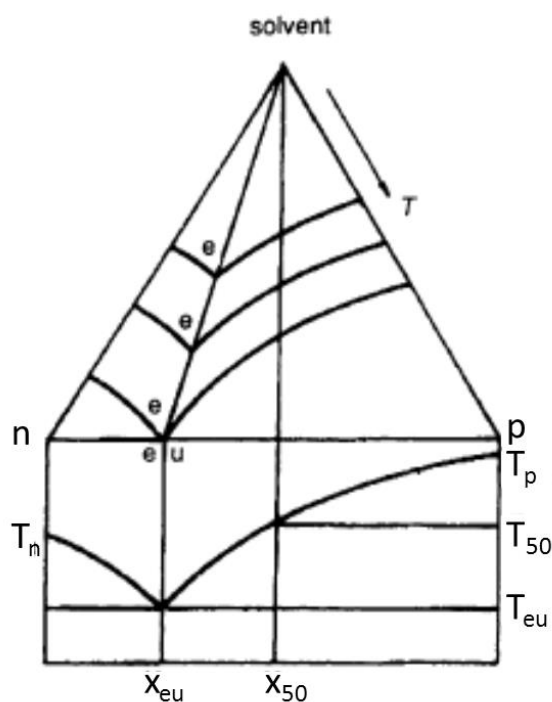


**Figure 1.16** If the composition of the eutectic is not affected by temperature, the composition of the eutectic in a ternary and a binary phase diagram should be the same [63].

When a sample is heated, in the temperature range where no phase change occurs, the heat capacity of the sample and reference cell are the same, and therefore a nearly horizontal signal line is obtained. However, when a phase transition occurs, more energy must be supplied (or removed, if the transition is exothermic) to the sample cell, and the additional heat supplied a signal is recorded, the area of which provides the enthalpy for that given transition.

The graph on the right on Figure 1.17 shows a typical DSC thermogram for a binary mixture of diastereomers exhibiting a eutectic. The graph is in fact turned 90° anticlockwise to help show how the data relates to the melting point phase diagram. Typically the temperature runs along the x-axis while the energy supplied is on the y-axis. An endothermic phase transition is normally recorded upwards. The data obtained in this graph can be used to plot the binary phase diagram shown on the left. The first peak corresponds to the beginning of melting and corresponds to the eutectic temperature. This temperature also defines the solidus, i.e. the temperature under which only solid phase is present. This is marked on the binary phase diagram as  $T_{eu}$ . The second peak corresponds to the termination of fusion and defines the liquidus for a particular mixture of composition  $x_y$ . This is represented as  $T_y$  on the binary phase diagram on Figure 1.17.

The melting point phase diagram can therefore be determined experimentally by measuring the melting behaviour of a set of mixtures of known compositions. In order to be able to locate the composition of the eutectic accurately usually more measurements are taken around this area, once the region where it is located has been delimited.

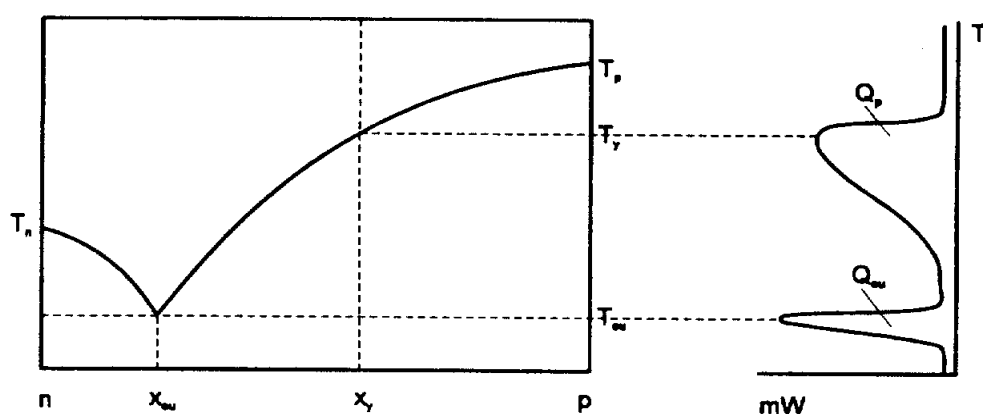


**Figure 1.17** Example of the construction of a binary phase diagram from DSC data [68].

The experimental construction of the binary phase diagram by DSC to determine the composition of the eutectic and to use as a method to calculate resolution efficiency is much faster and easier than the construction of the ternary phase diagram, especially nowadays with the availability of automated DSC instruments. The limiting factor in this technique is the accurate preparation of mixtures of known compositions, which would require the use of very accurate microbalances.

However, it is also possible to calculate the liquidus curve for the melting point phase diagram of a conglomerate forming system using the simplified form of the Schröder-van Laar equation. The Schröder-van Laar equation relates the mixture composition to their melting points as follows:

$$\ln x = \frac{\Delta H_i^f}{R} \left( \frac{1}{T_i^f} - \frac{1}{T^f} \right) \quad 1.10$$

where  $x$  is the mole fraction of a mixture whose melting point is  $T^f$ , and  $\Delta H_i^f$  and  $T_i^f$  are the enthalpy of fusion and melting point of the diastereomer  $i$ , and  $R$  is ideal gas constant. The Schröder-van Laar equation is valid under three conditions:

- i) Immiscibility of the diastereomers in the solid state
- ii) Ideality of the diastereomer mixture in the liquid phase and
- iii) The heat of fusion does not depend on the temperature.

Using this method the binary phase diagram can be easily constructed using a few milligrams of both pure diastereomeric salts. The validity of this method was tested by Leclercq and Jacques who determined several phase diagrams in which the liquidus curves calculated by means of the Schröder van Laar equation from the enthalpies of fusion and melting points of the pure salts matched the experimentally measured points [67].

#### **1.6.2.5 Limitations in the use of Binary Phase Diagrams to predict resolution efficiency**

Although DSC is a very easy and quick method that can be used to predict the efficiency of a resolution by the measurement or calculation of the binary phase diagram, its use has some inherent limitations that must be acknowledged since they might be serious enough to make the method useless. The first obvious one is that the samples must not undergo decomposition before melting in order to be able to measure the melting temperature and heat of fusion. This can prove to be quite an important limitation, since organic salts decompose quite easily upon heating. Secondly, if the melting point and heat of fusion of the

diastereomeric salts can be measured and are used to calculate the binary phase diagram using the Schröder-van Laar equation, it is assumed that the diastereomeric salt pair behaves ideally (for a discussion on the validity of the Schröder-van Laar equation see section 2.7). Furthermore, in order to approximate the binary phase diagram to the ternary phase diagram it is assumed that the polysaturated solution has the same enantiomeric composition as the binary eutectic composition, regardless of the temperature. This has been found to be the case for a number of systems; however, this does not imply that it will hold true for all systems and therefore must be taken with care. A further limitation is that any solution effects that might affect the resolution efficiency, such as the appearance of solvates, are ignored with this method.

### 1.6.3 Crystal Structure-Resolvability Relationships

The analysis of crystal structures to rationalise the resolution processes has been very popular [59, 69-71], especially in recent years from the so called crystal engineering point of view, which tries to identify intermolecular interaction patterns in the packing arrangements of crystals structures, in order to be able to design supramolecular assemblies that might have desired properties [58, 72].

Early studies by Brianso [59, 73, 74] investigating the 1-phenylethylammonium salts of 2-phenylpropionic acid, 2-phenylbutyric acid and mandelic acid identified the problems in the crystallisation of at least one of the salt pairs of these systems. She found that the common morphology of these systems was thin needles that in most cases were not sufficiently good for X-ray diffraction studies [59]. Nonetheless, she managed to determine the structure of five of these six diastereomeric salts. It was found that the crystal structures of these diastereomeric salts consist of columns of hydrogen bonded ions along a helical  $2_1$  axis held together by weak van der Waals interactions. The problematic crystallisation behaviour observed in the diastereomeric salt pairs of 1-phenylethylammonium salts of 2-phenylpropionic acid and 2-phenylbutyric acid has also been observed in our crystallisation screens of (1R,2S)-ephedrine with 2-phenylpropionic acid and (1R,2S)-ephedrine with 2-phenylbutyric acid (Chapter 5).

In this area, extensive studies carried out by Kinbara *et al.* [58] provide a wide range of structural data supported with the resolvabilities of a range of similarly related systems. In their early studies involving the systematic study of the ability of mandelic acid to resolve a set of substituted 1-arylalkylamines, it was found that un-substituted, ortho and meta substituted 1-arylalkylamines could be efficiently resolved by mandelic acid but that para-substituted amines were very poorly resolved [75]. They hypothesised that the extended length of the amines hindered their resolution using shorter resolving agents. To support

their hypothesis, it was found that p-methylmandelic and p-methoxymandelic acid had a higher resolving ability than mandelic acid [75]. Through the determination of the crystal structures of three diastereomeric salt pairs they identified the formation of the characteristic hydrogen bonded columns around  $2_1$  screw axis that had been previously described by Brianso [73]. They also noticed that the columns pack so as to form a planar boundary surface that is thought to maximise van der Waals interactions (Figure 1.18 (a)) [76]. This hydrogen bonding and packing arrangement was commonly found in the less soluble salts, suggesting that these crystals were stabilised with respect to both the hydrogen bonding and van der Waals interactions. On the other hand, it was found that the corresponding more soluble salts displayed either  $2_1$  columnar hydrogen bonding or planar boundary surfaces but not both [76]. The crystal structures of the mandelic salts of the poorly resolved para-substituted amine were also determined, and showed that, when the van der Waals interactions were maximised by the planar boundary surface, the hydrogen bonding network was very complicated. On the other hand, when the efficient hydrogen bonded  $2_1$  columns did form, the packing of the columns was hindered by the methyl on the phenyl group projecting out of the layer (Figure 1.18 (b)). The fact that none of these salts were able to crystallise so as to maximise both the hydrophobic interactions and the hydrogen bonding network, provide an explanation to why the difference in solubility between the diastereomeric salt pair are so similar and hence why the poor resolvability of the system. Extending the length of the resolving agent did lead to the desired effect of stabilising the crystal structure of the less soluble salts from the viewpoint of both the hydrogen bonding and the van der Waals interactions [76].

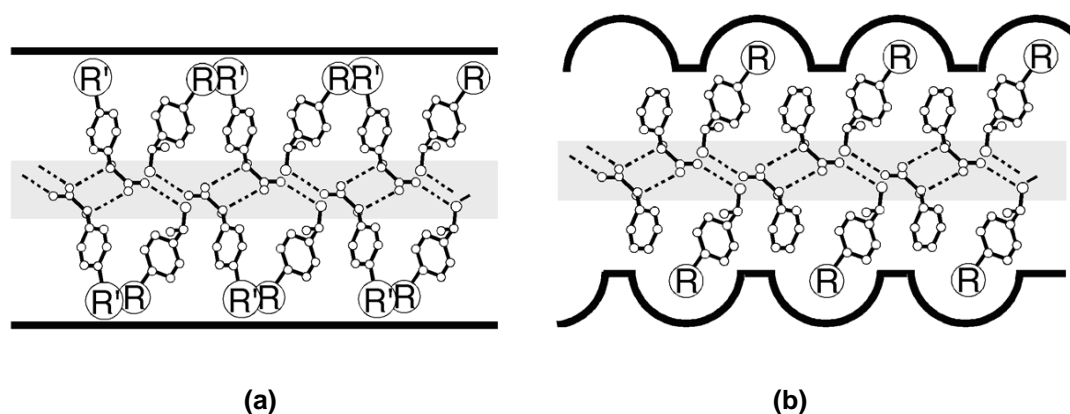


**Figure 1.18** (a) Packing of hydrogen bonded columns forming an efficient planar hydrophobic surface (b) Inefficient packing of hydrogen bonding columns in which substituents at the para position project out of the plane [58].

Although the resolution of the para-substituted amines had improved considerably by using a longer resolving agent, the results were not sufficient for practical applications. One of the



reasons that were suggested was that the flexibility of the substituent on the para position of the phenyl ring of the resolving agent does not provide a stable molecular length. This hypothesis led Kinbara *et al.* to synthesise and use (2-naphthyl)glycolic acid (shown in Figure 1.19) as a resolving agent for a wider set of para substituted 1-arylalkylamines [77, 78].

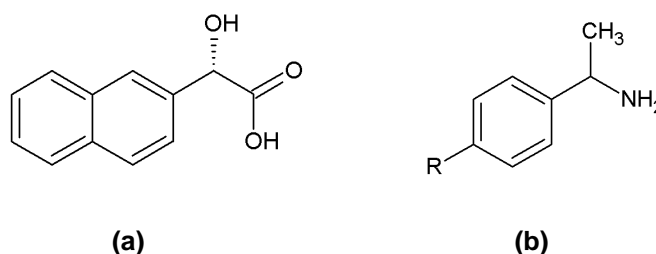


**Figure 1.19** Systems studied by Kinbara *et al* for the design of an acidic resolving agent [77] **(a)** (2-naphthyl)glycolic acid, **(b)** 1-arylalkylamine R can be Me, Et, Pr, OMe, c-Hex, Cl, Br, NO<sub>2</sub> or Phe.

Again, an improvement in the resolution was seen. Inspection of the crystal structures of three diastereomeric salt pairs showed that, in addition to the importance of hydrogen bonding and hydrophobic interactions to the stability of the crystals of diastereomers salts, the aromatic group of the ammonium ions were further stabilised by CH- $\pi$  interactions with neighbouring naphthyl groups from the anions [50]. In fact, in these structures, CH- $\pi$  interactions were more important to the relative stability of the crystal structures than stabilisation by hydrophobic interactions. The structures of the less and more soluble salts were in this case very similar, with similar hydrogen bonded columns joined to form sheets with planar hydrophobic surfaces. The differences in stability between them arise from subtle differences in hydrogen bonding or in how effective the CH- $\pi$  interactions are. In two of the pairs the position of the hydroxyl group in the less soluble salt enabled the formation of one extra hydrogen bond with the ammonium group of the cation, conferring these salts improved stability. In the third pair, the number of hydrogen bonds was the same with very similar bonding pattern. However, the inter-planar angle between the aromatic groups of the less soluble salts was 84°, close to the ideal 90° for efficient CH- $\pi$  interaction. On the other hand, the inter-planar angle between phenyl groups in the more soluble salts was 54° i.e. far from ideal. Their finding on the apparent importance of CH- $\pi$  interactions in the stereoselectivity of resolving agents led them to the design of a basic resolving agent (shown in Figure 1.20) for arylalkanoic acids based on the naphthalene moiety which resulted in good resolvability coefficients [79].

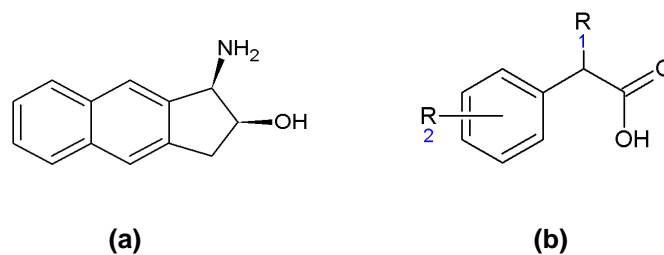


**Figure 1.20** Systems studied by Kinbara *et al* for the design of a basic resolving agent [79] **(a)** cis-1-aminobenz[f]inan-2-ol (ABI) **(b)** arylalkanoic acids where  $R_1 = \text{Me, Et or Pr}$  and  $R_2 = \text{H, o-Me, m-Me, p-Me, p-Cl, p-Bu, Phe, or Phe-p-OMe}$ .

Another important contribution made by Kinbara *et al.* to the field of chiral resolution by crystallisation from a crystal engineering point of view was the study of the salts of chiral primary amines with achiral carboxylic acids in order to find commonly supramolecular assemblies that would lead to the formation of conglomerate salts [80]. During these studies, two commonly occurring hydrogen-bonding motifs were found. The first one, common to all the conglomerate forming salts, are the  $2_1$ -columns consisting of two ammonium and two carboxylate ions related by a twofold screw axis. The two anion and cations form a ten-membered ring which can be represented  $R_4^3(10)$  in the graph set notation proposed by Etter *et al* [81]. Salts with this motif normally crystallise either in space group  $P2_12_12_1$  or  $P2_1$ . This type of hydrogen-bonding motif can also be found in racemic compounds (i.e. racemates which contain both enantiomers in equal amounts in the unit cell – refer to section 2.7). In this case, columns of opposite chirality will alternate either parallel or antiparallel depending on the space group adopted. The second hydrogen-bonding motif, which is only found in salts crystallising as racemic compounds, consists of ammonium ions related by an inversion centre. This motif is therefore known as *i*-columns. The motif consists of two different alternating hydrogen bonded rings. The first ring is  $R_4^2(8)$  and the second is  $R_4^4(12)$ .

Further work carried out by Lemmerer *et al* [82] studied the crystal structures of the salts formed by naphthalene-2-carboxylate and naphthalene-2,6-dicarboxylate with enantiopure and racemic 1-phenylethylammonium, and provided thermal data to investigate their relative stabilities. Their results showed that the same hydrogen bonding motifs that were described in Kinbara's study were conserved. The structures of the salts consisting of homochiral ammonium cations consisted of the  $P2_1$  columns whereas the structure of the racemic salts consisted of *i*-columns. The thermal data suggested that the first type of hydrogen bonded network is more stable, given that the melting points of these structures were considerably higher [83].

Though many efforts have been made, there is a lack of systematic studies linking the structural characteristics of both salts of a diastereomeric pair with thermodynamic and

stability data. It is also important to note that the approach of most of these studies is qualitative and do not give quantitative measures of the contribution of intermolecular forces such as repulsion-dispersion and polarisation.

Therefore, this approach is not entirely suitable to explain and predict the stereoselectivity of certain resolving agents for particular racemates. At most, these studies provide an idea about what functionalities to look for when deciding what resolving agent one should use. A quantitative evaluation of different intermolecular interactions is done using crystal structure prediction methods, as described below in Section 1.6.4.

#### **1.6.4 Theoretical Basis for the use of Computational Crystal Structure Prediction methods to understand chiral resolution**

This section will begin with the thermodynamic rationale that is behind the use of crystal structure prediction methods to predict the resolution ability of different resolving agents. Once the reasoning is established the theoretical basis for computational crystal structure prediction methods will be explained, followed by an outline of the methods used in this research. This is done in some detail as the major theme of this thesis is the provision of experimental data, both structural and thermodynamic, to test and validate CSP methods.

##### **1.6.4.1 Rationale for CSP use in predicting Spontaneous Resolution**

In order for spontaneous resolution to occur, provided the crystallisation process is thermodynamically controlled, racemic crystals must be less stable and hence have a higher Gibbs free energy than homochiral crystals.

In other words, the Gibbs free energy difference for the formation of racemic crystals from homochiral crystals must be positive.



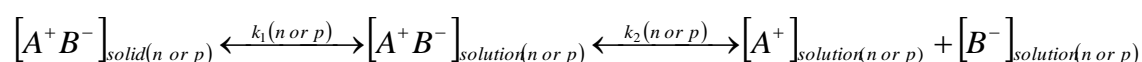
Since entropy differences are generally small between low energy crystal structures [51], lattice energy calculations can provide insights into spontaneous resolution by estimating the

lattice energy differences between homochiral and racemic crystals. However, the accuracy of the prediction requires highly accurate models of intermolecular forces [52-54, 84].

#### 1.6.4.2 Thermodynamic Basis for CSP use in Classical Resolution

The application of molecular modelling techniques to predict the resolution ability of a given resolving agent, was first investigated by Leusen et al [56]. In their study the authors provided a thermodynamic rationale linking resolution efficiency to the diastereomeric salts' lattice energies, thereby opening the doors to the use of crystal structure prediction methods to predict the resolution efficiency in classical resolution.

It was first noted that an effective resolution depends on the following solvation equilibria:



1.12

Where  $A^+$  and  $B^-$  are the acid and base ions respectively. If the difference in the pKa between the acid and base is large enough one can assume that the ions are fully dissociated and solvated, and therefore the Gibbs free energy of solvation can be related to the equilibrium constants by

$$\Delta G_{solv} = -RT \ln(K_{solv}) \quad 1.13$$

Where  $K_{solv}$  is the solvation equilibrium constant, given by

$$K_{solv} = \frac{[A^+]_{solution}[B^-]_{solution}}{[A^+ B^-]_{solid}} \quad 1.14$$

Since  $[A^+ B^-]_{solid} \equiv 1$  the solvation equilibrium constant can be expressed as the square of the concentration i.e.

$$K_{solv} = [A^+]_{solution}[B^-]_{solution} = c_{(n \text{ or } p)}^2 \quad 1.15$$

where  $c$  is the concentration of the salt in solution. The difference between the Gibbs free energies of solvation of the two diastereomeric salts can therefore be linked to the salts' solubilities by

$$\Delta\Delta G_{solv} = RT \ln(c_p^2) - RT \ln(c_n^2) \quad 1.16$$

$$\Delta\Delta G_{solv} = 2RT \ln\left(\frac{c_p}{c_n}\right) \quad 1.17$$

Although the difference in Gibbs free energy of solvation between diastereomeric salts cannot be calculated using current computational methods, this difference can be approximated to the static lattice energy of the salts, which is amenable to current computational methods (see Section 1.6.4.10). Using the thermodynamic cycle shown in Figure 1.21, and assuming that the salts are completely solvated so that there is no inter-ionic interactions in solution, i.e. an ideal solution, the Gibbs free energy difference between the two salts in solution (i.e.  $\Delta G_{solution}$ ) is negligibly small. Therefore it is possible to approximate the difference in Gibbs free energy of the salts in the solid state (i.e.  $\Delta G_{solid}$ ) to

the difference in Gibbs free energy of solvation or  $\ln\left(\frac{c_p}{c_n}\right)$ , i.e.

$$\Delta\Delta G_{solv} \approx \Delta G_{solv(p)} - \Delta G_{solv(n)} \approx \Delta G_{solid} \approx 2RT \ln\left(\frac{c_p}{c_n}\right) \quad 1.18$$

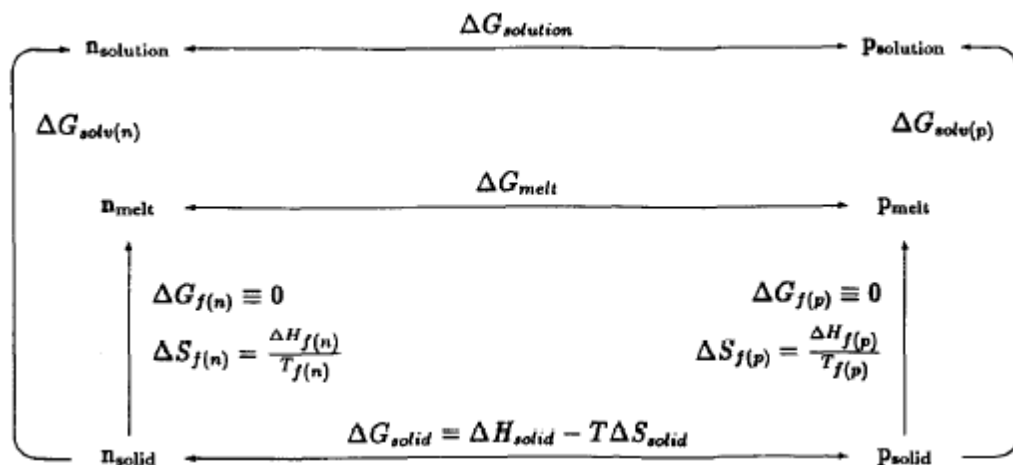


**Figure 1.21** Thermodynamic cycle used to describe the link between the resolution of diastereomeric salts, n and p, and the solid state properties of the diastereomeric salts. The outer cycle corresponds to the resolution process. The inner cycle is used to approximate the difference in Gibbs free energy to the lattice enthalpy of the salts [56].

Computational prediction of the free energy difference is still not accessible with current molecular modelling methods because the zero-point energy, entropy, and temperature dependent contributions to the enthalpy need to be very accurately determined and have to

consider molecular flexibility and thermal expansion. However, the experimental investigation of 11 diastereomeric salt pairs of ephedrine with phenyl-substituted cyclophosphoric acid showed that the solubility ratio between diastereomeric salts correlates well with their enthalpy difference [56]. Therefore it is possible to assume that the entropy of the two salts is the same, i.e.  $S_p \approx S_n$ . If one further assumes that the zero-point energy and specific heat capacities of the two diastereomers are similar, then it is possible to approximate the solubility difference of the diastereomeric salts by their static lattice energies:

$$U_{latt}^p - U_{latt}^n \approx 2RT \ln\left(\frac{c_p}{c_n}\right) \quad 1.19$$

where  $U_{latt}$  is the static lattice energy, which is the sum of the intermolecular interaction energies between all the rigid molecules in the crystal.

The computational calculation of static lattice energies is a more realistic target to modern computational chemistry developments. Indeed, recent advances in computational chemistry and the constant improvement in the computer power available is opening the possibility that crystal structure prediction (CSP) might be used as a tool to aid the design of resolution methods by diastereomeric salt formation [56, 57, 85, 86].

CSP methods work on the assumption that crystallisation is thermodynamically controlled. Under this assumption the most stable unit cell must be the one that has a lowest Gibbs free energy:

$$G = U + PV - TS \quad 1.20$$

where  $U$  is the internal energy,  $V$  the volume and  $S$  the entropy. Most approaches approximate the free energy by the lattice energy (which refers to the internal energy) at 0K and 0 Pa, neglecting zero point contributions. At normal pressures, and given that organic solids are not very compressible, the contribution of pressure to the relative stability of similarly dense structures is negligible and therefore it is possible to neglect the pressure term. The thermal and entropic effects cannot be accurately modelled with current methods. Nevertheless, it is plausible that the magnitude of these contributions is small compared to the errors inherent in the lattice energy minimisations.

Having noted the thermodynamic approximations, the following sections will look at the accuracy in the methods used to evaluate the lattice energies.

### 1.6.4.3 Intermolecular forces

The lattice energy is defined as the energy released when molecules in their lowest energy conformation that were previously infinitely separated and randomly arranged, form a regular perfect lattice to form a static crystal. For such a process to occur the Gibbs free energy change ( $\Delta G = \Delta H - T\Delta S$ ) related to this process has to be negative. The loss of entropy arising from the arrangement of the molecules in the system has to be outweighed by a gain in enthalpy.

The enthalpy of the system is determined by the magnitude of the attractive and repulsive forces that arise on bringing the molecules together, so as to minimise the empty space within the crystal, as outlined in Kitaigorodskii's principle of close packing [87]. Therefore, the main challenge of crystal structure prediction is to be able to accurately quantify the magnitude of these attractive and repulsive forces, as they determine the packing of the molecules and hence the density and morphology of the crystal.

For spherical molecules, the intermolecular energy ( $U_{(R)}$ ) between two molecules can be represented by a plot of the intermolecular energy as a function of intermolecular separation, as shown in Figure 1.22 [88]. The energy gain for such a system is maximised at a certain intermolecular separation ( $R_e$ ) where the balance between attractive and repulsive forces is at an optimum value leading to a minimum in the interaction energy between the two molecules ( $-\epsilon$ ). Most molecules however are non-spherical and therefore the problem is further complicated as the orientation of the molecule has to be taken into account. The intermolecular energy has to be expressed as a function of intermolecular distance ( $R$ ) and orientation ( $\Omega$ ).

Intermolecular interactions are generally classified into two categories, long-range and short-range interactions, depending on the extent of the overlap in the electron density of a pair of molecules. At short distances, where there is a considerable overlap in the electron densities of the two molecules, the main interaction is the exchange-repulsion energy. The dominant repulsion contribution arises so that the Pauli exclusion principle [89] (i.e. that electrons with the same spin cannot occupy the same space) is not infringed. At these short intermolecular distances, however, there is also a weak attractive interaction, stemming from the delocalisation of electrons between the different molecules. This is known as the exchange energy. The interaction energy at these short distances decreases exponentially with intermolecular distance, i.e.  $U(R) = A\exp(-BR)$  at short range.

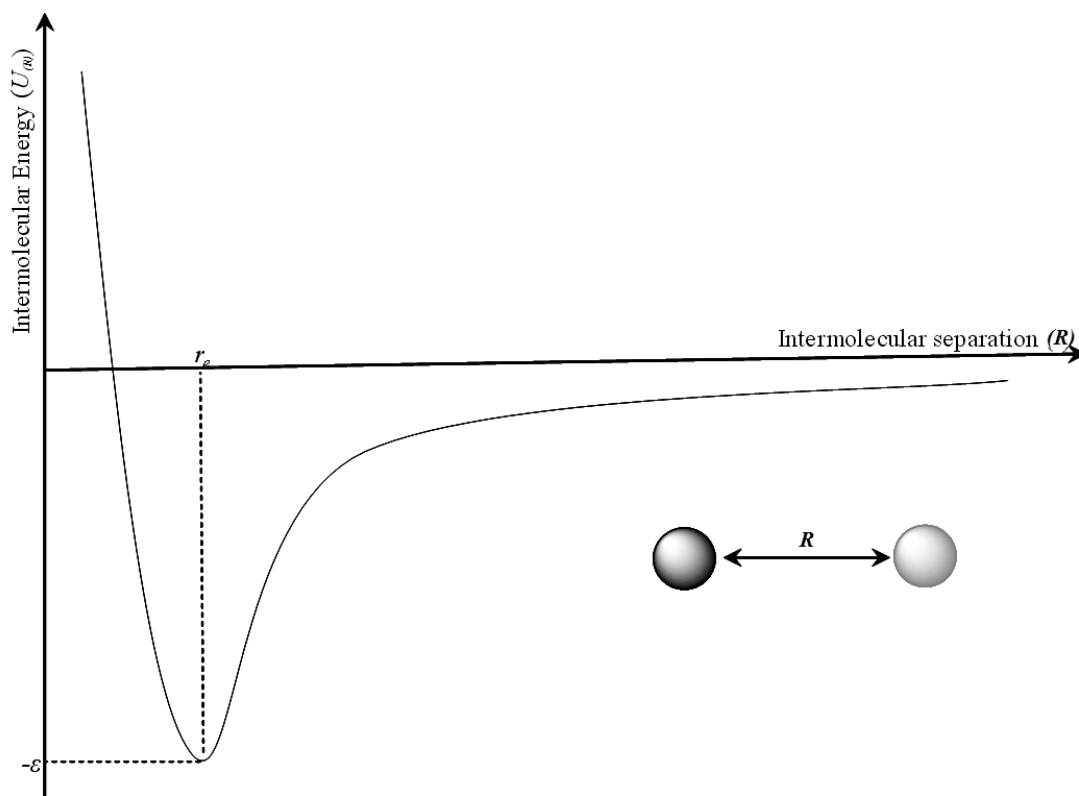


**Figure 1.22** Intermolecular energy  $U_{(R)}$  as a function of the intermolecular separation ( $R$ ) between two spherical molecules. The energy minimum at the equilibrium distance of separation ( $R_e$ ) [88].

On the other hand, for molecules that are separated by relatively large distances, the electron density overlap is negligible and is therefore assumed to belong to the individual molecules. Forces arising from long-range interactions are generally attractive and the magnitude of the interaction energy is related by some inverse power of the intermolecular distance. The main contributions to the long-range range interactions are: electrostatic, induction (sometimes referred to as polarisation) and dispersion interactions.

Electrostatic effects arise from the Coulomb like interactions between the static charge distributions of two molecules, and can be attractive or repulsive. The electrostatic energy is pairwise additive i.e. that for a collection of molecules, the energy is equal to the sum of all two body interactions. For example, for a system consisting of molecules A, B and C the potential will be calculated as the sum of the interactions  $AB+AC+BC$ , where the energy for AB interaction is calculated as if C was not present.

Induction energy is always attractive, and is caused by the changes in molecular charge distribution due to the electric field of the neighbouring molecules. Because the fields of neighbouring molecules might reinforce each other or cancel out induction is non-additive.



Finally, dispersion forces arise as the result of the instantaneous correlation in the charge fluctuations of the molecules. Dispersion is universal, always attractive and approximately pairwise additive.

#### 1.6.4.4 Modelling Electrostatic Interactions

The simplest way of calculating the electrostatic potential energy is the use of Coulomb's law, from the pair-wise interactions of isotropic (spherical) point charges placed on each atom of the molecule:

$$U_{elec}^{MN} = \sum_{i \in M, k \in N} \frac{1}{4\pi\epsilon_0} \frac{q_i q_k}{R_{ik}} \quad 1.21$$

where  $\epsilon_0$  is the vacuum permittivity constant, also known as the dielectric constant. In this form, the electrostatic interaction energy,  $U_{elec}^{MN}$ , between two atoms,  $i$  and  $k$  of type  $\iota$  and  $\kappa$  which are in molecule M and N respectively, depends only on the distance between the atoms,  $R_{ik}$  and their respective charges,  $q_{i(or\kappa)}$ . Unfortunately, site charges cannot be measured experimentally or computed directly as they depend on the method of dividing the molecular charge distribution into atomic sites. This is not a trivial problem and many methods exist to assign charge density to atoms, such as Hirshfeld's stockholder partitioning method [90] or Bader's atoms in molecules approach. The latter, which is perhaps the most rigorous, uses a zero flux surface to divide the molecular charge density into a set of atomic charges. The zero flux surface is a two dimensional surface on which the charge density is a minimum in the direction normal to the surface. For molecular systems minima are found between atoms, and hence these points are taken to partition the electron density into a set of atomic volumes. However, problems arise if the electrostatic energy is calculated using atomic charges solely, as the different methods of partitioning the charge distribution will lead to differences in the net charges and the neglect of the effects of the electron densities (that are not represented by the point charges) and hence in the electrostatic potential. Most modelling programs therefore use potential derived atomic charges, which are calculated by directly fitting the numerical values of the atomic charges to the electrostatic potential around the molecule [91, 92] as this gives the most accurate representation of the electrostatic potential. The electrostatic potential can be computed through quantum mechanical calculations, or from the experimental charge density analysis of X-ray diffraction data [93-95].

Due to the anisotropy of the charge distribution, in many instances it is still necessary to introduce additional non-nuclear charges in chemically sensible positions (bond centres and lone pair positions) in order to be able to accurately reproduce the electrostatic potential, as

noted by Williams [96, 97]. The method for calculating the potential derived charges implemented in CrystalPredictor, the search algorithm used in this thesis, optimises the number and location of these non-nuclear sites [98]. The CrystalPredictor algorithm is described in more detail in section 1.6.4.8.

Another approach used in this thesis to represent the molecular charge distribution to give more accurate electrostatics is the more elaborate distributed multipole model [88, 99, 100]. In the distributed multipole model, the electron density is described by a series of individual multipole moments (i.e. charge, dipole, quadrupole, etc. up to the hexadecapole level) that are centred at the atomic nuclei. The multipoles can either be fitted to the electrostatic potential [101, 102] or derived from the isolated molecule wavefunction [99, 100]. The multipole moments calculated in this thesis are computed from the molecule's wavefunction using the program GDMA [100]. The representation of the electron density by a set of dipoles and quadrupoles has been shown to give a much better representation of electron density distribution associated to lone pairs and  $\pi$ -electron densities in molecular organic crystals [102-104]. The use of distributed multipoles is therefore a necessary improvement for CSP so as to accurately model hydrogen bonding and  $\pi$ - $\pi$  stacking.

#### 1.6.4.5 Modelling repulsion-dispersion interactions

There are many different mathematical expressions for the repulsion-dispersion potential, but the two isotropic expressions that are more commonly used in crystal structure prediction methods are the 12-6 Lennard-Jones model [105] and the exp-6 Buckingham potential [106]. An empirically derived repulsion-dispersion potential based on the Buckingham *exp-6* function is used in this thesis as it is more realistic, and is represented by equation 1.22 below:

$$U_{rep-disp}^{MN} = \sum_{i \in M, k \in N} A_{ik} \exp(-B_{ik} R_{ik}) - \frac{C_{ik}}{R_{ik}^6} \quad 1.22$$

where the interactions are between atom  $i$  of type  $\iota$  in molecule  $M$  and atom  $k$  of type  $\kappa$  in molecule  $N$  separated by a distance  $R_{ik}$ . The exponential term represents the repulsion occurring at short distances whereas the negative  $R_{ik}^{-6}$  term deals with the long range dispersion contributions. The empirical atom-atom parameters ( $A_{ik}$ ,  $B_{ik}$ ,  $C_{ik}$ ) describe the extent of the repulsion-dispersion forces for each type of atom and are obtained by fitting

heats of sublimation of different crystal structures of organic molecules. In using this model it is assumed that the interactions between molecules are a result of the sum of all interactions between their constituent atoms, and that the empirical atom-atom parameters ( $A_{ik}$ ,  $B_{ik}$ ,  $C_{ik}$ ) are transferable between different molecules. The latter assumption is reasonable in situations where the functional groups present in the molecules to be modelled are the same as those found in the molecules to which the Buckingham potential has been parameterised. The values of the heteroatomic parameters,  $A_{ik}$ ,  $B_{ik}$ , and  $C_{ik}$ , can be derived from the homoatomic values are known, using the following combining rules:

$$A_{ik} = \sqrt{A_{ii}A_{kk}} \quad 1.23$$

$$B_{ik} = \frac{1}{2}(B_{ii} + B_{kk}) \quad 1.24$$

$$C_{ik} = \sqrt{C_{ii}C_{kk}} \quad 1.25$$

The parameters used in this thesis were derived by Williams et al [107] by fitting C and H parameters to a set of hydrocarbon crystal structures and subsequently, once these had been optimised, held constant for the parametrisation of oxygen [108], nitrogen [109], fluorine [110] and chlorine [111]. These parameters are included in the FIT force field. The WILL force field has also been tested in this thesis, and contains parameters of C, H, N and O which depend on the hybridisation state and atomic connectivity [112].

#### 1.6.4.6 Modelling Induction

Induction is not explicitly modelled in this thesis. However, the need for explicitly modelling the induction contribution has been the subject of much debate [113-115]. It is generally assumed that the empirical intermolecular pair potentials used for the calculation of repulsion-dispersion effects (described previously in Section 1.6.4.5), will have absorbed the effects of induction during the fitting to organic crystal structures. It is worth noting though, that the induction contribution towards the lattice energy has been shown to be of importance, especially for ionic salts, but also for some non-polar organic molecules [116, 117]. Furthermore, Welch et al [115] found that in situations where the hydrogen bonding of two polymorphs differ significantly, explicit inclusion of the induction energy contribution, obtained from high quality wavefunctions and large basis sets, improved the relative ranking of structures based on their lattice energies. The approach described, however, is very computationally expensive. Performing isolated-molecule charge energy calculations within a

continuum dielectric to approximate the molecule's environment in the solid state has been suggested as a cheaper alternative. Cooper et al [118] showed that the use of a Polarizable Continuum Model (PCM) [119] to introduce the continuum dielectric influenced the relative conformational energies and electrostatic interactions in the crystal structure prediction of polar, flexible molecules. Thus, the lack of an explicit model for the induction energy is one of the major approximations in the lattice energy calculations in this thesis.

#### **1.6.4.7 Computational methodology for the generation of plausible crystal structures**

The methodology used in this thesis for the generation of plausible crystal structures of organic molecules including diastereomeric salts is a three stage approach [120], in which the accuracy of the lattice energy calculations is improved as the number of crystal structures that need to be modelled is reduced. The first stage is the generation of trial unit cells with local minimisation of an isotropic atom-atom model as implemented in CrystalPredictor [121] search algorithm. The second stage is the refinement of a set of low energy structures using a more realistic distributed multipole electrostatic model. Finally, for conformational flexible molecules, a selection of the most stable structures is subjected to the relaxation of their flexible degrees of conformational freedom and corresponding cell refinement using the CrystalOptimizer [122] algorithm.

#### **1.6.4.8 Generation of structures using CrystalPredictor [121]**

The first stage in the process of a crystal structure prediction method is the generation of a set of close packed, dense candidate crystal structures that are energetically feasible, without any prior knowledge of the unit cell. This step is crucial since missing the experimental structure at the initial stage would make the accuracy of later stages irrelevant. Therefore, the programmes used to generate the candidate structures must be efficient enough to provide a thorough sampling of the space, but also accurate enough to ensure that the experimentally most stable structures are not discarded. The difficulty of the search for all possible crystal structures is increased considerably by increasing the number of independent molecules in the asymmetric unit, as well as by increasing the molecules' flexibility.

The approaches that have been used to tackle the packing problem are quite varied and have been reviewed elsewhere [123, 124] The algorithm used in this thesis, CrystalPredictor [125], tackles the search using a purely mathematical approach in contrast to simpler programs such as MOLPAK [126] that use analyses of known crystal structures to restrict the search. The CrystalPredictor algorithm generates structures in a user defined search

space, i.e. the user defines the number of molecules in the asymmetric unit and the set of space groups that need to be considered. Although CrystalPredictor is able to carry out searches in all possible space groups, searches are in fact generally restricted to the most common space groups. Importantly, searches for the crystal structures of homochiral molecules can be restricted further to non-centrosymmetric space groups. Out of these normally the five most common -  $P2_12_12_1$ ,  $P2_1$ ,  $P1$ ,  $C2$  and  $P2_12_12$  – are chosen.

Given the number of molecules in the asymmetric unit and the set of space groups that have to be sampled, the decision variables that have to be defined in order to create trial unit cells of flexible molecules are the space group, the magnitudes of the lattice parameters (i.e. lattice lengths and lattice angles) the position and orientation of the independent molecules in the unit cell and also the values of selected torsion angles. The first of these decision variables that CrystalPredictor selects is the space group. The extent of search in a particular space group, i.e. the number of structures generated, is proportional to the number of symmetry elements for that particular space group and the number of times it appeared in the CSD for organic crystals at the time the programme was written. Once the space group has been selected, the algorithm then selects values for the other decision variables. In order to ensure good coverage of the multidimensional search space for the remaining decision variables, CrystalPredictor uses Sobol' deterministic low-discrepancy sequences [127]. Sobol' sequences have been shown to give more uniform coverage when compared to the Monte Carlo or grid methods that are employed in other search methods [128]. The resulting unit cells are checked to see whether they are sensible or not by looking at their density and possible steric hindrance (structures where the intermolecular atom-atom distances are less than  $0.5\text{\AA}$  are eliminated). The lattice energy of the structures are estimated using a Buckingham exp-6 potential and an electrostatic model that consists of atomic charges derived by fitting to the electrostatic potential of the ab initio single molecule wavefunction [98]. Each structure is then optimised to reach a local minimum in the lattice energy. The last step in the generation stage is to check whether the generated structures are unique. CrystalPredictor does this by comparing the lattice energy, density and intermolecular distances between atoms for the minima in the energy landscape.

Given that CrystalPredictor only uses a crude model to calculate the lattice energy, the unique structures that are within a carefully considered energy range from the global minimum, usually 20kJ/mol, are refined further. Typically 1000 structures are carried forward to the next stage.

#### **1.6.4.9 Refinement of Low Energy Hypothetical Structures**

The second step in the process is to refine the structures that lie within 20 kJ/mol from the global minimum, by introducing a better representation of the electrostatic energy. At this

stage single point ab initio calculations are performed on the isolated molecules retrieved from each of the structures to be refined, using GAUSSIAN with an improved level of theory and a distributed multipole analysis is performed on the calculated wave-function using GDMA [99, 100]. DMACRYS[129] is then used to re-minimise the crystal structures keeping the molecules rigid, and calculating the lattice energy using the distributed multipoles previously calculated and the FIT parametrisation of the *exp*-6 repulsion-dispersion potential.

#### 1.6.4.10 Calculation of the Lattice Energy using CrystalOptimizer [122]

The molecules and diastereomeric salts considered in this thesis are flexible, in that small changes in the position of the hydrogen bonding protons can make a significant difference to the lattice energy (see Chapter 6). Hence, there is a need to account for the effect of packing forces on the molecular conformations.

The representation of molecular flexibility in the CrystalOptimizer algorithm assumes that most intra-molecular degrees of freedom will not change much compared to those of the gas phase optimised molecular conformation (such as torsions in aromatic systems and most bond lengths and angles), and that therefore only a few selected flexible degrees of freedom (such as torsion around single bonds) need to be considered to represent the extent of molecular flexibility. Therefore, the more rigid degrees of freedom and the intra-molecular energy can be approximated as a function of the flexible degrees of freedom. It is also important to note that the estimation of the intra-molecular energy is done with respect to the global - or local - minimum gas-phase molecular energy.

For flexible molecules the lattice energy is estimated according to equation

$$E_{latt} = U_{inter} + \Delta E_{intra} \quad 1.26$$

where  $U_{inter}$  is the inter-molecular lattice energy and  $\Delta E_{intra}$  is the energy penalty for the molecular distortion from the most stable molecular conformation that occurs to improve the intermolecular interactions.

To allow for changes in  $\Delta E_{intra}$  CrystalOptimizer algorithm breaks the lattice energy minimisation problem into a two-level optimisation problem. In the first level of the optimisation, the intra-molecular energy is evaluated using GAUSSIAN for varying flexible degrees of freedom. For each flexible degree of freedom results in a value for the rigid degrees of freedom and for the intra-molecular energy penalty,  $\Delta E_{intra}$ . In the second level of the optimisation, the intermolecular energy and lattice variables is evaluated for each conformation generated in the previous optimisation using DMACRYS [129].

In order to reduce the high computational costs associated with having to perform a quantum mechanical calculation every time the flexible degrees of freedom are varied, CrystalOptimizer estimates  $\Delta E_{\text{int } ra}$  using a Local Approximate Model (LAM) which is based on a quadratic Taylor expansion constructed around a reference conformation, taken to be the gas phase optimised conformation. LAM's are updated regularly, every time the flexible degrees of freedom change by more than 4°. When this happens CrystalOptimizer performs a constrained geometry optimisation fixing the torsions to the new values, and calculates the new molecular charge density. Multipole moments and intra-molecular energies for each point are stored in a database that can be later re-used. While the change in conformation from the last stored LAM is smaller than 4° the multipole moments are rotated with the local environment, a method that has been previously described and shown to considerably reduce computational cost [120].

### **1.6.5 Previous work on the Crystal Structure Prediction of Diastereomeric salts**

Examples of the application of molecular modelling techniques to predict resolution by diastereomeric salt formation are not very numerous and, in recent years, consist mainly on the research done by Leusen [56, 85] and Karamertzanis and Price [57, 86]. It was Leusen in 1993 who proposed the approximate thermodynamic relations that link resolution ability with solid state properties (see equations 1.18 and 1.19) that are amenable to computational prediction methodologies [56]. However, at that time the computational methods and computational power available were not sufficient for the prediction of potential structures and relative lattice energies of the diastereomeric salts of ephedrine with a series of phosphoric acids. Further work carried out 10 years later using the CFF95 force field for the energy calculations, and using Polymorph Predictor for the generation of crystal packing alternatives (starting from the low energy gas phase conformers of ephedrine and chlocyphos identified with CFF95 force field [130]) managed to find the experimental crystal structures of the diastereomeric salts of ephedrine chlocyphos. Unfortunately these structures were not the global minimum in lattice energy but within 3 kcal/mol [85]. Although the study did show a significant advance in CSP given the complexity of the mathematical search problem, the accuracy of the lattice energy calculation was not good enough to provide a predictive method for the resolution ability.

One of the main characteristics of a novel approach described by Karamertzanis and Price for the prediction of the crystal structures of the diastereomeric salt pair of (R)-1-phenylethylammonium (R/S)-2-phenylpropionate, was the use of statistical information obtained from the CSD to form a range of ion-pair clusters with defined geometries that are most representative of the database to be used as starting point in the generation of crystal

structures [57]. This method proved to be a very effective solution to the problem of the vast number of different possible packing arrangements diastereomeric salts can adopt, by providing an efficient way of generating initial structures. The choice of the ions' starting conformations was also done by comparison of the low energy gas phase conformation with the most represented conformations in the CSD, hence reducing the number of starting conformations. The repulsion-dispersion contribution to the intermolecular interactions was modelled with Williams's empirical force field, and the electrostatic contribution was calculated by a set of atomic multipoles. Lattice energy minimisations were carried out with DMAREL [131].

Using the methodology described, Karamertzanis and Price managed to predict the known crystal structure of the least soluble most stable salt of (R)-1-phenylethylammonium-2-phenylpropionate as the global minimum [57]. On the other hand, the predictions for the more soluble salt pair were found to be extremely sensitive to the molecular conformations, and a vast range of possible packing arrangements were generated. It was suggested that this finding could help explain the polymorphic nature of the less soluble salt and the difficulty in growing good crystals. Overall, this study did not manage to provide a quantitative prediction of the resolution efficiency although it did provide a qualitative agreement with experimental results.

In a subsequent study, the potential of the computational methods developed were further scrutinised by comparison with a set of experimental data for three diastereomerically related salt pairs formed by (R)-phenylethylammonium with (R/S)-2-phenylpropionate, (R/S)-2-phenylbutyrate and (R/S)-mandelate [86]. The validity of the results obtained from the predictions were tested against structural and thermodynamic data obtained by solution calorimetry and thermal measurements [132-134]. In the method described, the generation of initial structures was done by CrystalPredictor [121], using the method describe in Section 1.6.4.8. The optimisation of the best structures was done with the DMAflex method [135], which allows the rotation of torsion angles under crystal packing forces (an earlier version of CrystalOptimizer that did not include the LAM database). This study managed to reproduce qualitatively the relative stabilities of the diastereomeric salt pairs and of the different polymorphic forms. The importance of the accurate modelling of the intra and intermolecular energies was highlighted by the only exception in which the stability of (R)-phenylethylammonium-(S)-mandelate compared to (R)-phenylethylammonium-(R)-mandelate was overestimated.

Although the search strategy employed in this study managed to generate all known crystal structures for the systems studied, two of the polymorphs of phenylethylammonium-2-phenylbutyric acid were found outside the range usually considered for further refinement (see Section 1.6.4.9), and were only modelled in later stages because they were known experimentally [86]. Again, this highlighted the difficulty in achieving an efficient, extensive



and accurate search of the complex lattice energy surface for diastereomeric salts. Furthermore, the predictions for (R)-phenylethylammonium-(S)-2-phenylbutyrate suggested that there might be a 36 kJ/mol more stable and 10% denser structure than the experimentally observed structure. Further computational investigations [136] suggested that the experimental observed structure could be a hydrate as the incorporation of one or two water molecules in the voids present would stabilise the structure. However the redetermination of the structure from powder X-ray diffraction data together with elemental analysis data excluded this possibility [136]. In this study an extended polymorph screen was also conducted to see whether the predicted more stable structure could be crystallised. Although two more metastable polymorphs were identified, they did not match the hypothetical predicted structure [136]. Hence, this illustrates that either the method was giving great errors or that the crystallisation experiments were producing metastable forms of the diastereomeric salts. As shown in Chapter 5, obtaining the most stable form from a crystallisation experiment is not always very easy.

These studies have shown that, despite the progress made in the last 20 years in the prediction of diastereomeric salt structures, there is considerable progress to be made in order to be able to provide a quantitative prediction of the resolution efficiency. Given the exponential dependence of the solubility ratio on the Gibb's free energy, the quantitative prediction of the Gibb's free energy as a function of temperature in which the vibrational contributions are considered might be necessary. The degree of polymorphism of the diastereomeric salt pairs also raises the question as to whether in a usual experiment it is the solubility of the most stable form of each salt that is being compared.

## 1.7 Thesis Outline

The work presented in this thesis attempts to provide a systematic set of experimental data, both thermodynamic and structural, that is often lacking when trying to understand the process of chiral resolution by crystallisation. Furthermore, the data is intended to serve as a standard against which crystal structure prediction methods can be compared to, to validate their results. Emphasis is placed on the critical examination of the approximations made in the crystal structure prediction programmes.

Chapter 2 provides a short summary of the process of crystallisation from solution, giving a brief overview of the theories of nucleation and growth, and giving an introduction to the particularities of crystallisation of chiral molecules from solution.

Chapter 3 describes the experimental and computational methods that are used in the thesis to study the crystallisation behaviour of Naproxen (Chapter 4) and a set of closely related diastereomeric salts (Chapter 5).

Chapter 4 describes the experimental work performed on Naproxen, a non-steroidal anti-inflammatory drug that is used as a model compound to understand the crystallisation of racemic solutions. Relative stability data for both racemic and enantiopure crystals measured experimentally at two different temperatures is presented and used as a comparison for the relative stability data obtained with a computational method. The solid phase characteristics of Naproxen are also established.

In Chapter 5, the resolution of chiral molecules by diastereomeric salt formation is investigated. In it, the results of a set of crystallisation screens on a family of closely related diastereomeric salt pairs is presented. For the (1R,2S)-Ephedrine-2-Phenylpropionate salts, the relative stability data of all the most stable crystal forms were measured using different techniques. Furthermore, the ternary phase diagrams of the two most stable phases of the salt pair in a solvent measured at two different temperatures is also presented, to understand whether a resolution of 2-phenylpropionic acid is possible using ephedrine as a resolving agent. This chapter provides the experimental data necessary for the validation of the methods used in Chapter 6.

Chapter 6 describes the computational work performed on (1R,2S)-Ephedrine-2-Phenylpropionate salts. The work in this chapter aims to test whether the computational models used are able to calculate the relative stabilities of all the different forms found for this system in Chapter 5. Furthermore, attempts are also made to try to see whether the different forms are found in a search for plausible crystal packings using a novel crystal structure prediction method.

Finally Chapter 7 provides an overall conclusion to the work presented in this thesis and identifies some areas which could benefit from further research.

# Chapter 2 Crystallisation from Solution

## 2.1 Introduction

In order to be able to design a resolution process by crystallisation it is important to understand the principles of crystallisation. Since the resolution processes will be carried out in solution, this section will focus on the theory of crystallisation from solution. Furthermore, the special characteristics of the crystallisation of racemic solutions will be discussed.

The formation of crystals from solution can be understood as the product of a sequential progression of three general stages: generation of supersaturation, nucleation and crystal growth. The following sections will concentrate on each of these steps.

## 2.2 Supersaturation

The first step in any crystallisation process is the generation of supersaturated conditions, the driving force of crystallisation. In order for a solute in solution to crystallise, the concentration of solute in solution must exceed its equilibrium (saturation) concentration, and reach a condition of supersaturation or supersolubility. Every solution has a particular composition range between the saturation concentration and supersaturation point called the metastable zone, under which spontaneous nucleation is very unlikely to occur. These characteristic solution properties can be shown on a solubility diagram. A typical solubility diagram is depicted in Figure 2.1

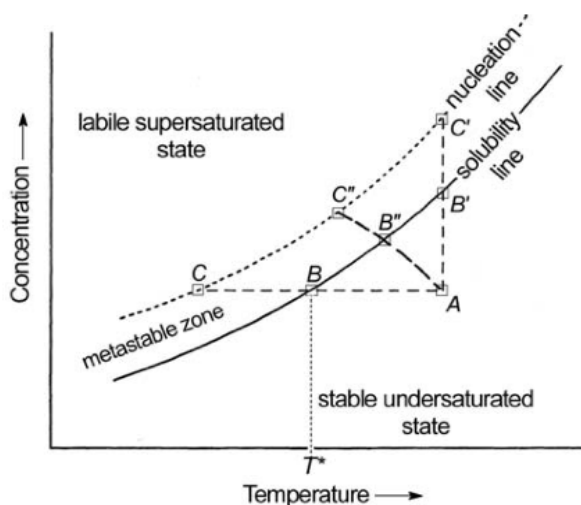


Figure 2.1 A typical solubility diagram [137].

The three distinct zones in the graph that define the crystallisation event are:

- 1) An undersaturated stable zone where no nucleation or crystal growth can occur. Added crystals would dissolve until the concentration reached the liquidus curve or solubility line. Point A on Figure 2.1 is a point in this zone.
- 2) The metastable zone where crystal growth is possible but where spontaneous nucleation is very unlikely. This is the area between the solubility and nucleation lines.
- 3) Supersaturated zone where rapid nucleation occurs. This is any point above the line joining C and C'' and C'.

The formation of a supersaturated solution is normally achieved in either of three ways: cooling of a saturated solution (e.g. going from A to C), loss of solvent by evaporation or addition of more solute (e.g. A to C') or both (e.g. A to C'').

Supersaturation can be defined as the difference in chemical potential between molecules in solution and molecules in the bulk of the crystal phase:

$$\Delta\mu = \mu_{solute} - \mu_{crystal} \quad \mathbf{2.1}$$

This is usually expressed as:

$$\Delta\mu = kT \ln S \quad \mathbf{2.2}$$

Where  $k$  is the Boltzmann constant,  $T$  is the absolute temperature and  $S$  is the supersaturation ratio (for a derivation of this expression please refer to [138]). A solution is supersaturated when  $\Delta\mu > 0$ . The supersaturation ratio  $S$  is usually defined as the ratio between the actual activity of the solute in solution and the equilibrium activity according to:

$$S = \frac{a_0}{a_{eq}} \quad \mathbf{2.3}$$

where  $a_0$  is the actual activity and  $a_{eq}$  is the equilibrium activity. The activity of a solute in solution is defined as

$$a = \gamma x \approx \gamma C \quad \mathbf{2.4}$$

where  $\gamma$  is the activity coefficient and  $x$  is the molar fraction, although this is usually replaced by the actual concentration of solute in solution,  $C$ . A further simplification is to use the concentration based supersaturation ratio:

$$S = \frac{C_0}{C_{eq}}$$

2.5

where  $C_0$  is the actual solution concentration and  $C_{eq}$  is the equilibrium concentration at a given temperature. This approximation is generally valid for readily soluble solutes where  $\gamma_0 \approx \gamma_{eq}$ . For poorly soluble solutes the activity based supersaturation ratio should be used.

## 2.3 Nucleation

Once a supersaturated solution has been obtained, nucleation is the next step in the crystallisation process. Since nucleation is the first step in the formation of crystals from solution it is crucial in any crystallisation process, as it will affect aspects of the crystal products' quality such as the crystal size distribution and the crystalline phase produced. As noted by Mullin [137], nucleation is believed to occur by either of two mechanisms, primary or secondary nucleation. Primary nucleation occurs when no crystalline material is present in solution, whereas the formation of nuclei from solutions containing crystallites is referred to as secondary nucleation [137]. Primary nucleation in turn is believed to occur either homogeneously or heterogeneously, in which non crystalline foreign particles help induce nucleation.

### 2.3.1 Homogeneous Primary Nucleation

Primary nucleation is a first order phase transition that involves the formation of a new crystal phase from a clear solution. Under supersaturated conditions collisions between solute molecules due to Brownian motion lead more efficiently to the formation of solute clusters. This process is quite dynamic and molecules attach and detach successively, as depicted in Figure 2.2.

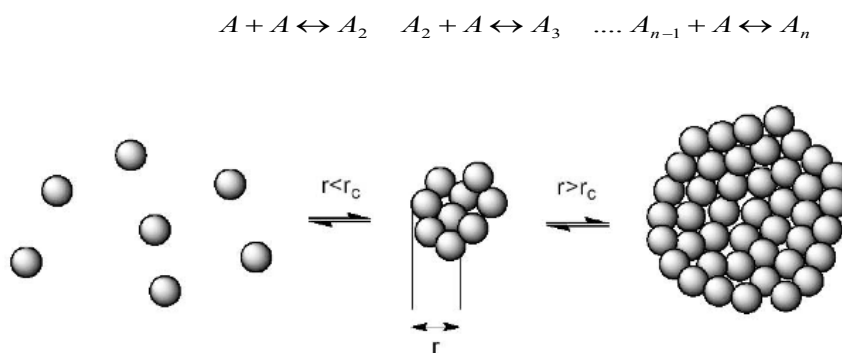


**Figure 2.2** Schematic representation of the primary nucleation process.

When these molecular clusters form two things occur. First, a volume of molecules is created, and secondly, an interface between the molecular cluster and the solution is formed. When a volume is created there is a gain in Gibbs free energy which is related to the number of molecules in the cluster and the force driving the molecules into the cluster.

$$\Delta G_v = -n\Delta\mu = -nkT \ln S \quad 2.6$$

On the other hand the formation of a surface is not energetically favourable. The energy loss due to the creation of an interface is related to the surface area of the cluster formed and the interfacial energy.

$$\Delta G_s = A\gamma = c(vn)^{2/3} \gamma \quad 2.7$$

Where  $c$  is a shape factor (6 for cubes and  $(36\pi)^{1/3}$  for spheres),  $v$  is the molecular volume,  $n$  is the number of molecules and  $\gamma$  is the interfacial energy.

The total change in Gibbs free energy for formation of a spherical molecular cluster is therefore:

$$\Delta G = \Delta G_v + \Delta G_s = -nkT \ln S + (36\pi)^{1/3} (vn)^{2/3} \gamma \quad 2.8$$

The effect of molecular cluster size on the change in Gibbs free energy with respect to the surface, volume and on the whole system can be seen in Figure 2.3.

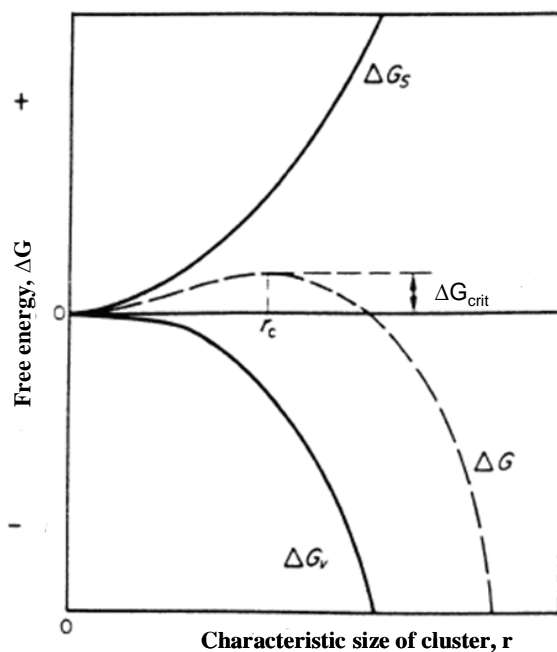


**Figure 2.3** Free energy diagram for nucleation [137].

The nucleus is the molecular cluster that requires the largest change in Gibbs free energy for its formation, and is in labile thermodynamic equilibrium with the system. Any loss or addition of molecules to the nucleus will result in a lowering of the Gibbs free energy of the system. In other words, for nucleation to occur the system must be able to overcome an energy barrier, noted as  $\Delta G_{crit}$  in Figure 2.3. The rate per unit volume at which this happens can be expressed in the form of the Arrhenius equation

$$J = A \exp\left(\frac{\Delta G_{crit}}{kT}\right) \quad 2.9$$

where  $k$  is the Boltzmann constant and  $A$  is a kinetic factor.

The nucleus critical size, i.e. the smallest molecular cluster that can form a stable nucleus, can be calculated by differentiating equation 2.8 with respect to the cluster size and equating to zero, as the gradient of the  $\Delta G$  curve is zero at that point.

$$\frac{dG}{dn} = 0 = -kT \ln S + \frac{\frac{2}{3} cv^{2/3} \gamma}{n^{1/3}} \quad 2.10$$

$$n^* = \left(\frac{2cv^{2/3} \gamma}{3kT \ln S}\right)^3 = \frac{8c^3 v^2 \gamma^3}{27k^3 T^3 \ln^3 S} \quad 2.11$$

Replacing equation 2.11, the expression obtained for the nucleus critical size, into equation 2.8, the change in Gibbs free energy for the formation of a molecular cluster; one obtains an expression for  $\Delta G_{crit}$ , the change in Gibbs free energy that needs to be overcome for the formation of a stable nucleus.

$$\Delta G_{crit} = \frac{4c^3 v^2 \gamma^3}{27k^2 T^2 \ln^2 S} \quad 2.12$$

Introducing expression 2.12 into 2.9 and simplifying, leads to the version of the nucleation rate equation usually used.

$$J = A \exp\left(\frac{-B}{\ln^2 S}\right) \quad 2.13$$

where  $B = \frac{16\pi v^2 \gamma^3}{3k^3 T^3}$  for spherical molecules

From 2.13 one can see how the nucleation rate is highly non-linear with respect to the supersaturation, and that there must be a metastable concentration zone within which, despite there being supersaturated conditions, crystallisation is negligible and after which nucleation occurs rapidly, exemplified in Figure 2.4. The observation that nucleation tends to occur wherever there is a localised higher supersaturation is a corollary from this realisation, and influences the design of the crystallisation process. For example, nucleation will tend to occur on cooling surfaces for cooling crystallisation processes and at the feed point for precipitation and anti-solvent crystallisation.

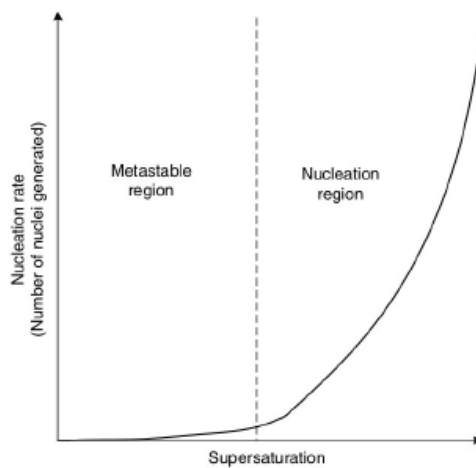


**Figure 2.4** Nucleation rate as a function of supersaturation [139]

The effect of relative supersaturation on primary nucleation can also be clearly seen in Figure 2.5. Increase in supersaturation results in a decrease of the critical cluster size and  $\Delta G_{crit}$ . Eventually supersaturation reaches a point where the activation energy is so low that spontaneous nucleation occurs.

All of the considerations made above regarding the nucleation process assume that supersaturation is the only driving force and that nucleation occurs spontaneously. According to Mullin's classification this is known as homogeneous primary nucleation [137]. Homogeneous nucleation is thought to rarely occur since the removal of all foreign particles is extremely difficult, and particles such as atmospheric dust, which can easily be introduced into crystallisation vessels involuntarily, may have an effect. When nucleation is induced by foreign particles the process is known as heterogeneous primary nucleation (note that the foreign particles do not include solute crystalline material since then it would be secondary nucleation). Recent advances in the use of microfluidic devices for crystallisation provide a



good platform in which homogeneous nucleation can be studied [140-142]. In these systems solutions can be confined to micro-sized droplets and hence reduce the chance of foreign particles being present in the droplet. Furthermore, many identical droplets can easily be made [143-145]. Each droplet can be seen as an independent batch experiment offering the possibility of obtaining statistically relevant data.

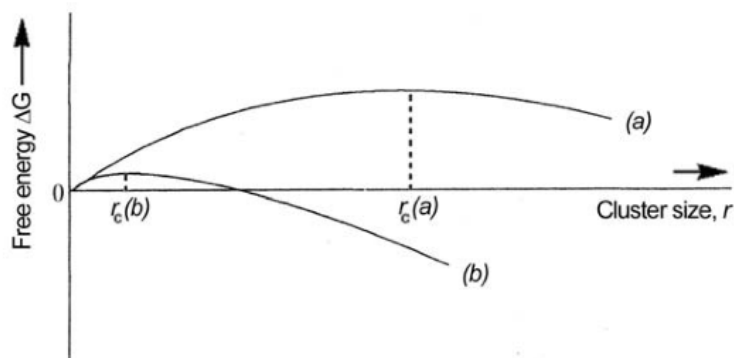


**Figure 2.5** Gibbs free energy change as a function of  $r$  for (a) low supersaturation concentration and (b) high supersaturation [146].

Recently, work investigating the nucleation of protein crystals has resulted in theories suggesting that nucleation might be a two-step process, where first a droplet of dense liquid forms, which is metastable with respect to the crystalline phase, followed by ordering of the molecules and crystallisation within the droplet [147, 148]. In fact, similar observations have been made for small molecules, through a process commonly known as oiling out. For example, Groen and Roberts, cooling an 80% (w/w) aqueous solution of citric acid monohydrate, observed an increase in turbidity before a change in concentration, an indication that oiling out was taking place before crystallisation [149].

### 2.3.2 Heterogeneous Primary Nucleation

Surfaces and the presence of foreign particles in solution can drastically influence nucleation, increasing the nucleation rate considerably. Foreign particles and surfaces are thought to lower the minimum energy required for nucleation, by lowering the surface energy penalty that has to be paid by the system when a molecular cluster forms. For heterogeneous nucleation, the effective interfacial energy of the system,  $\gamma$  in equation 2.7, is:

$$\gamma_{eff} = \psi\gamma$$

2.14

Where  $\psi < 1$  and is an activity factor introduced by the foreign particle and is a function of the contact angle between the cluster and the foreign particle or surface.

Mersmann developed a method to predict whether nucleation occurs through a homogenous or heterogeneous mechanism, by plotting the rates for homogeneous nucleation and for heterogeneous nucleation as a function of the dimensionless driving force:

$$\Delta C / C_c = (C_0 - C_{eq}) / C_c \quad 2.15$$

and of the dimensionless solubility [150]:

$$C_0 / C_c \quad 2.16$$

where  $C_c = 1/v_0$  and  $v_0$  is the molecular volume. For a compound of known solubility and defined experimental supersaturation ratio the position in such a plot predicts the nucleation mechanism.

### 2.3.3 Secondary Nucleation

Secondary nucleation occurs as a consequence of the presence of existing crystals in the metastable zone. Secondary nucleation therefore takes place under lower supersaturation levels. In some cases it has been demonstrated that secondary nucleation by seeding leads to better reproducibility. Secondary nucleation is the basis for preferential crystallisations or resolution by entrainment (see section 1.4.4.1), in which seeds of one enantiomer are added to a solution of a conglomerate forming racemate under metastable conditions in order to produce the desired enantiomer [32].

## 2.4 Crystal Growth

Once an ordered nucleus surpassing the critical nucleus size has been formed, it will begin to grow into crystallites of visible size. Kossel proposed a step growth mechanism for a growing crystal face. In Kossel's theory of crystal growth, the crystals are considered to be formed of a three dimensional arrangement of cubes, where each cube represents a growth unit. What constitutes a growth unit is still a matter of some debate. In some occasions growth units represent single molecules whereas in others, when some kind of pre-assembly occurs in solution, growth units can be dimers or larger aggregates of molecules. Growth

units diffusing from the supersaturated solution are adsorbed on a face and can spontaneously form an island monolayer. This island constitutes the beginning of the next layer on the crystal face. The edge of the island monolayer is a step site on the crystal face on which kinks can occur (see Figure 2.6). Growth units diffusing from the solution are most easily incorporated into the crystal at a kink site. Therefore growth units that are adsorbed onto a flat surface diffuse until they reach a step, subsequently diffusing to a kink site where it is incorporated into the lattice. In this way, steps slowly grow along a face, eventually forming a new face.

It is clear that the limiting step in such a mechanism is surface nucleation, which is necessary for the formation of new steps and kink sites onto which diffusing growth units can attach to. The dependence of the Kossel mechanism on surface nucleation makes this theory unrepresentative, since crystals often grow at considerable rates even at supersaturation levels far below those needed to induce surface nucleation.

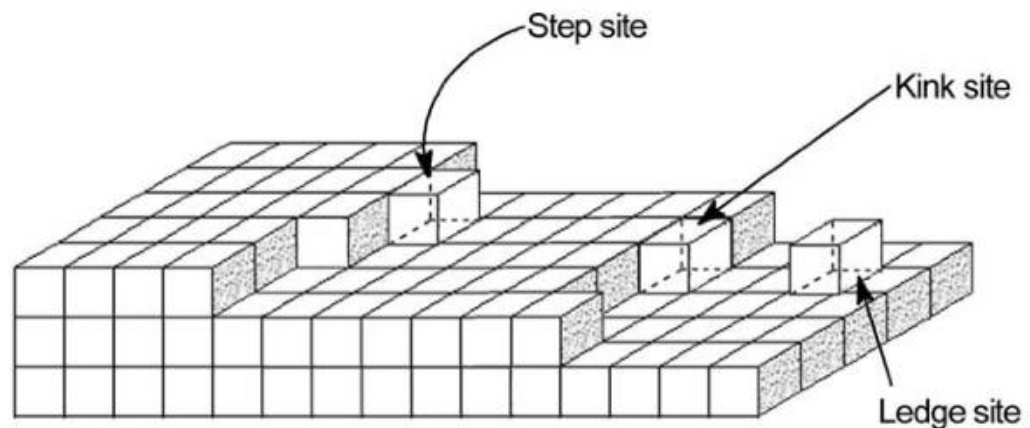


**Figure 2.6** Kossel's model of a growing crystal surface [151].

In order to overcome this problem Burton-Cabrera-Frank (BCF) [152] proposed a theory of crystal growth in which defects created by stress inside the crystal lattice provide monomolecular height steps (see Figure 2.7) that are energetically favourable for the attachment of growth units. In this way, there is no need for surface nucleation and, once such a screw dislocation has been formed, the crystal face can in theory grow perpetually spirally upwards, since the dislocation never grows out.

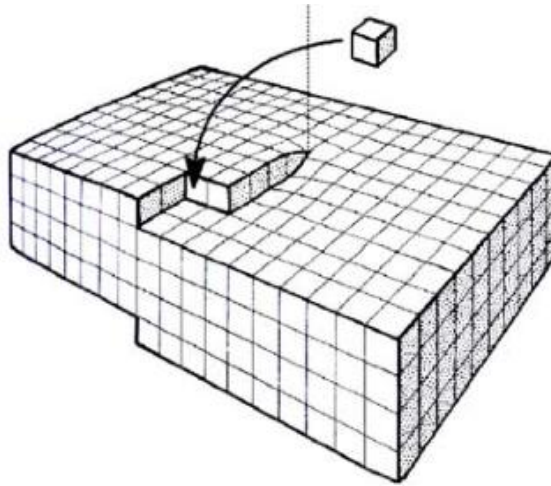


**Figure 2.7** Crystal growth at a screw dislocation as proposed by Burton-Cabrera-Frank [152].

### 2.4.1 Crystal Habit

The crystal habit or morphology of a crystal is the macroscopic shape a crystal adopts. Crystal habit is determined by the differences in the growth rates of the faces of a crystal. Faces that grow very quickly will eventually grow out and therefore will have no effect on the morphology of the crystal. On the other hand, slow growing faces are morphologically important since these will be the ones observed in the macroscopic crystal. The slowest growing faces are those that are closely packed and have the lowest Miller indices.

The growth of the different faces depends on the crystal structure and its defects and on environmental conditions. Hartman and Perdok [153] investigated the influence of internal crystal structure on the growth rate of the different faces. They suggested that the ability of the growth units to attach to the surface of a crystal depends on the number and strength of the possible interactions, and will therefore occur more readily where they are more numerous and the attractive forces strongest. In their model, the faces can be classified as one of three types: kinked (K-face), stepped (S-faces) or flat (F-faces) faces. K-faces are those with which growth units have the possibility of forming three bonds; S-faces are those with which two bonds are possible, and surfaces with which only one strong interaction can occur are F-faces. Given that the strongest intermolecular interactions are of the order of 20 kJ/mol the addition of units to flat surfaces, where there is only one possible interaction site, would only happen very slowly. Therefore assuming that the linear growth rate of a face is proportional to the total binding energy of a growth unit to that surface, it would be expected that the growth rates of the faces with respect one another are:  $K > S > F$ . The approach developed by Hartman and Perdok [153-155] and known as the periodic bond chain (PBC)

approach was shown to be successful in the prediction of the morphologies for a number of molecular crystals. Since then, variations on this approach such as the attachment energy model have also been found to be successful for the prediction of the morphology of molecular crystals [156].

One of the most important factors that influence the crystal morphology is the solvent used in crystallisation [157]. Given that the functional groups at crystal surface vary depending on the crystal face, crystal faces will be solvated to different degrees in a solvent. The faces that present polar groups at their surface will be more solvated when using polar solvents. On the other hand less polar functional groups would be less solvated. The degree of solvation of a face would affect its growth rate since, if strongly solvated, the solvated layer would inhibit the diffusion of growth units onto the faces' surface and would therefore hinder the integration of growth units into the crystal. Another factor that has been shown to greatly affect the outcome of a crystallisation is the presence of impurities in solution [158]. Computational methods based on the attachment energy model [159, 160] have been used to help rationalise the effect of solvents and impurities on crystal growth. These studies successfully reproduced the morphologies of crystals grown in the presence of different solvents and impurities [161, 162].

## 2.5 Polymorphism

From the greek poly = many and morph = form, in chemistry the ability of a compound to exist in more than one crystal form is known as polymorphism. The definition of polymorphism has been much debated and often its use depends on each authors' criteria on what the term includes. Perhaps a definition that is commonly used and has survived the pass of the years is that of McCrone "two polymorphs will be different in crystal structure but identical in the liquid and vapour states" [163]. This definition hence excludes amorphous solids and solvates.

### 2.5.1 Relative Stability of Polymorphs

At constant pressure, the relative stability of two polymorphs can be determined quantitatively from the difference in their Gibbs free energies:

$$\Delta G = \Delta H - T\Delta S \qquad \qquad \qquad \mathbf{2.17}$$

where  $\Delta H$  is the enthalpy difference between polymorphs, and corresponds to the difference in the lattice energy of the two forms;  $\Delta S$  is the entropy difference and T is the temperature.

A pair of polymorphs can be thermodynamically related in one of two ways. One of the possibilities is that one of the polymorphs is the most thermodynamically stable with respect to the other form in the entire temperature region below their melting points. When this occurs, the polymorphs are said to be monotropically related. On the other hand, if each of the polymorphs have a temperature range below their melting point where they are stable with respect to the other form, the polymorphs are said to be enantiotropically related.

Figure 2.8 depicts the energy vs. temperature diagram of a pair of monotropically related polymorphs labelled I and II. An energy/temperature diagram describes the temperature dependence of the enthalpy and Gibbs free energy of polymorphs. Figure 2.9 on the other hand, depicts an energy/temperature diagram for a pair of enantiotropic related polymorphs.

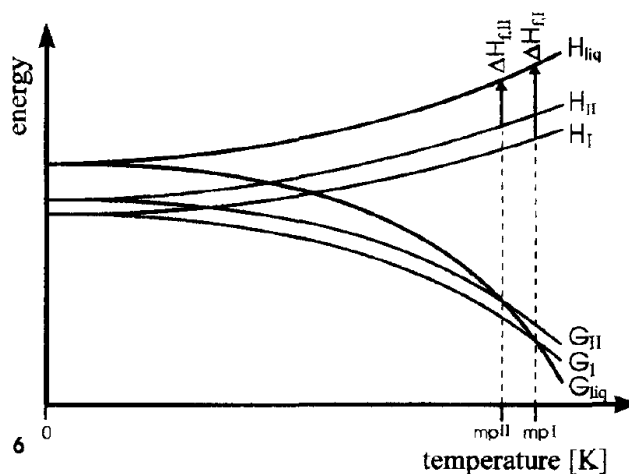


**Figure 2.8** Free energy relationship of a dimorphic monotropic system [164].

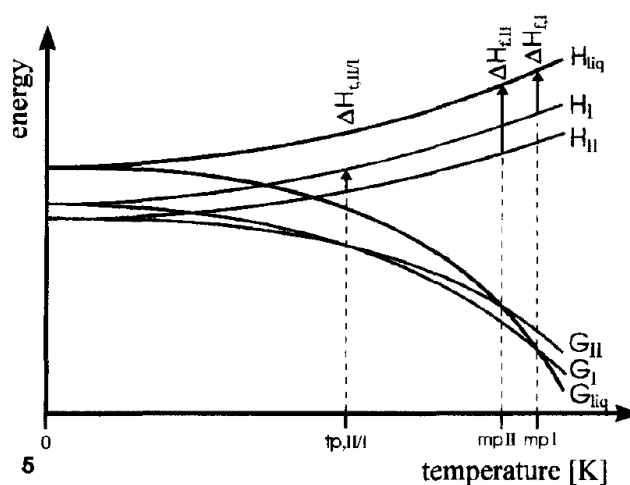


**Figure 2.9** Free energy relationship of a dimorphic enantiotropic system [164].

These diagrams provide the basis for two thermodynamic rules that can be used to determine the thermodynamic relationship between two polymorphs.

The heat of transition rule states that if an endothermic polymorphic transition is observed at a particular temperature, the transition point must lie below this temperature [164]. This happens when two polymorphs are enantiotropically related. If the phase transition is exothermic then the polymorphs are monotropically related. It is also possible however that this might apply to an enantiotropic system in which the thermodynamic transition point is higher than the measured transition temperature.

The second rule, the heat of fusion rule, states that in an enantiotropic system the higher melting polymorph has the lower heat of fusion [164]. On the contrary, in a monotropic system the higher melting polymorph has the highest heat of fusion.

## 2.5.2 Nucleation and growth in Polymorphic systems

It is important to note that the process of nucleation is not necessarily thermodynamically controlled and kinetic factors might affect the crystallisation process. At the early stages of nucleation, before a nucleus has grown past the cluster critical size, nuclei of different polymorphs might be present in the crystallisation. These nuclei are at the stage where dissolution is more energetically favoured than growth and thus most nuclei re-dissolve. The form that will eventually grow into a crystal will be the one that reaches its cluster critical size most quickly.

Figure 2.10 depicts the energy vs. reaction diagram in a dimorphic system of polymorphs II and I, in which form II is the most stable phase ( $G_I > G_{II}$ ). However, it is possible to see that the nucleation of the metastable phase has lower activation energy than that of the thermodynamically stable phase and hence kinetics will favour the formation of form I. If the crystallisation conditions are left so as it is kinetically controlled, the outcome of crystallisation will be the metastable phase. However, if the crystallisation is run under thermodynamic control form I will eventually transform to form II [165].

The Ostwald rule of stages, postulated in 1987, suggests that, for systems that can crystallise in more than one phase, the crystallisation from a supersaturated solution to equilibrium proceeds in a sequence of stages, each stage representing the smallest possible change in free energy. Hence, a polymorphic system would go through various possible polymorphs before reaching the most stable form. It is important to note that the Ostwald rule of stages is based on observation and is not a physical law.

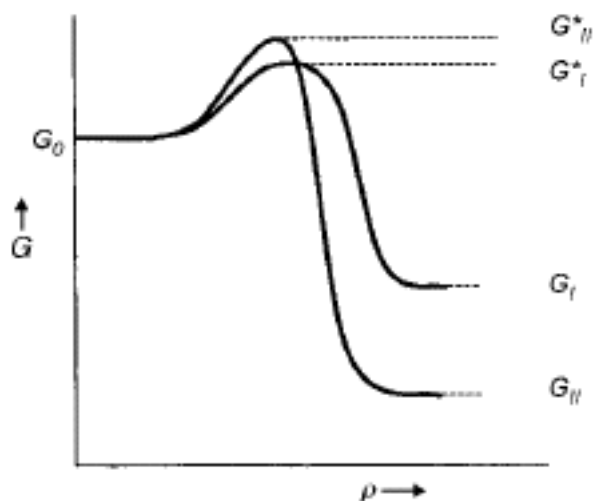


**Figure 2.10** Reaction pathways for the crystallisation of a dimorphic system [165].

Attempts to rationalise Ostwald's rule in kinetic terms [146, 166, 167] have been made by applying the nucleation rate equation defined in section 2.3.1, considering the supersaturation ratios of the different polymorphs with regards to the most stable phase. These considerations showed that Ostwald's rule is not generally valid as the phase with the highest nucleation rate will vary depending on supersaturation conditions. Obtaining the right crystallisation conditions for different polymorphs can be somewhat problematic. There may even be conditions under which the nucleation rates of two different polymorphs are equal, making the probability that they appear also almost equal. This might lead to the occurrence of what has been termed concomitant polymorphism [165].

## 2.6 Crystallisation of Racemic Mixtures

When crystalline, racemates may fall into one of three categories. The first, known as *racemic crystals*, involves the presence of both enantiomers in equal quantities in the unit cell, and is the most common type of racemate occurring in the solid state. The second, termed *conglomerate* occurs when, upon crystallisation, the racemic mixture *spontaneously resolves* and an equimolar mechanical mixture of crystals of the two pure enantiomers is formed. Conglomerate forming racemates may be resolved by means of entrainment, a process in which, under supersaturation conditions, crystallisation cycles of the pure enantiomers are achieved by seeding with one enantiomer or the other (see section 1.4.4). The third type of crystalline racemate only rarely occurs, and entails the formation of a solid



solution in which both enantiomers are present in the unit cell but with no fixed stoichiometry. This is generally known as *racemic solid solution* or *pseudoracemate*.

The characterisation of racemate type can be achieved by means of a binary melting point phase diagrams. The typical melting point phase diagrams for the three racemate types are shown in Figure 2.11

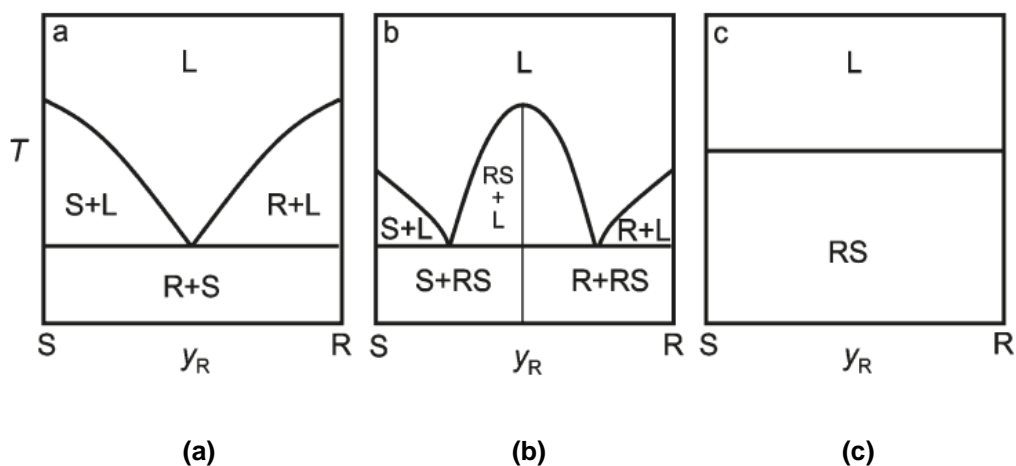


**Figure 2.11** Melting Point Phase diagram of (a) conglomerate (b) racemic crystal and (c) pseudoracemates [47].

The melting point phase diagrams for binary mixtures of enantiomers can be readily obtained by measuring the melting points of a range of mixtures of known compositions. Melting point measurements are now commonly measured using differential scanning calorimeters, which can at the same time provide enthalpy fusion data (see section 1.5.2).

For conglomerate forming systems, it is possible to calculate the melting point phase diagram just from the melting point and enthalpy of fusion data of the pure enantiomers, by using the simplified form of the Schröder - van Laar equation [168]:

$$\ln x = \frac{\Delta H_A^f}{R} \left( \frac{1}{T_A^f} - \frac{1}{T^f} \right) \quad 2.18$$

where  $x$  is the mole fraction of the most abundant enantiomer of a mixture whose melting point is  $T^f$ , and  $\Delta H_A^f$  and  $T_A^f$  are the enthalpy of fusion and melting point of the enantiomer.

This equation allows the calculation of the liquidus curve of R or S of the binary mixture. The Schröder-van Laar equation is valid under three conditions:

- i) Immiscibility of the enantiomers in the solid state
- ii) Ideality of the enantiomer mixture in the liquid phase and
- iii) The difference between the specific heat capacity of the liquid and of the solid enantiomer, i.e.  $C^l$  and  $C_A^s$  respectively, being constant with temperature.

It is the second condition on which the validity of this equation rests that needs careful consideration. A mixture is ideal in solution if its enthalpy of mixing is equal to zero. For a racemate that would mean that in order for it to behave ideally in solution its entropy of mixing is equal to  $R\ln 2$ , since:

$$\Delta S_l^m = -R(x_R \ln x_R + x_S \ln x_S) \quad \mathbf{2.19}$$

and  $x_R = x_S = 0.5$ . It is clear that the enthalpy of mixing of enantiomers is not necessarily equal to zero since the energy of intermolecular homochiral and heterochiral interactions in solution are probably different. The endothermic or exothermic nature of the mixing process will depend on which of these has stronger interactions. However, because the enthalpies of mixing are very small compared to the enthalpies of fusion used in the Schröder-van Laar equation (less than 1%) they are considered to be negligible [36].

Furthermore, Jacques *et al* describe a thermodynamic approach that allows the calculation of the entropy of mixing from melting points and enthalpies of fusion [36]. Assuming that the formation of a racemic crystal from its solid enantiomers occurs at the melting point of the lower melting species (i.e. racemic or enantiomer) it is possible, using the thermodynamic cycle described in Figure 2.12 to derive the entropy of mixing in the liquid state

$$\Delta S_l^m = \frac{\Delta H_{SR}^f}{T_{SR}^f} - \frac{\Delta H_S^f}{T_S^f} - \frac{\Delta H_{SR}^f - \Delta H_S^f}{T_{SR}^f - T_S^f} \ln \frac{T_{SR}^f}{T_S^f} \quad \mathbf{2.20}$$

A study of a set of pharmaceutical related compounds showed that for conglomerate forming compounds entropy of mixing is very close indeed to  $R\ln 2$  [169].

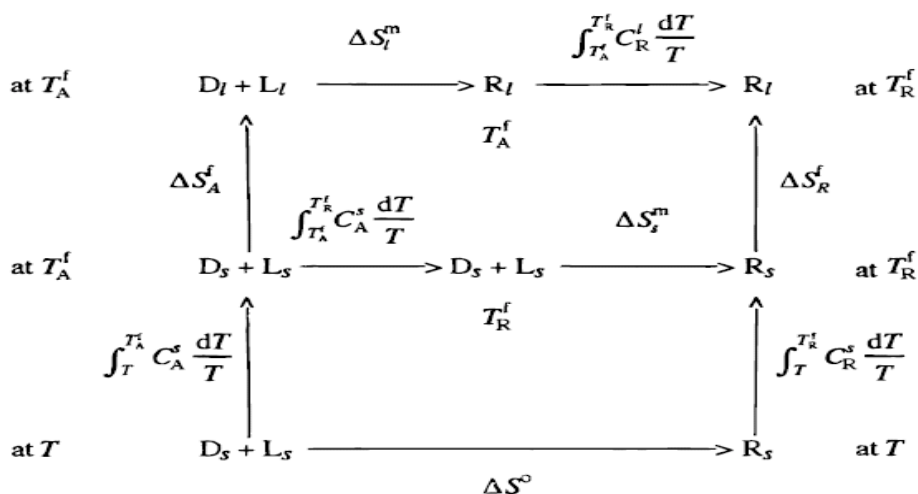


**Figure 2.12** Thermodynamic cycle showing the entropy changes between stages [169].

For racemic crystals it is also possible to calculate the binary phase diagram. As before, the liquidus curve between the melting point of the pure enantiomer and the eutectic is calculated by means of the Schröder-van Laar equation. However, the part of the curve between the eutectic and the melting point of the racemate, below which the solid phase consists of pure racemic compound, is defined by the Prigogine-Defay equation [168].

$$\ln 4x(1-x) = \frac{2\Delta H_R^f}{R} \left( \frac{1}{T_R^f} - \frac{1}{T^f} \right) \quad 2.21$$

In order to validate the model the comparison of calculated data to experimental data must be done. Jacques *et al* report good agreement between calculated and experimental values for available experimental data [36], suggesting that this method might provide a quick way of determining the solid phase characteristics of racemates.

A new quick screening method to determine the solid-state nature of chiral compounds (i.e. whether they crystallise as a racemic compound, conglomerate or solid solution) has been recently described by Srisanga and ter Horst [47] in which the binary phase diagram is constructed by measuring the saturation temperatures of solutions of known composition. The advantage of this method is that it provides data at temperatures at which crystallisations actually occur, as opposed to phase diagrams constructed based on the melting temperatures which might not be representative for certain systems at lower

temperatures. Furthermore, this method provides the opportunity of constructing ternary phase diagrams, which are extremely useful when designing resolution experiments.

## Chapter 3 Experimental and Computational Methods

### 3.1 Introduction

This chapter describes the manual crystallisation screens undertaken in the thesis, together with the analytical techniques that have been employed to analyse the crystalline samples obtained in the different crystallisation experiments. The methods to measure and calculate the thermodynamic values that are used as validation of the computational studies are also outlined here, as well as the computational methodology used in the thesis to calculate the lattice energies of the different forms found in the crystallisation screen.

Section 3.2 details the different crystallisation experiments that have been used in the screenings performed in this thesis, i.e. solvent evaporation, cooling crystallisation, solvent diffusion and solvent assisted grinding.

Section 3.3 outlines the analytical techniques used in this thesis for the routine identification of crystal forms obtained in the crystallisation experiments and include X-ray diffraction methods, spectroscopic and elemental analysis. This section also describes the methods used to measure thermodynamic values for the different crystalline phases that are employed as validation for computational studies.

The computational workflow followed to assess the ability of computational models to accurately predict the relative stability of a pair of diastereomeric salts is delineated in Section 3.4

### 3.2 Crystallisation Screening Method

Crystallisation experiments consisted of evaporation and cooling crystallisation, solvent assisted grinding and solvent diffusion experiments. A summary of the experiments performed for each of the systems studied in this thesis is found in the appropriate Chapters.

#### 3.2.1 Quick determination of Solubility Profile

The first step in the crystallisation screen was to assess the solubility of the two diastereomeric salts in a range of solvents. The solubility profile of the two salts in a range of 19 solvents (methanol, ethanol, 2-butanol, isopropanol, water, ethyl acetate, diethyl ether, dibutyl ether, diisopropyl ether, methyl butyl ether, dichloromethane, dichloroethane, toluene,

xylene, dioxane, tetrahydrofuran, hexane, acetonitrile, and dimethylsulphoxide) was roughly assessed by adding the solvents drop-wise into previously weighed 100 mg aliquots of the diastereomeric salts while constantly stirring at room temperature (~25°C), and visually determining the point at which all the salt had dissolved. The solubility of the salts in the different solvents fell broadly into three categories. They were either very soluble (>100mg/ml), soluble (20 > x > 4mg/ml) or hardly soluble (<3 mg/ml).

### **3.2.2 Solvent Evaporation Experiments**

Saturated solutions were prepared at room temperature by slurring an excess of compound in a solvents for two hours. The solutions were then filtered using Grade 1 qualitative filter papers (Whatman, UK) in order to remove any excess crystals, and placed into glass vials and covered with stoppers that had had one hole pierced through. Experiments were performed in two types of glass vials, large and small. The large sample tubes were 25 mm in diameter and 75 mm in height and could contain a maximum volume of 32.5 ml. The smaller sample tubes were 15 mm in diameter and 50 mm in height and could contain up to 5 ml of solvent. All crystallisations were set up in virgin glassware to prevent possible cross contamination that could arise had washed vials been used. Evaporation experiments were also performed using slightly under-saturated solutions. The solutions obtained after filtration were diluted by adding 1 part of solvent to 3 parts of the saturated solution and thoroughly mixed. These solutions were left to stand at room temperature, covered with one holed lids.

### **3.2.3 Cooling crystallisation**

Hot saturated solutions were prepared to a maximum of 65 °C. For experiments involving solvents with boiling points below 65 °C the saturated solutions were prepared close to their boiling point. In fast cooling experiments, solutions in small vials were allowed to cool in ambient conditions after heating. In slow cooling experiments the solutions were cooled at 1°C/min by placing the vials inside a jacketed vessel which was temperature controlled by a circulator (Grant LTC 12-50).

### **3.2.4 Solvent Assisted Grinding**

The use of neat and solvent assisted grinding has been widely used in the study of co-crystallisation and therefore was applied to the diastereomeric salt systems as it provides a quick and very reproducible method. Experiments were conducted by adding 3 drops of the appropriate solvent into a 1.5 ml stainless steel jar containing approximately 0.25g of the

appropriate salt and one 5mm grinding ball inside, and grinding the salt and solvent mixture for 99 minutes at a frequency of 30Hz using a Retsch MM200 grinding mill.

### 3.2.5 Vapour Diffusion

For the vapour diffusion experiments first saturated solutions of the compound under investigation were prepared at room temperature in butan-2-ol, toluene and dimethyl sulphoxide, by filtering slurries of the compound kept at room temperature using Grade 1 qualitative filter papers (Whatman, UK). These solutions were placed in small vials and placed, uncovered, in larger vials containing the volatile anti-solvent. The large vials were then sealed. The volatile anti-solvents used were diethyl ether, dibutyl ether, diisopropyl ether and methyl butyl ether.

## 3.3 Crystal Form Analysis

Routine solid state identification of the solid forms obtained from the crystallisation experiments were performed using powder X-ray diffraction and infrared spectroscopy data. Elemental analysis was used to determine whether double salts, hydrates and solvates had been formed in the diastereomeric salt study described in Chapter 5. When good single crystals were obtained in a crystallisation experiment, single crystal X-ray diffraction data was collected. In cases where no good single crystal X-ray diffraction data could be obtained, powder X-ray diffraction data was used to solve the crystal structures.

The properties and the thermodynamic data of the different crystalline phases obtained in the crystallisation screens were analysed using thermal methods and solution based methods.

### 3.3.1 Single Crystal X-ray Diffraction

Three different instruments were used in this thesis for the collection of single crystal X-ray diffraction data. The first instrument used for ERP I<sup>o</sup>, ESP I, PSP Hydrate, PRB and PSB was a Bruker SMART APEX CCD diffractometer equipped with CCD camera and a Bruker AXS Kryoflex cryostat. The second instrument was a Bruker Apex II CCD instrument and was used to collect X-ray diffraction data of ESB I at Strathclyde University by Dr. Jean-Baptiste Arlin. All data were measured at  $150 \pm 2$  K using monochromatic Mo-K $\alpha$  radiation ( $\lambda = 0.71073$  Å). The data were corrected for Lorentz-polarization effects as well as for absorption using SADABS [170]. Accurate unit cell parameters were determined by a least-squares fit of the most intense reflections using SAINT+ [171]. The structures were solved

and refined using SHELXS [172] as implemented in Crystals [173], a crystal structure refinement program. For all structures, all non-hydrogen atoms were located from Fourier difference maps and refined anisotropically. All hydrogen atom positions were fixed at idealised positions and refined using a riding model except for the polar protons attached to O and N, which were located from the difference Fourier map and refined freely.

Finally, the diffraction data for PRP Hydrate was collected by Dr. Sarah Barnett at Diamond. The single crystal X-ray experiment was performed using a Crystal Logic diffractometer with a Rigaku Saturn 724+ CCD detector (silicon 111 monochromated radiation,  $\lambda = 0.6889 \text{ \AA}$ ;  $\omega$  scans) also at  $150 \pm 2 \text{ K}$ . The applied absorption correction was based on multi-scans using REQAB within the d\*TREK program [174]. A colourless crystal (dimensions  $0.30 \times 0.07 \times 0.01 \text{ mm}$ ) was mounted on a MiTeGen micromount. There was no deterioration of the crystal during the data collection. The data was merged (MERG 3) during refinement as there was not enough information to reliably determine the Flack parameter of this system at this wavelength. The structure was solved by direct methods using SHELXS-97 [172] and all atoms were located using subsequent difference-Fourier methods. Hydrogen atoms were located from the difference Fourier map and freely refined.

### 3.3.2 Powder X-ray Diffraction

The routine collection of powder X-ray diffraction data for phase identification was done on a Stoe StadiP transmission geometry diffractometer using Ge (111) monochromated  $\text{CuK}\alpha_1$  radiation ( $\lambda = 1.54046 \text{ \AA}$ ) operating at 40kV and 30mA, and using a linear position sensitive detector (aperture  $4.5^\circ 2\theta$ ). Samples were loaded into 0.5 - 0.7mm borosilicate glass capillaries and rotated throughout the data collection to minimise preferred orientation effects. Data were collected at ambient temperature and over a range of  $2 - 45^\circ 2\theta$ , with  $0.2^\circ 2\theta$  steps and 20 seconds per step count time.

Powder X-ray diffraction data for structure determination of racemic Naproxen (Chapter 4) and ESP II and ESP III (Chapter 5) were collected by Dr. Jean-Baptiste Arlin and Ms Rajni Miglani at Strathclyde University on a Bruker AXS D8 X-ray powder diffractometer equipped with a primary monochromator ( $\text{CuK}\alpha_1$ ,  $\lambda = 1.54056 \text{ \AA}$ ) and Lynxeye position sensitive detector. The samples were loaded in 0.7 mm borosilicate glass capillaries and rotated throughout the measurement. Data was collected at room temperature using a variable count time scheme [175, 176]. Diffraction patterns were indexed using the first twenty peaks with DICVOL04 and their space groups determined based on statistical assessments of the systematic absences [177], as implemented in the DASH structure solution package [178, 179].



### 3.3.3 FT Infrared spectroscopy

Infrared spectra were recorded with a diamond ATR crystal on a Perkin Elmer Spectrum One Fourier Transform spectrophotometer (Perkin Elmer, Norwalk Ct., USA). The spectra were recorded over a range of 4000 to 600  $\text{cm}^{-1}$  with a resolution of 2  $\text{cm}^{-1}$  (24 scans). The analysis was done with the Opus v 5.5 software.

### 3.3.4 Elemental Analysis

Elemental analysis measurements were performed on samples to investigate the possible formation of solvates and also to check the stoichiometry of the salts. Measurements were performed on an Exeter Analytical CE-440 Elemental Analyser.

### 3.3.5 Thermal Analysis

Thermomicroscopic investigations were carried out with a polarizing microscope (Reichert, A) fitted with a Kofler hot-stage (Reichert, A).

Differential Scanning Calorimetry (DSC) was performed on a TA Instruments Q2000 system using the TA Universal Analysis 2000 software (Manchester, UK). The instrument was calibrated for temperature and energy in the respective temperature range with pure indium (purity 99.999%, m.p. 156.6 °C, heat of fusion 28.45  $\text{J g}^{-1}$ ). For Naproxen, approximately 3 – 4 mg of sample was accurately weighed (AD-6 microbalance, Perkin Elmer, Norwalk, CT) into sealed aluminium  $T_{\text{zero}}$  pans with a hermetic  $T_{\text{zero}}$  lid. Dry helium was used as a purge gas (purge: 20  $\text{mL min}^{-1}$ ). For the diastereomeric salts approximately 2 – 3 mg of sample were accurately weighed (Mettler-Toledo Microbalance) into sealed Aluminium  $T_{\text{zero}}$  pans with  $T_{\text{zero}}$  lid (TA instruments). Dry nitrogen was used as a purge gas (purge 50ml/min). A heating rate of 10K/min was used for all the measurements. The errors of the stated temperature and enthalpy values are calculated at 95% confidence intervals based on at least five measurements for the thermal data.

Thermogravimetric analysis was conducted on a NETZSCH STA 449 C differential scanning calorimeter equipped with the Proteus® Software. Helium was used as purge gas at a flow rate of 50  $\text{ml min}^{-1}$ . The temperature was calibrated with indium (~3mg, 99.9%, m.p. 156.6 °C) and the energy sensitivity was calibrated with a range of standards: Sn (-60.5 J/g), Bi (-53.3 J/g), Zn (-107.5 J/g) and Al (-397 J/g). Samples of 2.0  $\pm$ 0.5 mg in open aluminium pans were heated at a rate of 10 K/min.

### 3.3.6 Isothermal Solution Calorimetry

Enthalpies of solution for the different polymorphic phases of ERP and ESP in absolute ethanol were measured using a Thermal Activity Monitor (TAM, Thermometric AB, Jarfalla, Sweden), which was housed in a temperature controlled environment ( $298 \pm 0.1\text{K}$ ). The calorimeter was calibrated periodically using the electrical substitution method, and was fitted with a three blade impeller to ensure complete dispersion of solids into the solution. The experiments were performed at 298 K. Approximately 5 mg of sample were accurately weighed using a Mettler-Toledo microbalance into reusable stainless steel capsules. The capsules consist of three pieces, two stainless steel walls which fit into a circular bottom piece. The bottom piece has an O-ring to ensure the capsule is sealed when fitted into the lid of the calorimeter. To further ensure that the capsule was sealed, a film of inert oil was applied to the bottom of the capsule so that any possible space between that and the lid would be closed. Once a baseline stability of  $\pm 0.1 \mu\text{W}$  had been attained, the capsule was dropped into the calorimeter. The heat flow, in or out, of the calorimeter was recorded using the dedicated Digitam 2.0 software. Data analysis was performed using the software package ORIGIN<sup>TM</sup> (Microcal Software In., MA, U.S.A)

### 3.3.7 Solubility Determination

The solubility of (S)-naproxen and (RS)-naproxen as a function of temperature was established at 10, 15, 20, 25, 30, 35, and 40 °C in an ethanol:water mixture (4:1, v/v). The solubility of ERP I° and ESP III°, the thermodynamic stable phases of ERP and ESP, were determined at 5, 10, 15, 20, 25 and 30 °C in ethanol.

The solubility apparatus consisted of a jacketed glass vessel maintained at a constant temperature by water circulated from a water bath (Grant LTC 12-50). The jacket temperature could be maintained within  $\pm 0.01$  °C in the used temperature range. An excess of substance was added to 50 mL of the co-solvent mixture and stirred with a magnetic stirrer (400 r.p.m.) for 5 days to reach equilibrium (this equilibrium time was established by quantifying that the drug concentration had reached a constant value). After this time stirring was discontinued and the solid phase was allowed to settle before withdrawing the liquid phase. Three samples were withdrawn from each suspension and temperature in 12 hours intervals, with volumetric pipettes attached to filter holders (Swinnex, Millipore) and  $0.22\mu\text{m}$  membrane filters (Millipore). To maintain the sample temperature during sampling, the filter attachments were conditioned in an empty vessel in the water bath.

For Naproxen, samples withdrawn at 25 °C and above were diluted by a factor of 2. (S)-NPX samples withdrawn at 40 had to be diluted by a factor of 3. HPLC measurements were made

with a Shimadzu LC-2010CHT system (Milton Keynes, U.K.) to determine the concentration of Naproxen in solution.

For the solubility measurements of ERP I° and ESP III° a gravimetric method was used. Approximately 1ml aliquots of ERP I° and ESP III° solutions were introduced into pre-weighed vials and the ethanol left to evaporate on a hot plate kept at 60 °C. Once the ethanol had completely evaporated the vial was weighed using an AD HR-200 microbalance (Advanced Instruments, UK).

To ensure that the solid phases present in the suspension corresponded to the thermodynamically most stable phase throughout the measuring range, solid samples were analysed using PXRD and infra-red spectroscopy. The samples were kept wet to for the IR analysis in order to prevent de-solvation, had a solvate been formed.

### 3.4 Computational Methodology

In order to correctly rank the diastereomeric pairs and their polymorphs according to their relative stability, an accurate representation of all the components of the lattice energy - the intermolecular energy contributions,  $U_{\text{inter}}$ , dominated by electrostatic interactions, and the energy cost associated with distorting the molecule from its gas-phase conformation,  $\Delta E_{\text{intra}}$  - is required. The accurate calculation of these two components requires elaborate energy models based on quantum mechanical calculations. This is especially demanding for flexible molecules and two component systems (such as the diastereomeric salts), as the conformation adopted by the molecules also greatly affects the intermolecular interaction energy.

The workflow followed in this thesis to calculate the relative energies of the Ephedrine – 2 – Phenylpropionate salts and the different polymorphs found in the crystallisation screen (see Chapter 5) could be summarised in three steps:

1. Molecular Conformational Analysis (for the evaluation of  $\Delta E_{\text{intra}}$ )
2. Selection of Intermolecular Energy model (for the evaluation of  $U_{\text{inter}}$ )
3. Accurate Evaluation of the Lattice Energy

The three steps are described in more detail in Sections 3.6.1, 3.6.2 and 3.6.3 respectively.

Finally, a search for hypothetical low energy crystal structures using CrystalPredictor [121] was also performed in order to assess whether the search algorithm would predict the experimental structures found in the crystallisation screen and also to see what other possible packing arrangements might be competing with the experimentally observed ones.

### 3.4.1 Molecular Conformation Analysis

The molecular conformation analysis and evaluation of  $\Delta E_{\text{intra}}$  is done using the programme GAUSSIAN, using the HF method at the 6-31G(d,p) level of theory. Results obtained with this method were compared to an analysis of the Cambridge Structural Database (CSD), looking at the range of values that the ions' flexible torsion angles have adopted in the crystalline state of experimentally determined crystal structures. The analysis of the CSD (Version 5.31, November 2009) was performed using ConQuest [180].

### 3.4.2 Selection of Intermolecular Energy Model

The intermolecular energy model,  $U_{\text{inter}}$ , is comprised of repulsion-dispersion and electrostatic contributions. The electrostatic energy is modelled using Coulombs law, using a distributed multipole model for the representation of the charge. In the distributed multipole model the electron density is described by a series of multipole moments (i.e. charge, dipole, quadrupole, etc. up to the hexadecapole) that are centred at the atomic nuclei. The programme used to perform the distributed multipole analysis [99] of the wavefunction of the isolated molecules was GDMA [100]. In turn, the wavefunction for distributed multipole analysis was calculated using GAUSSIAN at the MP2 6-31G(d,p) level of theory. For the repulsion-dispersion model, two empirically derived force fields, FIT [129] and WILL [181], were tested. These potentials were used in DMACRYS [182] to carry out rigid body lattice energy minimisations starting with the experimental molecular conformations, to see how well the experimental structures were reproduced. The FIT force field was considered to be more adequate and so was used in the accurate calculation of the lattice energies with the CrystalOptimizer algorithm.

### 3.4.3 Accurate Evaluation of the Lattice Energies

Finally, the evaluation of the lattice energy is done using the CrystalOptimizer [122] algorithm (see Chapter 1 for details of the main features of this algorithm). CrystalOptimizer uses GAUSSIAN to compute the intra-molecular energy, and to calculate the wavefunction which is subsequently analysed with GDMA to compute the charge multipoles. The algorithm uses DMACRYS [182] to carry out rigid molecule lattice energy minimisations to compute the lattice energy, using the FIT force field. The main feature of CrystalOptimizer is that it allows the molecular conformation to vary, to find the optimum balance between the intra and inter molecular energies. This process would be very computationally demanding as one would expect to have to perform a quantum mechanical (QM) calculation every time the conformation was varied. However, CrystalOptimizer uses Local Approximate Models (LAMS) to calculate the intramolecular energy with respect to a reference conformation

without requiring new QM calculations. A new QM calculation is run every time the conformation changes by  $4^\circ$ . Similarly, the charge distribution calculation also uses LAMs. In this case, if the conformation change is less than  $4^\circ$  the multipole moments of the reference conformation are rotated with the local environment.

# Chapter 4 Racemic Naproxen: a multidisciplinary structural and thermodynamic comparison with the enantiopure form

## 4.1 Introduction

Racemic mixtures can exist in the solid state as a racemic crystal, where both enantiomers are present in the unit cell in equal stoichiometry; a conglomerate, where enantiomers “spontaneously resolve” into an equimolar mechanical mixture of the two enantiomers; or finally a pseudoracemate (or racemic solid solution), where both enantiomers are found in the crystal lattice but with no fixed stoichiometry (refer to chapter 2 section 2.6 for more details). The manner in which a 1:1 mixture of enantiomers crystallises from solution dictates the approaches used to separate enantiomers, and hence there have been considerable efforts in industry to develop methods with which to identify the solid nature of racemic mixtures with relative swiftness.

X-ray powder diffraction and spectroscopic methods have been commonly used to identify the structural differences between the racemate and its enantiomers [169]. However, being able to obtain thermodynamic stability data across the whole phase diagram and all the metastable phases, together with a complete picture of the atomic arrangement of the different species is very laborious and is often not possible due to problems in obtaining suitable crystals for X-ray diffraction studies.

The significant advances that have been observed in recent years in the crystal structure prediction of small and organic molecules from first principles [183-185] has meant that there has been an increasing interest in developing computer modelling to predict chiral crystallisation [54, 84, 86, 186-188]. With crystal structure prediction (CSP) methods one is able to generate thermodynamically feasible homochiral and racemic crystals and to estimate their relative stabilities. Therefore the use of CSP methods can be employed to rationalise the crystallisation behaviour of chiral compounds. In order for a conglomerate to be formed, provided the crystallisation process is thermodynamically controlled, racemic crystals must be less stable (have a higher Gibbs free energy) than homochiral crystals. In other words, the Gibbs free energy difference for the formation of racemic crystals must be positive. Since entropy differences are generally small between low energy crystal structures [51], lattice energy calculations can provide insights into spontaneous resolution by estimating the lattice energy differences between homochiral and racemic crystals, although it has also been shown that highly accurate models of intermolecular forces are needed [52-54].

In order to develop reliable computer models for the design of chiral separation processes (or indeed for any purpose) careful validation of the assumptions and accuracy by comparison with experimental studies is essential. Although improvements in CSP methods together with the continuous advances and affordability of computational resources have resulted in a considerable increase in the types and number of systems that are amenable to computational studies, the experimental work and techniques required for the validation of the computer models have not necessarily advanced accordingly and are still very time consuming and, perhaps more importantly, are considered to be quite unglamorous and therefore less likely to be part of modern research projects. Therefore, it is not so unlikely that, in the future, an increasing number of computational studies involving the estimation of the relative energies of hypothetical crystals structures will be hampered by the lack of experimental data rather than by the availability of computational resources. This might be especially the case when dealing with chiral compounds as very often only data for either the enantiopure or the racemic compound is available [188].

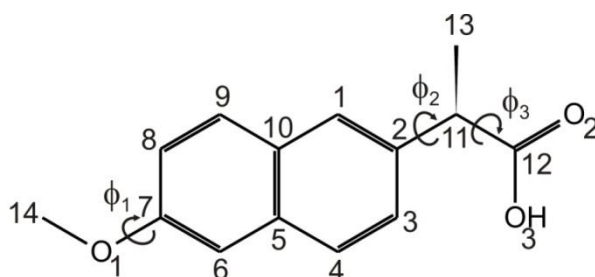


**Figure 4.1** Molecular diagram of naproxen (C<sub>14</sub>H<sub>14</sub>O<sub>3</sub>, Mr = 230.26), with the three main torsion angles considered during computational modelling studies defined as  $\Phi_1 = \text{C14-O1-C7-C8}$ ,  $\Phi_2 = \text{C12-C11-C2-C1}$  and  $\Phi_3 = \text{O2-C12-C11-C2}$

An example of such a situation is Naproxen [(±)-2-(6-methoxy-2-naphthyl)propionic acid, shown in Figure 4.1]. Naproxen is a nonsteroidal anti-inflammatory (NSAID) that, unlike other NSAIDs such as ketoprofen and fluriprofen which are marketed as racemic compounds, is marketed as the enantiopure (S)-enantiomer. The (S)-enantiomer is 28 times more active than the (R)-enantiomer and is normally obtained by separation after the synthesis of the racemate [189, 190]. Most available experimental data is for the enantiopure phase only. For example, the structure of the enantiopure phase has been characterised, deposited in the CSD under the refcode family COYRUD [191, 192]. Similarly, solution studies are only available for (S)-naproxen, with accessible solubility data for common organic solvents (methanol, ethanol, acetone, ethyl acetate, 2-propanol, octanol, isopropyl mystrate,

chloroform, cyclohexane, benzene, lower alcohols up to n-octanol and water [193-196]), water cosolvents [193, 197], and propylene glycol cosolvents [198]. The melting point, heat/entropy of fusion and the solid and liquid heat capacities of (S)-Naproxen have also been reported [199-201]. Perlovich *et al.* also measured the heat of sublimation of (S)-Naproxen and compared it with crystal energy calculations using two different force fields [196]. Surprisingly, the only available data for (RS)-Naproxen is the melting point and heat/entropy of fusion [201].

The crystal energy landscape for Naproxen<sup>5</sup> unequivocally predicted that crystallisation of a 1:1 racemic solution should form a racemic compound (Figure 4.2) with a very different crystal packing from (S)-Naproxen (Figure 4.3) [202].

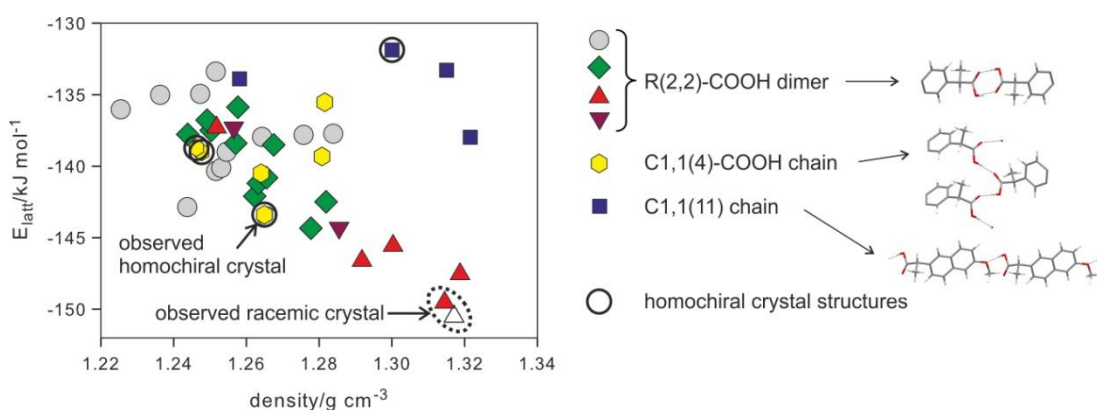


**Figure 4.2** Lattice energy landscape for naproxen ( $E_{\text{latt}}=U_{\text{inter}}+\Delta E_{\text{intra}}$ ) after relaxation of the conformation within the crystal structure and considering molecular polarization in the crystal (PCM,  $\epsilon=3$ ), classified by the hydrogen-bonding motif. Each symbol denotes a crystal structure which is a lattice energy minimum. The empty triangle corresponds to the lower symmetry version of the experimental racemic crystal structure [202].

Furthermore, the experimentally observed structure for (S)-Naproxen was correctly calculated to be the most stable of the computationally generated homochiral structures ( $\text{rmsd}_{15} = 0.380 \text{ \AA}$ , Figure 4.4 (a)) providing evidence for the reliability of these calculations. The modelling of the (S)-NPX crystal structure also correctly reproduced the bending of the naphthalene ring: the observed angle between the two aromatic rings was  $175.61^\circ$  compared with the experimental value of  $174.88^\circ$  (Figure 4.4 (b)).

<sup>5</sup> The computational investigation in this study was performed by Dr. Doris Braun and Dr. Emiliana D’Oria



However, due to the lack of experimental data on the racemate, an assessment of the ability of this state-of-the-art computational modelling method, based on lattice energy minimisation, to reproduce the crystal structure of the racemate and the experimentally determined relative stability was not possible.

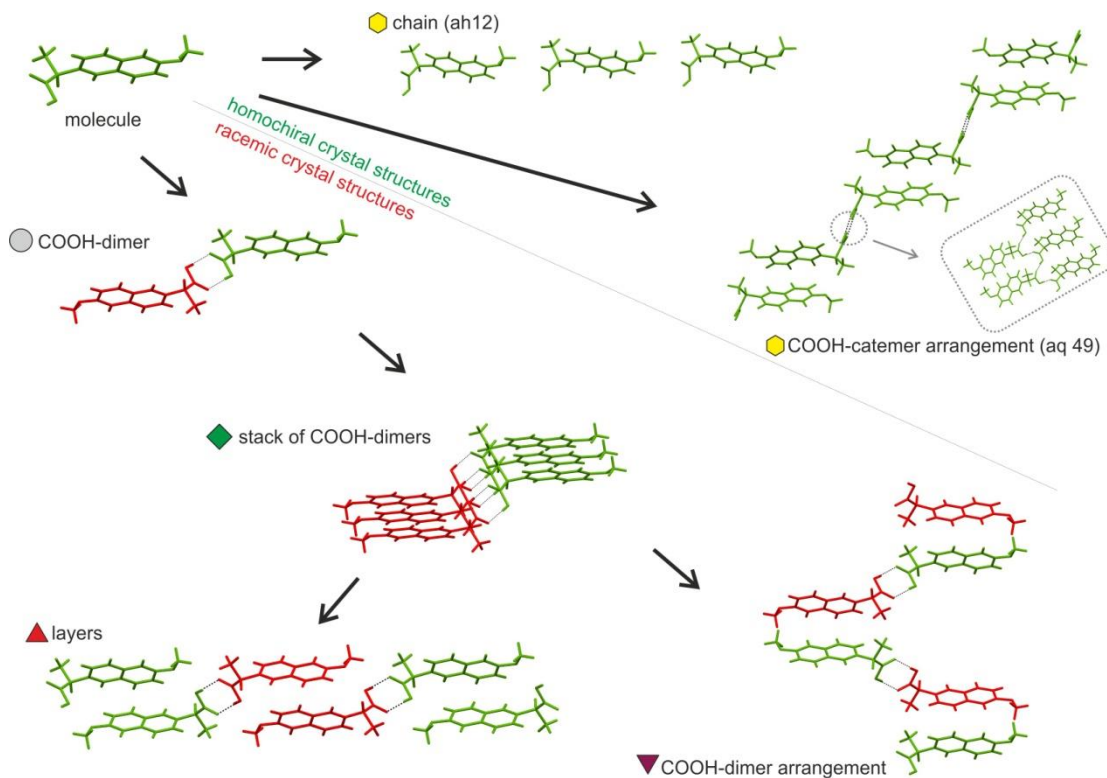


**Figure 4.3** Structure similarities (building blocks) observed between the experimental NPX crystal structures and all predicted low energy structures. The two hands ((R) and (S)) are coloured differently [202].

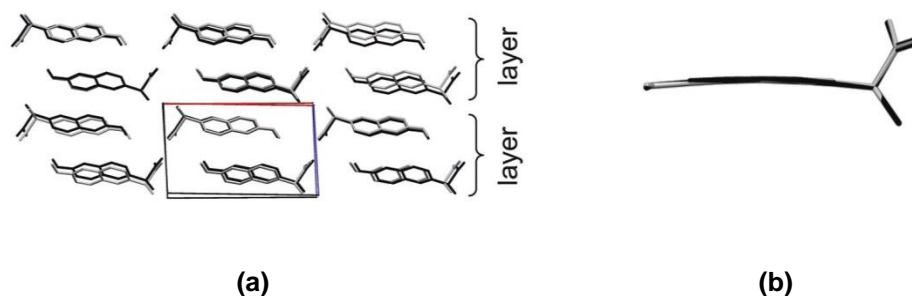


**Figure 4.4** Structure overlays of experimental (black) and calculated (grey) NPX structures: (a) (S)-NPX viewed along c, (b) modelling of the bending observed in (S)-NPX. The braces indicate the layers in Figure 4.3.

## 4.2 Objectives

The work presented in this chapter aims to overcome to some extent the asymmetry in the availability of thermodynamic data for the racemic and enantiopure sample with regards to the pharmaceutical system Naproxen. By providing structural and thermodynamic data will be used to validate the computational results obtained for this system and gauge the progress towards the ultimate aim of developing computational methods to predict the experimentally observed structures and thermodynamic stability of chiral crystals without relying on experimental data.

Crystallisation experiments with the racemic and enantiopure forms of Naproxen were therefore performed to see whether (RS)- and (S)- Naproxen displayed polymorphism and to try to obtain single crystals of (RS)-Naproxen. Furthermore, experiments to characterise the binary melting phase diagram, and to contrast the thermal and solution behaviour of all the solid phases were also performed. Since suitable crystals of (RS)-naproxen for single crystal structure determination could not be obtained its structure was solved from powder diffraction data by our collaborators at Strathclyde University.

## 4.3 Summary of the Crystallisation screen

(S)-naproxen (purity > 98%) and (RS)-naproxen (purity > 97%) were purchased from Sigma Aldrich and Manchester Organics, respectively. The samples were recrystallized for purification from ethanol. Optical sample purity was determined with HPLC, using a chiral (R,R)Whelk-01 column (Regis Technologies, Morton Grove, IL, USA) and ultraviolet detection at 254nm, under isocratic conditions using hexane:isopropanol (60:40) + 0.1% acetic acid as eluant at a flow rate of 1 mL min<sup>-1</sup>. The retention time for (S)-Naproxen is  $R_t = 5.5$  min and for (R)-Naproxen  $R_t = 7$  min.

Slow evaporation and slow cooling crystallisation experiments described in Chapter 3 Section 3.2 were carried out to see whether (S)-naproxen or (RS)-naproxen would exhibit polymorphism and to try to obtain good quality single crystals of (RS)-Naproxen for single crystal X-ray diffraction. Experiments were performed in a range of 10 solvents including methanol, ethanol, 2-propanol, 2-butanol, acetone, acetonitrile, dioxane, tetrahydrofuran, ethyl acetate and diethyl ether. All solvents used were of p.a. quality and purchased either from Fluka or Aldrich. Analysis of the phases obtained in the crystallisation experiments was performed as discussed in Chapter 3, Section 3.3. The structure of racemic Naproxen was solved from powder X-ray diffraction data.

## 4.4 Results and Discussion

### 4.4.1 Crystallisation Results

The crystallisation screen using ten solvents for (S)- and (RS)-naproxen always resulted in the same anhydrous form of the homochiral or racemic compound, respectively, as confirmed with infrared (Figure 4.5) and powder X-ray diffractometry (Figure 4.6). The therapeutic form, (S)-naproxen, readily crystallises with either a plate or needle morphology, whereas the (RS)-NPX crystallised very slowly in the shape of needles or multilayered elongated plates, as shown in Figure 4.7, which were unsuitable for laboratory X-ray single diffraction studies, or microcrystalline powder.

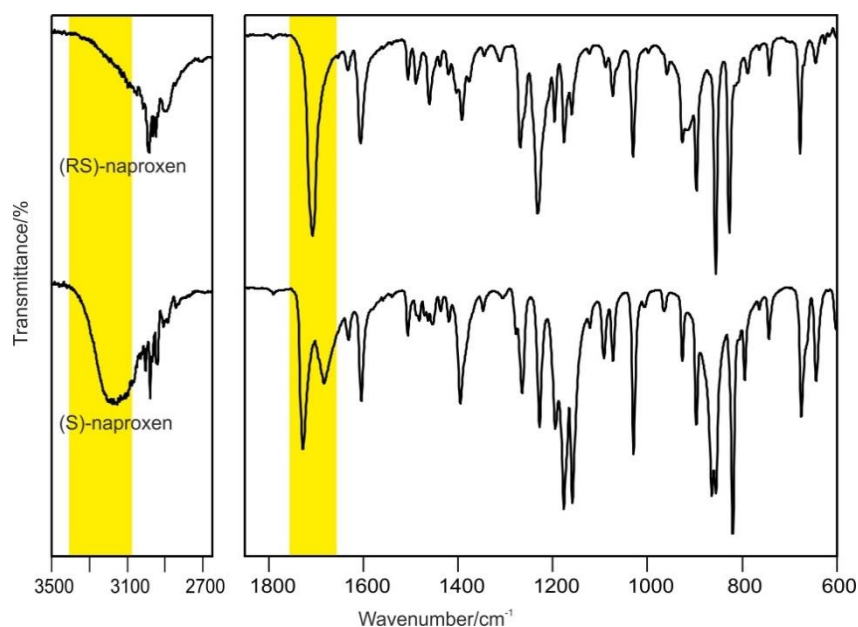


**Figure 4.5** FT-IR spectra of (S)- and (RS)-naproxen. Highlighted are the regions of the C=O stretching vibrations.

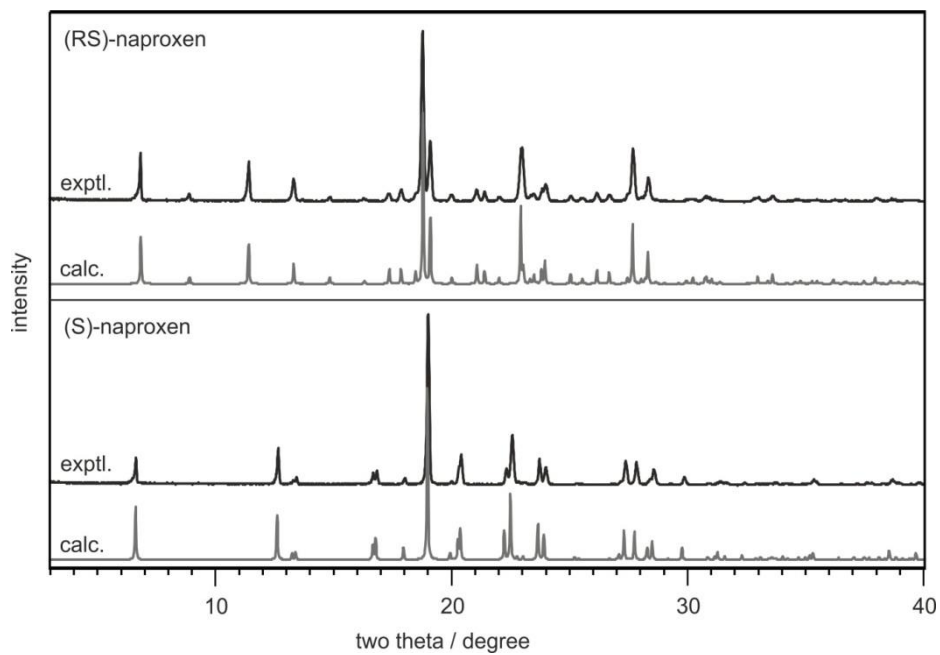


**Figure 4.6** X-ray powder diffraction patterns of (S)- and (RS)-naproxen. The experimental diffractograms are contrasted with the calculated powder patterns (S: single crystal data, COYRUD11 [192], RS: own structure solution).



**Figure 4.7** Example of a multilayered (SR)-naproxen crystal (size 0.6mm x 0.3mm x 0.07mm). This was the largest crystal grown in the attempts to obtain single crystals over a period of a few months.

#### 4.4.2 Comparison of the Crystal Structures of Enantiomeric and Racemic Naproxen

COYRUD11, the monoclinic  $P2_1$   $Z'=1$  crystal structure of the (S)-enantiomer that had been previously deposited in the Cambridge Structural Database [191, 192], was used for comparison with the structure of the racemate. (RS)-NPX crystallizes in  $Pbca$  ( $Z'=1$ ). The molecular conformations in the two crystal structures differ in the dihedral angles  $\phi_2$  and  $\phi_3$  by  $13.5^\circ$  and  $28.5^\circ$ , respectively, but both have the methoxy group approximately coplanar with the naphthalene moiety ( $\phi_1 \sim 180$ ). The naphthalene ring in the (S)-enantiomer is markedly non-planar as shown in Figure 4.4 (b), but was assumed to be planar in the (RS) structure refinement. The fact that a planar conformation of the naphthalene moiety led to a lower profile  $\chi^2$  fit to the data and that the bending of the two aromatic rings was calculated as  $177.02^\circ$  in the predicted structure (a much smaller bend compared to the predicted homochiral structure) support the assumption that naproxen could be modelled as planar in the PXRD structure determination. Had naproxen not been modelled as planar, the strain introduced by the bend of the aromatic rings would have contributed to the conformational energy of the molecule and in turn to the energy differences between the two.

Strong intermolecular interactions are only formed between carboxylic acid groups, and form infinite  $C_1^1(4)$  chains mediated by  $2_1$  symmetry in the case of the homochiral crystals (as depicted in Figure 4.8(b)) and inversion related  $R_2^2(8)$  acid dimers of the two hands in the racemic crystals, shown in Figure 4.8 (a). Both structures exhibit weak C-H $\cdots$  $\pi$  interactions between the naphthalene rings and the layers containing the strong hydrogen bonding. However, XPac [203, 204] analysis gave no packing similarity between the two experimental forms confirming that the stacking of the aromatic rings is markedly different. The very different hydrogen bonding patterns therefore not only contribute to the energy differences between the enantiopure and the racemic compound but also to the difference in packing of the aromatic rings.

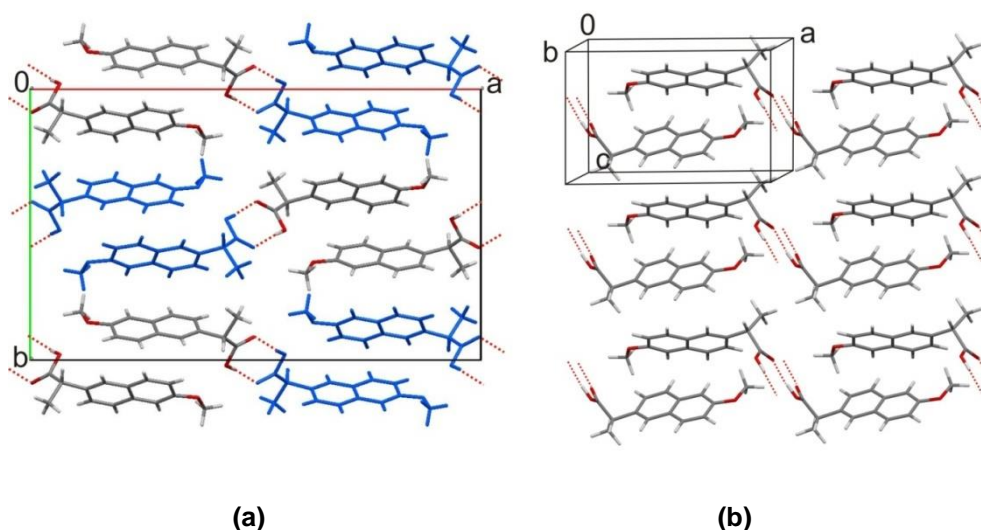


**Figure 4.8** Packing diagrams of (a) racemic and (b) enantiopure naproxen (COYRUD11).

### 4.4.3 Thermal measurements and binary melting point phase diagram

#### 4.4.3.1 Melting points and Heats of Fusion of (S) and (RS)-NPX

The melting points and heats of fusion of (S)-NPX and (RS)-NPX were obtained by means of differential scanning calorimetric measurements and are summarised in Table 4.1. The DSC curves of the racemate (0.5 mol) and single (S)-enantiomer (1.0 mol) exhibited one sharp endothermic peak at  $155.8 \pm 0.3$  and  $156.2 \pm 0.1$  °C, respectively (Figure 4.9), corresponding to the melting of the two compounds. DSC curves from samples obtained from all crystallisation experiments displayed the same melting behaviour, with a single sharp endotherm, supporting the observation that under the crystallisation conditions investigated, (RS)-NPX and (S)-NPX do not exhibit polymorphism. The melting temperatures of (S)- and (RS)-NPX were also confirmed using hot stage microscopy in order to further check that the only phases obtained from the crystallisation experiments were those of the (S) and (RS)-NPX. The entropy of fusion was calculated from the melting temperature and heat of fusion as  $\Delta S_{fus} = \Delta H_{fus} / T_{fus}$ .

As seen from Figure 4.9 and the data summarised in Table 4.1, the racemic compound has a slightly lower melting point (0.4 °C) and slightly higher heat and entropy of fusion than the enantiopure crystal. However, the differences are small relative to our error estimates and less than the error estimate from previous literature measurements of (S)-NPX.

|  | (S)-NPX                          | (RS)-NPX    | Eutectic    | $\Delta[(S)-(RS)]$ |
|--|----------------------------------|-------------|-------------|--------------------|
| <b>Thermal Measurements (155-156 °C)</b>   |                                  |             |             |                    |
| $T_{fus}$ , °C   | 156.2 ± 0.1                      | 155.8 ± 0.3 | 147.4 ± 0.7 | 0.4 ± 0.3          |
| <i>Lit. Values</i> , °C  | 157.3[205],155.4[206],158.1[207] | 155.4[205]  | -           | 1.9[205]           |
| $\Delta H_{fus}$ , kJmol <sup>-1</sup>   | 39.6 ± 0.2                       | 41.5 ± 0.4  | 30.3 ± 0.5  | -1.9 ± 0.4         |
| <i>Lit. values</i> , kJmol <sup>-1</sup>   | 31.3[205], 31.5 ± 2.1[206]       | 32.3[205]   | -           | -1.0[205]          |
| $\Delta S_{fus}$ , J mol <sup>-1</sup> K <sup>-1</sup>                                       | 92.2 ± 0.5                       | 96.7 ± 0.9  | 72.0 ± 1.2  | -4.5 ± 1.0         |
| <b>Solubility Measurements (10-40°C, ethanol/water <math>T_{hm}=25^\circ\text{C}</math>)</b> |                                  |             |             |                    |
| $\Delta H_{sol}^\circ$ , kJ mol <sup>-1</sup>  | 31.4 ± 0.3                       | 33.8 ± 1.0  | -           | -2.4 ± 1.0         |
| $\Delta S_{sol}^\circ$ , J mol <sup>-1</sup> K <sup>-1</sup>                                 | 62.8 ± 0.3                       | 66.4 ± 1.0  | -           | -3.6 ± 1.0         |
| $\Delta G_{sol}^\circ$ , kJ mol <sup>-1</sup>  | 12.7 ± 0.1                       | 14.0 ± 0.1  | -           | -1.0 ± 0.1         |
| <b>Lattice energy calculations (~0 K)</b>  |                                  |             |             |                    |
| $-E_{latt}$ , kJ mol <sup>-1</sup>   | 143.8                            | 150.3       | -           | -7.1 to -9.2       |

**Table 4.1** Values of the Thermodynamic Parameters of Enantiomer, Racemic compound and Eutectic of Naproxen. Parameters were obtained from Differential Scanning Calorimetry and van't Hoff plots. The experimentally determined values are contrasted to literature values and lattice energies calculated by DE Braun.

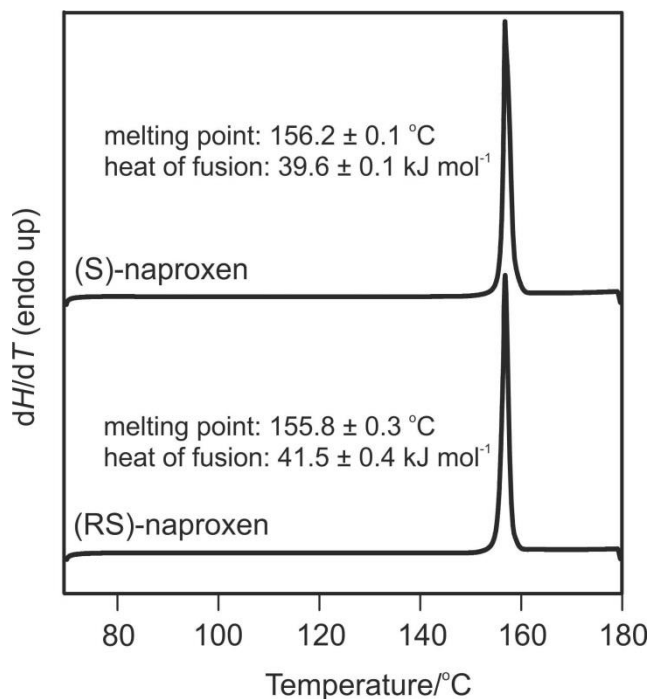


**Figure 4.9** DSC curves of (S)- and (RS)-Naproxen (heating rate 10 K/min).

#### 4.4.3.2 Binary Phase Diagram

DSC traces of mixtures of (S)- and (RS)-NPX of varying enantiomeric compositions presented two distinct peaks thus enabling the construction of the binary phase diagram shown in Figure 4.10. The first endothermic peak observed upon heating the mixtures represents the fusion of the eutectic, whereas the second represents the liquidus temperature, i.e. the melting of the excess phase. The eutectic temperature was also experimentally determined using Kofler's contact method [208], using a hot stage microscope. In this technique, the enantiopure compound is melted on one side of a cover slip and the racemic on the other and allowed to crystallise. Where the two compounds meet a eutectic is formed. Upon heating, the melting of this eutectic zone can be easily observed, and the temperature at which this happens established.

The melting data obtained for the different mixtures of (S) and (RS)-NPX follows the solid-liquid equilibria seen in ideal binary systems that can be calculated using the simplified forms of the Schröder-Van Laar (4.1) and Prigogine-Defay (4.2) equations [65]:

$$\ln x = \frac{\Delta H_{fus}(S)}{R} \left( \frac{1}{T_{fus}(S)} - \frac{1}{T_{fus}} \right) \quad 4.1$$



$$\ln 4x(1-x) = \frac{2\Delta H_{fus}(RS)}{R} \left( \frac{1}{T_{fus}(RS)} - \frac{1}{T_{fus}} \right) \quad 4.2$$

where  $x$  is the mole fraction of the more abundant enantiomer of the mixture,  $R$  the gas constant ( $8.314 \text{ J K}^{-1} \text{ mol}^{-1}$ ),  $T_{fus}(S)$ ,  $T_{fus}(RS)$ ,  $T_{fus}$  the melting temperature of the enantiomer, racemic compound and mixture, and  $\Delta H_{fus}(S)$ ,  $\Delta H_{fus}(RS)$  the enthalpy of fusion of the enantiomer and racemic compound (taken from Table 4.1). The eutectic point was taken as the point of intersection of the curves obtained from equations 4.1 and 4.2.

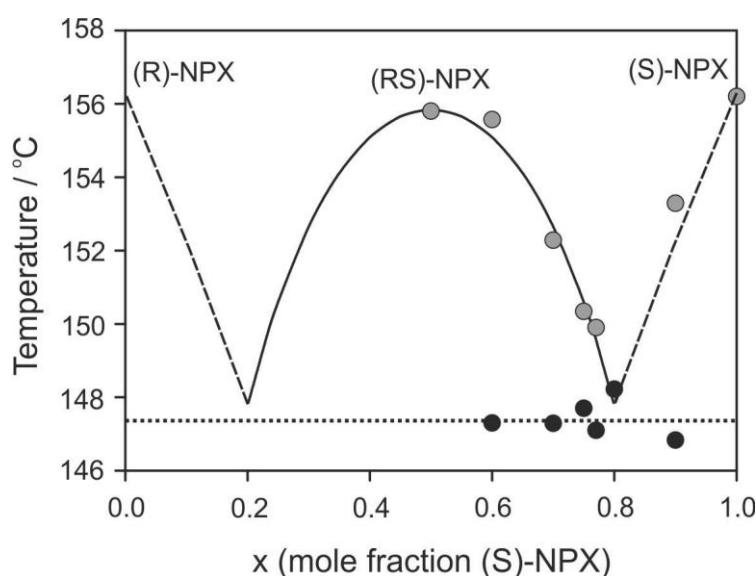


**Figure 4.10** Binary (melting point) phase diagram of naproxen showing racemic compound formation. Black circles represent the eutectic temperature and grey circles the liquidus or melting temperatures measured with DSC. The dotted line represents the eutectic temperature as measured by hot-stage microscopy ( $147.0 - 147.5 \text{ }^\circ\text{C}$ ). The dashed line represents equation (4.1) and the solid line equation (4.2) calculated using DSC thermal data from Table 4.1.

The binary phase diagram obtained for NPX excludes the existence of a racemic conglomerate, i.e. a physical mixture of the two enantiomers. Had a racemic conglomerate formed, the theoretical melting point of (RS)-NPX, obtained by extrapolating the dashed line on Figure 4.10 using Equation 4.2, would have been  $131.0 \text{ }^\circ\text{C}$ , far below the experimental value of  $\sim 147.5 \text{ }^\circ\text{C}$ . Furthermore, the presence of a eutectic between (RS)- and (S)-NPX not only excludes the possibility of a conglomerate but also the occurrence of a pseudoracemate. It is also worth pointing out that all DSC measurements and hot-stage

microscopy observations showed no signs of any phases other than (S)-NPX, (RS)-NPX and their eutectic.

#### 4.4.4 Solubility measurements and Thermodynamic functions of solution

The experimental solubilities of (S)- and (RS)-NPX in EtOH/water (4:1 v/v) were measured between 10 and 40 °C (Table 4.2) and exhibit the usual pattern of increasing solubility with temperature. There is good agreement with the published values [209] for (S)-NPX. For both (S) and (RS)-NPX a linear van't Hoff plot of  $\ln X_2$  against  $(1/T - 1/T_{hm})$  is obtained (Figure 4.11) showing that  $\Delta H_{sol}$  is constant over the range  $T_{hm} \pm 15$  °C, where  $T_{hm}$ , the mean harmonic temperature, is 25 °C. This suggests that there is no phase transformation in the temperature range studied for any of the samples. IR spectra of the solid residuals from the solubility measurement corroborated this.

The apparent standard enthalpy change,  $\Delta H_{sol}^\circ$ , and standard free energy,  $\Delta G_{sol}^\circ$ , of solution could be obtained using Krug's approach [210] from the van't Hoff plot for both solids. The calculated values are summarized in Table 4.1. The enthalpies and entropies of solution are positive for (S)- and greater for (RS)-NPX, suggesting that the process is always endothermic and driven by solution entropy.

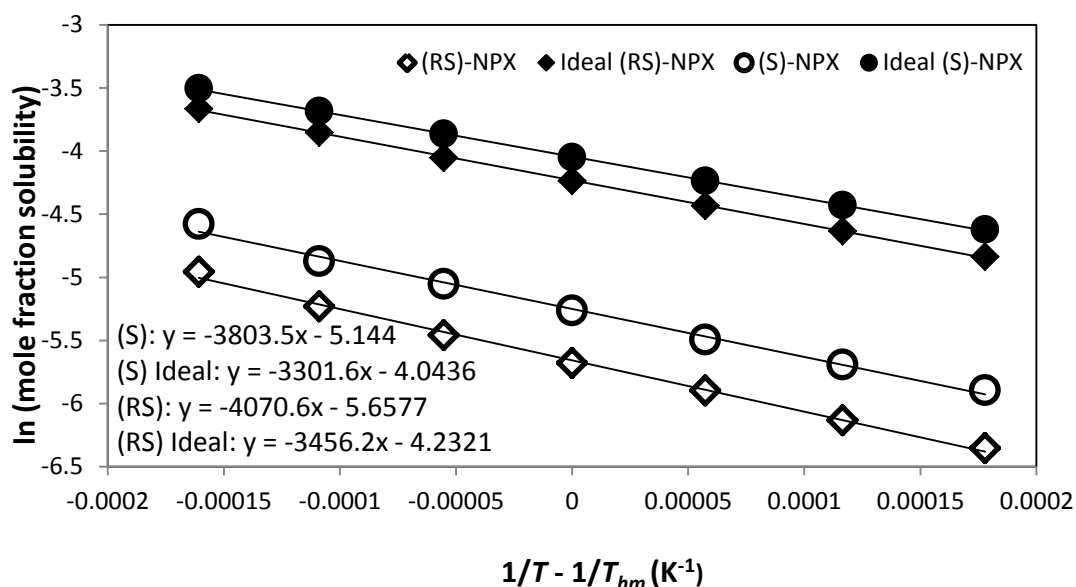


**Figure 4.11** Temperature dependence for solubility of (S)- and (RS)-NPX in EtOH:water (4:1, v/v) expressed in mole fraction. The gradient is  $-\Delta H_{sol}^\circ / R$  and the intercept is  $-\Delta G_{sol}^\circ / RT_{hm}$ .

| Temperature | (S)-NPX             |                                  | (RS)-NPX            |                                  |
|-------------|---------------------|----------------------------------|---------------------|----------------------------------|
| °C          | mol L <sup>-1</sup> | mole fraction                    | mol L <sup>-1</sup> | mole fraction                    |
| 10          | 0.0684 (0.0003)     | 2.757 (0.014) x 10 <sup>-3</sup> | 0.0434 (0.0002)     | 1.738 (0.008) x 10 <sup>-3</sup> |
| 15          | 0.0832 (0.0010)     | 3.375 (0.040) x 10 <sup>-3</sup> | 0.0517 (0.0043)     | 2.172 (0.036) x 10 <sup>-3</sup> |
| 20          | 0.1009 (0.0026)     | 4.107 (0.109) x 10 <sup>-3</sup> | 0.0676 (0.0005)     | 2.743 (0.020) x 10 <sup>-3</sup> |
| 25          | 0.1255 (0.0010)     | 5.174 (0.044) x 10 <sup>-3</sup> | 0.0840 (0.0003)     | 3.412 (0.014) x 10 <sup>-3</sup> |
| 30          | 0.1522 (0.0016)     | 6.265 (0.067) x 10 <sup>-3</sup> | 0.1027 (0.0006)     | 4.260 (0.025) x 10 <sup>-3</sup> |
| 35          | 0.1867 (0.0011)     | 7.641 (0.162) x 10 <sup>-3</sup> | 0.1298 (0.0005)     | 5.355 (0.022) x 10 <sup>-3</sup> |
| 40          | 0.2383 (0.0058)     | 10.14 (0.260) x 10 <sup>-3</sup> | 0.1693 (0.0077)     | 7.033 (0.010) x 10 <sup>-3</sup> |
| 25 (ideal)  |                     | 17.426 x 10 <sup>-3</sup>        |                     | 14.449 x 10 <sup>-3</sup>        |

**Table 4.2** Experimental solubility of (S)- and (RS)-NPX in EtOH/water (4:1, v/v) expressed in molarity and mole fraction at several temperatures.

#### 4.4.5 Thermodynamic Energy Difference between (RS) and (S)-NPX

##### 4.4.5.1 Relative Stability of the racemic compound from calculations

The relative stability of a racemic compound can be defined through the free energy difference,  $\Delta G_{R+S \rightarrow RS}^{cry}$  corresponding to the “reaction” between the crystalline (R)- and (S)-enantiomers in the racemic conglomerate that gives rise to the crystalline racemic compound (RS) [211]:



4.3

The simplest estimate for the thermodynamics of this reaction is to note that the lattice energy of each crystal is the energy required to separate the static lattice into infinitely separated molecules in their lowest energy conformation. The difference between this ideal gas for (S)-NPX and (RS)-NPX is only the configurational entropy term, and so the energy gap between the most stable homochiral and racemic structure, 7.1 kJ mol<sup>-1</sup> (see Figure 4.2) provides a first estimate of the  $-\Delta U_{R+S \rightarrow RS}^{cry}$  for this reaction. The approximations used in

calculating the lattice energy in the CSP search, such as the quality of the ab initio method and use of the polarization continuum model [118], were tested and using the lower symmetry version of (RS)-NPX gives a resulting range of values of  $\Delta U_{R+S \rightarrow RS}^{cry}$  from  $-7.1$  to  $-9.2 \text{ kJ mol}^{-1}$  providing an estimate of the modelling uncertainties.

The usual thermodynamic comparison is between the heat of sublimation and the lattice energy, as a simple thermodynamic cycle [212] relates the enthalpy of sublimation at the temperature  $T$ ,  $\Delta H_{subl,T}$  as:

$$\Delta H_{subl,T} = -E_{latt} - E_0 + \int_0^T \Delta C_p dT \quad 4.4$$

where  $E_{latt}$  and  $E_0$  are the lattice energy and zero-point energy, respectively and  $\Delta C_p$  the heat capacity difference of the gaseous and solid state. Usually,  $E_0$  is less than 1% of  $E_{latt}$ , and the  $\Delta C_p$  contribution is not greater than 10% of  $E_{latt}$  [212]. Since it is rather difficult to measure temperature-dependent values for the heat capacity of the gas and crystal, approximate relationships have been proposed, either using a constant value for  $\Delta C_p$  of  $-60$  to  $-40 \text{ J K}^{-1} \text{ mol}^{-1}$  [213], or empirical forms [214], implying that the stability of  $E_{latt}$  may be overestimated with an error of up to 10% if contrasted to  $\Delta H_{subl}$ . Perlovich et al [196] measured the heat of sublimation ( $\Delta H_{subl}$ ) of (S)-NPX as  $128.3 \pm 0.5 \text{ kJ mol}^{-1}$ , and estimated the lattice energy with two different empirical force fields to be  $-128$  and  $-145 \text{ kJ mol}^{-1}$ , whereas variations in  $E_{latt}$  within our approach vary from  $-125$  to  $-147 \text{ kJ mol}^{-1}$ , with the higher value corresponding to the electrostatic model used in empirically fitting the repulsion-dispersion potential, and the more stable being an overestimate of 14% if directly compared to  $\Delta H_{subl}$ .

If the zero point and heat capacities are the same for racemic and homochiral crystals, then the enthalpy for the hypothetical racemisation within the crystal (Equation 4.3), can be calculated:

$$\Delta H_{R+S \rightarrow RS}^{cry} = \Delta \Delta H_{subl} = \Delta H_{subl}(S) - \Delta H_{subl}(RS) \approx -\Delta E_{latt} \quad 4.5$$

However, there is a qualitative difference between the effects of zero-point motion in (RS)- and (S)-NPX. In addition, homochiral crystals often have lower frequency modes [215], due to lower density [216], that gives typically greater entropic stabilisation. Approximations of the free energies at 298 K [217] based on rigid body,  $k = 0$  vibrational modes [218] and elastic constants [219] shows that the difference in calculated zero-point and thermal energies are small, with (S)-NPX being stabilised over (RS)-NPX by  $0.1 \text{ mol}^{-1}$  and  $0.6 \text{ kJ mol}^{-1}$ , respectively. This estimate excludes thermal expansion, which will be anisotropic in both

crystals [220]. NPX conforms to Wallach's rule as the racemic compound is denser than the enantiomeric crystal [216]. The difference in cell volume at room temperature is  $8.404 \text{ \AA}^3$  per molecule, so the  $P\Delta V$  contribution to  $\Delta H_{R+S \rightarrow RS}^{cry}$  for the racemization reaction at  $5 \times 10^{-4} \text{ kJ mol}^{-1}$  is negligible.

#### 4.4.5.2 Relative Stability of the racemic compound from thermal measurements

The thermodynamic quantities,  $\Delta G_{R+S \rightarrow RS, T_{fus}(RS)}^o$ ,  $\Delta H_{R+S \rightarrow RS, T_{fus}(RS)}^o$  and  $\Delta S_{R+S \rightarrow RS, T_{fus}(RS)}^o$ , for the hypothetical racemisation reaction within the crystal (Equation 4.3) cannot be directly measured. However these values can be determined from the data in Table 4.1, at the melting point of (RS)-NPX,  $T_{fus}(RS)$ , the maximum temperature at which the "reaction" of the racemic compound from its enantiomers in the solid state may occur. The relationships, due to Jacques et al [65] and Li et al [221] are:

$$\Delta H_{R+S \rightarrow RS, T_{fus}(RS)}^o = \Delta H_{fus}(S) - \Delta H_{fus}(RS) + (C^l - C_S^s)(T_{fus}(RS) - T_{fus}(S)) \quad 4.6$$

$$\Delta S_{R+S \rightarrow RS, T_{fus}(RS)}^o = \Delta S_{fus}(S) - \Delta S_{fus}(RS) + R \ln 2 + (C^l - C_S^s) \ln \frac{T_{fus}(RS)}{T_{fus}(S)} \quad 4.7$$

$$\begin{aligned} \Delta G_{R+S \rightarrow RS, T_{fus}(RS)}^o &= \Delta H_{T_{fus}(S)} \left[ 1 - \frac{T_{fus}(RS)}{T_{fus}(S)} \right] - T_{fus}(RS) R \ln 2 \\ &+ (C^l - C_S^s) \left[ T_{fus}(RS) - T_{fus}(S) - T_{fus}(RS) \ln \frac{T_{fus}(RS)}{T_{fus}(S)} \right] \end{aligned} \quad 4.8$$

where  $T_{fus}(S)$  and  $T_{fus}(RS)$  are the melting temperature of the enantiomer and racemic compound,  $\Delta H_{fus}(S)$  and  $\Delta H_{fus}(RS)$  the enthalpy of fusion of the enantiomer and racemic compound,  $\Delta S_{fus}(S)$  and  $\Delta S_{fus}(RS)$  the entropies of fusion of the enantiomer and racemic compound.

We assumed a typical heat capacity difference between racemic and enantiopure forms of  $0.08368 \text{ kJ mol}^{-1} \text{ K}^{-1}$  for  $(C^l - C_S^s)$  [65]. However, since the difference in the melting temperatures of the enantiopure and racemic forms is small, the contribution from the heat capacity terms in equations 4.6 to 4.8 is negligible. For (RS)-NPX the enthalpy, entropy and

free energy of formation of the racemic compound from the pure enantiomers (Equations 4.6–4.8) are  $-1.9 \text{ kJ mol}^{-1}$ ,  $1.2 \text{ J mol}^{-1} \text{ K}^{-1}$ , and  $-2.4 \text{ kJ mol}^{-1}$  respectively confirming that the formation of the racemic compound from its enantiomers in the solid state is exothermic. The configurational entropy of mixing term in Equation 4.7 and Equation 4.8,  $R \ln 2$ , favoring the racemic compound makes a significant relative contribution to the entropy and free energy difference for racemization. However, the assumption behind this treatment is that the enantiopure and racemic melts only differ by the entropy of mixing,  $R \ln 2$ . This is true if one assumes that the two melts have the same structure and hence the enthalpy of mixing is zero. However, this is not generally true for enantiomers, although the differences in the melts are likely to be less than in the crystalline form because of the lack of long range order and decreased density. Nevertheless, in the specific case of NPX, significant differences between enantiopure or racemic clusters or melts are unlikely due to the molecular flexibility of the carboxylic acid or the possibility of proton exchange within carboxylic acid dimers.

#### 4.4.5.3 Relative stability of the racemic compound from solubility measurements

The enthalpy of solution ( $\Delta H_{\text{sol}}$ ) can be described as the sum of the contributions from the bonds that are broken when the crystal lattice breaks up ( $\Delta H_{\text{subl}}$ ) and the bonds formed when the molecules are solvated ( $\Delta H_{\text{solvation}}$ ). If the solvation energy is the same for (S) and (RS)-NPX, then the lattice energy difference between (RS) and (S) is approximately the difference in the heat of solution difference of the two compounds

$$\Delta\Delta H_{\text{sol}} = \Delta H_{\text{sol}}(\text{S}) - \Delta H_{\text{sol}}(\text{RS}) \approx -\Delta E_{\text{latt}} \approx \Delta H_{\text{R+S} \rightarrow \text{RS}}^{\text{cry}} \quad 4.9$$

Hence, the difference in the heats of solution between (RS) and (S)-NPX,  $-2.4 \pm 1.0 \text{ kJ mol}^{-1}$ , could be taken as an initial estimate for the hypothetical racemization reaction within the crystal (Equation 4.3) if we assume that there is no thermodynamic difference in the stability of the chiral and racemic solution.

This is equivalent to assuming that the solubility we have measured for (S)-NPX is the same as it would be in a solution of the (R)-enantiomer. Measurements of the transfer enthalpy involved in co-crystal formation from solution are significant (of order  $\pm 1 \text{ kJ mol}^{-1}$ ) for the difference between dissolving carbamazepine and analogues in methanol, with or without the presence of saccharine in the solution [222]. Transfer energies would be zero for ideal solutions and reflect the different interactions of the solutes. We can estimate the ideal solubility of a crystalline solute as a mole fraction  $X_2^{\text{id}}$  in an unspecified liquid solvent by

$$\ln X_2^{id} = -\frac{\Delta H_{fus}(T_{fus} - T)}{RT_{fus}T} + \left(\frac{\Delta H_{fus}}{RT_{fus}}\right) \left[\frac{(T_{fus} - T)}{T} + \ln\left(\frac{T}{T_{fus}}\right)\right] \quad 4.10$$

where  $T$  is the absolute solution temperature, using our values in Table 4.1. The measured solubilities are considerably lower than ideal implying significant solute-solute interactions. At 25°, the solubility corresponds to 316 water and 262 ethanol molecules to two NPX molecules for the (RS) racemic solution and 212 and 172 for the enantiopure solution. From the published solubility data for the (S)-NPX, the number of solvent molecules vary from 75 for ethyl acetate [223], in which it is most soluble, to over 7000 for water [209]. Thus the solvation shell is therefore likely to be sufficient to even out the small differences in molecular shapes between the two enantiomers in our solubility measurements, and the transfer energy is likely to be negligible. However, this may be less true for other solvents, or for other chiral molecules, but transfer energies involving the two hands of a chiral molecule would generally be much lower than these involved in co-crystal formation.

## 4.5 Discussion

### 4.5.1 Lattice energy landscape

This interdisciplinary study on NPX proved that (RS)-NPX forms a racemic compound, which is more stable than the therapeutically used (S)-enantiomer. The computationally generated lattice energy landscape successfully predicted the racemic compound, as well as the homochiral structure at the global minimum and lowest homochiral structure in lattice energy, respectively. No signs of polymorphs were observed in our limited screen [224]. This is consistent with an energy gap of almost 4 kJ mol<sup>-1</sup> between the observed and second lowest homochiral structure (Figure 4.2). The smaller energy differences between different packings of the carboxylic acid layers in (RS)-NPX may be more indicative [225] of the likelihood of stacking faults than true polymorphs, as found for progesterone [226] and aspirin [227] in contrast to aprepitant [228]. A tendency for stacking faults would account for our inability to grow good quality single crystals suitable for structural determination from single crystal diffraction. Thus, although (RS)-NPX is more stable, the nature of its crystal packing makes characterizing the structure intrinsically more difficult, with the computational prediction adding confidence to the solution from powder.

## 4.5.2 Comparison of calculated and experimental energy differences between racemic and enantiopure NPX

The calculations, thermal and solubility measurements all give the same qualitative result that the racemic compound is more stable than the homochiral phase, consistent with the expectation that formation of a racemic crystal can have significant enthalpic stability advantage over homochiral crystal structures [36, 221]. However, the three estimates (Figure 4.12) are comparing breaking up the racemic and enantiopure crystals into different phases at different temperatures. The experimentally derived  $\Delta H_{R+S \rightarrow RS}^{cry}$  was found to be approximately  $-1.9 \pm 0.3 \text{ kJ mol}^{-1}$  (Table 4.1) calculated from thermal measurements at  $T \sim 156 \text{ }^\circ\text{C}$  and  $-2.4 \pm 1.0 \text{ kJ mol}^{-1}$  from solubility measurements in the range of  $25 \pm 15 \text{ }^\circ\text{C}$ , respectively. The lattice energy difference gives an estimate of  $-7.1 \text{ kJ mol}^{-1}$ , which is significantly more stabilising, although the neglect of zero-point and thermal effects reduces the difference by approximately  $1 \text{ kJ mol}^{-1}$ . There is a variation of at least  $1 \text{ kJ mol}^{-1}$  with the quality of the wavefunction. Hence, the calculations are overestimating the energy difference between the two idealised crystal structures by at least  $1.5 \text{ kJ mol}^{-1}$ . This error is small as a percentage of the lattice energy, and also is sufficiently accurate for this crystal energy landscape (Figure 4.2) to give reliable ordering of the different structural types, but it is still significant for applications.

NPX was studied in order to characterise the racemic phase of a pharmaceutical, and there are features of the two structures which are particularly challenging to the accurate calculation of relative lattice energies. The unusual bending of the naphthalene ring in (S)-NPX and inability to determine this for the racemic structure introduce uncertainties into the estimate of the conformational contribution to the lattice energy. The two structures differ in their hydrogen bonding motifs, and the differential polarization of the carboxylic acid groups in the two motifs is not well represented by the empirically fitted isotropic atom-atom potentials. Moreover, the empirical fitting of the repulsion-dispersion parameters to known crystal structures and sublimation energies partially absorbs some of the approximations in the thermodynamics and form of the model potential. Hence, we can hope that more accurate modelling of the intermolecular forces, using molecule-specific intermolecular potentials [229] and including molecular polarisability and flexibility, or dispersion-corrected periodic density functional calculations, [230] may improve the reliability of relative energies. However, we note that the flexibility of most chiral molecules means that good estimates of thermal effects are also needed. Hence, the experimental measurements of both absolute and relative thermodynamic quantities provide an essential validation target for emerging computational chemistry methods.



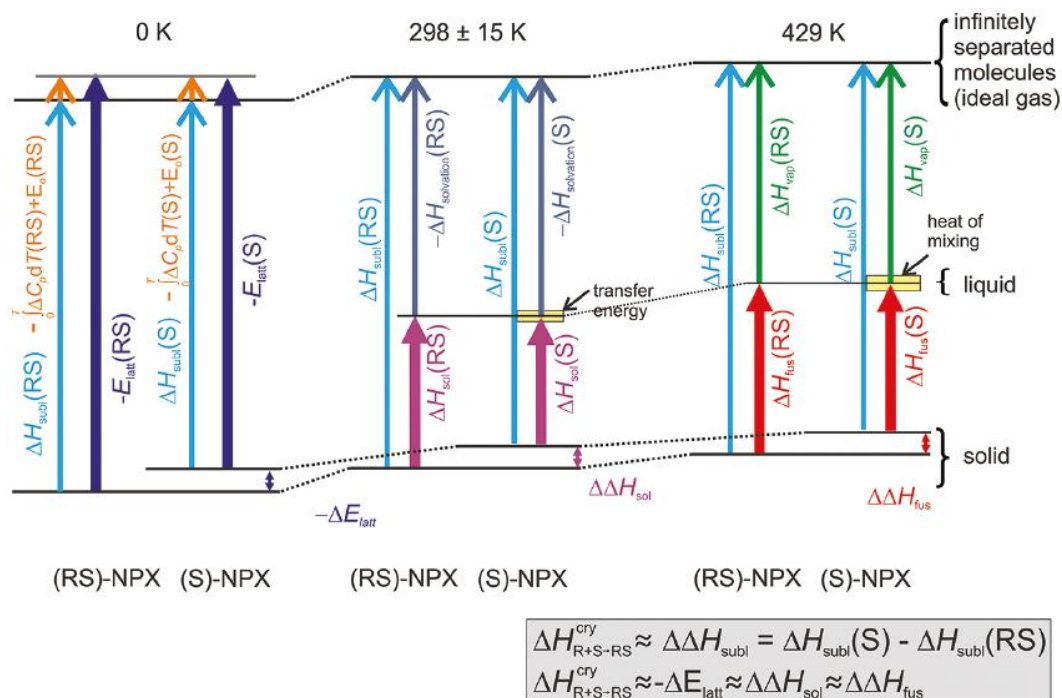


**Figure 4.12** Diagrammatic summary of the measured thermodynamic quantities (thick lines) and other enthalpic contributions relating the solid forms to the gas phase. Contributions that are probably negligible for naproxen but could be significant for other chiral systems with a more distinctive shape difference are indicated by yellow boxes.

## 4.6 Conclusions

The structure of (RS)-naproxen has been solved by powder X-ray diffraction and its solubility and thermal melting behavior contrasted with that of the therapeutically used (S)-naproxen. The binary melting point phase diagram, the solubility measurements, limited solid-state screening and the calculated crystal energy landscape are all consistent with the racemic *Pbca* and enantiopure *P2<sub>1</sub>* compounds being the only practically relevant solid phases of the free acid naproxen. This degree of consistency within this interdisciplinary study provides a level of confidence in the experimental findings, though the results also quantify the need to further improve computational modeling of crystal thermodynamic for aiding pharmaceutical development.

# Chapter 5 Ephedrine and Pseudoephedrine Diastereomeric Salts: A study of Classical Resolution.

## 5.1 Introduction

Though often seen as not technologically advanced, the separation of chiral compounds by crystallisation has been, and still is, one of the preferred techniques in industry, especially the so called classical resolution where a resolving agent is used to form diastereomeric pairs and the least soluble diastereomer is precipitated out [18, 19] (see 1.4.4.2). The effectiveness of this approach depends on the resolving agent, which determines the stability of the diastereomeric salts formed [56]. Despite its importance, the choice of resolving agent is often made based on a trial and error basis, by screening through large numbers of possible resolving agents and quickly assessing their resolution efficiency [55]. These fast screening methods however have obvious drawbacks, such as that they can easily miss the formation of other phases that can greatly affect the outcome of the resolution process (hydrates, solvates or polymorphs, for example).

In section 1.6 in Chapter 1 the efforts that over the years have gone into making the choice of resolving agents more rational were highlighted. Studies have mainly focused on structural analysis of the diastereomeric salt pair [58, 59, 76, 80]. As with fast screening methods, one of the main problems these studies have is that they often do not perform extensive crystallisation screens and so do not consider the possible effects that polymorphism or hydrate/solvate formation might have on the resolution efficiency. More recently, the use of computational structure prediction methods have also been employed to offer insight into the resolution ability of resolving agents, by calculating the static lattice energy differences between the hypothetical thermodynamically stable phases of the diastereomeric salts pairs [52, 53, 57, 85, 86]. These methods produce a number of hypothetical dense low energy crystal structures, and can be used to predict whether a compound will have other polymorphs [231, 232]. However, again, crystallisation screens are necessary in order to be able to validate the computational methods used, to see whether the experimentally observed phases are present in the range of low energy structures produced using the search algorithms and to see whether they are ranked in the correct stability order.

## 5.2 Objectives

In this chapter, the results of the crystallisation screens performed on a set of closely related diastereomeric salt pairs are presented. The first objective of the crystallisation screens was to perform a systematic study to try to identify all of the possible crystal phases for the systems in the 2x4 grid shown in Table 5.1, and to provide the crystal structure data for these forms, to see whether the search algorithms used in Chapter 6 would be able to predict all the experimental structures.

Secondly, the study also aimed to provide thermodynamic and relative stability data of the different forms and diastereomeric salt pairs, again necessary to assess the ability of the computational methods to predict the relative stability ordering and to quantify the energy difference between salt pairs by calculation of their lattice energies.

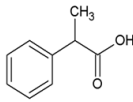
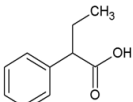
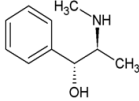
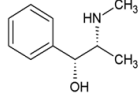
Since the resolution efficiency depends on the whole ternary phase and not just on the solubility and stability difference of the diastereomeric pairs, the final objective was to obtain ternary phase diagrams for the diastereomeric salt pairs in a solvent not only to assess the resolution ability of the different resolving agents but also again to identify whether predicting resolutions by computing the relative stabilities of two diastereomeric salts is valid.

## 5.3 Experimental

The systems studied, shown in Table 5.1, were the diastereomeric salts of (1R,2S)-Ephedrine and (1R,2R)-Pseudoephedrine with 2-Phenylpropionic acid and 2-Phenylbutyric acid. This set of similar and closely related systems were chosen in order to get a better understanding of the crystallisation behaviour of diastereomeric salts, to see what effect slight changes – varying the chirality of the resolving agent and increasing the length of a side chain on the acid to be resolved – would have on the resolution outcome.

Ephedrine was initially chosen as a model resolving agent as there are numerous examples in the literature of its use as a resolving agent. For example, ephedrine has been widely used in the resolution of simple substituted mandelic acids [233, 234]. Its applicability as a resolving agent was also investigated with a set of cyclophosphoric acids [235-237]. Ephedrine is a naturally occurring alkaloid present in plants of the Ephedra genus [238], and is the active ingredient present in Ma Huang (Ephedra Sinica) used in Chinese medicine for the treatment of asthma, hay fever and common cold. Ephedrine has also been commonly used in dietary supplements for weight loss, in combination with caffeine and aspirin [239]. 2-Phenylpropionic acid was chosen as Ephedrine was expected to be able to efficiently resolve a mixture of both enantiomers, given its similarity to mandelic acid. Pseudoephedrine and 2-Phenylbutyric acid were therefore picked based on these two

molecules, to introduce the slight changes that might provide some insight into the crystallisation of diastereomeric salts. Furthermore, despite the flexibility of the molecules and the added complexity of dealing with two components systems, the molecules chosen and their resulting diastereomeric salts were thought to be amenable for computational studies.

|   | <br>2-Phenylpropionic Acid | <br>2-Phenylbutyric Acid |
|---|---|---|
| <br>(1R,2S)<br>Ephedrine             | R   | R   |
| <br>(1R,2R)<br>Pseudo<br>ephedrine | R   | R   |
|   |   | S   |
|   |   | S   |

**Table 5.1** 2x4 grid of the diastereomeric salt systems studied. The objective is to obtain crystal structures of all experimentally observed phases as well as thermodynamic and stability data.

### 5.3.1 Diastereomeric Salt synthesis

(1R,2S)-Ephedrine and (1R,2R)-Pseudoephedrine (99%) were obtained from Acros Organics. Both enantiomers of 2-phenylpropionic acid and 2-phenylbutyric acid (97%) were obtained from Alfa Aesar. All solvents were HPLC grade and were used without further purification. The four diastereomeric salts were prepared by dissolving the appropriate 2-phenylpropionic acid or 2-phenylbutyric acid enantiomer in ethanol and adding an equimolar quantity of ephedrine or pseudoephedrine to the solution. The solutions were warmed up in order to dissolve the entire resolving agent. For the less soluble salts, salt formation was

observed as the appearance of a white precipitate upon complete dissolution of the base. To ensure that the entire base had reacted with the acid, ethanol was added until all the white precipitate had dissolved. On the other hand, the more soluble salts did not precipitate upon dissolution of the resolving agent. The salts were crystallised by completely removing the ethanol using a rotavapour (Buchi R210), by setting the water bath at 60 °C and the pressure at 175 mbar. The solid forms of the salts obtained after the complete evaporation of ethanol in the rotavapour were ground with a mortar and pestle and used in the crystallisation experiments. The following notation is used for the different salt systems throughout the thesis: ERP for Ephedrine-R-2-phenylpropionate, ESP for Ephedrine-S-2-phenylpropionate, ERB for Ephedrine-R-2-phenylbutyrate, ESB for Ephedrine-S-2-phenylbutyrate, PRP for Pseudoephedrine-R-2-phenylpropionate, PSP for Pseudoephedrine-S-2-phenylpropionate, PRB for Pseudoephedrine-2-R-phenylbutyrate and PSB for Pseudoephedrine-2-S-phenylbutyrate salts.

### **5.3.2 Summary of the Crystallisation Experiments**

An initial limited screen consisting of evaporation crystallisation experiments in methanol, ethanol, isopropanol, acetonitrile, dichloromethane, water, ethyl acetate, diethyl ether and toluene was performed on all systems. A more extensive crystallisation screen including evaporation, cooling crystallisation, solvent assisted grinding and solvent diffusion experiments in an extended solvent list was then performed on the ERP/ESP diastereomeric salt pair system. This was due to the fact that good quality single crystals were obtained and that the crystallisation experiments suggested that they were highly polymorphic. Furthermore, the solubility difference between the ERP and ESP diastereomeric salt pair was very pronounced and therefore seemed to be a good model system to use as validation of CSP methods. The crystallisation experiments performed as part of the screen are summarised in Table 5.2 and Table 5.3. The experimental details are described in Chapter 3. The results of the extended crystallisation screen for ERP and ESP are summarised in the appendix at the end of this Chapter.

A detailed description of the best method to prepare each of the polymorphs identified in the crystallisation screen of ERP/ESP diastereomeric salt pair is presented in Section 5.3.3.

### **5.3.3 Preparation of the Individual Forms of ERP and ESP**

The different polymorphs of ERP and ESP identified during the crystallisation screen were named using the Kofler notation using Roman numerals in the order of their melting points, where the highest melting point form is named form I. The thermodynamically stable form at room temperature is identified with the symbol “∞”.

### 5.3.3.1 Preparation of ERP forms

ERP I° was easily prepared by evaporation or cooling crystallisation from a number of solvents including methanol, ethanol, isopropanol, 2-butanol, ethyl acetate. ERP II could only be prepared by quench cooling a melt of ERP. The dichloromethane solvate was prepared by solvent-mediated transformation of ERP I° in dichloromethane at room temperature or by fast cooling crystallisation in dichloromethane.

### 5.3.3.2 Preparation of ESP forms

ESP III° could not be prepared by evaporation, cooling or anti-solvent crystallisation experiments. Solvent drop grinding experiments, which usually produce the thermodynamically stable phase, resulted in ESP I, the stable phase at high temperatures. This was probably due to the fact that relatively high temperatures are reached inside the grinding cell. The best way to produce ESP III° was therefore by solvent mediated transformation starting from either ESP I or ESP II, using water-free solvents to avoid the formation of the Hydrate form. Despite many attempts at obtaining a pure phase, traces of impurities of forms I or II were often detected in the DSC measurements. Care was taken to avoid evaporation of the mother liquor when filtering the salt by vacuum filtration, as this might have led to the formation of ESP I or ESP II. The fact that the transition temperatures of the three polymorphs are relatively close to room temperature makes it possible for the polymorphs to grow at these temperatures.

ESP I could be formed by solvent crystallisation experiments although not reproducibly and often concomitantly with ESP II. The easiest method to produce ESP I was by heating any of the ESP forms above their polymorphic transition  $\text{ESP III}^\circ \rightarrow \text{ESP II} \rightarrow \text{ESP I}$ . This was done by placing samples in an oven set at around 60 °C. Decomposition of the salt at this temperature, if any, was much slower compared to the polymorphic transformation.

Again, although possible, the preparation of ESP II from solvent crystallisation experiments usually contained impurities of ESP I. De-solvation of all the solvated forms of ESP led to ESP II. Therefore, ESP II could be reproducibly made by first preparing a solvate through solvent mediated transformation of any form of ESP in the suitable solvent (dichloromethane, tetrahydrofurane, acetonitrile, dioxane or water) and then de-solvating the solvate at ambient conditions. Full de-solvation at room temperature occurs relatively fast, in less than 30 minutes for all solvates except the hydrate. The hydrate can form at ambient conditions and has to be warmed up slightly, to 40 °C to de-solvate fully. The solvates were also easily prepared by cooling crystallisation in the relevant solvents.

| Solvent            | Evaporation |       |       |       | Cooling |       |       |       | Grinding |       |       |       |
|--------------------|-------------|-------|-------|-------|---------|-------|-------|-------|----------|-------|-------|-------|
|                    | ERP /       | ERB / | PRP / | PRB / | ERP /   | ERB / | PRP / | PRB / | ERP /    | ERB / | PRP / | PRB / |
|                    | ESP         | ESB   | PSP   | PSB   | ESP     | ESB   | PSP   | PSB   | ESP      | ESB   | PSP   | PSB   |
| Methanol           | X           | X     | X     | X     | X       | X     | -     | -     | X        | X     | -     | -     |
| Ethanol            | X           | X     | X     | X     | X       | X     | -     | -     | X        | X     | -     | -     |
| Isopropanol        | X           | X     | X     | X     | X       | X     | -     | -     | X        | X     | -     | -     |
| 2-Butanol          | X           | X     | -     | -     | X       | X     | -     | -     | X        | X     | -     | -     |
| Water              | X           | X     | X     | X     | X       | X     | -     | -     | X        | X     | -     | -     |
| Ethyl Acetate      | X           | X     | X     | X     | X       | X     | -     | -     | X        | X     | -     | -     |
| Diethyl ether      | X           | X     | X     | X     | X       | X     | -     | -     | X        | X     | -     | -     |
| Diisopropyl ether  | X           | X     | -     | -     | X       | X     | -     | -     | X        | X     | -     | -     |
| Dibutyl ether      | X           | X     | -     | -     | X       | X     | -     | -     | X        | X     | -     | -     |
| Methyl butyl ether | X           | X     | -     | -     | X       | X     | -     | -     | X        | X     | -     | -     |
| Dichloromethane    | X           | X     | X     | X     | X       | X     | -     | -     | X        | X     | -     | -     |
| Dichloroethane     | X           | X     | -     | -     | X       | X     | -     | -     | X        | X     | -     | -     |
| Toluene            | X           | X     | X     | X     | X       | X     | -     | -     | X        | X     | -     | -     |
| Xylene             | X           | X     | -     | -     | X       | X     | -     | -     | X        | X     | -     | -     |
| Dioxane            | X           | X     | -     | -     | X       | X     | -     | -     | X        | X     | -     | -     |
| Tetrahydrofuran    | X           | X     | -     | -     | X       | X     | -     | -     | X        | X     | -     | -     |
| Hexane             | X           | X     | -     | -     | X       | X     | -     | -     | X        | X     | -     | -     |
| Pentane            | X           | X     | -     | -     | X       | X     | -     | -     | X        | X     | -     | -     |
| Acetonitrile       | X           | X     | X     | X     | X       | X     | -     | -     | X        | X     | -     | -     |
| Dimethylsulphoxide | X           | X     | -     | -     | X       | X     | -     | -     | X        | X     | -     | -     |

**Table 5.2** Summary of the crystallisation experiments performed for the different diastereomeric salt pairs for the crystallisation screen. An X indicates that the experiment was performed at least three times, whereas – indicates that this crystallisation experiment was not set up.

| Solvent    | Anti-solvent       |
|------------|--------------------|
| Butan-2-ol | Diethyl Ether      |
| Butan-2-ol | Dibutyl Ether      |
| Butan-2-ol | Diisopropyl Ether  |
| Butan-2-ol | Methyl Butyl Ether |
| Toluene    | Diethyl Ether      |
| Toluene    | Dibutyl Ether      |
| Toluene    | Diisopropyl Ether  |
| Toluene    | Methyl Butyl Ether |
| DMSO       | Diethyl Ether      |
| DMSO       | Dibutyl Ether      |
| DMSO       | Diisopropyl Ether  |
| DMSO       | Methyl Butyl Ether |

**Table 5.3** Summary of the solvent diffusion experiments performed for the ERP/ESP diastereomeric salt pair system.

#### 5.3.4 Ternary Phase Diagram Determination to assess the ability of Ephedrine to resolve 2-phenylpropionic acid.

The isothermal ternary phase diagram for the ERP I° – ESP III° - ethanol system was determined at 30°C and 10°C. Solid phases were prepared by mixing ERP I° and ESP III° in different ratios, varying by 10% from sample to sample i.e. 90% ERP:10% ESP III°, 80% ERP:20% ESP III°, etc. The compositions of the different starting mixtures are detailed in Table 5.4 and Table 5.5 for measurement at 30 °C and 10 °C respectively. Suspensions of the solid mixtures in absolute ethanol were left to equilibrate at 30°C and 10°C for one week in sealed glass vials to ensure that no ethanol would evaporate. The temperature of the samples were kept constant within  $\pm 0.01$  °C using a jacketed glass vessel maintained at a constant temperature by water circulated from a water bath (Grant LTC 12-50). For experiments at 30°C, ~1.5g of the salt mixtures were suspended in 5ml of absolute ethanol, while for experiments at 10°C, ~1g of the salt mixtures were suspended in 5ml of absolute ethanol. After one week the stirring was discontinued and the slurries left to settle for one day. Following the settling of the solid dispersion the liquid phase was removed using a syringe attached to a 0.22  $\mu\text{m}$  membrane filter, and poured into a pre-weighed glass vial. The composition of the liquid phase for each suspension was determined at least twice. The second liquid phase aliquot was tested after resealing the glass vial and letting the mixture to slurry for a further two days in order to ensure that the suspension had completely equilibrated and that there was no further change in composition. First, the mass of solute in



the liquid phase was determined by a gravimetric method, by allowing all the ethanol to evaporate. Finally the proportion of ERP and ESP in the solute was determined using HPLC. The composition of the solid phase in equilibrium with the liquid phase was calculated using the method of algebraic extrapolation [240] from a mass balance on the whole system. The wet solids were also analysed using IR spectroscopy in order to see whether the solid phase in equilibrium was a hydrate.

| Salt Mixture | Mass of ERP I° | Mass of ESP III° | Mass of EtOH |
|--------------|----------------|------------------|--------------|
| 9R:1S        | 1.3513         | 0.1514           | 3.1560       |
| 8R:2S        | 1.2075         | 0.3019           | 3.1560       |
| 7R:3S        | 1.0459         | 0.4482           | 3.1560       |
| 6R:4S        | 0.9044         | 0.6029           | 3.1560       |
| 1R:1S        | 0.7495         | 0.7495           | 3.1560       |
| 4R:6S        | 0.6028         | 0.9042           | 3.1560       |
| 3R:7S        | 0.4535         | 1.0581           | 0.7890       |
| 2R:8S        | 0.3043         | 1.2173           | 2.3670       |

**Table 5.4** Composition of the initial mixtures in the determination of the ternary phase diagram of ERP I° and ESP III° in ethanol at 30 °C.

| Salt Mixture | Mass of ERP | Mass of ESP III | Mass of EtOH |
|--------------|-------------|-----------------|--------------|
| 9R:1S        | 0.9073      | 0.1021          | 7.8900       |
| 8R:2S        | 0.8003      | 0.1999          | 7.8900       |
| 7R:3S        | 0.7009      | 0.3030          | 7.8900       |
| 6R:4S        | 0.6050      | 0.3655          | 7.8900       |
| 1R:1S        | 0.4980      | 0.4980          | 7.8900       |
| 4R:6S        | 0.2540      | 0.3218          | 3.9450       |
| 3R:7S        | 0.2988      | 0.7035          | 2.7053       |
| 1R:9S        | 0.1073      | 0.9094          | 1.5046       |

**Table 5.5** Composition of the initial mixtures in the determination of the ternary phase diagram of ERP I° and ESP III° in ethanol at 10 °C.

## 5.4 Results

The results of the limited crystallisation screens for the different diastereomeric salt pairs are presented in Section 5.4.1. The results of initial crystallisation experiments on all four diastereomeric salt pairs already highlighted the difficulty in growing good quality single crystals for X-ray diffraction studies. Based on these experiments, Ephedrine-2-phenylpropionate salts were selected to undergo an extended crystallisation screen as there was evidence of highly polymorphic behaviour of the most soluble salt, the difference in solubility between the pair was large and single crystals were obtained for the least soluble salt and one polymorph of the more soluble one. Furthermore, it was possible to solve the structure of two further polymorphs of the more soluble salt from powder X-ray diffraction data. It was therefore believed that this system would provide a good test for the CSP methods in Chapter 6. The results of the extended crystallisation screen on Ephedrine-2-phenylpropionate diastereomeric salt pair are presented in more detail in Section 5.4.2. The crystal structures of all the phases that were solved in this work are described and compared in Section 5.4.3. Finally, the ability of Ephedrine as a resolving agent for 2-phenylpropionic acid is discussed in Section 5.4.4.

### 5.4.1 Identification of Solid-State forms of Diastereomeric Salts from a limited crystallisation screen

#### 5.4.1.1 Pseudoephedrine-2-phenylpropionate salts (PRP/PSP)

Although the crystallisation screen for pseudoephedrine-2-phenylpropionate salts was more limited than those performed for the Ephedrine salts, a complicated crystallisation behaviour was observed for this system, with the formation of different polymorphs and solvates.

In the limited crystallisation screen performed on Pseudoephedrine-2-(R)-phenylpropionate salt (PRP), two crystal forms were identified, a stable hydrate and an anhydrous form. The two forms could be unequivocally identified from their FT-IR spectra as can be seen in Figure 5.1. The hydrate phase formed readily from a number of solvents, not just from water, and was stable in ambient conditions for months.

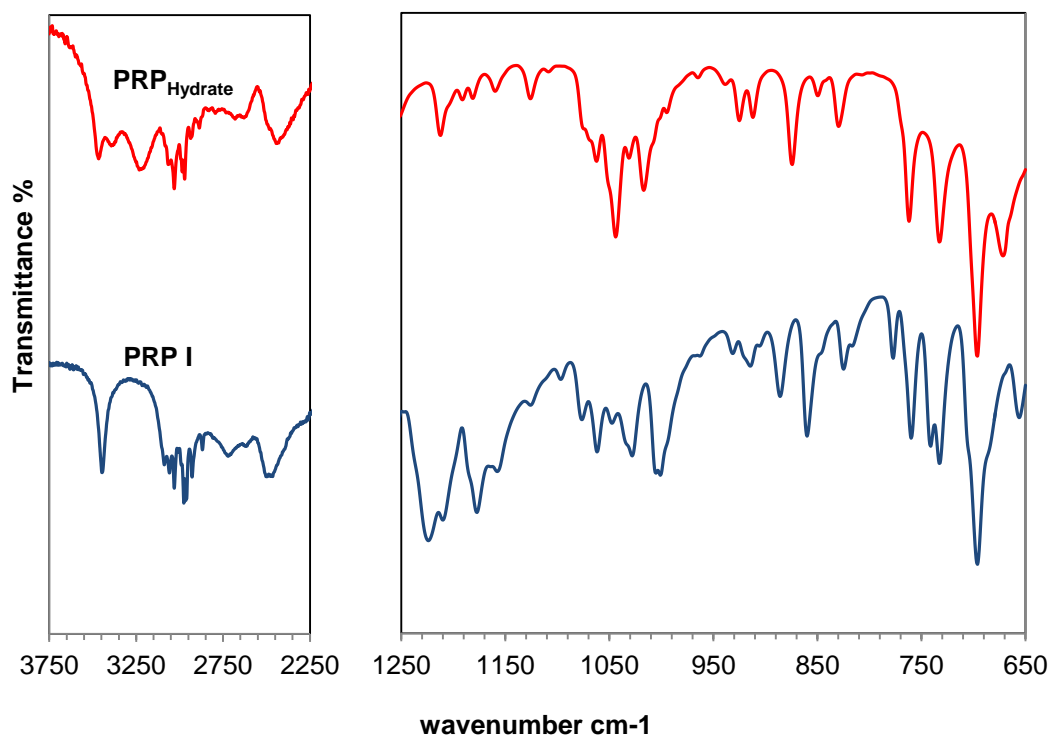


**Figure 5.1** FT-IR Spectra of the different forms of PRP. One stable hydrate and one anhydrous phase were identified in the crystallisation experiments.

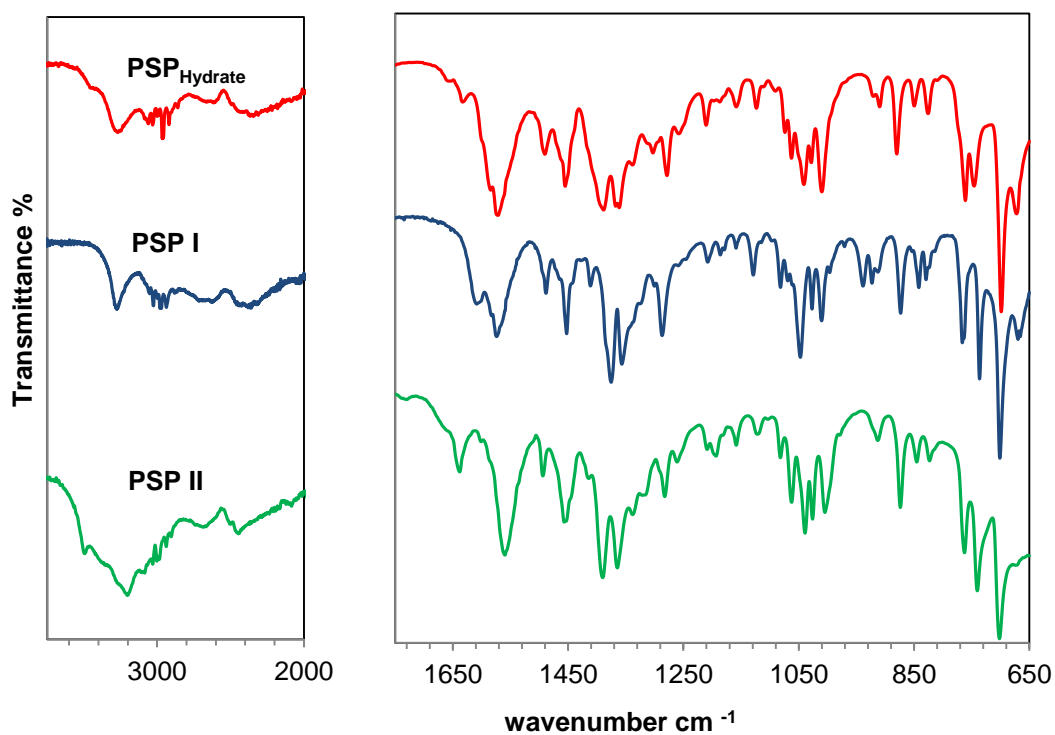


**Figure 5.2** FT-IR Spectra of the different forms of PSP. One stable hydrate and one anhydrous phase were identified in the crystallisation experiments.

Three different phases of pseudoephedrine-2-(S)-phenylpropionate salt (PSP) were identified. The three phases could be also unequivocally distinguished from the differences in the FT-IR spectra (Figure 5.2).

#### 5.4.1.2 Pseudoephedrine-2-phenylbutyrate salts (PRB/PSB)

During the limited crystallisation experiments on the pseudoephedrine-(R)-2-phenylbutyrate (PRB) salt, two anhydrous phases were identified which could be distinguished from their FT-IR spectra (Figure 5.3). The structure of PRB I was solved from X-ray diffraction data and is shown in Figure 5.30 in Section 5.4.3.8.

Similarly, crystallisation experiments on the opposite diastereomer, pseudoephedrine-(S)-2-phenylbutyrate (PSB) resulted in two new phases, one of which was found to be a hydrate (Figure 5.4). The structure of the hydrate was also solved from X-ray crystal diffraction data and is shown in Figure 5.31 in Section 5.4.3.9.

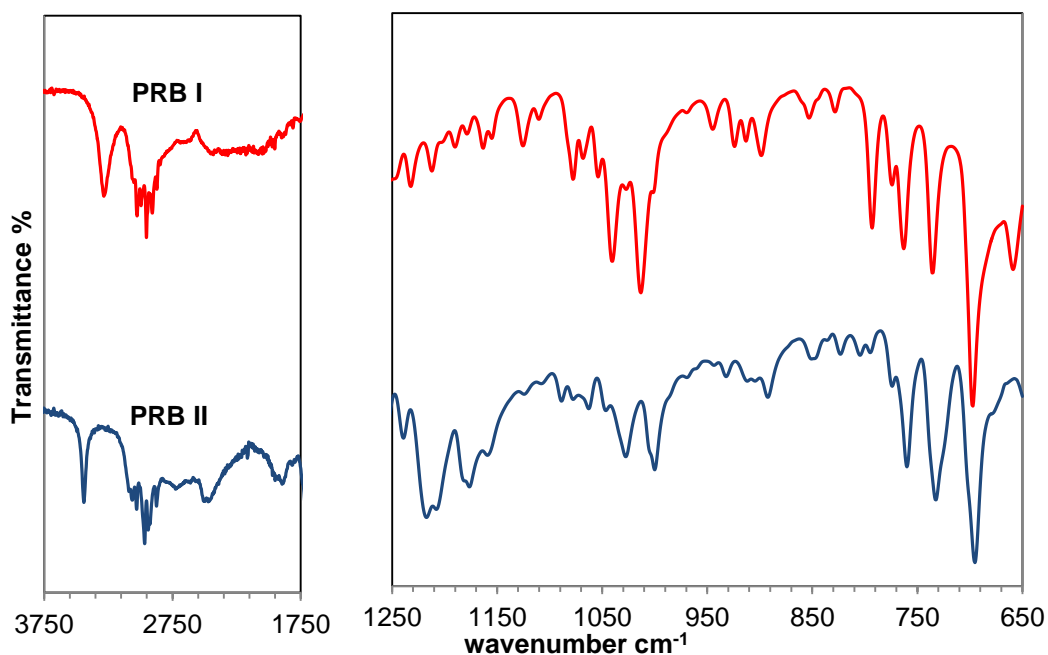


**Figure 5.3** FT-IR Spectra of the different forms of PRB identified in the limited crystallisation screen of (1R,2R) pseudoephedrine-2-phenylbutyrate salts.

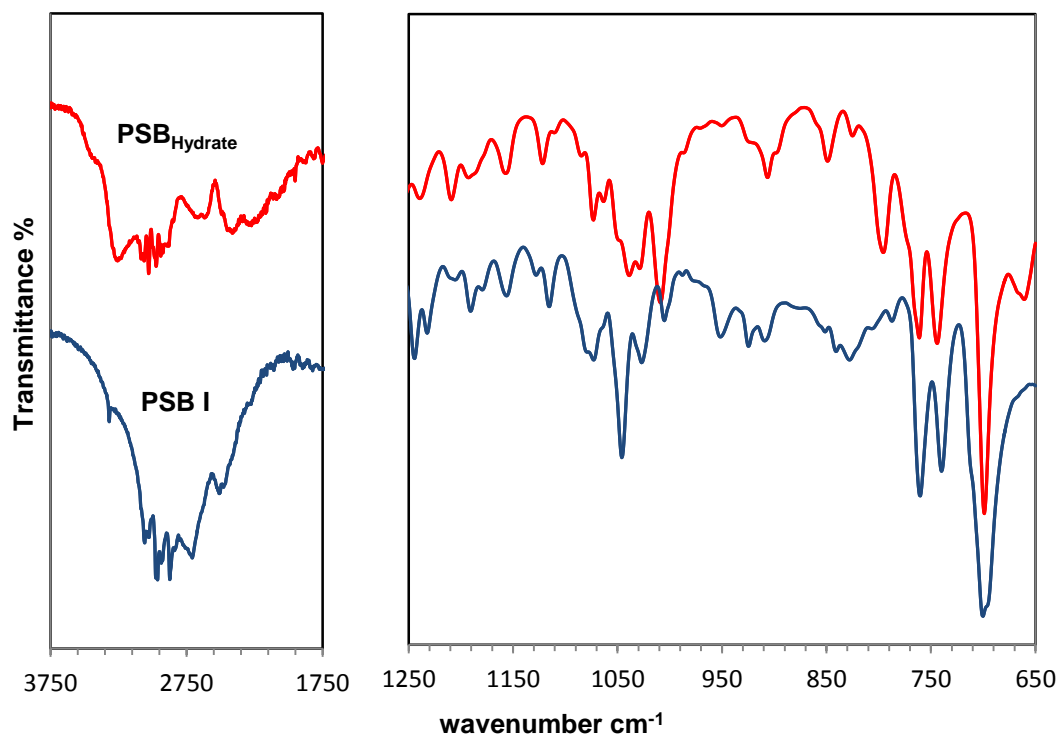


**Figure 5.4** FT-IR Spectra of the different forms of PSB identified in the limited crystallisation screen of (1R,2R) pseodephedrine-2-phenylbutyrate salts.

#### 5.4.1.3 Ephedrine-2-phenylbutyrate salts (ERB/ESB)

The crystallisation screen of Ephedrine-2-phenylbutyrate salts resulted in the identification of two polymorphs and six solvates of the Ephedrine-(R)-phenylbutyrate salt (ERB) and two polymorphs and one solvate of Ephedrine-(S)-phenylbutyrate salt (ESB). The different forms could be unambiguously identified from their FT-IR spectra shown in Figure 5.5 for ERB and Figure 5.6 for ESB. Only the crystal structures of one of the salt forms, ESB I could be determined from single crystal X-ray diffraction data (Figure 5.27 in Section 5.4.3.5). As observed in the crystallisation screen of Ephedrine-2-phenylpropionate and other diastereomeric salts, it was very difficult to obtain good quality single crystals for diffraction studies.

The limited crystallisation screen performed on Ephedrine-2-phenylbutyrate salts illustrates how sensitive the crystallisation behaviour of diastereomeric salts is to small changes in the chemical composition of the starting compounds. For the Ephedrine-2-phenylpropionate diastereomeric salt pair system (see section 5.4.2), ERP was found to be the most stable of the salts. The crystallisation behaviour of ERP was much less complicated than ESP, with two monotropically related polymorphs and one solvate compared to the three enantiotropically related polymorphs and five solvates that were found for the (S)-salt.

Extending the length of the aliphatic chain substituent in the chiral centre of the acid from a methyl to an ethyl seems to invert the relative stability of the two salts. Although the difference was not accurately quantified, ESB was found to be less soluble than ERB in all the solvents used in the screen. Furthermore, ERB, the more soluble salt, was also found to be more prone to solvation, with six solvates ( $S_{\text{DCM}}$ ,  $S_{\text{Dioxane}}$ ,  $S_{\text{MeCN}}$ ,  $S_{\text{THF}}$ ,  $S_{\text{Toluene}}$  and  $S_{\text{Xylene}}$ ) identified during the crystallisation screen. On the other hand, only one solvate ( $S_{\text{DCM}}$ ) was found in the ESB crystallisation screen. The solvates were not stable and quickly transformed to either ERB I or ESB I, as with the ERP/ESP diastereomeric salt system. The similarity in the FT-IR spectra at high wavenumbers (Figure 5.5 and Figure 5.6) of the solvated phases of ERB and ESB with the un-solvated phases suggest that the solvent molecules are not involved in hydrogen bonding. This is consistent with the observation that they readily de-solvate.

The FT-IR spectra of ERB I and ERB II at high wavenumbers are very similar, and very similar to that of ESB I, ERP I° and ESP III° (see Figure 5.8 and Figure 5.13 in Section 5.4.2). This suggests that the hydrogen bonding motif present in these forms might be the  $R_4^3(13)$  seen in ESB I, ERP I° and ESP III° and other Ephedrine salts.

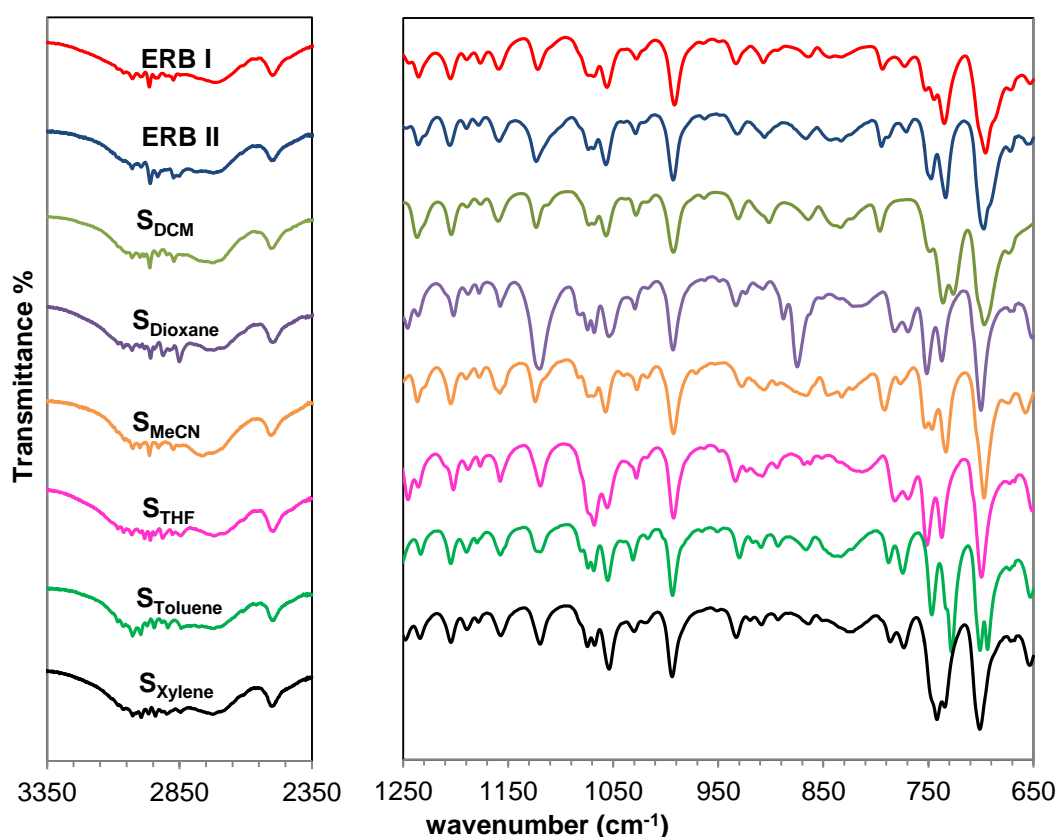


**Figure 5.5** FT-IR Spectra of the different forms of ERB. Two anhydrous phases were identified together with six solvates.

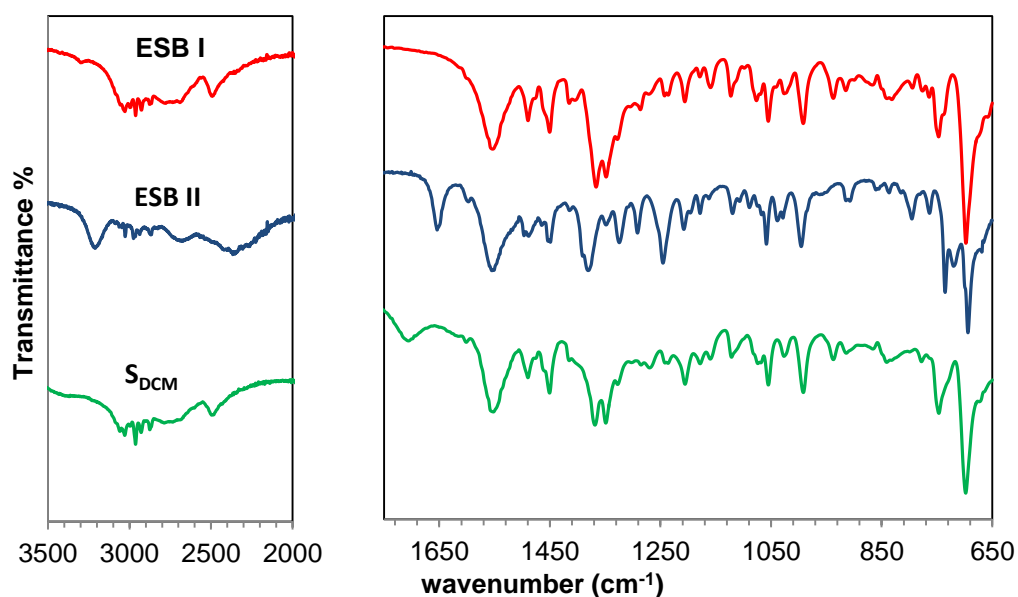


**Figure 5.6** FT-IR Spectra of the different forms of ESB. Two anhydrous phases were identified together with one solvate.

Although we could not determine the structure of ESB II, we can speculate that this polymorph forms a structure with an  $R_2^2(9)$  hydrogen bonded pattern since its FT-IR spectra (Figure 5.6) in the higher wavenumber region is almost identical to that of ESP I (Figure 5.13 in Section 5.4.2.2)

This screen did once again highlight that polymorphism and solvation might have an impact in the resolution efficiency.

#### 5.4.2 Extended Crystallisation Screen: Ephedrine-2-phenylpropionic salts

The solvent screening performed on the ephedrine-2-phenylpropionate diastereomeric salt pair resulted in two new ERP polymorphs and a dichloromethane solvate and three new ESP polymorphs, one hydrate and four solvates namely dioxane ( $S_{\text{Dioxane}}$ ), tetrahydrofuran ( $S_{\text{THF}}$ ), dichloromethane ( $S_{\text{DCM}}$ ) and acetonitrile ( $S_{\text{MeCN}}$ ). The relationships between the different ERP (Figure 5.10) and ESP (Figure 5.16) solid state forms are described in section 5.4.2.1 and section 5.4.2.2 respectively. The structures of ERP I° and the different polymorphs of ESP are described and compared in section 5.4.3. Finally, Section 5.4.2.3 looks at the relative stability of the two most stable phases of ERP and ESP.

#### 5.4.2.1 (1R,2S)-Ephedrine-2-(R)-phenylpropionate (ERP)

All the evaporation experiments led to ERP I°, as suggested by PXRD and FT-IR spectroscopic data (see Figure 5.7 and Figure 5.8 respectively). Elemental analysis confirmed that ERP I° was an un-solvated 1:1 salt. All cooling crystallisation experiments, except those carried out in dichloromethane, led also to ERP I°. Upon cooling a saturated solution of ERP in dichloromethane, a fine cotton like microcrystalline phase formed with a distinct FT-IR spectrum ( $S_{DCM}$ , depicted in blue in the FT-IR spectra in Figure 5.8).  $S_{DCM}$  transformed back to the stable anhydrous phase a few minutes after it had been removed from the mother liquor and dried with a filter paper. Such a fast transformation into the stable anhydrous phase, ERP I°, might explain why evaporation experiments from dichloromethane did not seem to produce the solvated phase. Solvent assisted grinding experiments were performed as a relatively fast method to screen for other possible solvates. No other solvates were found to form by solvent assisted grinding in the range of solvents used. Solvent mediated transformation experiments in which an excess of ERP I° was stirred in the range of solvents for an hour also did not produce other solvated phases.

A second polymorph of ERP, ERP II, was found after quench cooling a melt of ERP I°. A controlled experiment in a DSC showed that this new phase grows upon cooling at around 80°C. The powder X-ray patterns of the two polymorphs are depicted in Figure 5.7 and the FT-IR spectra in Figure 5.8

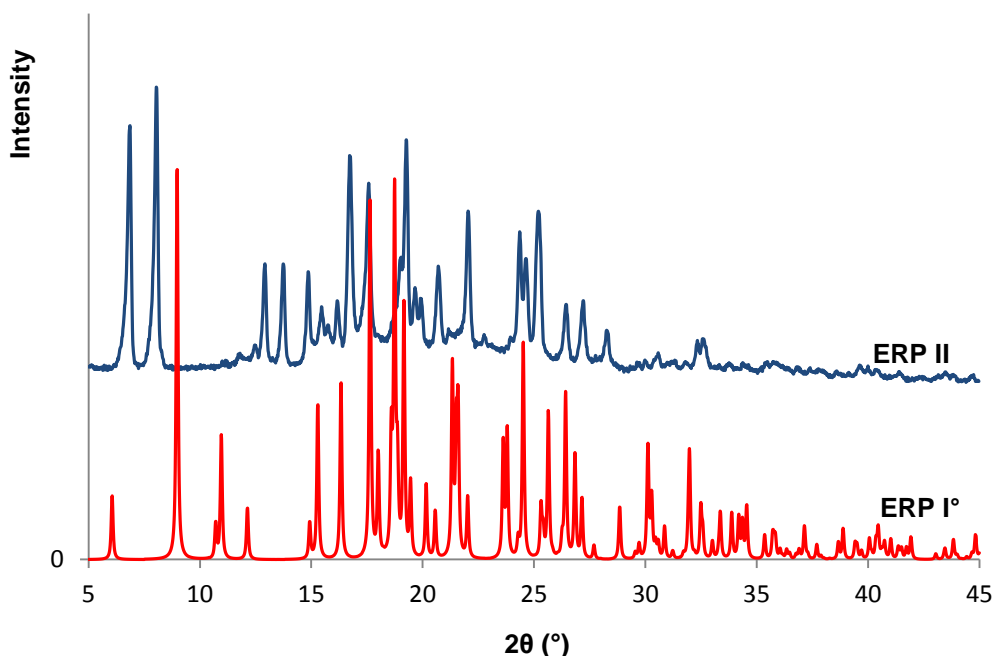


**Figure 5.7** Powder diffraction patterns for the two different polymorphs of ERP found in the crystallisation screen. ERP I° (diffraction pattern in red) is the most stable phase at room temperature, whereas ERP II (diffraction pattern in blue) is a metastable phase.



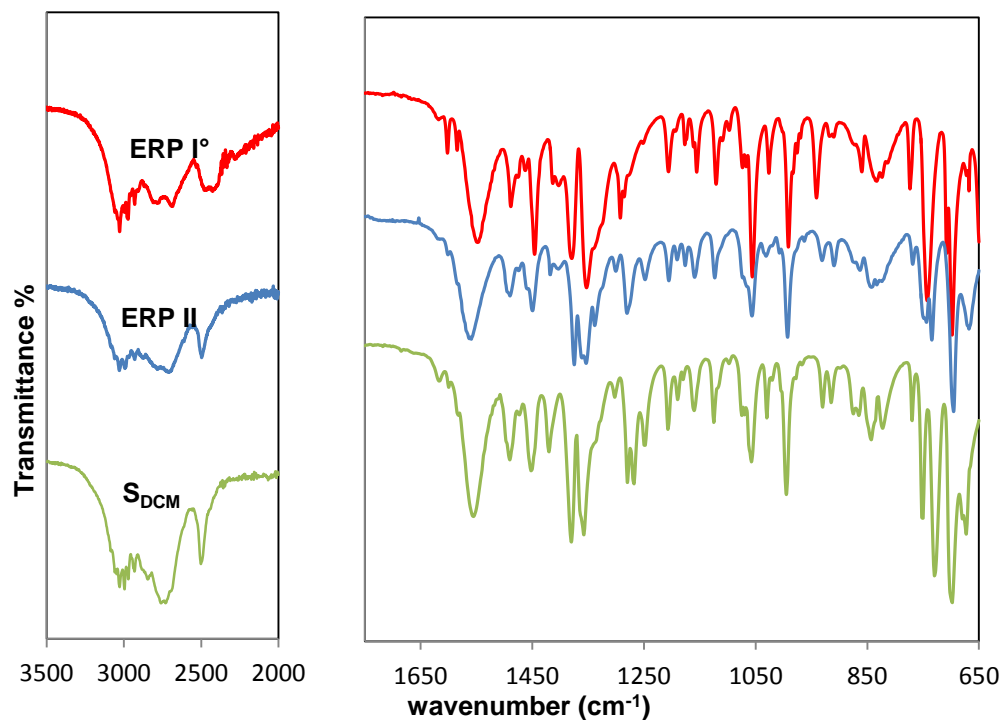


**Figure 5.8** FT-IR Spectra of the two polymorphs of ERP found in the screen (ERP I° in red and ERP II in blue) and the dichloromethane solvate ( $S_{DCM}$  in green).

DSC experiments revealed that ERP II transforms to Form I° upon heating at a temperature above 90°C (Figure 5.9). The weak exotherm in the DSC curve at an experimental transition temperature of 90.6 °C corresponds to the solid-solid transformation II → I° with a transition enthalpy of  $\Delta_{trs}H=8.13$  kJ/mol. The phases were analysed by X-ray powder diffraction before and after the transition point (and before the melt), and confirmed to be an ERP II → ERP I° transition. From the fact that the transition is exothermic it can be concluded that the two polymorphs are monotropically related, from the heat of transition rule [164]. ERP I° must therefore have the higher melting point and is the most thermodynamically stable phase under all temperature conditions, ERP II being a metastable phase. ERP II furthermore is not very kinetically stable at room temperature, transforming to ERP I° within hours when stored at ambient conditions. A schematic energy-temperature diagram of the two polymorphs derived from the thermoanalytical data is shown in Figure 5.10.

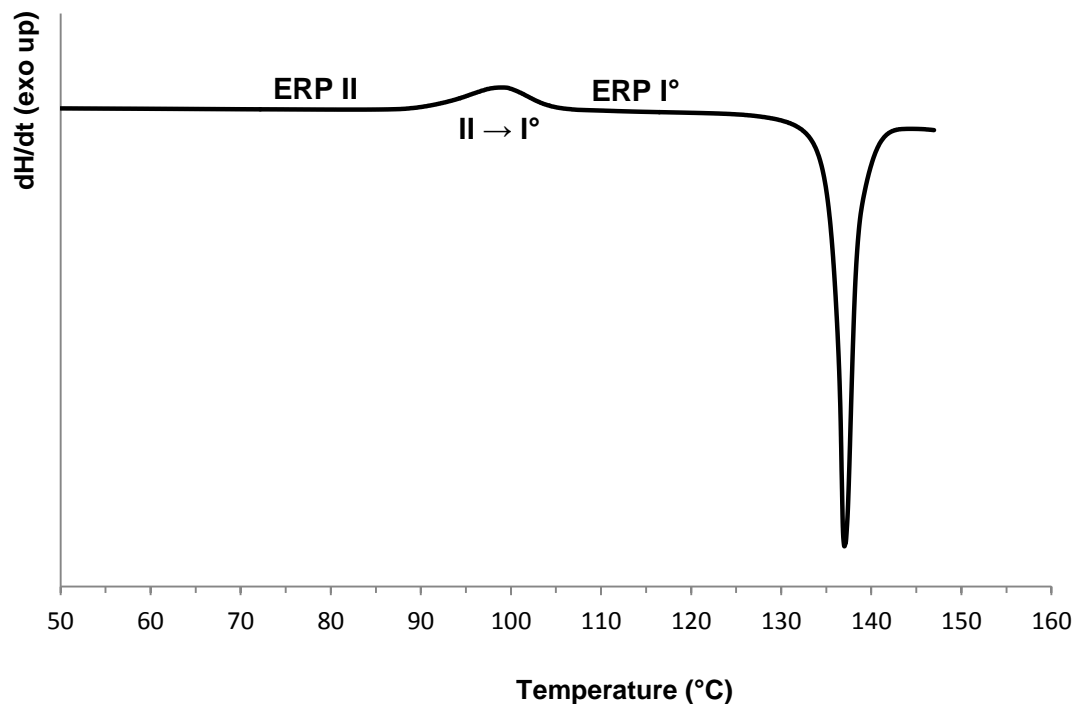


**Figure 5.9** DSC curve showing the transformation of ERP II to ERP I° (II → I°) and melting of ERP I°.

|   | ERP I°          | ERP II         |
|---|-----------------|----------------|
| $T_{\text{fus}}$ , °C   | $136.6 \pm 0.1$ | -              |
| $\Delta H_{\text{fus}}$ , kJ mol <sup>-1</sup>                | $52.51 \pm 0.9$ | -              |
| $\Delta S_{\text{fus}}$ , J mol <sup>-1</sup> K <sup>-1</sup> | $128.2 \pm 2.1$ | -              |
| $T_{\text{trs II - I°}}$ , °C                                 | -               | $90.6 \pm 0.2$ |
| $\Delta H_{\text{trs II - I°}}$ , kJ mol <sup>-1</sup>        | -               | $8.13 \pm 0.1$ |

**Table 5.6** DSC data collected for ERP I° and ERP II.  $T_{\text{fus}}$  = melting temperature;  $\Delta H_{\text{fus}}$  = enthalpy of fusion;  $\Delta S_{\text{fus}}$  = entropy of fusion calculated from  $\Delta H_{\text{fus}}/T_{\text{fus}}$ ;  $T_{\text{trs II - I°}}$  = transition temperature and  $\Delta H_{\text{trs II - I°}}$  = transition enthalpy.

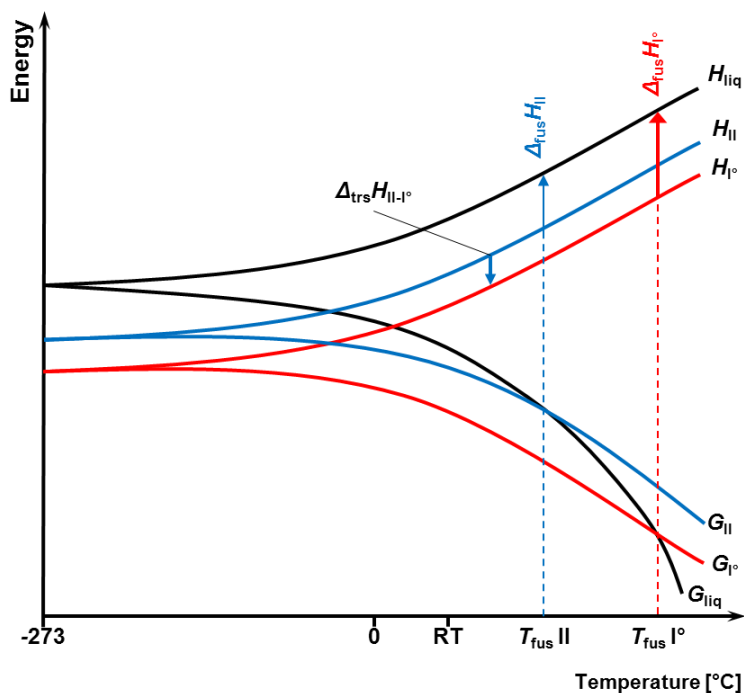


**Figure 5.10** Schematic energy/temperature diagram of ERP polymorphs.  $T_{fus}$ : melting point,  $G$ : Gibbs free energy,  $H$ : enthalpy,  $\Delta_{fus}H$ : enthalpy of fusion,  $\Delta_{trs}H$ : transition enthalpy and liq: liquid phase (melt), RT: room temperature ( $\sim 25^{\circ}\text{C}$ ).

Most crystallisations from solution failed to produce crystals of ERP I° of sufficient quality for single crystal X-ray diffraction studies. Experiments would usually yield white microcrystalline powder. In the cases when single crystals did grow, crystals were generally either very fine needles that would shatter into finer crystallites when cutting to an appropriate size for data collection, or blocks that, upon inspection under a polarised microscope proved to be stacks of very thin plates that would delaminate on manipulation. A suitable single crystal was only obtained from an evaporation experiment from an ethanol solution.

ERP II could not be characterised by single crystal diffraction as it was not possible to obtain single crystals from the melt. Furthermore, ERP II transforms to form I° within hours so it could not be characterised by powder X-ray diffraction.

#### 5.4.2.2 (1R,2S)-Ephedrine-2-(S)-phenylpropionate (ESP)

Three different polymorphs of ESP together with four solvates and one hydrate were found in the solvent crystallisation screen. The different forms were identified by their FT-IR spectra and their powder X-ray diffraction patterns which allow the unambiguous

identification of all forms (Figure 5.12, Figure 5.13 and Figure 5.14). The outcome of the crystallisation experiments are summarised in Table 5.12 and Table 5.13 in the Appendix at the end of the chapter. The transition pathways for all the identified forms of ESP are summarised in the scheme shown in Figure 5.11.

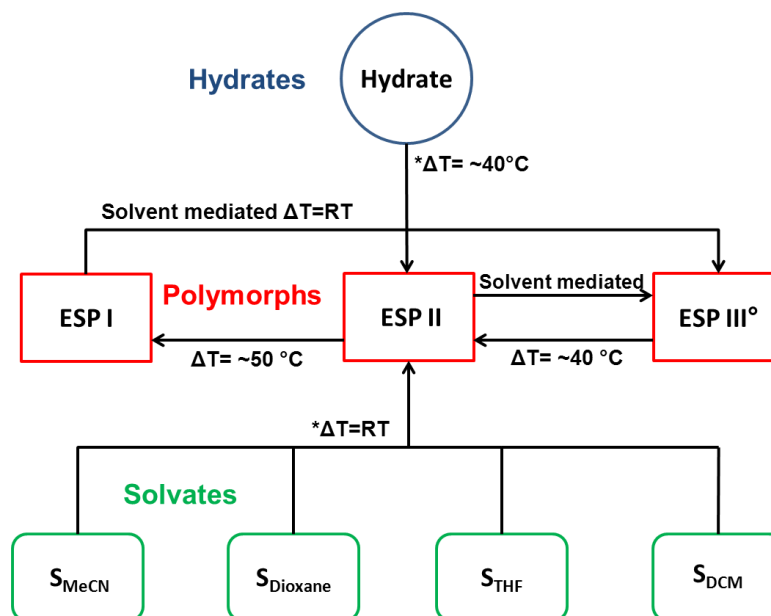


**Figure 5.11** Transition pathways of the different ESP forms under different conditions.  $\Delta T$  represents heating and \* denotes removing from the mother liquor.

The relationship between the three polymorphs of ESP was established from the melting points and heats of fusion measurements obtained using a DSC. The melting points and heats of fusion of the ESP polymorphs are summarised in Table 5.7. Unfortunately, the heat of fusion of ERP III°, the thermodynamically stable phase at room temperature, was difficult to measure accurately as ESP I or ESP II recrystallized immediately upon melting, as shown by the exothermic peaks in Figure 5.15, and so has a relatively large error in its measurement. Furthermore, often during the preparation of ESP III°, small impurities of ESP I were produced despite careful attempts to produce a pure sample, adding to the difficulty in obtaining an accurate measurement of the enthalpy of fusion. ESP I, the highest melting polymorph, has a melting point of  $106.7 \pm 0.1$  °C and a heat of fusion of  $31.17 \pm 0.1$  kJ/mol. ESP II melts at  $104.3 \pm 0.03$  °C with a heat of fusion of  $31.90 \pm 0.6$  kJ/mol. The fact that the higher melting polymorph has the lowest heat of fusion means that the polymorphs are enantiotropically related, following the heat of fusion rule [164]. Given how close the enthalpies of fusion were between ESP I and ESP II, solution calorimetry was used to obtain the enthalpy of solution of the different polymorphs of ESP at 25 °C and corroborated the fact that ESP I and ESP II are enantiotropically related, as ESP II has an enthalpy of solution

1.6 kJ/mol higher than ESP I. Furthermore, ESP III° had the highest enthalpy of solution proving that it is the most thermodynamically stable phase at room temperature. The relationship between the three polymorphs is shown schematically in the energy/temperature diagram shown in Figure 5.16.

Although both ESP I and ESP II are the metastable phases at room temperature with respect to ESP III°, they nevertheless show a high kinetic stability at room temperature. No transformation occurred at room temperature under low humidity conditions within 24 months. Furthermore, experiments performed in a DSC in which samples were heated at a rate of 10 °C/min showed no transformation from ESP II to ESP I. Nevertheless, a sample of ESP III° maintained for 12 hours at 40°C did transform to ESP II. Increasing the temperature to 60°C and maintaining for a further 12 hours resulted in ESP I. ESP III° was also confirmed to be the thermodynamically stable phase at room temperature by performing solvent-mediated transformation experiments. In these experiments seeds of ESP III° (<1mg) were added to a suspension of ESP I or ESP II at room temperature. Both polymorphs transformed into ESP III° over time. In fact, the conversion of ESP I and ESP II to ESP III° occurred relatively fast without the need of ESP III° seeds. The energy-temperature diagram for the three polymorphs of ESP derived from the DSC data and solution calorimetric data is shown in Figure 5.16.

One hydrate and four solvates, namely dioxane, dichloromethane, tetrahydrofuran and acetonitrile were identified during the screen for ESP. As seen from the FT-IR spectra in Figure 5.14 the different forms could be distinguished by the vibrations at lower wavenumbers. A comparison of the FT-IR spectra of the solvates and ESP III° suggests that the solvates adopt a similar hydrogen bonding motif to that seen in ESP III°. The FT-IR spectra therefore indicate that the solvents are not involved in hydrogen bonding. This might explain the ease with which de-solvation occurs.

As observed in the crystallisation experiments of ERP, it was very difficult to obtain single crystals of the different polymorphs of ESP. Evaporation experiments from solvents where ESP is very soluble did not yield single crystals. In these experiments, especially in those using alcohols, it was usual to observe the formation of an oil that was stable for months

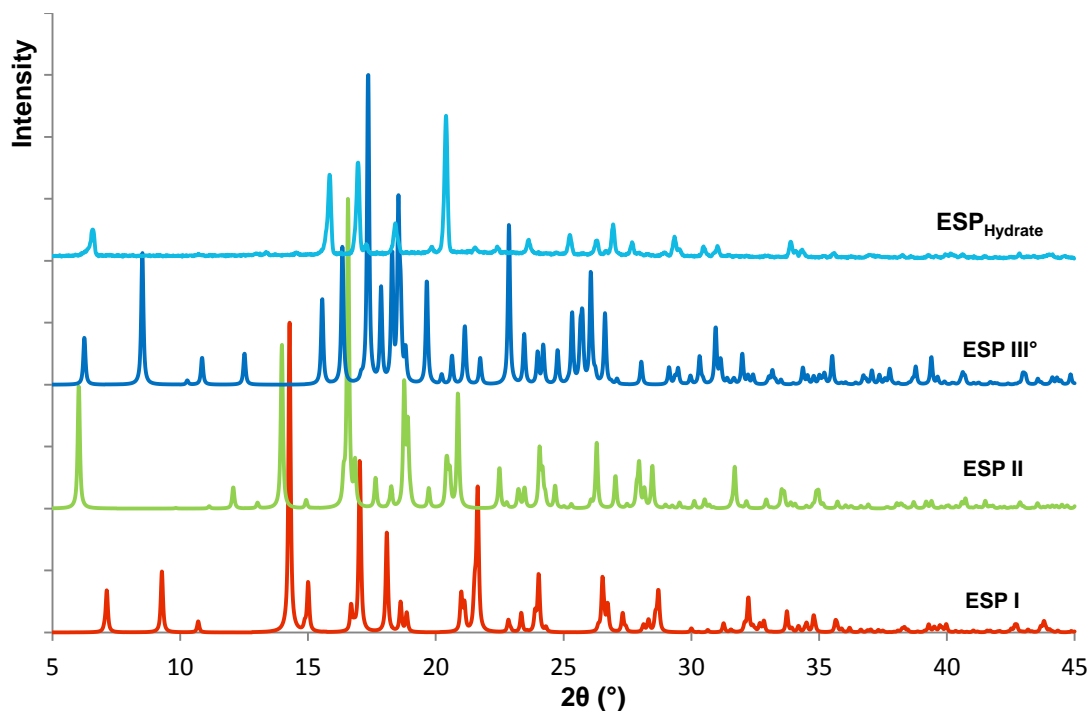


**Figure 5.12** Powder diffraction patterns for the three different polymorphs of ESP and the hydrate form found in the crystallisation screen. ESP I (diffraction pattern in red) and ESP II (diffraction pattern in green) are metastable phases at room temperature. ESP III° (diffraction pattern in dark blue green) is the most stable phase at room temperature. The hydrate form is shown in light blue.

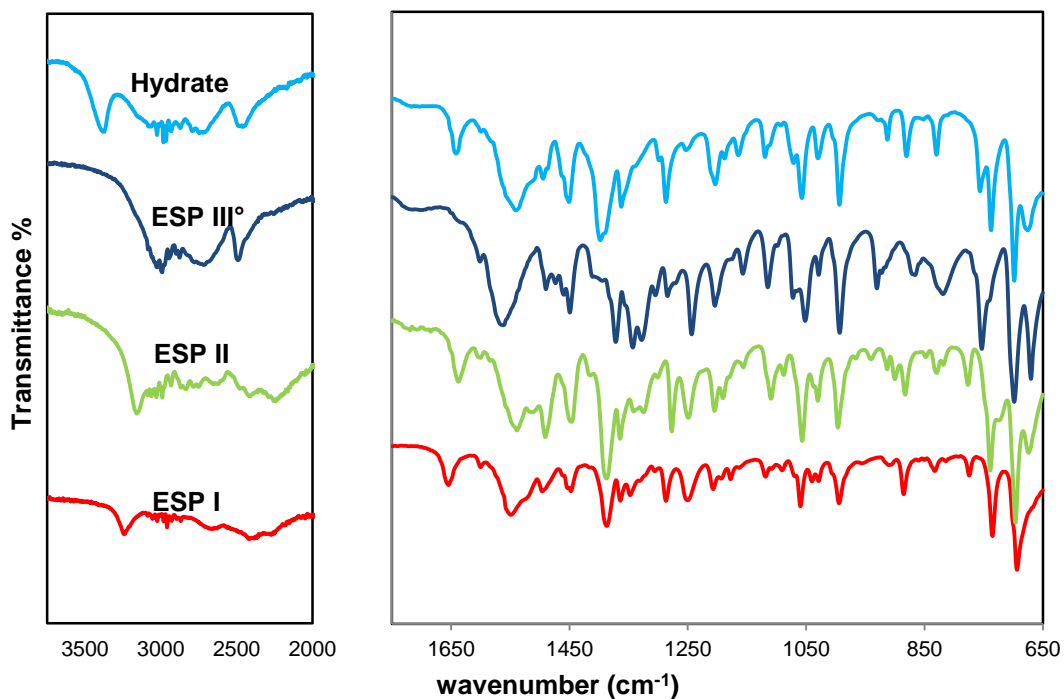


**Figure 5.13** FT-IR spectra of the different polymorphs of ESP found during the crystallisation screen plus the Hydrate phase. ESP I (shown in red) and ESP II (green) are metastable forms. ESP III° (dark blue) is the thermodynamically stable phase. The hydrate is shown in light blue.

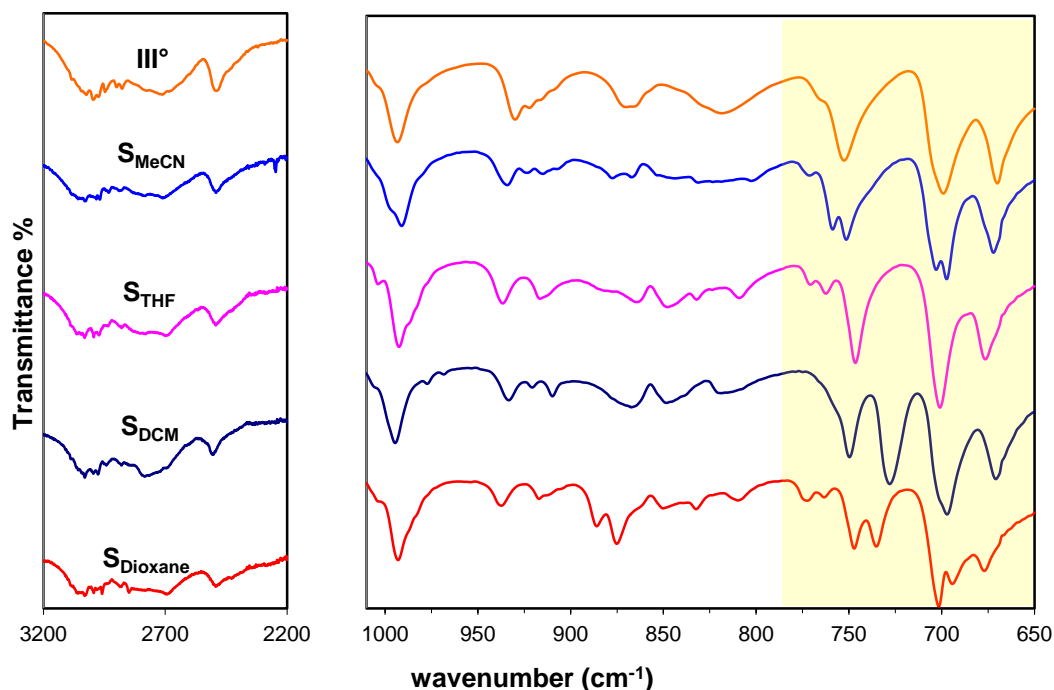


**Figure 5.14** FT-IR spectra of the solvate forms of ESP found during the screen from dioxane ( $S_{\text{Dioxane}}$  in red), dichloromethane ( $S_{\text{DCM}}$  in dark blue), tetrahydrofurane ( $S_{\text{THF}}$  in pink) and acetonitrile ( $S_{\text{MeCN}}$  in light blue). The thermodynamically stable phase ( $\text{III}^\circ$  in orange) is shown for comparison. Bands in the high energy region due to hydrogen bonding characteristics show that all the phases are very similar. Differences in the IR patterns are mainly in the low region and are highlighted in yellow.

|   | ESPI              | ESPII             | ESPIII $^\circ$   |
|---|-------------------|-------------------|-------------------|
| DSC Measurements  |                   |                   |                   |
| $T_{\text{fus}}$ , $^\circ\text{C}$                         | $106.7 \pm 0.1$   | $104.3 \pm 0.03$  | $94.4 \pm 0.1$    |
| $\Delta H_{\text{fus}}$ , $\text{kJ mol}^{-1}$              | $31.17 \pm 0.1$   | $31.90 \pm 0.6$   | $32.19 \pm 1.1$   |
| $\Delta S_{\text{fus}}$ , $\text{J mol}^{-1} \text{K}^{-1}$ | $82.1 \pm 0.3$    | $84.6 \pm 1.5$    | $87.6 \pm 3.0$    |
| Solution Calorimetric Measurements                          |                   |                   |                   |
| $\Delta H_{\text{sol}}^\circ$ , $\text{kJ mol}^{-1}$        | $-24.42 \pm 1.38$ | $-26.02 \pm 0.98$ | $-31.28 \pm 1.79$ |

**Table 5.7** Thermal data for the different polymorphs of ESP at high temperature (DSC measurements) and at room temperature (solution calorimeter). Melting points and heats of fusion of the different polymorphs of ESP were measured with a DSC and the entropies of fusion were calculated by  $\Delta H_{\text{fus}}/T_{\text{fus}}$ . The enthalpy of solution data was obtained with a solution calorimeter.

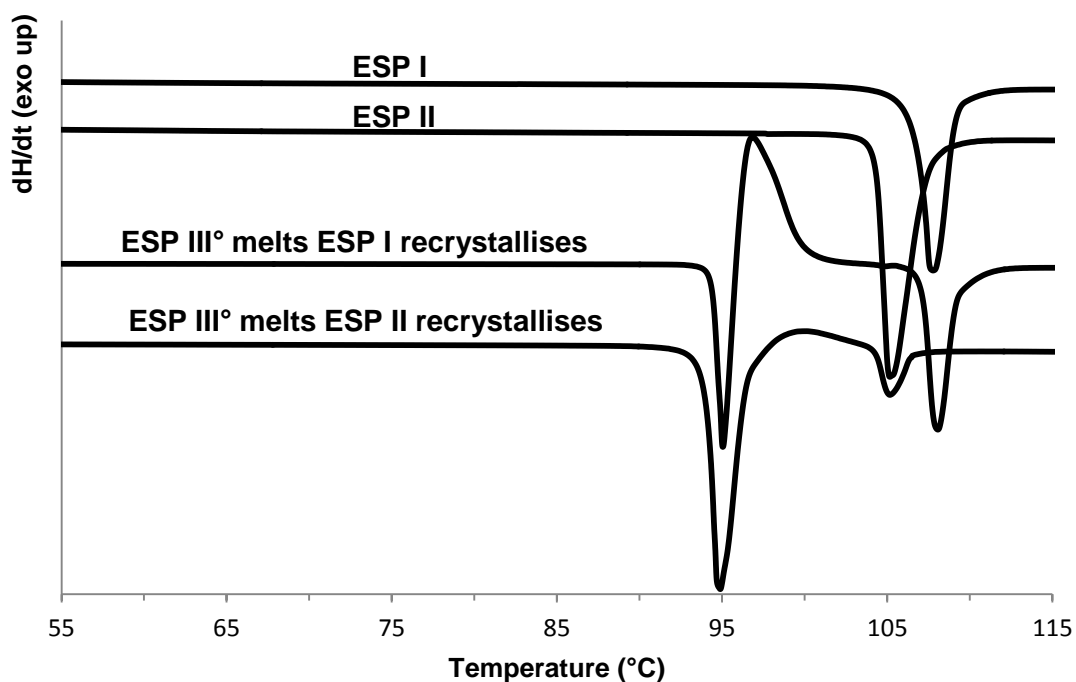


**Figure 5.15** DSC traces of the three forms of ESP, ESPI and ESP II and ESP III°. The melting is represented by the endothermic peaks around 95°C and 105°C. Melting of ESP III° is followed by a crystallisation exotherm and the melting of either ESP II or ESP I. All DSC traces were measured at a heating rate of 10 °C/min.

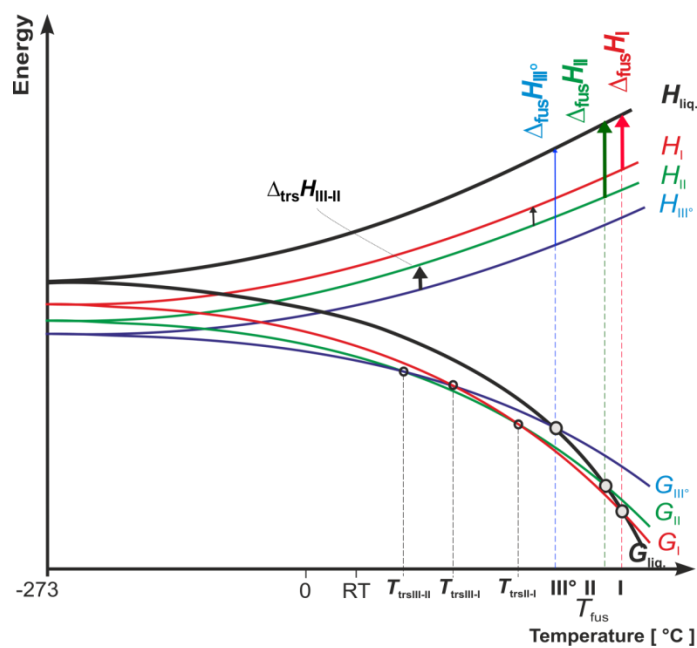


**Figure 5.16** Schematic energy/temperature diagram of ESP polymorphs.  $T_{fus}$ : melting point,  $G$ : Gibbs free energy,  $H$ : enthalpy,  $\Delta_{fus}H$ : enthalpy of fusion,  $\Delta_{trs}H$ : transition enthalpy and liq: liquid phase (melt).



### 5.4.2.3 Relative Stability of ERP I° and ESP III°

The relationship and the qualitative relative stability of the different polymorphs of ERP and ESP were discussed in section 5.4.2.1 and 5.4.2.2 respectively. In order to assess the ability of ephedrine to resolve the two enantiomers of 2-phenylpropionic acid the relative stability of the two thermodynamically stable phases at room temperature was determined. Three different methods were used to determine the relative stability at different temperatures: thermal measurements at temperatures close to their melting points using DSC, thermal measurements at room temperature using a solution calorimeter and solubility measurements. The solubility data for both diastereomeric salts were fitted to the van't Hoff equation. The applicability of this approach to estimate enthalpies and free energies of dissolution from solubility measurements was evaluated by comparing the results obtained to those using a solution calorimeter.

The solubilities of ERP I° and ESP III° in ethanol were measured between 5°C and 30°C in ethanol and exhibit the usual pattern of increasing solubility with temperature (Figure 5.17). In this temperature range there were no phase transitions for either diastereomeric salt. This was assessed by measuring the FT-IR spectra of the wet solids taken at each of the sampling points. For both ERP I° and ESP III° a linear van't Hoff plot of  $\ln X_2$  against  $(1/T - 1/T_{\text{hm}})$  shows that  $\Delta H_{\text{sol}}$  is constant over the range  $T_{\text{hm}} \pm 12.5$  °C, where  $T_{\text{hm}}$ , the mean harmonic temperature is 17.5 °C. This is consistent with the observation that there are no phase transitions in the temperature range studied. Both salts are very soluble in ethanol with the least soluble, ERP I°, having a solubility at 25°C of 0.0109 mol ERP / mol solution. As can be seen from Figure 5.17 and the solubility data summarised in Table 5.8 ESP III° is almost 10 times more soluble than ERP I°, consistent with the preliminary solubility screen in which ESP was observed to be much more soluble than ERP in all the solvents investigated.

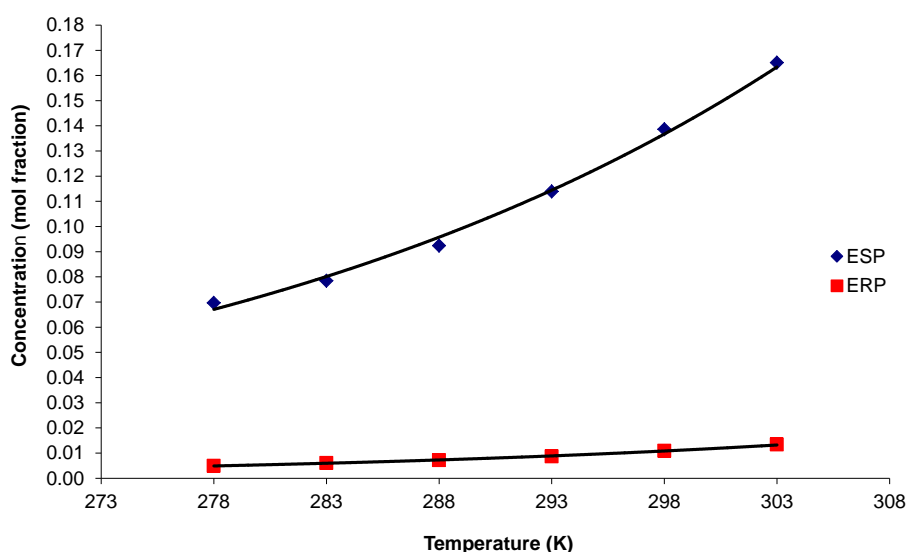


**Figure 5.17** Temperature dependence of the solubility of ERP I° and ESP III° in ethanol between 5°C and 30°C expressed in mol fraction.

| Temperature<br>(°C) | ERP I°<br>(mole fraction)        | ESP III°<br>(mole fraction)      |
|---------------------|----------------------------------|----------------------------------|
| 5                   | 4.928 (0.024) x 10 <sup>-3</sup> | 6.967 (0.008) x 10 <sup>-2</sup> |
| 10                  | 6.044 (0.093) x 10 <sup>-3</sup> | 7.841 (0.036) x 10 <sup>-2</sup> |
| 15                  | 7.187 (0.108) x 10 <sup>-3</sup> | 9.239 (0.020) x 10 <sup>-2</sup> |
| 20                  | 8.659 (0.221) x 10 <sup>-3</sup> | 1.139 (0.014) x 10 <sup>-1</sup> |
| 25                  | 1.091 (0.066) x 10 <sup>-2</sup> | 1.386 (0.025) x 10 <sup>-1</sup> |
| 30                  | 1.339 (0.017) x 10 <sup>-2</sup> | 1.651 (0.022) x 10 <sup>-1</sup> |

**Table 5.8** Solubility data for the two thermodynamically stable phases of the diastereomeric salt pair, ERP I° and ESP III°, in ethanol at different temperatures.

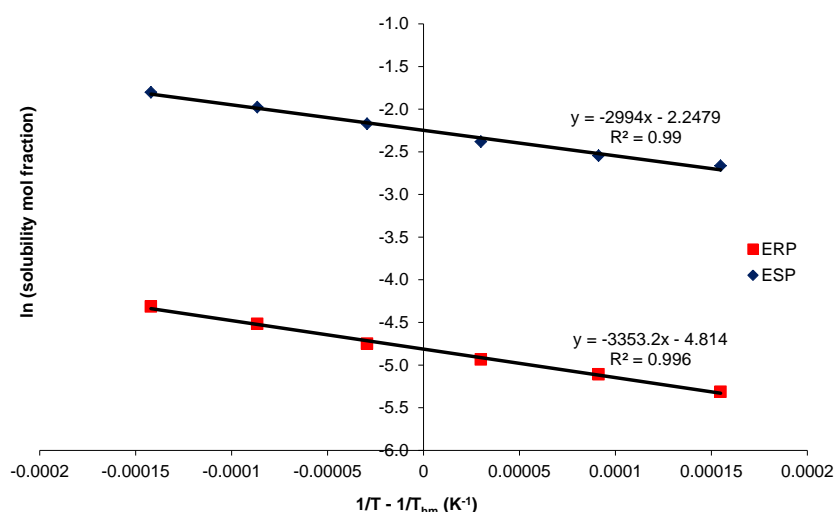


**Figure 5.18** van't Hoff plot for the temperature dependence of the solubility of ERP I° and ESP III° in ethanol. The gradient is  $-\Delta H_{sol}^{\circ}/R$  and the intercept is  $-\Delta G_{sol}^{\circ}/RT_{hm}$ .

The apparent standard enthalpy change,  $\Delta H_{sol}^{\circ}$ , and standard free energy of solution,  $\Delta G_{sol}^{\circ}$ , were obtained using Krug's approach [210] for both salts, and are summarised in Table 5.9. According to the solubility data, ERP I° has 2.9kJ/mol and 6.2kJ/mol lower enthalpy and free energy of formation than ESP III° at room temperature. The data obtained from the solubility data suggests that ESP III° is somewhat entropically stabilised.

|   | ERP I°       | ESP III°     | $\Delta$ (ESP III° – ERP I°) |
|---|--------------|--------------|------------------------------|
| Solubility Measurements   |              |              |                              |
| $\Delta H_{\text{sol}}^{\circ}$ , kJ mol <sup>-1</sup>                | 27.88 ± 0.86 | 24.90 ± 1.24 | -2.98 ± 1.52                 |
| $\Delta S_{\text{sol}}^{\circ}$ , J mol <sup>-1</sup> K <sup>-1</sup> | 55.95 ± 0.86 | 67.00 ± 1.24 | 11.05 ± 1.52                 |
| $\Delta G_{\text{sol}}^{\circ}$ , kJ mol <sup>-1</sup>                | 11.63 ± 0.02 | 5.43 ± 0.04  | -6.20 ± 0.04                 |
| Solution Calorimetric Measurements                                    |              |              |                              |
| $\Delta H_{\text{sol}}^{\circ}$ , kJ mol <sup>-1</sup>                | 38.25 ± 0.74 | 31.28 ± 1.79 | -6.97 ± 1.94                 |

**Table 5.9** Standard enthalpy and free energy of solution for ERP I° and ESP III° obtained by fitting the solubility data to the van't Hoff plot using Krug's approach as well as enthalpies of solution obtained from solution calorimetric measurements.

The difference in the enthalpies of solution of the two diastereomeric salts as measured with a solution calorimeter is slightly larger, -6.97 kJ/mol, but within the error estimates. Nevertheless differences are expected as the enthalpy of solution obtained from the solution calorimeter is in infinite dilution whereas the solubility measurements are at equilibrium. Furthermore, although the sample of ESP III° measured in the solution calorimeter was believed to be phase pure, traces of impurities were commonly observed in DSC curves, despite not having been detected in powder X-ray diffraction data or in the FT-IR. This is likely not to be a problem in the solubility measurements as it is believed that the impurities were formed during the isolation of ESP III° from the mother liquor, either by evaporative crystallisation, or a slight hydration in ambient conditions. Given that during the solubility measurements the crystals were constantly kept under the same conditions a phase transformation is less likely.

### 5.4.3 Crystal Structures of the Diastereomeric Salts

#### 5.4.3.1 Crystal Structure of ERP I°

An ERP I° single crystal suitable for X-ray diffraction study was grown from ethanol by slow solvent evaporation at room temperature. The crystal data for ERP I° are given in Table 5.14 in section 5.6.3 in the appendix at the end of the chapter. The salt crystallises in the monoclinic space group P2<sub>1</sub> and has one ephedrine cation and one phenylpropionate anion in the asymmetric unit (Figure 5.19).

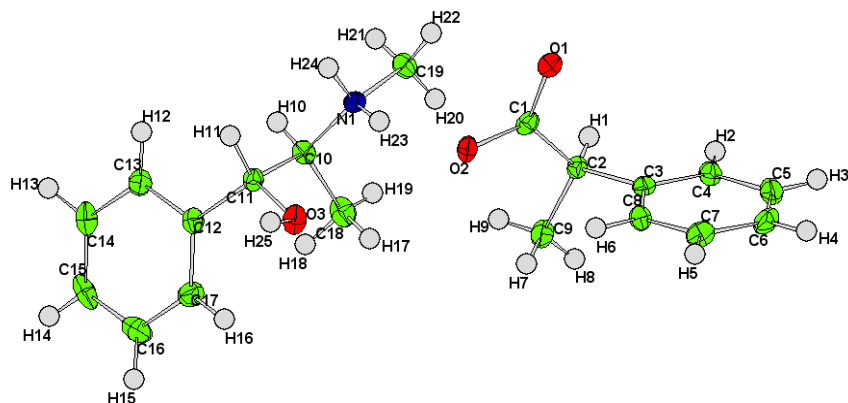


**Figure 5.19** Asymmetric unit of ERP 1°. Displacement ellipsoids are drawn at the 50% probability level and hydrogen atoms are displayed as spheres of arbitrary radii.

The ephedrine cation adopts an extended conformation, in which the torsion angle defined by C19-N1-C10-C11 (Figure 5.19) is  $-175.4^\circ$  as shown in Figure 5.20. Furthermore, the position of the hydroxyl hydrogen, which defines the hydrogen bonding of the molecule, is pointing away from the amine group (Figure 5.20 (a)). This conformation of ephedrine allows the formation of three kinds of hydrogen bonds as can be seen in Figure 5.21 (b). One of the carboxylate oxygen atoms, O2 in Figure 5.19, forms a bifurcated N-H...O hydrogen bond with the ammonium hydrogen of two adjacent ephedrine molecules, whereas the other oxygen (O1 in Figure 5.19) forms an O-H...O hydrogen bond with the hydroxyl hydrogen in the ephedrine ion. This hydrogen bonding arrangement results in the ion pairs forming an infinite columnar hydrogen bond network with a two-fold screw axis along the shortest axis *b*. The  $2_1$  column can be represented by  $R_4^3(13)$  using the graph sets proposed by Etter et al [81]. The packing of the  $2_1$  columns parallel to each other, as depicted in Figure 5.21 (a) form the three dimensional crystal structure. The short contacts dominating the packing of the  $2_1$  columns are face-to-edge between phenyl rings of ephedrine and phenylpropionate ions or methyl-to-face short contacts shown as dashed green lines in Figure 5.21 (a). The face-to-edge H... $\pi_{\text{centroid}}$  distances, 1, 2 and 3 in Figure 5.21 (a), are 3.108, 2.827 Å and 3.122 Å whereas the methyl-to-face contact (4 in Figure 5.21 (a)) is 2.974 Å. The separation between adjacent  $2_1$  columns,  $d_1$  and  $d_2$  in Figure 5.21 (a) are 9.8471 Å and 14.583 Å as measured from the screw axis looking down *b*.

The observed  $R_4^3(13)$  hydrogen bonding motif has been previously reported for other carboxylic acid salts of ephedrine, such as ephedrine adipate, ephedrine glycolate, ephedrine hemimalonate [241] and a 2:1 salt of ephedrine and pimelic acid [242]. In all these structures, the ephedrine was found in the extended conformation with the hydroxyl hydrogen pointing away from the amine leading to the formation of the  $2_1$  hydrogen bonding

columns. The packing of the columns in the different structures was determined by the size and extra functionalities of the acids and therefore differs slightly from the one reported here.

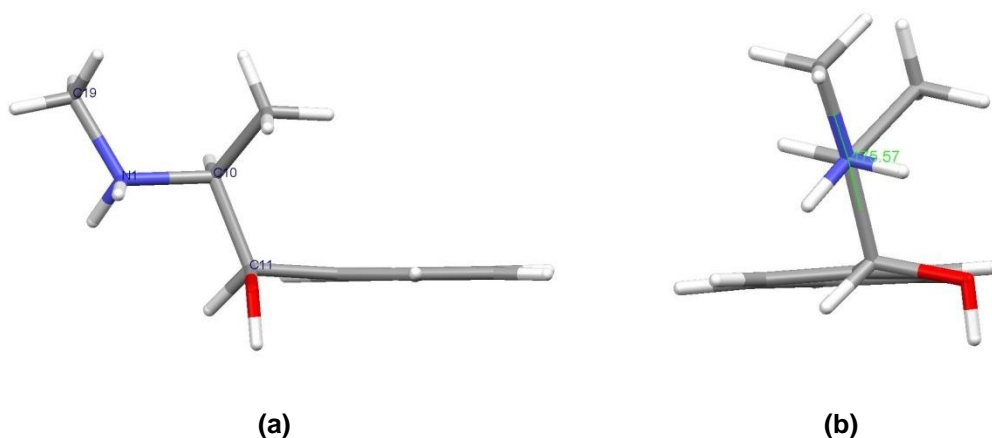


**Figure 5.20** Extended conformation of ephedrine in ERP I°. The view along O3-C11 in (a) shows the position of the hydroxyl hydrogen pointing away from the amine group. The view in (b) is along the N1-C10 bond. The value of the torsion angle defined by C19-N1-C10-C11 is marked in green.

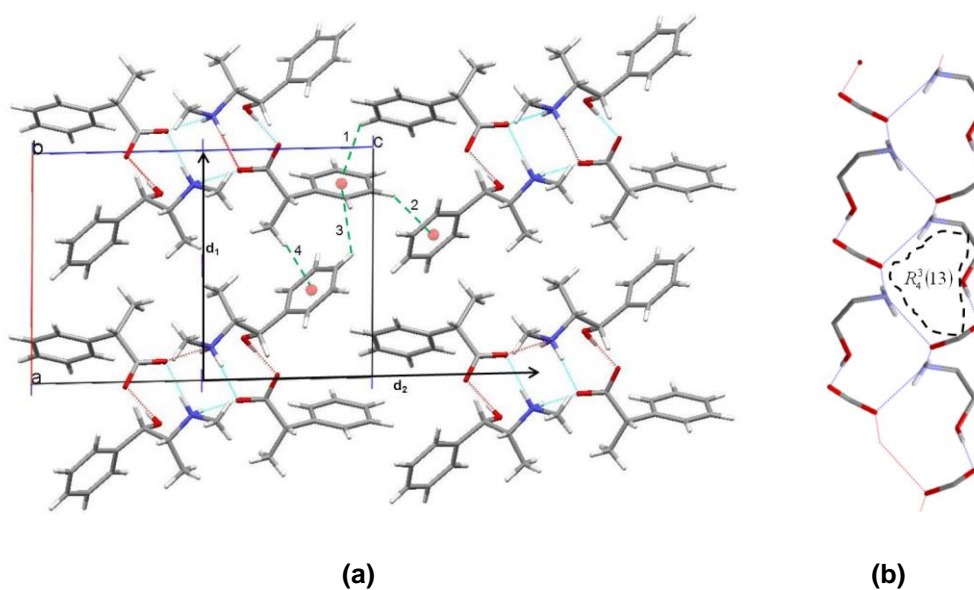


**Figure 5.21** (a) Packing diagram of (1R,2S)-ephedrinium-(R)-2-phenylpropionate (ERP I°) viewed along b. (b)  $2_1$  Columnar hydrogen bonding network viewed along a with the  $R_4^3(13)$  hydrogen bond motif highlighted with the dotted line (only the atoms involved in the hydrogen bonding are showed for clarity).

### 5.4.3.2 Crystal Structure of ESP I

A single crystal of ESP I was grown from ethanol in a slow cooling experiment in which a saturated solution at 30°C was slowly cooled and left to stand at 10°C. The crystal was removed after a month at 10°C and its structure solved using single crystal X-ray diffraction data. The crystal data for ESP I are given in Table 5.14 in section 5.6.3 in the appendix at the end of the chapter.

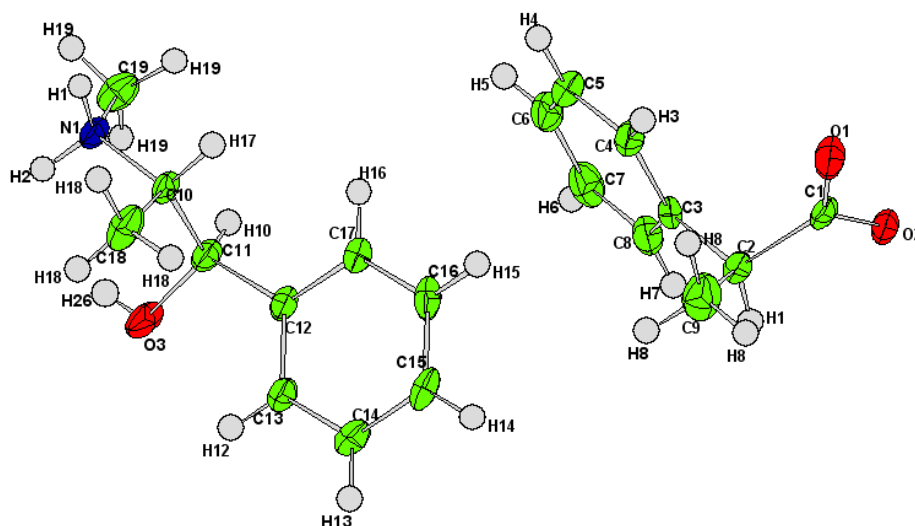


**Figure 5.22** Asymmetric unit of ESP I. Displacement ellipsoids are drawn at the 50% probability level and hydrogen atoms are displayed as spheres of arbitrary radii.

ESP I crystallises in the monoclinic space group  $P2_1$  with one ephedrine cation and one phenylpropionate anion in the asymmetric unit. One of the main differences between ESP I and ERP I° is the conformation of the ephedrine ion. In ERP I°, ephedrine adopts an extended conformation with the hydroxyl hydrogen atom pointing away from the amine group (Figure 5.20). In ESP I however, the ephedrine ion adopts a folded conformation, in which the torsion angle given by C19-N1-C10-C11 is more acute at  $-49.92^\circ$  as seen in Figure 5.23 (b). Furthermore, the hydroxyl hydrogen is pointing towards the amine group. This conformation leads to a hydrogen bonding pattern that differs considerably to that of ERP I°. With the hydroxyl hydrogen pointing towards the amine, the ephedrine ion is able to form a dimer with phenylpropionate anion in which one of the carboxylate oxygen (O2 in Figure 5.22) is hydrogen bonded to the hydroxyl hydrogen and the other (O1) is bonded to one of the amino hydrogen (H2). This hydrogen bonded dimer can be described by the graph set  $R_2^2(9)$ . The dimers are then joined by a hydrogen bond between the free hydrogen on the nitrogen and the O2 on the phenylpropionate ion, forming a chain or sheet

in which the phenyl groups from the ephedrine and the phenylpropionate ions are at the edge and the polar hydrogen bonded groups are in the middle. Unlike ERP I° and other chiral systems, ESP I does not form the characteristic  $2_1$  columns with a polar core and hydrocarbon shell as the two fold screw axis does not pass through the middle of the hydrogen bonding network. Instead, the screw axis is in between two parallel sheets. The packing of the sheets still results in polar and non-polar layers, with interdigitating phenyl groups that are dominated by very similar face-to-edge and methyl-to-face close contacts as in ERP I°. The close contacts are represented by dashed green lines in Figure 5.24 (a) and numbered 1 to 4. The lengths of the  $H \cdots \pi_{\text{centroid}}$  face-to-edge contacts, 1,3 and 4 in Figure 5.24 (a) are 3.175 Å, 2.769 Å and 3026 Å respectively. The methyl-to-face close contact, 2 in Figure 5.24 (a), is 3.105 Å. The number, type and distances of the close contacts are very similar to ERP I°. The packing of hydrogen bonded sheets in ESP I is very efficient with the distance between two adjacent sheets along a,  $d_1$  in Figure 5.24 (a), only 6.344 Å apart.

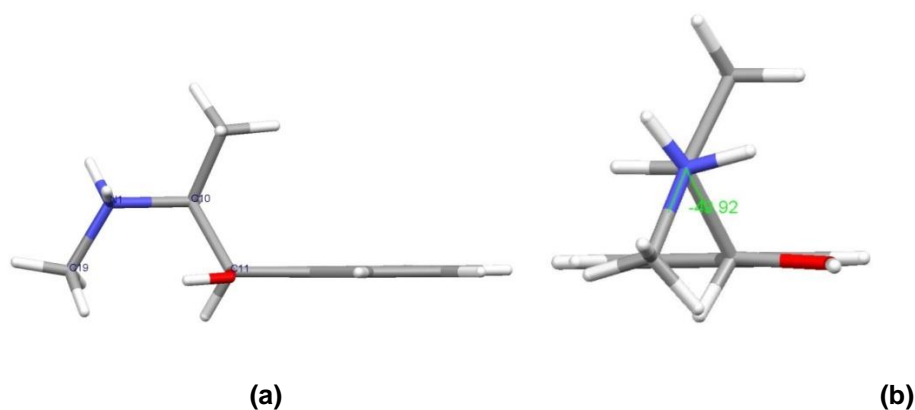


**Figure 5.23** Folded conformation of ephedrine in ESP I. The view along O3-C11 in (a) shows the position of the hydroxyl hydrogen pointing towards the amine group. The view in (b) is along the N1-C10 bond. The value of the torsion angle defined by C19-N1-C10-C11 is marked in green.

The hydrogen bonding motif found in ESP I is very similar to hydrogen bonding arrangements in other crystal structures of ephedrine salts in which ephedrine is in a folded conformation and the torsion angle that defines the position of the hydroxyl hydrogen in ephedrine is close to that of the ephedrine ion in ESPI. For example, (1R,2S)-Ephedrine-(R)-4-(3,4-dichlorophenyl)-4-(2-pyridyl)butanoate forms a  $R_2^2(9)$  hydrogen bonded motif that link together to form sheets that then pack parallel to each other as seen in Figure 5.24. In fact, the formation of  $R_2^2(9)$  hydrogen bonded dimers is dependent on the torsion angle defining the hydroxyl hydrogen position rather than on whether ephedrine adopts an extended or folded conformation. A set of crystal structures of related salts of ephedrine reported by A.M.G. Kok et al in shows the formation of these dimers in structures where ephedrine is in an extended conformation. The linking of  $R_2^2(9)$  dimers leads to two types of packing arrangements. In the first, where no symmetry passes through the middle of the

dimer, the chain forms sheets which then pack to form the crystal as in ESP I. In the other, a  $2_1$  screw axis is at the middle of the dimer chain. In this situation, a column forms. This is seen in the structure of ESP II, described in the following section.

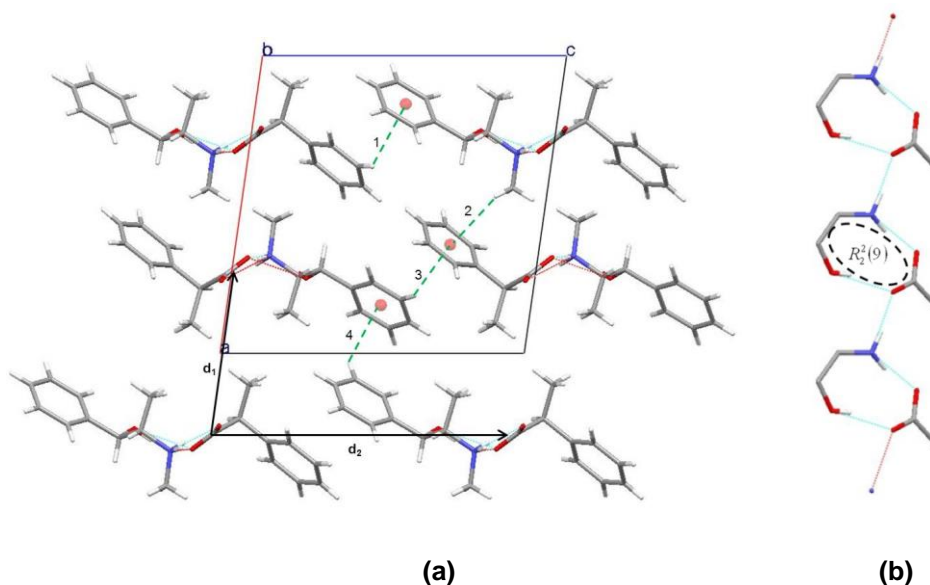
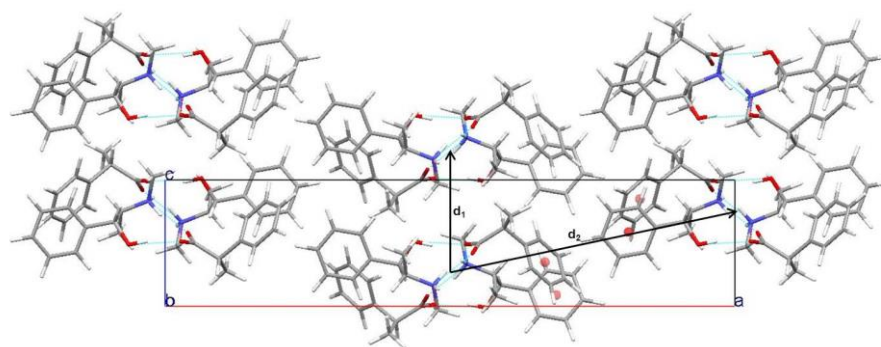


**Figure 5.24 (a)** Packing diagram of (1R,2S)-ephedrinium-(S)-2-phenylpropionate form I (ESP I). **(b)** Hydrogen bonded network

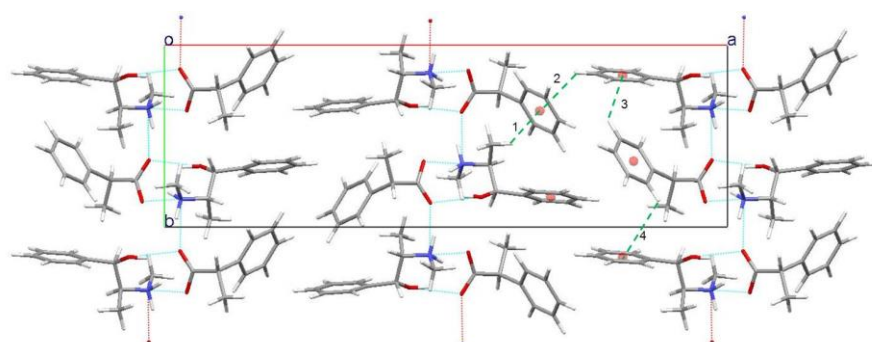
#### 5.4.3.3 Crystal Structure of ESP II

The crystal packing and hydrogen bonding characteristics of ESP II salt are shown in Figure 5.25 (a) and (b) respectively. As in the other two salts, ESP II was found to crystallise with one ephedrine cation and one (S)-2-phenylpropionate anion in the asymmetric unit. The ephedrine ion in ESP II also adopts the folded conformation (Figure 5.23) although the C19-N1-C10-C11 torsion angle is slightly less acute ( $68.8^\circ$ ). ESP II, in turn, has a very similar hydrogen bonding pattern to that of ESP I with the ephedrine and phenylpropionate ions forming an  $R_2^2(9)$  dimer that link via the free amino hydrogen to form a chain of  $R_2^2(9)$  rings. However, in this case the screw axis does lie in the middle of the hydrogen bonded network. Despite the differences in hydrogen bonding pattern, ESP II still displays helical hydrogen bonded column. The  $2_1$  column of the salt is represented by a  $C_2^2(6)R_2^2(9)$  motif.

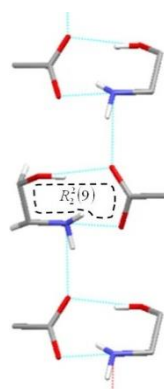




(a)



(b)



(c)

**Figure 5.25 (a)** Packing diagram of (1R,2S)-ephedrinium-(S)-2-phenylpropanoate (ESP form II) **(b)** Hydrogen bonding network.

#### 5.4.3.4 Crystal Structure of ESP III°

ESP III° was solved from powder X-ray diffraction data at Strathclyde University by Ms Rajni Miglani, as described in Section **Error! Reference source not found.**. The ephedrine ion in

ESP III<sup>o</sup>, like ERP I<sup>o</sup>, adopts an extended conformation (Figure 5.20). The hydrogen bonded network and packing is very similar to that found in ERP I<sup>o</sup>, represented by the graph set  $R_4^3(13)$ , in which the ion pairs form an infinite columnar hydrogen bond network with a twofold screw axis along the shortest axis b. The 2<sub>1</sub> columns pack parallel to each other to form the crystal structure.

The number and type of the short contacts dominating the packing of the columns are the same as in ERP I. The face-to-edge H $\cdots$  $\pi_{\text{centroid}}$  distances, 1, 2 and 3 in Figure 5.26 (a), are 2.854, 2.975 Å and 3.766 Å whereas the methyl-to-face contact (4 in Figure 5.26 (a)) is 2.939 Å. The separation between adjacent 2<sub>1</sub> columns, d<sub>1</sub> and d<sub>2</sub> in Figure 5.26 (a) are 10.393 Å and 14.167 Å as measured from the screw axis looking down b, very similar to ERP I<sup>o</sup>.

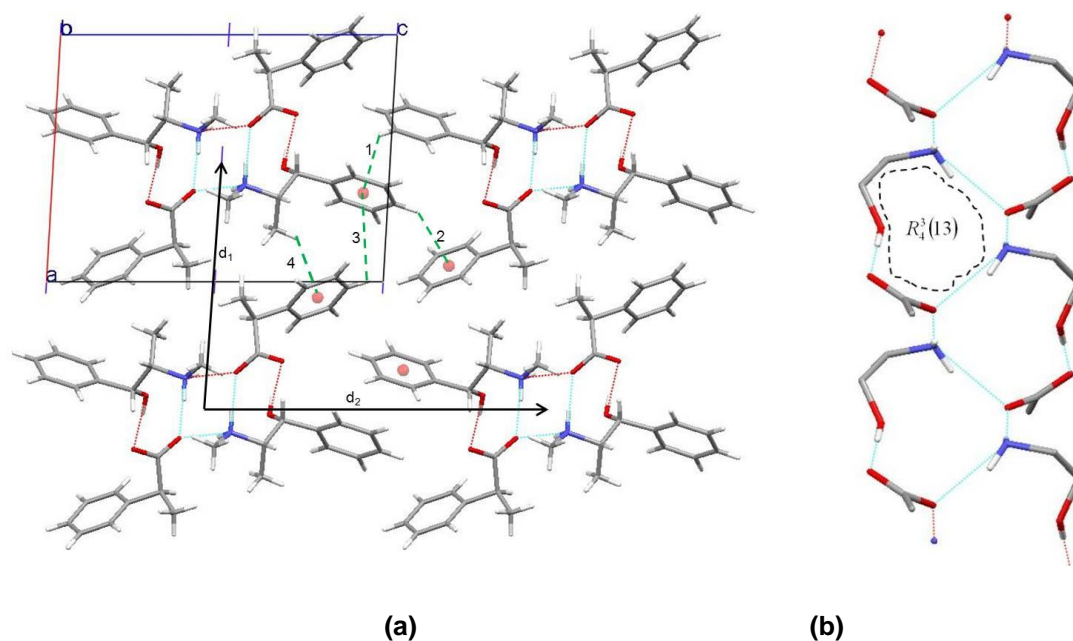


**Figure 5.26 (a)** Packing diagram of (1R,2S)-ephedrinium-(S)-2-phenylpropanoate (ESP form III) **(b)** Hydrogen bonding network.

#### 5.4.3.5 Crystal Structure of ESB I

A single crystal of ESB I was grown from ethanol by slow solvent evaporation. The ephedrine ion adopts an extended conformation, as that seen in ERP I<sup>o</sup> and ESP III<sup>o</sup>. The longer aliphatic chain of the acid ion does not affect the hydrogen bonding ability of the acid and base. In fact, the crystal structure of ESB I, determined from single crystal X-ray

diffraction data and shown in Figure 5.27, shows that the  $R_4^3(13)$  hydrogen bonded rings seen ERP I° and ESP III° form, leading to the  $2_1$  columns typical of other ephedrine salts.

Although the hydrogen bonding motif is the same, the packing of the columns differs from that seen in ERP I° and ESP III°. In ERP I° and ESP III° the interactions in the non-polar regions are dominated by the phenyl groups. In ESB I however, the phenyl groups intercalate with the ethyl chains from the acid. It is possible that the added bulkiness of the longer aliphatic substituent on the acid might lead the salts to more complicated crystallisation behaviours. Whereas the polymorphs of ESP (see section 5.4.2.2) showed differences in their hydrogen bonding arrangements, forming two distinct hydrogen bonding arrangements  $R_4^3(13)$  and  $R_2^2(9)$ , the FT-IR spectra of the two anhydrous phases of ERB (Figure 5.5, Section 5.4.1.3) suggest the ERB polymorphs only differ in the way that the  $2_1$  columns pack, since the spectra only show differences at lower wavenumbers. The results obtained in the search for plausible packing arrangements presented in Chapter 6 for Ephedrine-2-phenylpropionate salts show that it is possible that there might be a large number of competing ways of packing the hydrocarbons. Adding an extra degree of freedom to the molecules might therefore increase the number of possible competing packing arrangements. This might also help explain why the crystallisation does not often lead to good quality single crystals.

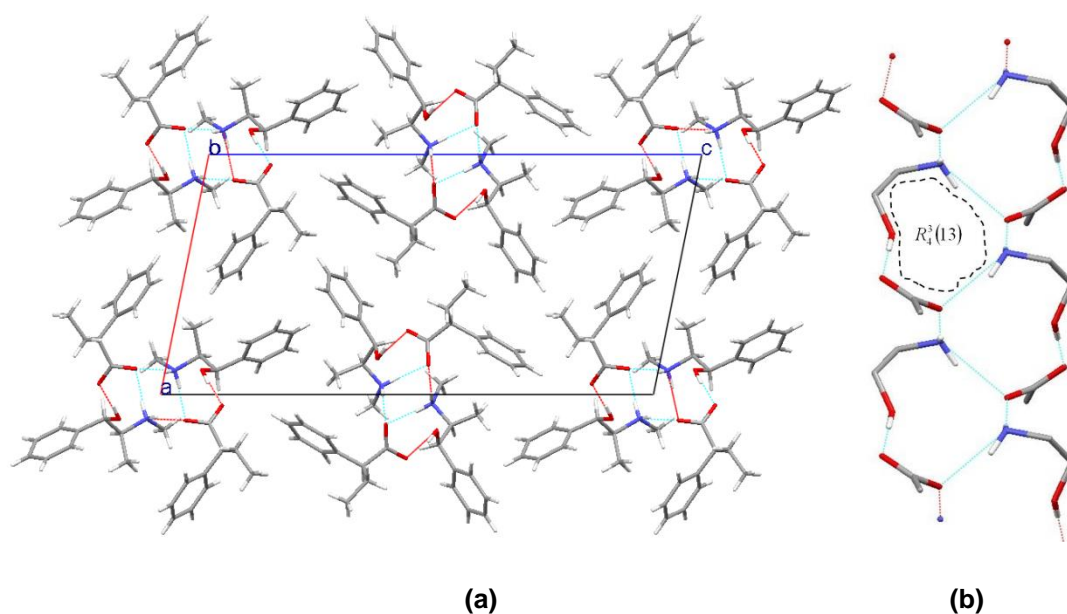


**Figure 5.27 (a)** Crystal structure of ESB I viewed down axis b. **(b)**  $2_1$  Columnar Hydrogen bonding network viewed along a with the  $R_4^3(13)$  hydrogen bond motif highlighted with the dotted line (only the atoms involved in the hydrogen bonding are showed for clarity).

#### 5.4.3.6 Crystal Structure of PRP Hydrate

The crystal structure of the hydrate of PRP could be solved from a single crystal grown in ethanol and is shown in Figure 5.28. As can be seen from the hydrogen bonding pattern shown in Figure 5.28 (b) the water molecule plays an important structural role, participating in the hydrogen bonding between the two ions, and probably why the hydrate is stable and does not de-solvate readily.

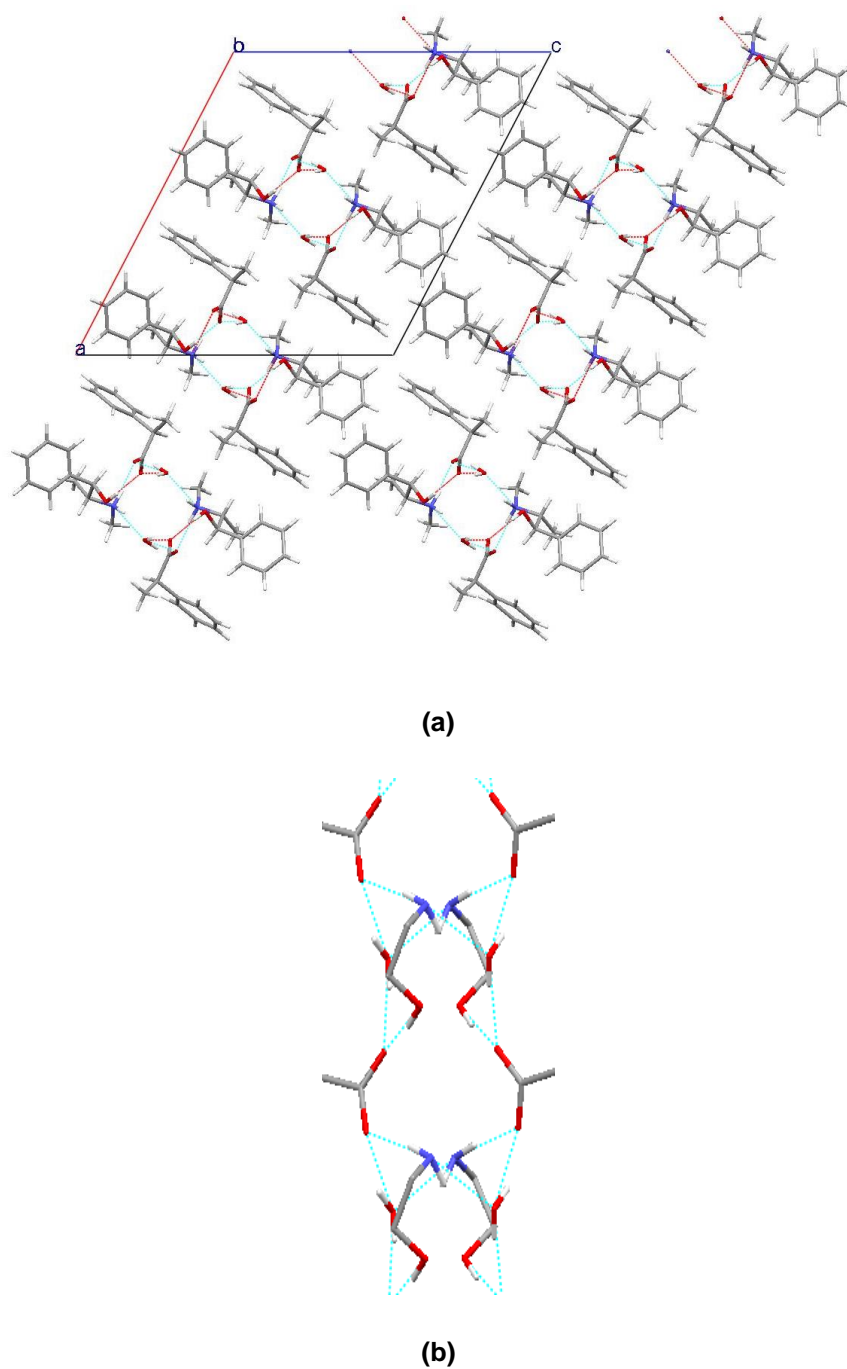
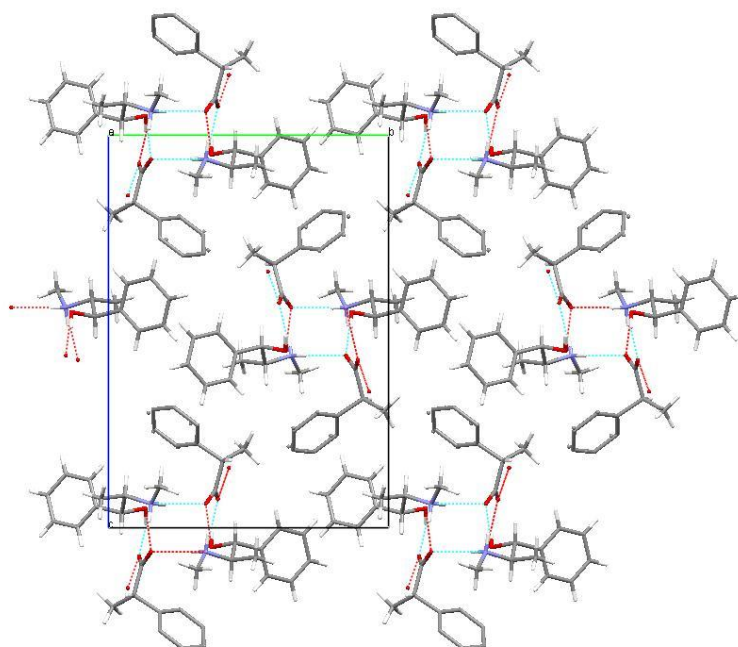


**Figure 5.28 (a)** Packing diagram of PRP Hydrate. The hydrogen bonding pattern is shown in **(b)**.

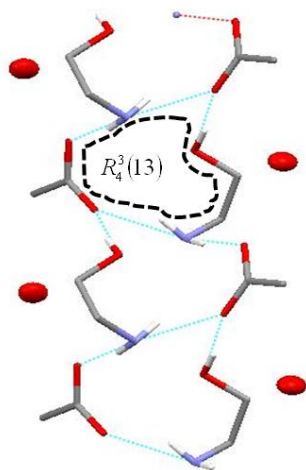
The bonding pattern seen in the hydrate phase of PRP has not been seen before and is not comparable to the hydrogen bonding patterns of the structures solved in this work. Nevertheless, there is a similarity with other diastereomeric salts, in that the hydrogen bonding pattern leads to columns with a polar core and an a-polar wall that pack together to form the crystal structure. In this case the interactions between columns seem to be dominated by  $\pi - \pi$  interactions between phenyl groups of neighbouring columns similar to the packing of the  $2_1$  columns in ESB I (see section 5.4.3.5).

#### 5.4.3.7 Crystal Structure of PSP Hydrate

The crystal structure of one of the phases of PSP could be solved by X-ray single crystal diffraction. However, the crystal structure was found to be disordered, and contain a third of a water molecule, (Figure 5.29). The presence of water was not detected in the elemental analysis and the stoichiometry of the hydrate was not investigated further. The water molecule however does not play any significant structural role and does not affect the hydrogen bonding of the ions. The hydrogen bonded pattern can be described by  $R_4^3(13)$  in the graph set notation and is the same as that seen in the structures of PRB and PSB (Section 5.4.3.8 and Section 5.4.3.9. respectively)



(a)

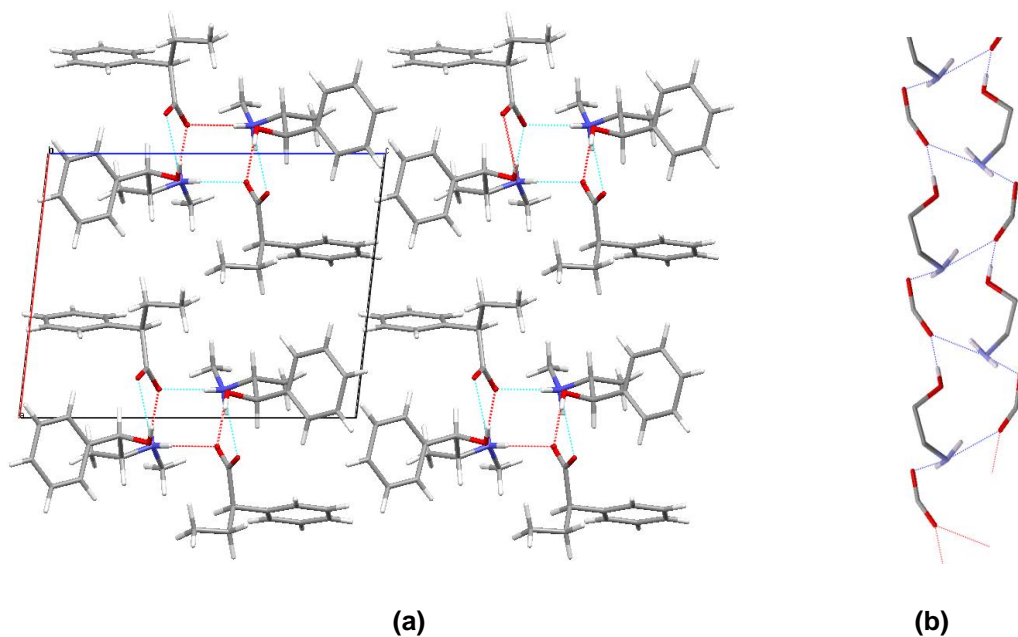


(b)

**Figure 5.29 (a)** Packing diagram of PSP Hydrate. The hydrogen bonding pattern is shown in **(b)**. The hydrogen bonding pattern can be represented using graph set notation as  $R_4^3(13)$ .

#### 5.4.3.8 Crystal Structure of PRB I

The crystal structure of PRB I was solved using single crystal X-ray diffraction data from a crystal obtained from ethanol in an evaporation experiment. PRB I adopts the same hydrogen bonding pattern found in the PSP hydrate (excluding the water), i.e.  $R_4^3(13)$ .



(a)

(b)

**Figure 5.30 (a)** Packing diagram of PRB. The hydrogen bonding pattern is shown in **(b)** and is the same as that seen in the disordered structure PSP.

#### 5.4.3.9 Crystal Structure of PSB Hydrate

The PSB<sub>Hydrate</sub> was also solved from single crystal X-ray diffraction from a single crystal grown in ethanol. The hydrogen bonded pattern in this structure is the same as in the PRB but has a water molecule every three salt pairs. The water molecule in the crystal structure of PSB has a structural role and is included in the hydrogen bonding arrangement between the two ions, although it does not affect the main hydrogen bonded pattern of  $R_4^3(13)$  rings. The hydrate is stable in ambient conditions and, as shown in Figure 5.32, no mass loss is seen before the melting supporting the observation that the water molecule plays a structural role, and is not easily liberated from the lattice before melting.

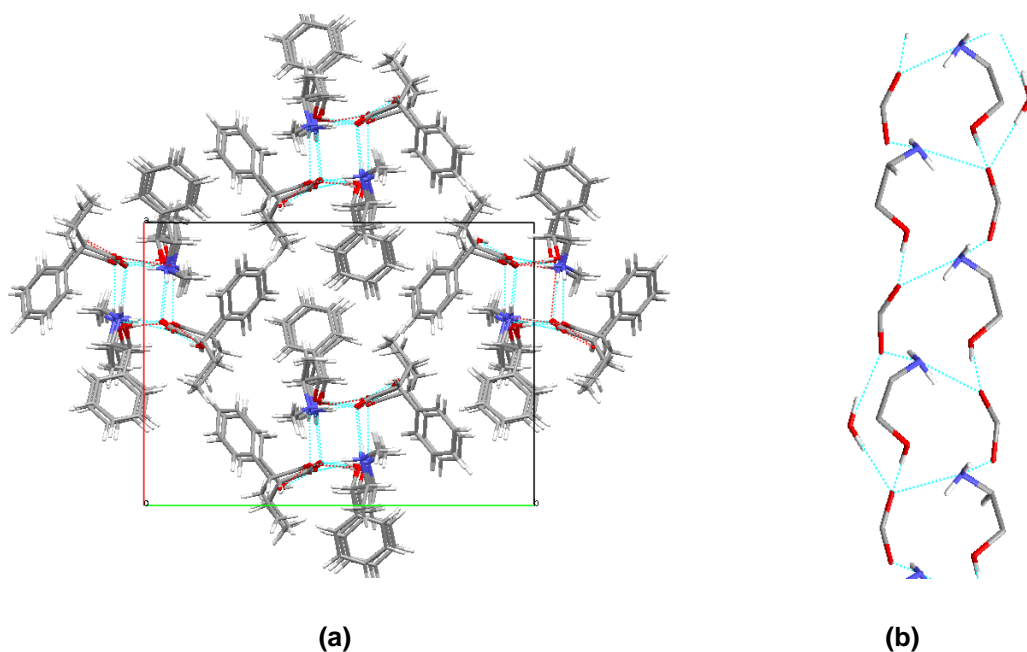


**Figure 5.31** (a) Packing diagram of PSB. The hydrogen bonding pattern is shown in (b).

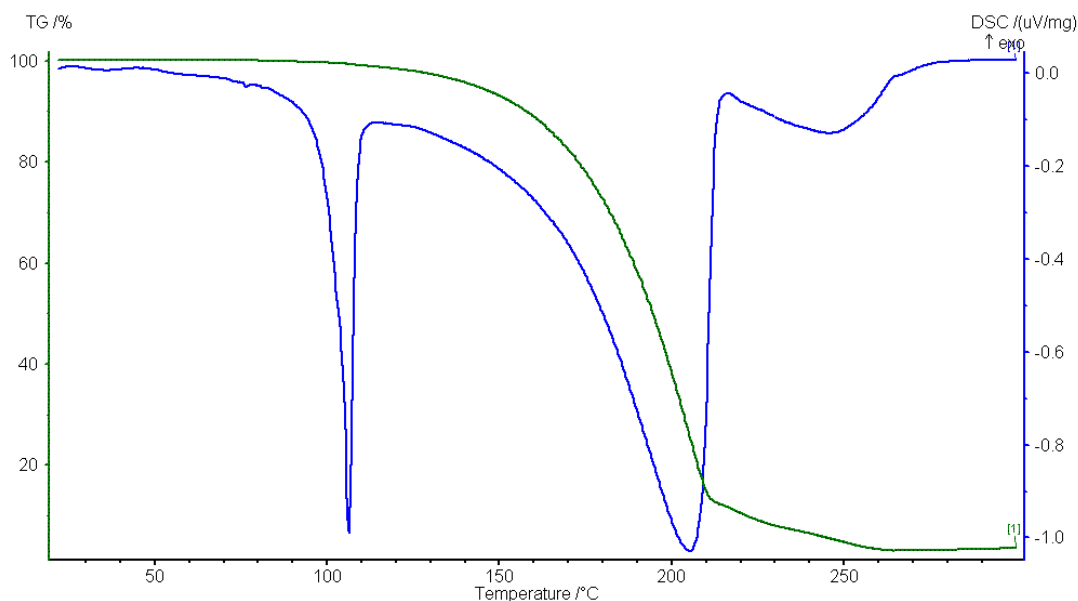


**Figure 5.32** Melting behaviour of the hydrate of PSB where the blue line represents the DSC thermogram and the green line shows the thermogravimetric data. Only one endotherm is seen and no mass loss upon heating, showing that the water is not lost before melting.

#### 5.4.4 Assessing the Ability of Ephedrine to resolve 2-Phenylpropionic acid

Despite having established that ERP I° is considerably less soluble and more stable than ESP III° (Figure 5.17), and hence expecting ephedrine to be a very good resolving agent for 2-phenylpropionic acid, it is still necessary to establish whether this would actually be the case. Although the solubility ratio of a pair of diastereomeric salts is a key aspect determining the resolvability of a given diastereomeric salt pair, the resolution efficiency depends on the whole ternary phase diagram. The appearance of solid solutions, in which the crystals in the solid phase contain both enantiomers, is not an uncommon occurrence. In such situations the level of resolution achievable would depend on the degree of miscibility of the unwanted enantiomer in the crystal lattice rather than on the solubility difference between the two pure diastereomeric salts. Other possible unwelcome phase behaviour that could aggravate the resolution process is the formation of salts of other stoichiometries and the formation of solvates. The latter should not be an issue in our case, given that we would hope to have identified solvents during the crystallisation screen where solvates do not occur. Therefore, the ternary phase diagram of ERP I° and ESP III° in ethanol at two different temperatures, 10°C and 30°C were measured to investigate whether a good resolution is achievable.



#### 5.4.4.1 Determination of the Ternary Phase Diagram of ERP I° and ESP III° in Ethanol

The ternary phase diagrams of ERP I° and ESP III° are shown in Figure 5.33 and Figure 5.34 measured at 10 and 30 °C respectively. The liquidus curves in both phase diagrams indicate a near-ideal pattern of solubility behaviour of the salt mixtures, as is often the case where the solubilities of two dissolved species differ markedly. In such cases, the effect of the less soluble species on the solvent activity is small, and so gives rise to near-ideal behaviour of the mixed system. The tie line data for both isothermal phase diagrams was obtained according to the method by Hill and Ricci [240] by extrapolating from the composition of mother liquor and the known starting compositions. This extrapolation is questionable and ideally the points on the solid line should have been determined experimentally. This however was not possible due to the high solubility and hygroscopicity of the samples and the difficulty of maintaining a constant temperature during filtration, so that it was impossible to filter off the small amount of solid residue to dryness at constant temperature. The extrapolation from the mass balance equations [240] suggest that the solid phases are composed of mixtures of ERP and ESP salts, indicating the formation of solid solutions. The formation of solid solutions is not uncommon and has been previously reported in a set of ephedrine salts [237]. In the aforementioned study, the ternary phase diagrams of set of three diastereomeric salt pairs of ephedrine with three closely related cyclophosphoric acids was investigated in order to compare to the results obtained with a computational model used to predict the formation of solid solutions. Results showed that all systems exhibited solid solution behaviour in at least part of the composition range [237].

Given the solid solution behaviour suggested by the ternary phase diagram of ERP I° and ESP III° in ethanol, the degree of diastereomeric enrichment achievable in a resolution experiment of 2-phenylpropionic acid with ephedrine in ethanol will depend on the extent of miscibility of the two enantiomers in the solid state and on the crystal yield that one wants to achieve [243]. Nevertheless, complete resolution of the two enantiomers will not be possible.

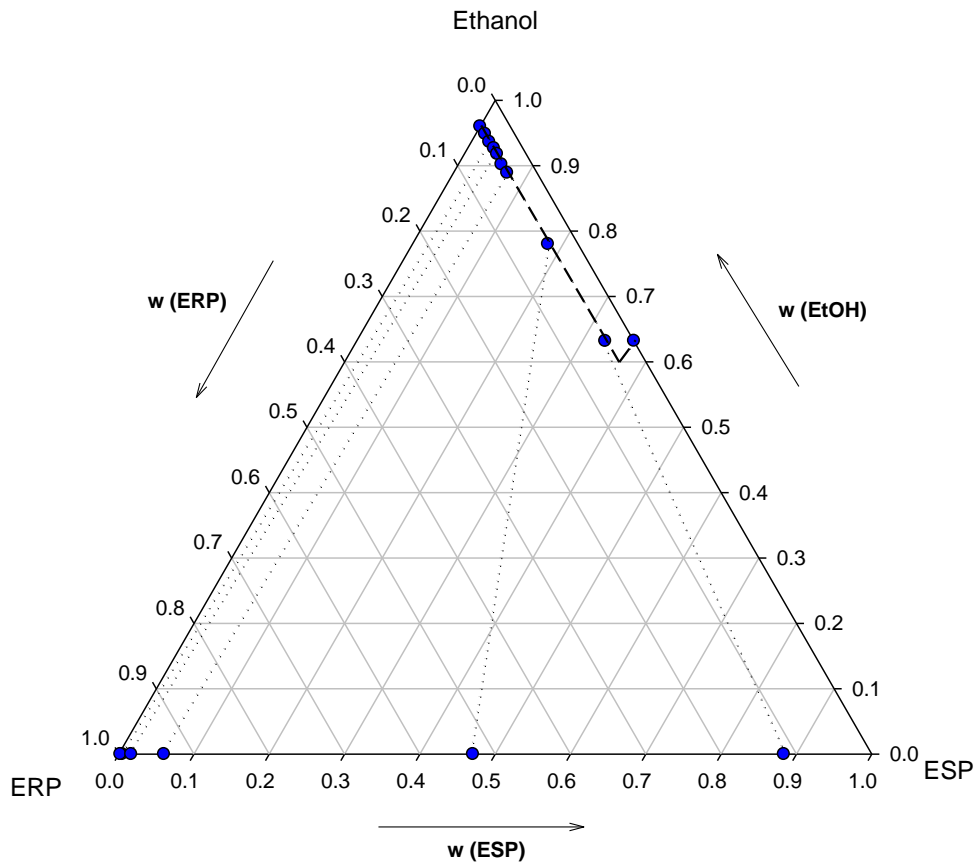


**Figure 5.33** Isothermal ternary phase diagram of ERP I° and ESP III° in ethanol measured at 10 °C. The dashed line represents the liquidus line and is included as a guide to the eye. Only the dots were measured experimentally. The tie lines are presented by the dotted lines and join the liquid phase composition with the solid phase composition. Tie lines have only been included for a few representative samples for clarity. Compositions are given in mass fractions.

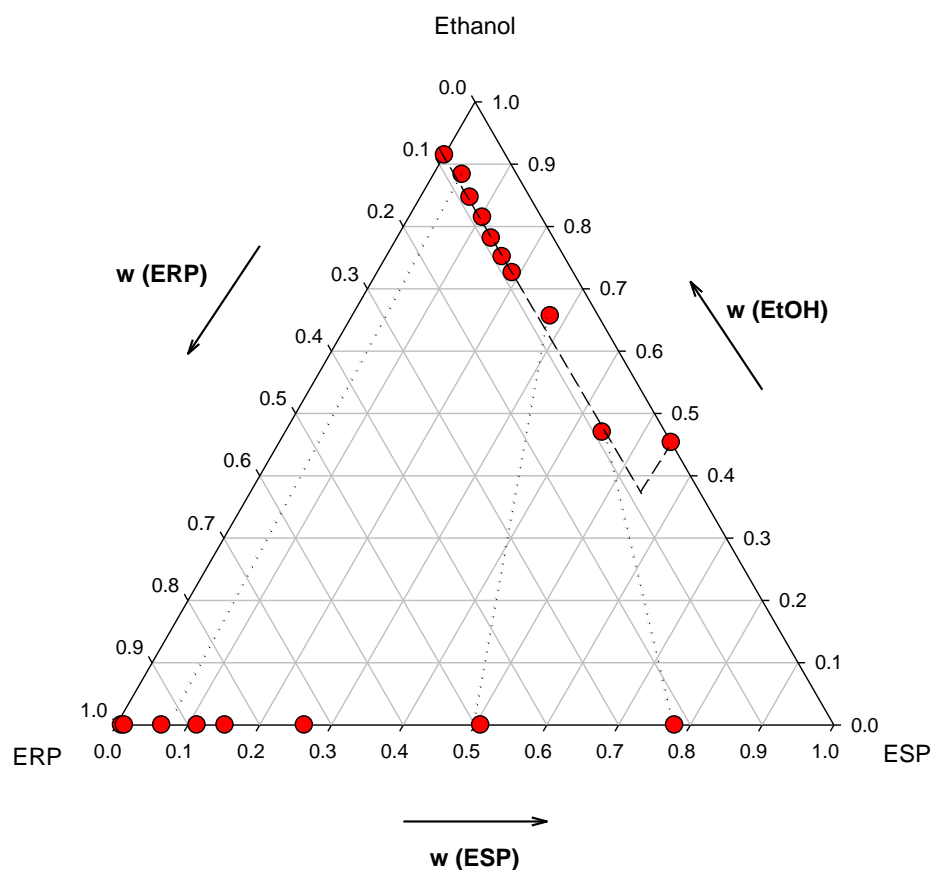


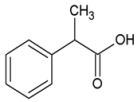
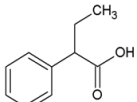
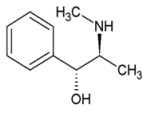
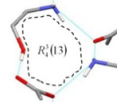
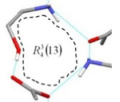
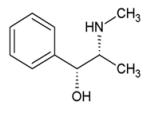
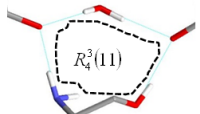
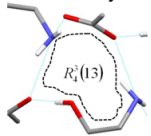
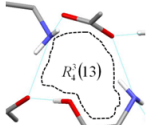
**Figure 5.34** Isothermal ternary phase diagram of ERP I° and ESP III° in ethanol measured at 30°C. The dashed line represents the liquidus line and is included as a guide to the eye. Only the dots were measured experimentally. The tie lines are displayed by the dotted lines and join the liquid phase composition with the solid phase composition. Tie lines have only been included for a few representative samples for clarity. Compositions are given in mass fractions.

## 5.5 Conclusions

Our initial aim was to perform a systematic study to try to identify as many crystal forms for a set of closely related diastereomeric salts (see Table 5.1). The results of the crystallisation experiments are summarised in the grid shown in Table 5.10.

The crystallisation experiments have shown that all the diastereomeric salts investigated have very complicated crystallisation behaviours and are quite prone to the formation of polymorphs and solvates. Furthermore, it was difficult to obtain phase pure samples of the different polymorphs for all the diastereomeric salts investigated. One of the reasons why this might have been the case is that, as seen with the crystallisation screen of ERP and ESP, the transition temperatures between polymorphs are very close to one another and

relatively close to room temperature and so it is possible that the experiments might have been performed under conditions under which transition between different polymorphs was quite easy. However, it was also observed that once crystallised, all the polymorphs were very stable at room temperature and did not transform when stored in dry conditions at room temperature. In any case, the effect of kinetics on the crystallisation outcome becomes very important and so the outcome of the crystallisation experiments much less predictable.

|   | <br>2-Phenylpropionic Acid   | <br>2-Phenylbutyric Acid  |   |
|---|---|--|---|
| <br>(1R,2S)<br>Ephedrine             | <b>R</b><br>2 Anhydrous phases:<br>ERP I° and ERP II<br>1 Solvate: S <sub>DCM</sub><br>H-Bonding Pattern<br>in ERP I°<br> | <b>R</b><br>2 Anhydrous phases:<br>ERB I and ERB II<br>6 Solvates:<br>S <sub>DCM</sub> , S <sub>Diox</sub> , S <sub>MeCN</sub> ,<br>S <sub>THF</sub> , S <sub>tol</sub> and S <sub>Xyl</sub><br>1 Solvate: S <sub>DCM</sub><br>H-Bonding Pattern<br>in ESB I<br> |   |
| <br>(1R,2R)<br>Pseudo<br>ephedrine | <b>R</b><br>1 Anhydrous phase:<br>PRP I<br>1 Hydrate<br>H-Bonding Pattern<br>in PRP Hydrate<br>                          | <b>R</b><br>2 Anhydrous phases:<br>PSP I and PSP II<br>1 Hydrate<br>H-Bonding Pattern<br>in PSP Hydrate<br>   | <b>R</b><br>2 Anhydrous phases:<br>PRB I and PRB II<br>1 Anhydrous phase:<br>PSB I<br>1 Hydrate<br>H-Bonding Pattern<br>in PSB Hydrate<br> |

**Table 5.10** 2x4 grid summarising the crystallisation outcome for a set of closely related diastereomeric salts. The hydrogen bonding patterns found in the experimentally determined structures are shown.

Recent studies trying to understand the reason that some families of closely related molecules, such as ROY derivatives [244], barbiturates [245] and fenamates [246] tend to be highly polymorphic have looked at the role that certain structural elements, what have been termed as polymorphophores [244], have on the tendency for polymorphism [247]. A comparison of the crystal energy landscapes of the monomorphous fenamic acid and one of its highly polymorphic derivatives, tolfenamic acid showed that all low energy structures shared the same hydrogen bonding motif but differed in the packing of phenyl rings sticking

out on either side of it. The increased conformational variability that the substituents confer tolfenamic acid resulted in an increased number of possible packing arrangements and so to the observed highly polymorphic behaviour [247]. These observations might help explain why all the diastereomeric acids studied showed polymorphic behaviour. As seen in the summary of crystallisation outcomes in Table 5.10, for diastereomeric salts which share the resolving agent, the hydrogen bonding motif is usually the same. The salts therefore do not have problems forming a robust hydrogen bonding backbone between the acidic and basic ions. However, at the outside of the  $2_1$  screw axis columns that form as a result of the hydrogen bonding motif, the phenyl rings and aliphatic chains are free to rotate. The ions can therefore vary their conformation to accommodate other columns upon packing. This high degree of conformation variability in turn leads to the ability of the columns to pack in many different ways and so to the polymorphic behaviour observed. This is consistent with the results of the computational search described in Chapter 6 in which the crystal energy landscapes obtained (Figure 6.10) suggested the ability of the columns to pack in many different ways.

Another consequence of the conformational variability of the phenyl groups might be the propensity of the salts to form solvates. The similarities in the FT-IR spectra of the solvated phases and the anhydrous phases suggest that the solvent molecules do not participate in the hydrogen bonding of the ions, and therefore only occupy space that is available due to packing inefficiencies. Solvent inclusion is probably possible because the phenyl rings are able to rotate to allow space for them. In the same way, this conformation variability enables the solvent molecules to leave with relative ease, making the de-solvation process so fast. When water is included in the crystal lattice, the water molecules do participate in the hydrogen bonding. However, they do not often alter the characteristic hydrogen bonding motif that is normally adopted as exemplified by the crystal structures of the hydrate of PSP and PSB shown in Figure 5.28 and Figure 5.31. In this case, the water molecule forms an extra hydrogen bond, but the original  $R_4^3(13)$  hydrogen bonding motif still forms. Only in the case of the PRP hydrate does the water molecule dictate the hydrogen bonding motif formed (Figure 5.28).

As with Naproxen in Chapter 4, it was very difficult to obtain good quality single crystals for X-ray diffraction studies. The considerations made above for the reasons that the diastereomeric salts might form different polymorphs could also be applied to explain why it is so difficult to grow single crystals. The problems in being able to pack the characteristic  $2_1$  screw axis columns that form as a result of the hydrogen bonding might lead to the difficulties encountered in growing single crystals. In the early studies by Brianso *et al* [59, 73, 74] the difficulties of growing single crystals suitable for X-ray diffraction data were already highlighted. Other studies have also highlighted this phenomenon and have shown that generally when the single crystals do grow they are often thin needles, with crystals growing in the direction of the  $2_1$  screw axis [248]. This observation is another indication that

packing the columns together is not easy. Instead, the crystals grow by adding more molecules to the columns that have already formed. The fact that the crystals grow in this morphology makes their analysis by X-ray diffraction techniques more difficult.

Despite numerous studies looking into the resolution of chiral compounds by diastereomeric salt formation, the issue of polymorphism in this area has rarely been documented and investigated in detail. The work by Valente *et al.* [234] on the salts of Ephedrine with a range of substituted mandelic acids showed that polymorphism is quite common, and seemingly more so in the more soluble salts. This appears to be in agreement with our results where three polymorphs of ESP, the more soluble salt, were found as opposed to two polymorphs for the less soluble salt. Furthermore, the more soluble salt was found to form four solvates and one hydrate. The crystallisation experiments by Valente *et al.* were mainly performed in 95% ethanol solutions so it is not possible to say whether the most soluble salts in their studies were more prone to the formation of solvated phases.

Another objective of this work was to obtain accurate thermodynamic and relative stability data of the diastereomeric salts, to use as a comparison to the computational methods presented in Chapter 6. Although one was not able to obtain this data for all systems, the relative stability order of the different anhydrous phases of ERP and ESP was identified. Thermodynamic and solubility data for the most stable phases of ERP and ESP was also obtained. This provides valuable data for assessing computational approaches for calculating relative stabilities.

Finally, our study has shown the importance of obtaining an isothermal ternary phase diagram of the diastereomeric salts in a solvent in order to assess the resolution ability of the resolving agent. Had one relied on the estimation of the resolution ability using the thermal methods described in Chapter 1 section 1.6.2.4, i.e. by constructing a binary phase diagram from the melting points and heats of fusion of the two most stable phases and using the Schröder-van Laar equation, one would have predicted the resolution to be very effective, since the composition of the eutectic would have been calculated to be close to the least stable phase, and would have missed the formation of solid solutions. In the work of Valente *et al.* [234] the resolution ability of ephedrine was assessed by performing crystallisations from 1:1 mixtures of the two diastereomeric salts in 95% ethanol stagnant solutions, and analysing the first crystals produced. Since the process was not run to a thermodynamic equilibrium, and only a few crystals were analysed, it is not possible to establish whether the formation of solid solutions might happen and if so whether a resolution process might have been feasible for the systems under investigation.

## 5.6 Appendix

### 5.6.1 ERP and ESP Solubility screen

The solubility of ERP and ESP was quickly assessed as described in section 5.3.2 in all the different solvents used in the crystallisation screen. The results of the solubility test are summarised below in Table 5.11.

| Solvent            | Solubility     |                |
|--------------------|----------------|----------------|
|                    | ERP            | ESP            |
| Methanol           | Very Soluble   | Very Soluble   |
| Ethanol            | Very Soluble   | Very Soluble   |
| Isopropanol        | Very Soluble   | Very Soluble   |
| 2-Butanol          | Very Soluble   | Very Soluble   |
| Water              | Very Soluble   | Very Soluble   |
| Ethyl Acetate      | Soluble        | Very Soluble   |
| Diethyl ether      | Hardly Soluble | Soluble        |
| Diisopropyl ether  | Hardly Soluble | Hardly Soluble |
| Dibutyl ether      | Hardly Soluble | Hardly Soluble |
| Methyl butyl ether | Hardly Soluble | Hardly Soluble |
| Dichloromethane    | Soluble        | Very Soluble   |
| Dichloroethane     | Soluble        | Very Soluble   |
| Toluene            | Hardly Soluble | Soluble        |
| Xylene             | Hardly Soluble | Hardly Soluble |
| Dioxane            | Soluble        | Soluble        |
| Tetrahydrofuran    | Soluble        | Very Soluble   |
| Hexane             | Hardly Soluble | Hardly Soluble |
| Pentane            | Hardly Soluble | Hardly Soluble |
| Acetonitrile       | Soluble        | Very Soluble   |
| Dimethylsulphoxide | Soluble        | Very Soluble   |

**Table 5.11** Rough assessment of the solubility of the diastereomeric salt pair in the 20 solvents used in the crystallisation screen. The different categories were defined as either very soluble (>100mg/ml), soluble (20 > x > 4mg/ml) or hardly soluble (<3 mg/ml).

## 5.6.2 ESP Crystallisation Screen Summary

The results of the crystallisation screen presented in section 5.3.2 are summarised in Table 5.12 and Table 5.13 below.

| Solvent            | Evaporation Experiments         | Cooling Experiments  | Solvent Assisted Grinding |
|--------------------|---------------------------------|----------------------|---------------------------|
|                    | Form                            | Form                 | Form                      |
| Methanol           | Hydrate                         | Oil                  | ESP I                     |
| Ethanol            | ESP I and ESP II                | ESP I and ESP II     | ESP I                     |
| Isopropanol        | ESP I and ESP II                | Oil                  | ESP I                     |
| 2-Butanol          | ESP I and ESP II                | Oil                  | ESP I                     |
| Water              | Hydrate                         | Hydrate              | Hydrate                   |
| Ethyl Acetate      | ESP II and Hydrate              | ESP II               | ESP I                     |
| Diethyl ether      | ESP I and ESP II                | ESP I and ESP II     | ESP I                     |
| Diisopropyl ether  | ESP I and ESP II                | ESP II               | ESP I                     |
| Dibutyl ether      | ESP I and ESP II                | ESP I                | ESP I                     |
| Methyl butyl ether | -                               | -                    | ESP I                     |
| Dichloromethane    | Form II and S <sub>DCM</sub>    | S <sub>DCM</sub>     | S <sub>DCM</sub>          |
| Dichloroethane     | ESP I and ESP II                | ESP II               | ESP I                     |
| Toluene            | ESP I and ESP II                | ESP I and ESP II     | ESP I                     |
| Xylene             | -                               | Hydrate              | ESP I                     |
| Dioxane            | ESP II and S <sub>Dioxane</sub> | S <sub>Dioxane</sub> | S <sub>Dioxane</sub>      |
| Tetrahydrofuran    | ESP II and S <sub>THF</sub>     | S <sub>THF</sub>     | S <sub>THF</sub>          |
| Hexane             | Hydrate                         | ESP I and ESP II     | ESP I                     |
| Pentane            | Hydrate                         | ESP I and ESP II     | ESP I                     |
| Acetonitrile       | ESP II and S <sub>MeCN</sub>    | S <sub>MeCN</sub>    | S <sub>MeCN</sub>         |
| Dimethylsulphoxide | -                               | -                    | ESP I                     |

**Table 5.12** Summary of the evaporation and cooling crystallisations.



| Solvent    | Anti-solvent       | Form             |
|------------|--------------------|------------------|
| Butan-2-ol | Diethyl Ether      | ESP I and ESP II |
| Butan-2-ol | Dibutyl Ether      | ESP I and ESP II |
| Butan-2-ol | Diisopropyl Ether  | ESP II           |
| Butan-2-ol | Methyl Butyl Ether | ESP I and ESP II |
| Toluene    | Diethyl Ether      | ESP I and ESP II |
| Toluene    | Dibutyl Ether      | ESP I and ESP II |
| Toluene    | Diisopropyl Ether  | ESP I and ESP II |
| Toluene    | Methyl Butyl Ether | ESP I and ESP II |
| DMSO       | Diethyl Ether      | ESP I and ESP II |
| DMSO       | Dibutyl Ether      | ESP I and ESP II |
| DMSO       | Diisopropyl Ether  | ESP I and ESP II |
| DMSO       | Methyl Butyl Ether | ESP I and ESP II |

**Table 5.13** Summary of the solvent diffusion experiments performed with ESP.

### 5.6.3 Crystallographic data of the Diastereomeric salts

|  | ERP I°  | ESP I   |
|--|---|---|
| <b>Formula</b>                             | C <sub>19</sub> H <sub>25</sub> NO <sub>3</sub> | C <sub>19</sub> H <sub>25</sub> NO <sub>3</sub> |
| <b>Formula weight</b>                      | 315.23  | 315.23  |
| <b>T (K)</b>                               | 150(2)  | 150(2)  |
| <b>Wavelength</b>                          | 0.71073   | 0.71073   |
| <b>Crystal Size (mm)</b>                   | 0.5x0.25x0.08                                   | 0.55x0.35x0.12                                  |
| <b>Crystal system</b>                      | monoclinic                                      | monoclinic                                      |
| <b>Space group</b>                         | P2 <sub>1</sub>                                 | P2 <sub>1</sub>                                 |
| <b>a (Å)</b>                               | 9.8471(19)                                      | 12.524(4)                                       |
| <b>b (Å)</b>                               | 5.8414(12)                                      | 5.7174(19)                                      |
| <b>c (Å)</b>                               | 14.583(3)                                       | 12.688(4)                                       |
| <b>α (°)</b>                               | 90  | 90  |
| <b>β (°)</b>                               | 91.428(3)                                       | 98.120(5)                                       |
| <b>γ (°)</b>                               | 90  | 90  |
| <b>V (Å<sup>3</sup>)</b>                   | 838.566   | 899.377   |
| <b>Z</b>                                   | 2   | 2   |
| <b>D<sub>calc</sub> (g/cm<sup>3</sup>)</b> | 1.249   | 1.165   |
| <b>μ(mm<sup>-1</sup>)</b>                  | 0.084   | 0.078   |
| <b>F(000)</b>                              | 340   | 340   |
| <b>Measured Reflections</b>                | 7097  | 7202  |
| <b>Independent Reflections</b>             | 3773  | 2250  |
| <b>Observed[ I  &gt; 2σ(I)] Reflins</b>    | 3267  | 1491  |
| <b>GOOF on F<sup>2</sup></b>               | 1.054   | 1.136   |
| <b>R<sub>1</sub> [ I  &gt; 2σ(I)]</b>      | 0.0447  | 0.0334  |
| <b>wR<sub>2</sub> [ I  &gt; 2σ(I)]</b>     | 0.1006  | 0.0789  |
| <b>R<sub>1</sub> (all data)</b>            | 0.0547  | 0.0478  |
| <b>wR<sub>2</sub> (all data)</b>           | 0.1080  | 0.0858  |

**Table 5.14** Crystallographic data for ERP I° and ESP I

|  | ESB            | PRP <sub>Hydrate</sub> | PSP             | PRB              | PSB <sub>Hydrate</sub> |
|--|----------------|------------------------|-----------------|------------------|------------------------|
| Formula                                | C20H27NO3      | C19H25NO3·H2O          | C19H20NO3·0.3O  | C20H27NO3        | C60H81N3O9·H2O         |
| Formula weight                         | 329.43         | 333.42                 | 315.35          | 329.43           | 1006.29                |
| T (K)                                  | 150(2)         | 150(2)                 | 150(2)          | 150(2)           | 150(2)                 |
| Wavelength                             | 0.68890        | 0.71073                | 0.71073         | 0.71073          | 0.71073                |
| Crystal Size (mm)                      | 0.17x0.09x0.05 | 0.3 x 0.07 x 0.01      | 0.5 x 0.5 x 0.1 | 0.5 x 0.1 x 0.02 | 0.45 x 0.3 x 0.03      |
| Crystal system                         | Monoclinic     | Monoclinic             | Orthorhombic    | Monoclinic       | Orthorhombic           |
| Space group                            | <i>P21</i>     | <i>C2</i>              | <i>P212121</i>  | <i>P21</i>       | <i>P212121</i>         |
| a (Å)                                  | 12.4638(9)     | 18.272(8)              | 6.9611(6)       | 9.9461(15)       | 14.1840(11)            |
| b (Å)                                  | 5.9764(4)      | 6.771(3)               | 13.7309(12)     | 7.0829(10)       | 19.5458(15)            |
| c (Å)                                  | 25.0708(18)    | 17.008(7)              | 19.2387(16)     | 13.495(2)        | 20.6900(16)            |
| α (°)                                  | 90.00          | 90                     | 90              | 90               | 90                     |
| β (°)                                  | 101.369(5)     | 117.556(4)             | 90              | 96.774(3)        | 90                     |
| γ (°)                                  | 90.00          | 90                     | 90              | 90               | 90                     |
| V (Å <sup>3</sup> )                    | 1830.8(2)      | 1865.6(14)             | 1838.9(3)       | 944.1(2)         | 5736.7(8)              |
| Z                                      | 4              | 4                      | 4               | 2                | 4                      |
| D <sub>calc</sub> (g/cm <sup>3</sup> ) | 1.195          | 1.187                  | 1.138           | 1.159            | 1.165                  |
| μ (mm <sup>-1</sup> )                  | 0.080          | 0.049                  | 0.078           | 0.077            | 0.078                  |
| F(000)                                 | 712            | 720                    | 669             | 356              | 2176                   |
| Measured Reflections                   | 25502          | 12132                  | 15453           | 8170             | 49592                  |
| Independent Reflections                | 6996           | 3402                   | 2556            | 4364             | 7657                   |
| Obs [ I  > 2σ(I)] Reflections          | 5512           | 2859                   | 2247            | 3132             | 5480                   |
| GOOF on F <sub>2</sub>                 | 1.150          | 0.977                  | 1.077           | 0.989            | 1.034                  |
| R1 [ I  > 2σ(I)]                       | 0.0599         | 0.0375                 | 0.0590          | 0.0523           | 0.0509                 |
| wR2 [ I  > 2σ(I)]                      | 0.1539         | 0.827                  | 0.1700          | 0.1238           | 0.1301                 |
| R1 (all data)                          | 0.0822         | 0.0442                 | 0.0659          | 0.0829           | 0.0799                 |
| wR2 (all data)                         | 0.1626         | 0.0861                 | 0.1787          | 0.1585           | 0.1445                 |

**Table 5.15** Crystallographic Data for ESB, PRP<sub>Hydrate</sub>, PSP, PRB and PSB<sub>Hydrate</sub>

# Chapter 6 Computational Investigation of the Resolution Efficiency of Ephedrine with (R/S)2-Phenylpropionic acid

## 6.1 Introduction

The idea that the resolution efficiency in a classical resolution experiment can be predicted by calculating the differences in the lattice energies of the two diastereomeric salts was first presented by Leusen et al [56], on the theoretical basis presented in Chapter 1, section 1.6.4. Assuming that the acid and base ions are fully solvated it can be shown that the solubility ratio of the two diastereomeric salts is related to their free energy difference. The computational prediction of the free energy difference is however, very demanding. If one assumes that the entropies of the two diastereomers as well as the zero-point energy and specific heats are very similar, the solubility ratio can be estimated by comparing the diastereomers' static lattice energies, which is amenable to theoretical predictions [85, 86].

Although in theory the difference in the static lattice energy of the diastereomeric salts might be able to help predict the resolution efficiency of a given resolving agent, it is still necessary to test whether the assumptions made in the process hold. Furthermore, one needs to validate the methods used to compute the lattice energies, to understand whether the approximations and assumptions on which the algorithms rely are suitable or not. In order to do so, one needs to have good structural and thermodynamic data against which to validate ones results. The work presented in this chapter investigates the ability of a computational methodology to predict the relative stability of all the experimentally determined solid phases of the diastereomeric salt pair formed between ephedrine and 2-phenylpropionic acid found during the extensive crystallisation screen presented in Chapter 5.

The computational modelling method used in this study splits the lattice energy into intra-molecular and intermolecular energy contributions,  $\Delta E_{intra}$  and  $U_{inter}$  respectively:

$$E_{latt} = U_{inter} + \Delta E_{intra} \quad 6.1$$

Here  $\Delta E_{intra}$  is the energy required to deform the molecule from the lowest energy conformation of the isolated molecule in the gas phase, so as to improve intermolecular contacts.

## 6.2 Molecular Conformation Analysis

If one ignores methyl rotations, ephedrine and 2-phenylpropionic acid have 6 flexible torsion angles between the two, as shown in Figure 6.1. Some regions in the conformational space are so energetically unfavourable that despite possible improvements in intermolecular contacts they are highly improbable in the solid state. Therefore, the range where the flexible torsion angles are energetically feasible must be delimited. In order to do so, an analysis of the Cambridge Structural Database (CSD) on both ions was performed together with *ab initio* intra-molecular energy scans of the different flexible torsion angles. The CSD search fragments did not include the proton positions and so both neutral molecules and ions were included.

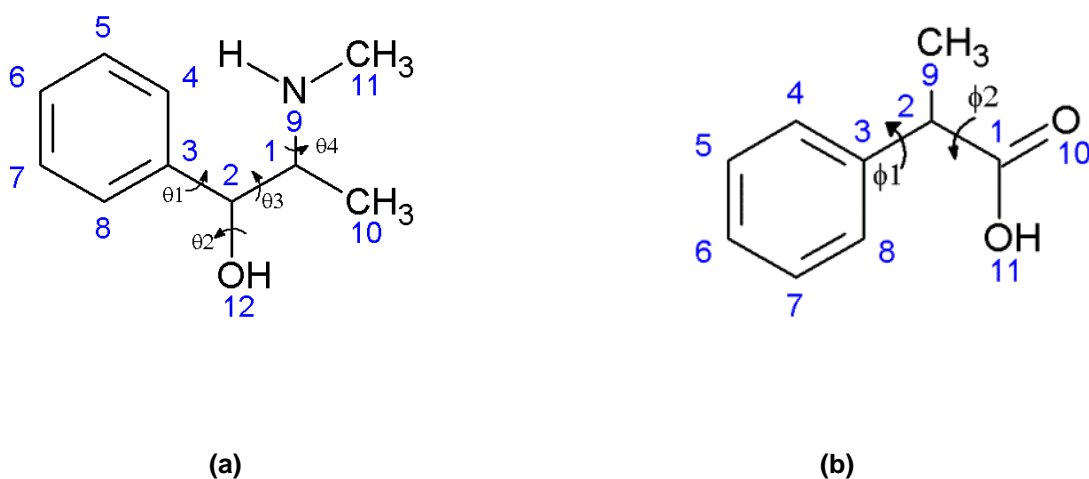


**Figure 6.1.** Flexible torsion angles considered in the search for (a) (1R,2S)-Ephedrine and (b) 2-phenylpropionic acid. The torsion angles in ephedrine were defined as  $\theta_1 = \text{C1-C2-C3-C4}$ ,  $\theta_2 = \text{H-O12-C2-C1}$ ,  $\theta_3 = \text{N9-C1-C2-C3}$  and  $\theta_4 = \text{C1-N9-C1-C2}$ . For 2-phenylpropionic acid the torsion angles in were defined as  $\phi_1 = \text{C9-C2-C3-C4}$  and  $\phi_2 = \text{O11-C1-C2-C3}$ .

### 6.2.1 Analysis of experimental structures containing ephedrine and 2-phenylpropionic acid

ConQuest [180] was used to search through the Cambridge Structural Database (CSD, Version 5.31, November 2009) for structures that contained either ephedrine or 2-phenylpropionic acid in the asymmetric unit and whose coordinates were fully determined with no disorder and with R-factors of less than 10%. The query for ephedrine was built using the ephedrine backbone, allowing for any substituents on the phenyl ring, and specifying the chirality at both centres so as to include both possible enantiomers of

ephedrine (i.e. 1R, 2S and 1S,2R) but to exclude pseudoephedrine enantiomers (i.e. 1R,2R and 1S,2S). The search on 2-phenylpropionic acid also allowed substituents on the phenyl group and included both enantiomers. The CSD search fragments did not include the proton positions and so both neutral molecules and ions were included. In total 55 experimental structures containing ephedrine and 62 that contained 2-phenylpropionic acid were found that met these criteria. The results of the CSD search are summarised in Figure 6.2 for ephedrine and Figure 6.4 for 2-phenylpropionic acid.

## 6.2.2 Conformational analysis using *ab initio* methods

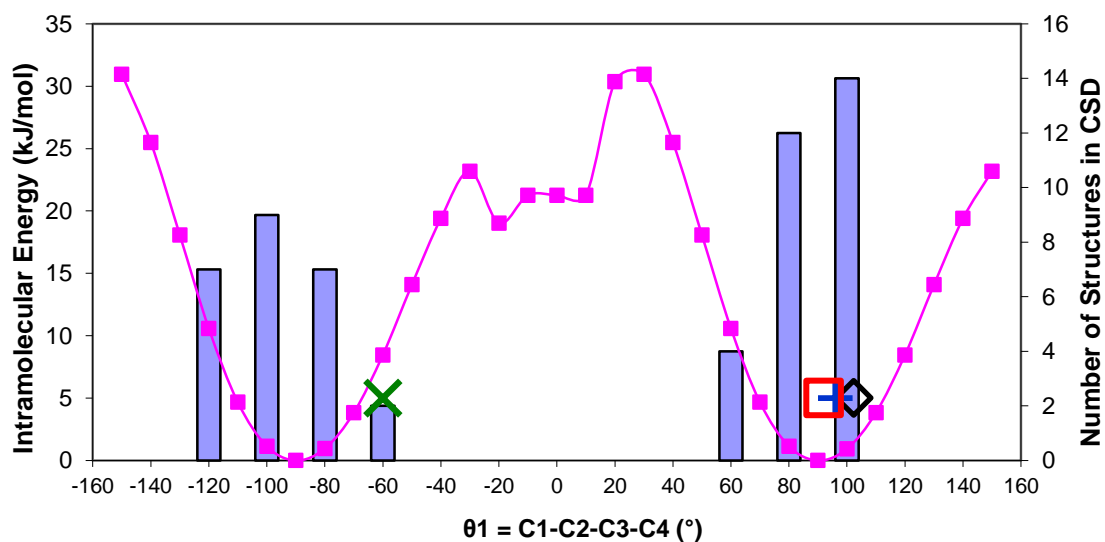
Scans around the flexible torsion angles defined in Figure 6.1 were performed using GAUSSIAN, employing the HF method at the 6-31G(d,p) level of theory. For ephedrine, all the identified flexible torsion angles except  $\theta_1$  were scanned around  $360^\circ$  in  $20^\circ$  steps.  $\theta_1$  was only scanned through  $180^\circ$  due to the symmetry of the phenyl ring. At each  $20^\circ$  step, the intra-molecular energies of the molecules were computed, fixing the value of the torsion angle being scanned but allowing the rest of the flexible degrees of freedom to relax. The extended conformation of ephedrine was used as a starting point for all the torsional angle scans. Scans for  $\theta_2$  were also performed using the folded conformation as the starting point to see whether this would affect the intra-molecular energies for rotating the hydroxyl group in this conformation. For 2-phenylpropionic acid a 2D scan in which both  $\Phi_1$  and  $\Phi_2$  were varied in  $10^\circ$  steps was performed. Due to symmetry relations, the scan was confined to the region between 0 to  $180^\circ$ .

## 6.2.3 Results of the Molecular Conformational Analysis of Ephedrine

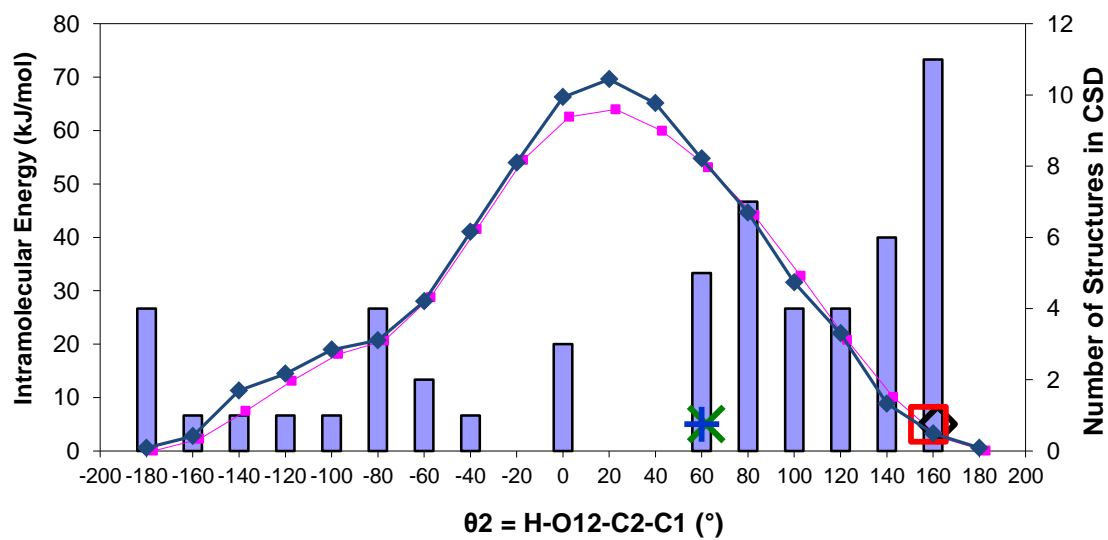
The results of the scans around the flexible torsion angles of ephedrine, together with the analysis of the CSD are summarised in Figure 6.2. The results of the CSD analysis are represented as bar charts, showing the number of structures in the CSD within  $15^\circ$  of the marked value for the torsion angle under investigation. The values for the intra-molecular energy of the ephedrine molecule as the torsion angles are varied are represented by the line graphs.

As Figure 6.2 shows, the conformations of ephedrine found in experimental structures deposited in the CSD generally correspond to the wells in the intra-molecular energy surface for all torsion angles except  $\theta_2$ . One would expect this to be so [249], as the most energetically feasible conformations of molecules in isolation would also be likely to be those found in solution and to be integrated into the crystal lattice. Furthermore, the molecule

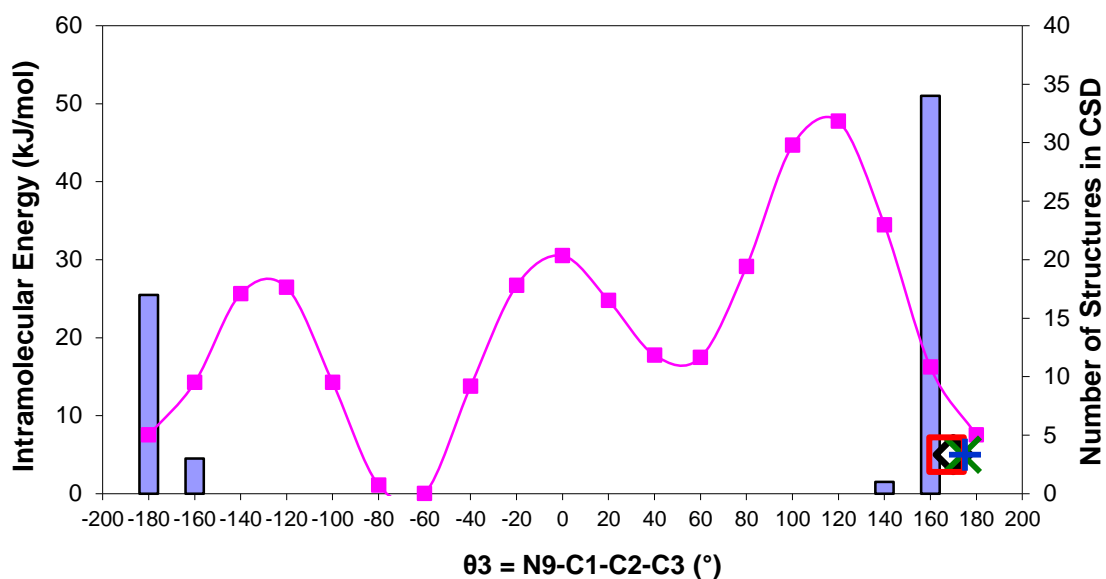
would only adopt a high energy conformation if the gain in the intermolecular energy contribution would balance the loss from the intra-molecular energy,  $\Delta E_{intra}$ .



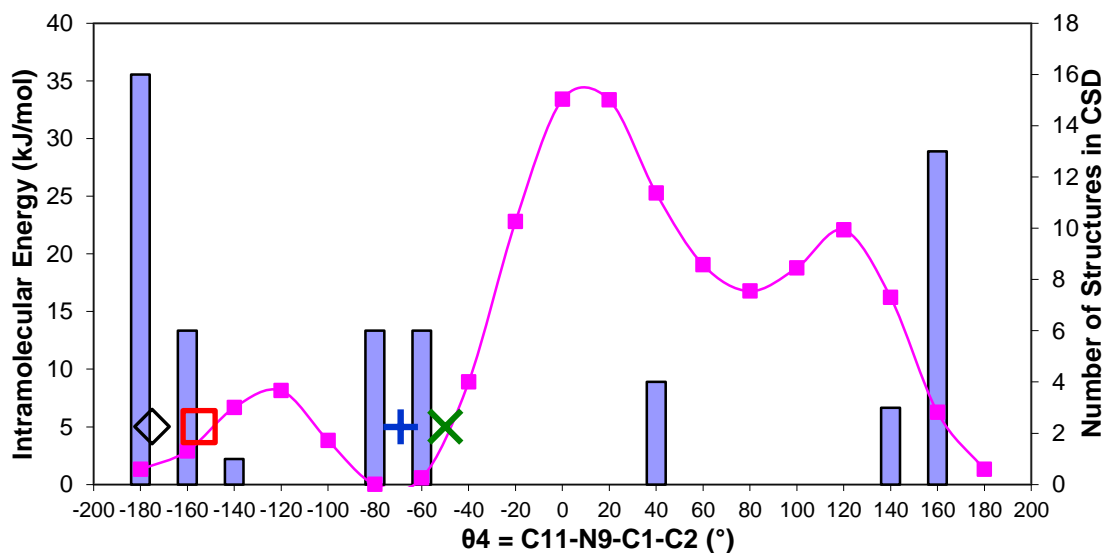
(a)



(b)



(c)



(d)

**Figure 6.2** CSD searches and 1D potential energy surface scans for ephedrine with respect to (a)  $\theta_1$  (b)  $\theta_2$  (extended conformation in pink and folded conformation in blue) (c)  $\theta_3$  (d)  $\theta_4$ , at the HF level of theory with the 6-31G(d,p) basis set. The values of the torsion angles found in the experimental crystal structures of ephedrine-2-phenylpropionate salts are indicated in the graphs by the squares and crosses. The extended conformations of ephedrine are represented by the squares (  $\diamond$  ERP  $\square$  ESP III) whereas the crosses represent the folded conformation (  $\times$  - ESP I  $+$  - ESP II).



Molecular beam Fourier transform microwave spectroscopic studies have shown that neutral ephedrine can adopt three distinct conformations in the gas phase [250]. However, studies in which the crystal structures and packing arrangements of a set of ephedrine salts were investigated [60, 236, 241] showed that ephedrine adopts two distinct conformations under crystal packing forces, extended and folded, which mainly vary in the value of  $\theta_4$ . These two conformations are well represented in the CSD as can be clearly seen from Figure 6.2 (d), and are also present in the crystal structures of ephedrine 2-phenylpropionate determined in this study in Chapter 5. ERP I° and ESP III°, the thermodynamically stable phases at room temperature, contain the extended conformation of ephedrine, whereas ESP I and ESP II adopt the folded conformation. The gas-phase conformations of neutral ephedrine found in the study by Alonso et al. [250] correspond to the folded and extended conformations in the crystal structures of the salts (AGa and AGb in [250] respectively), plus another conformation, GGa which corresponds to the low energy conformation with  $\theta_3 \sim -70^\circ$  identified in Figure 6.2 (c). The difference between the neutral and ionic ephedrine is the additional proton on the nitrogen. In the neutral molecule the hydroxyl group forms a hydrogen bond to the nitrogen stabilising all three observed conformations [250]. In the ion the  $N^+ - H$  “hydrogen bonds” to the hydroxyl oxygen in the extended and folded conformation. This, however, is not possible when the ion is in the conformation equivalent to GGa for the neutral molecule conformation. The similarities between the  $N^+ - H \cdots O$  and  $O - H \cdots N$  hydrogen bonds in stabilising the ephedrine ion and neutral molecule respectively explains why the extended and folded conformations are observed in crystal structures of salts and neutral.

The distinction between the salt and the neutral ephedrine is clearest in  $\theta_2$  which defines the position of the hydroxyl hydrogen. For neutrals the hydrogen is close to 0, to hydrogen bond to the Nitrogen, whereas in salts this area is occupied by the  $N^+ - H$  proton and is therefore high in energy in the salts. In the isolated ephedrine ion Figure 6.2 (b) the hydroxyl is most favourable pointing away from the nitrogen and shows a wide range of low energy conformations where it can form an intermolecular hydrogen bond. On the other hand, the values of  $\theta_2$  adopted in experimental structures do not seem to cluster so tightly around the intra-molecular minima, as shown in Figure 6.2 (b), but rather adopt a wide range of values, often with relatively high intra-molecular energies.  $\theta_2$  defines the position of the hydroxyl hydrogen which is crucial in the hydrogen bonding ability of ephedrine. The position of the hydroxyl hydrogen will therefore also have a significant effect on the intermolecular energy. This highlights how important it is that the computational models manage to get the right balance between the intra and inter molecular energies, especially for flexible molecules with hydrogen bonding donors and acceptors.

Although the extended conformation is the most frequently occurring conformation in crystals, according to the intra-molecular energy scan the folded conformation is slightly

more stable. Furthermore, NMR studies also found the folded conformation to be the preferred ephedrine conformation in solution [60, 251, 251]. This is due to the ability to form an intra-molecular hydrogen bond between the hydroxyl oxygen and the hydrogen atoms on the amine. The intra-molecular hydrogen bond requires  $\theta_2 \sim 180$  and  $\theta_4 \sim 70$ . Our scan in Figure 6.2 (d) suggests that the energy barrier between the extended and folded conformers is no more than 8.13 kJ/mol for the isolated ion, slightly more than the 4.19 kJ/mol energy difference previously reported [236]. Nevertheless, this energy barrier could be overcome during nucleation and crystal growth. Indeed the scan of  $\theta_2$  for varying the hydroxyl torsion angle shows that there are many structures without the internal hydrogen bond, where  $\theta_2$  is far from  $180^\circ$ , with a high intra-molecular energy penalty, that is presumably compensated for by better intermolecular hydrogen bonding. None of our crystal structures and only one of Davey's [241] have the intra-molecular hydrogen bond.

The folded conformation adopted in ESP I and ESP II is nevertheless different to that identified in previous studies, and much more unstable. The torsion angle defining the hydroxyl hydrogen is in a high energy region, its position preventing the formation of the intra-molecular hydrogen bond. Two *ab initio* conformation scans for  $\theta_2$  were performed, one in which the ephedrine molecule was set to the extended conformation and the second in which it was set in the folded conformation, to see whether being in the folded conformation made the rotation of the hydroxyl group more energetically feasible. As shown in Figure 6.2 (b) this is not the case. The folded conformations in our experimental structures are higher in intra-molecular energy ( $\Delta E_{intra}$ ).

The conformational analysis for ephedrine seems to suggest that there is large range of conformations that ephedrine can adopt. There is considerable sensitivity of the energy to  $\theta_2$ , the hydroxyl hydrogen involved in hydrogen bonding. This in turn leads to a huge range in  $\Delta E_{intra}$  values, which poses a problem for computational calculations since they would be very sensitive to the quality of the wavefunction used.

#### 6.2.4 Results of the Conformational Analysis of 2-Phenylpropionic Acid

The results of the conformational scan for 2-phenylpropionic acid show that the range of torsion angles that the phenyl and carboxylic acid can adopt in 2-phenylpropionic is quite wide and strongly correlated, with two low energy minima (Figure 6.3). The conformation of the acid in ESP III is in a different minimum compared to the other structures. If the phenyl torsion ( $\Phi_1$ ) is within  $-110^\circ$  to  $-50^\circ$  (or equivalently  $50^\circ$  to  $110^\circ$ ) range, the intra-molecular energy for the full rotation of the carboxylic acid ( $\Phi_2$ ) does not exceed 10 kJ/mol at any point. There is a local minimum for  $\Phi_1 \sim -10$  and  $\Phi_2 \sim -70$  deg. The conformations of 2-phenylpropionic in the structures determined in this study are not the most stable

conformations. Nevertheless the energy penalty that has to be paid in order to distort them from their most stable conformation is only about 10kJ/mol, much less than the energies involved in the deformation of ephedrine from their optimum conformation.

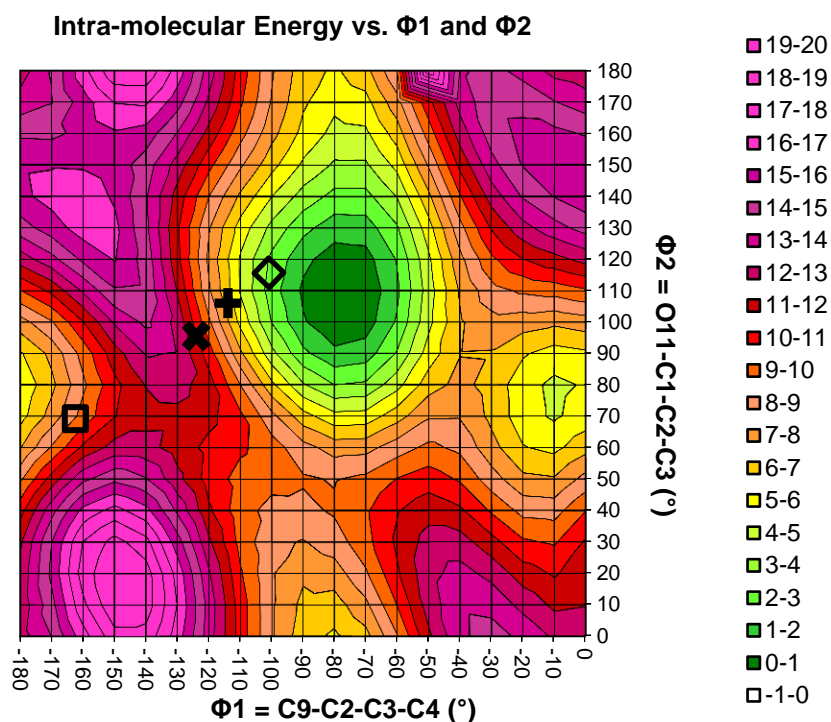
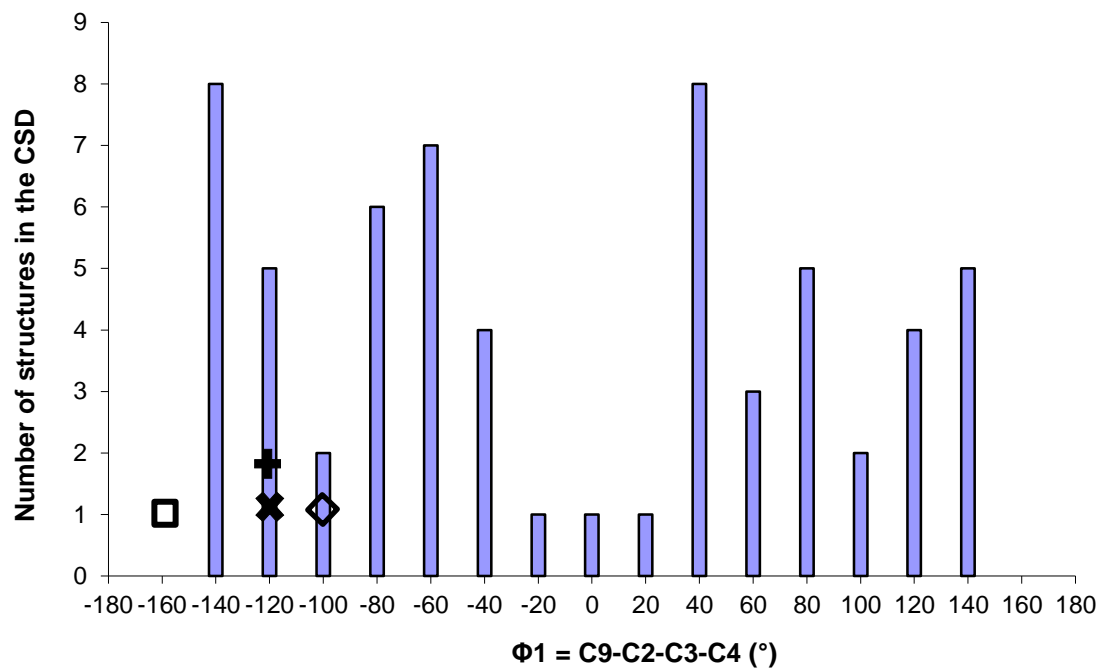
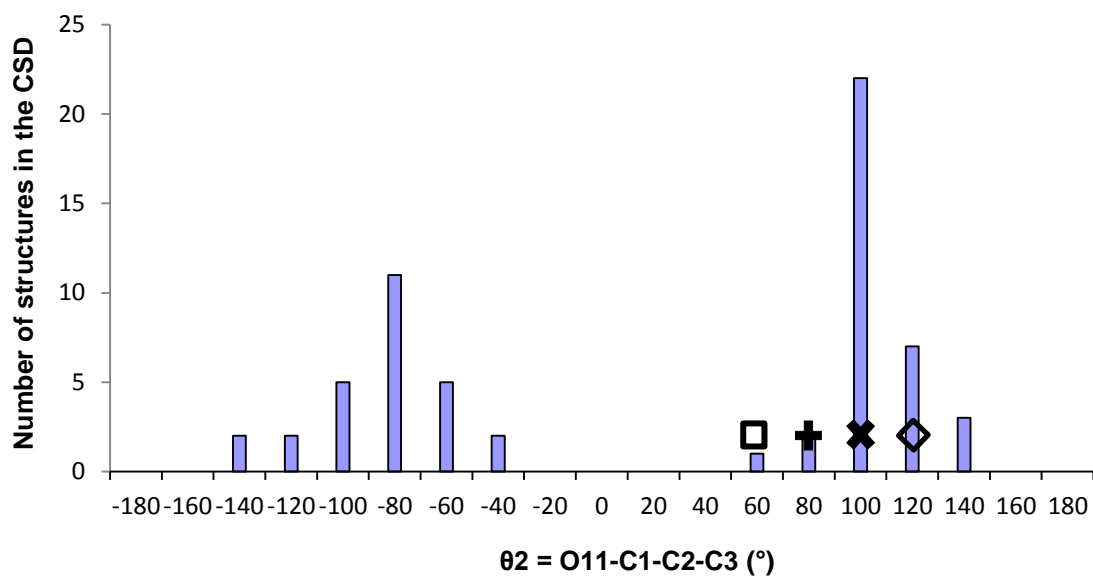


**Figure 6.3** Potential energy surface scan for 2-phenylpropionate ion with respect to  $\theta_1$  and  $\theta_2$  at the HF level of theory with the 6-31G(d,p) basis set. The experimental conformation found in the diastereomeric salts are represented by  $\diamond$  for ERF  $\square$  for ESP III  $\times$  for ESPI and  $+$  for ESP II.



(a)



(b)

**Figure 6.4** CSD searches for 2-phenylpropionic acid for (a)  $\theta_1$  and (b)  $\theta_2$ . The values of the dihedral angles in the experimental structures are represented by  $\diamond$  for ERP  $\times$  for ESP I  $+$  for ESP II and  $\square$  for ESP III°.

The experimental values for  $\Phi_1$  and  $\Phi_2$  retrieved from the CSD show the wide range of conformations that 2-phenylpropionic acid molecule can adopt (Figure 6.4). The phenyl

rotation shows more variability whereas the carboxylic acid rotation values tend to cluster around the minima in the intra-molecular energy surface.

## 6.3 Intermolecular Energy

The intermolecular energy model,  $U_{inter}$ , takes into account repulsion-dispersion and electrostatic contributions [88]. The electrostatic energy is commonly modelled, including in CrystalPredictor [121], using Coulomb's law and an atomic point charge representation of the molecular charge distribution:

$$U_{elec}^{MN} = \sum_{i \in M, k \in N} \frac{1}{4\pi\epsilon_0} \frac{q_i q_k}{R_{ik}} \quad 6.2$$

where  $\epsilon_0$  is the vacuum permittivity constant, also known as the dielectric constant. In this form, the electrostatic interaction energy,  $U_{elec}^{MN}$ , between two atoms,  $i$  and  $k$  that are in molecule  $M$  and  $N$  respectively, depends only on the distance between the atoms,  $R_{ik}$  and their respective charges,  $q_i$  and  $q_k$ . The charges are usually derived by fitting them to the electrostatic potential on a grid of points around the molecule, as calculated from the *ab initio* wavefunction.

A better representation of the electron distribution is a distributed multipole model [88, 99, 100], in which the electron density is described by a series of multipole moments (i.e. charge, dipole, quadrupole, etc. up to the hexadecapole) that are centred at the atomic nuclei, and is the method used to represent the charge density in the algorithm used in this section. The multipoles are derived from the isolated molecule wavefunction [99, 100].

The repulsion-dispersion interactions on the other hand are modelled using an empirically derived repulsion-dispersion potential based on the Buckingham *exp-6* function, where the potential parameters can be assumed to be the same for similar atoms:

$$U_{rep-disp}^{MN} = \sum_{i \in M, k \in N} A_{i\kappa} \exp(-B_{i\kappa} R_{ik}) - \frac{C_{i\kappa}}{R_{ik}^6} \quad 6.3$$

where the interactions are between atom  $i$  of type  $\iota$  in molecule  $M$  and atom  $k$  of type  $\kappa$  in molecule  $N$  separated by a distance  $R_{ik}$ . The exponential term represents the repulsion occurring at short distances whereas the negative  $R^{-6}$  term deals with the long range dispersion contributions. The empirical atom-atom parameters ( $A_{i\kappa}$ ,  $B_{i\kappa}$ ,  $C_{i\kappa}$ ) are obtained by fitting to different crystal structures of organic molecules and some of their heats of sublimation. In using this model it is assumed that the empirical atom-atom parameters are

transferable between different molecules. This is reasonable in situations where the functional groups present in the molecules to be modelled are the same as those found in the molecules to which the Buckingham potential was parameterised against. The parameters used in this thesis were derived by Williams et al [107] who started by fitting C, H and N parameters to a set of azahydrocarbon crystal structures and subsequently fitted for the parameters for other elements such as oxygen [108], nitrogen, fluorine [110] and chlorine [111] by considering structures containing only three atomic types. These parameters were found adequate, when combined with new parameters for polar protons and a distributed multipole electrostatic model [252] and are listed in the FIT force field [182]. The WILL force field was also tested in this thesis, and contains parameters of C, H, N and O which depend on the hybridisation state and atomic connectivity [253].

### 6.3.1 Choice of Repulsion-Dispersion Potential

The two dispersion-repulsion intermolecular potentials described above, FIT and WILL [181], were tested so as to assess which one would better reproduce the experimental crystal structures. Rigid-body lattice energy minimisations using DMACRYS [182] using the molecular conformations of the experimental structures with the bond lengths to hydrogen corrected to eliminate the systematic error in X-ray structures, were performed with both potentials. A distributed multipole analysis [99] of the charge density computed at the MP2/6-31G(d,p) level of theory was used to calculate the electrostatic contribution to the intermolecular energy.

The indicators used to assess which repulsion-dispersion potential would be more suitable were the changes in the unit cell parameters following the lattice energy minimisation, the root mean square deviation ( $\text{RMSD}_{15}$ ) for overlaying 15 molecules in the experimental and the lattice energy minimised structure, and the deviation in the intermolecular contact distances between oxygen and nitrogen involved in hydrogen bonding, as depicted in Figure 6.5.

The results of the rigid-body lattice energy minimisations using the experimentally observed molecular conformations were quite similar for both potentials (Table 6.1 in the Appendix at the end of the Chapter). Nevertheless, WILL potential consistently underestimated the O...O distances for all the experimental structures. Day also observed unreasonably short oxygen-oxygen intermolecular distances when using the carboxylic acid H(3) potential – as implemented in the WILL force field [254] – to co-crystal XV (aminopyridimidine:otoluic acid) in conjunction with distributed multipoles in the fourth international blind test of crystal structure prediction [185]. Furthermore, it has also been previously shown that in some occasions the WILL force field seriously underestimates O...N distances [255], although this wasn't observed in our calculations. Overall, the FIT force field was considered to be more

suitable for the lattice energy minimisations, and therefore was used in all lattice energy minimisations performed with CrystalOptimizer [122].

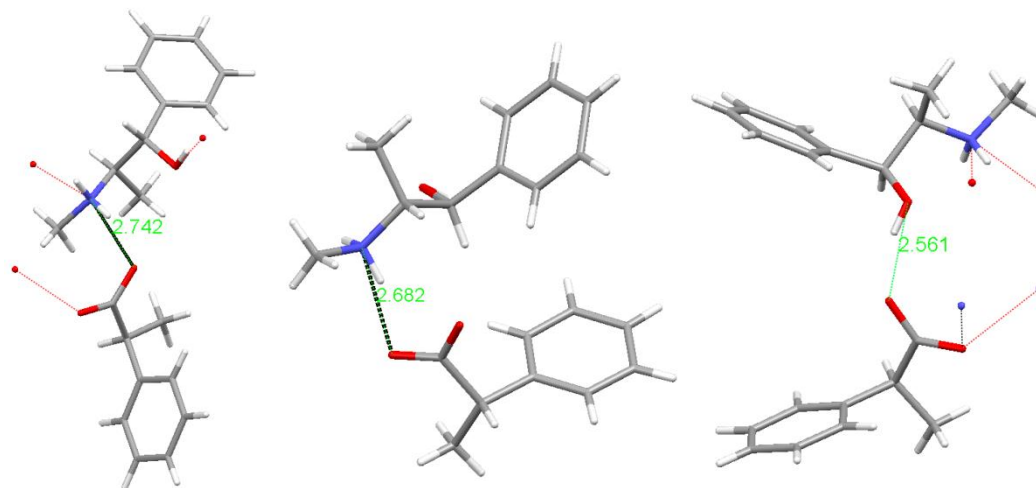


**Figure 6.5** The intermolecular distances used to guide the choice of intermolecular potential. The specific illustration is for the ExminExp structure of ERP I°, showing the extended conformation.

It is notable that the two different repulsion-dispersion models give very different estimates of the intermolecular contribution to the lattice energy ( $U_{inter}$ ), which will be comparable to the differences in  $E_{latt}$  since the conformational energy differences,  $\Delta E_{intra}$ , are the same for both models for a given crystal structure. The  $U_{inter}$  values relative to ERP I°, the most stable phase, are 0.77, 37.68, 22.83 kJ/mol for ESP I, II and III° for the FIT potential, and -3.34, 17.83 and 9.96 kJ/mol for the WILL parameterisation. Thus, even the stability order of these structures will be different for either of the two repulsion-dispersion models. The size of these energy differences call into question the use of repulsion-dispersion parameters that have been fitted to neutral molecule crystal structures.

### 6.3.2 Effect of molecular conformation on $U_{inter}$

ERP I° and ESP I, the experimental structures that had been solved by single crystal X-ray diffraction and contain the extended and folded ephedrine conformations respectively, were also used to establish the sensitivity of the lattice energy minimisations to the molecular conformation. The *ConOpt* structures were obtained by performing an *ab initio* optimisation on the isolated ions, with the six torsion angles ( $\theta_1$  to  $\theta_4$  and  $\Phi_1$  and  $\Phi_2$  in Figure 6.1)

constrained to the experimental values. The quality of the reproduction of the crystal structure, in either cell lengths or hydrogen bond lengths only deteriorated slightly, as seen in the data summarised in Table 5.2. However, despite these relatively small changes, the changes in lattice energies were huge, in the order of 25-35 kJ/mol. From the overlay of the constrained optimised molecules onto the experimental conformations (Figure 6.6), one can see that the variation in the methyl torsion angles, all bond angles and bond lengths that haven't been fixed is only very subtle. The implication that the lattice energy is so sensitive to the small changes in the other degrees of freedom is a matter for concern and implies that the structure is very sensitive to other angles and bond lengths. This is of special importance considering that the hydrogen atoms are not necessarily well located, especially in structures that have been solved by powder X-ray diffraction (note that in the experimental conformations used for Table 6.1, the hydrogen atom positions were corrected so that the bond lengths corresponded to neutron values). However, the ConOpt structures are less stable than the ExminExp structures, which is consistent with the subtle differences being mainly due to packing effects rather than experimental error. Furthermore, the fact that even small changes in the position of atoms that are not involved in hydrogen bonding have such a big effect on the intermolecular contribution to the lattice energies, highlight how crucial and difficult is to get the right balance between the intra-molecular and intermolecular energies.

The difference between the experimental ion conformations and the nearest isolated ion conformation calculated by full optimisation at HF 6-31G(d,p) level is shown in Figure 6.7. The molecular conformations in both experimental structures are fairly similar to the gas-phase optimised conformations, with the main difference being the carboxylic acid rotation ( $\Phi_2$  in Figure 6.1) in ERP I° and the hydroxyl rotation ( $\theta_2$  in Figure 6.1) in ESP I. Lattice energy minimisation on crystals in which the gas phase optimised molecular structures for the two ions were pasted into the lattice were performed, to see to what extent varying the six flexible torsion angles to the most energetically favourable conformations would affect the lattice energy. The results of these calculations are summarised in Table 5.2 in the Appendix, described as *Opt*. The variations from the experimental conformations of the ions resulted in large changes to the crystal structures, making it impossible to overlay 15 molecules. The changes to the molecular conformations affected the ions' ability to form hydrogen bonds, in effect inhibiting their formation and resulting in the breaking of some of the experimentally observed hydrogen bonds. This in turn led to a decrease in density and a great increase in the lattice energy. This confirms that the crystal structures are very sensitive to the conformation of the ions which is being affected by the intra-molecular forces.



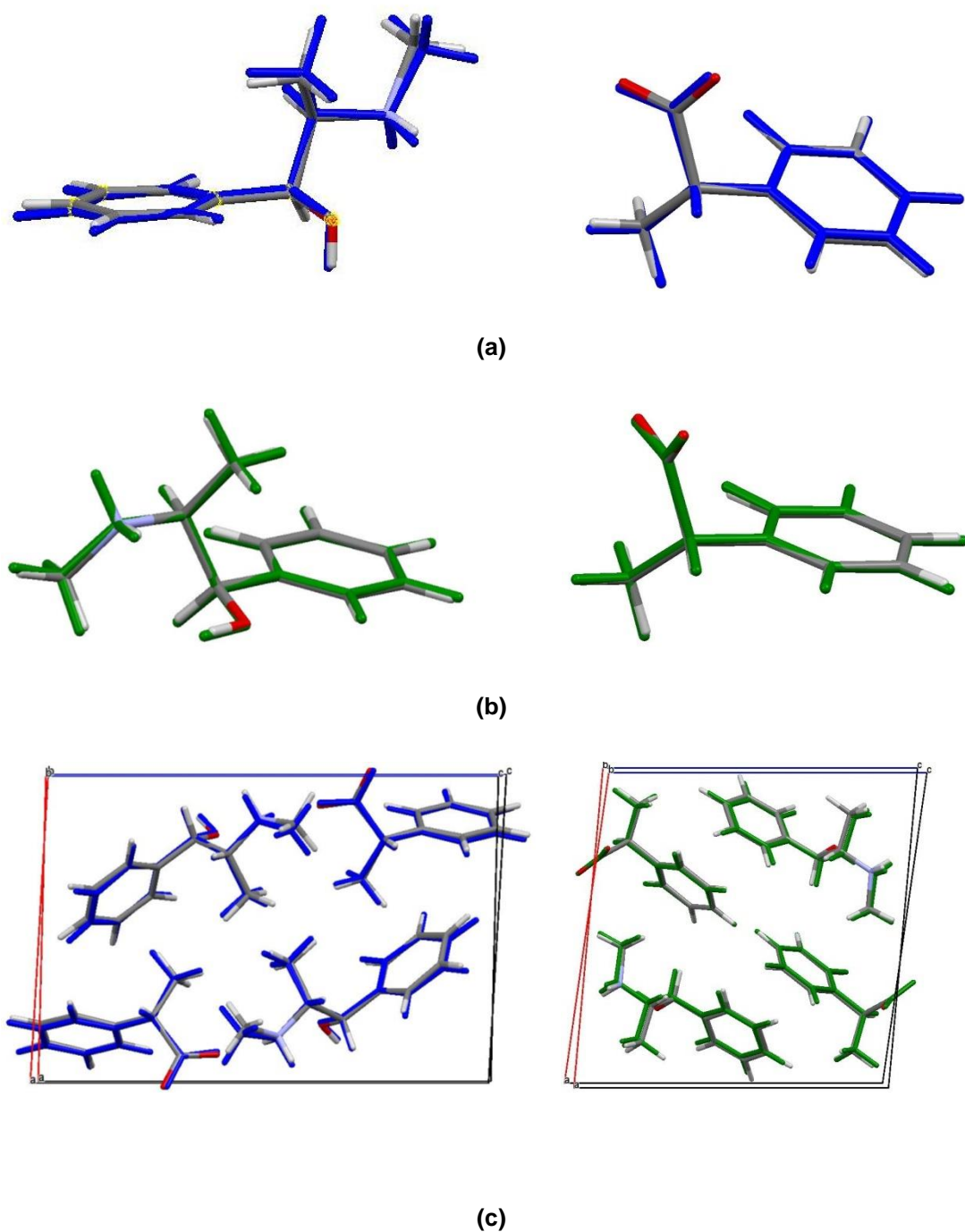


**Figure 6.6.** Overlay of the constrained optimised (ConOpt) conformations of ephedrine and 2-phenylpropionic acid for **(a)** ERP I° and **(b)** ESP I. The ions were overlaid by optimising atoms C2, C3, and C4 in ephedrine and in 2-phenylpropionic acid molecules (see Figure 6.1). The minimum RMSD<sub>15</sub> overlays of the unit cells of ERP I° (ConOpt in blue) and ESP I (ConOpt in green) with the experimental crystal structures are shown in **(c)**.

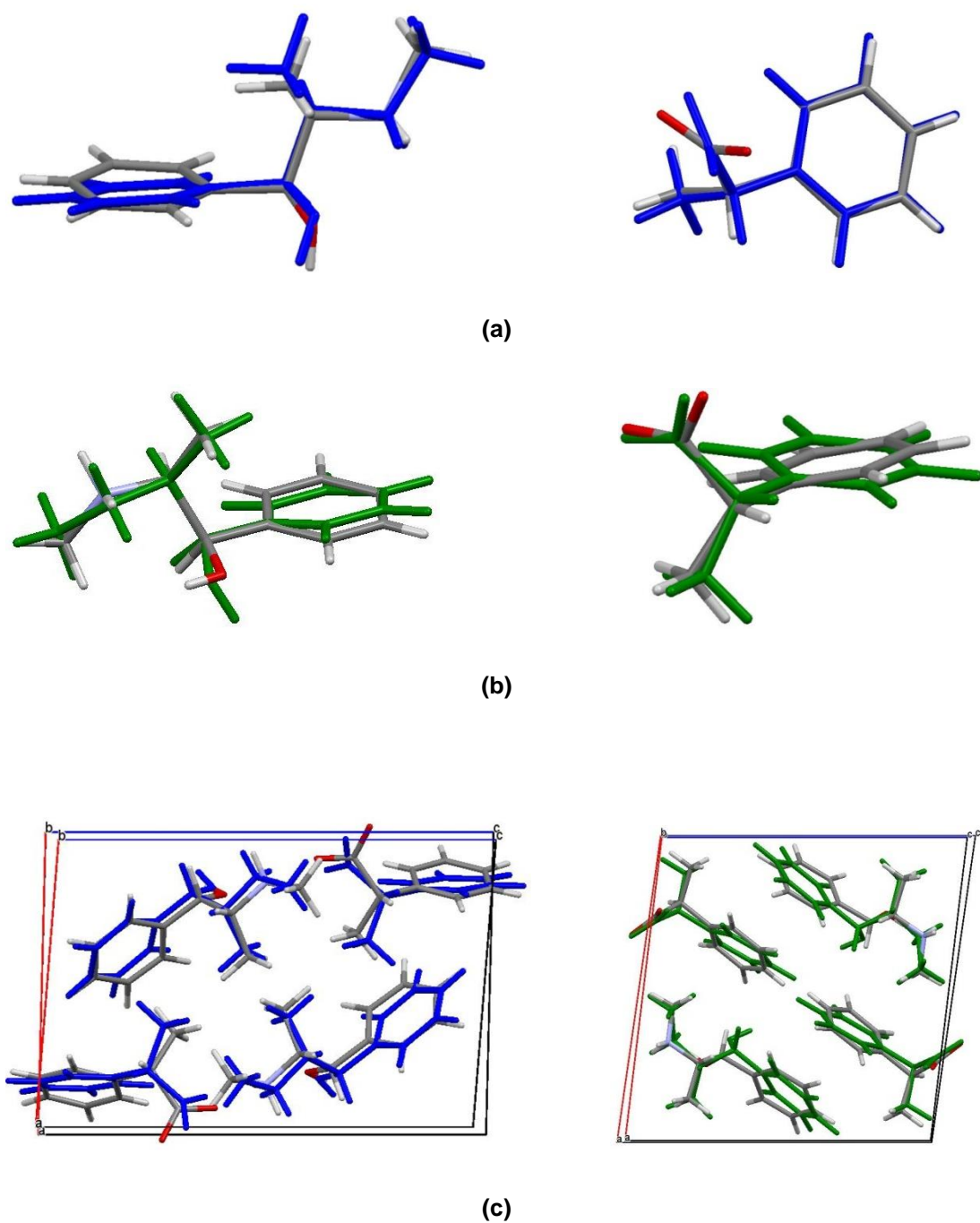


**Figure 6.7** Overlay of the fully optimised “gas-phase” conformations of ephedrine and 2-phenylpropionic acid with the **(a)** extended ephedrine conformation in ERP I° and **(b)** the folded conformation ESP I. **(c)** shows the poor reproduction of the crystal structures when these conformations are used (“Opt” in Table 6.2) for ERP I° (in blue) and ESP I (green).

## 6.4 Calculation of the Lattice Energies using CrystalOptimizer

The CrystalOptimizer algorithm [122] works by simultaneously optimising the balance between inter ( $U_{inter}$ ) and intra molecular ( $\Delta E_{intra}$ ) energies. This would involve multiple evaluations of the wavefunction which would make the computation of the lattice energy very expensive. However, CrystalOptimizer does so in a computationally efficient manner by using local approximate models (LAMs) to represent the intra-molecular energy and the conformational-dependent charge density, without losing accuracy. The main features of the algorithm were described in Chapter 1 Section 1.5.4.10. One of the main advantages of this algorithm is that it allows the optimisation of many more atomic positions without necessarily introducing prohibitive computational costs. Given the sensitivity of our calculations to small changes in torsion angles, CrystalOptimizer was used to compute the lattice energies of the experimental crystal structures to see whether it would correctly predict the relative stability of the diastereomeric salt pair and their polymorphs.

### 6.4.1 Effect of wavefunction quality on the computed relative stability

During the lattice energy minimisations all the flexible torsion angles in ephedrine and 2-phenylpropionic acid including methyl rotations were allowed to vary in response to packing forces, i.e. 9 torsion angles (see Figure 6.1) as well as the cell parameters and relative orientations of the ions were optimised within space group symmetry. The sensitivity of the lattice energy minimisations to the quality of the wavefunction used was tested. In the first instance the intra-molecular energy penalty,  $\Delta E_{intra}$  was calculated at the HF/6-31G(d,p) level of theory whilst the intermolecular energy,  $U_{inter}$ , was calculated using the charge density computed at the MP2/6-31G(d,p) level of theory. In the second case both intra and inter molecular energy contributions were calculated using PBE1/6-31G(d,p) level of theory. The non-electrostatic contributions to the intermolecular energy were modelled using the FIT parameterisation of the exp-6 isotropic atom-atom potential in all cases. The results of the minimisations are summarised in Table 6.3 at the end of the Chapter in the Appendix. CrystalOptimizer managed to correctly reproduce the experimental structures, as shown by the low RMSD<sub>15</sub> values and illustrated in Figure 6.8; nevertheless, CrystalOptimizer does not improve much on the constrained optimised rigid-body minimisations performed with DMACRYS (see Table 6.2). Although CrystalOptimizer managed to reproduce the experimental structures well, the calculated relative energies were not. Experimentally, ERP I° is much more stable at room

temperature than all the polymorphs of ESP. Out of the experimentally found ESP polymorphs, ESP III° is the thermodynamically most stable at room temperature, followed by ESP II and ESP I. CrystalOptimizer instead predicted that ESP III° is more stable than ERP I° by 14 to 15 kJ/mol, depending on the wavefunction used. ESP I and ESP II were correctly predicted to be less stable than the thermodynamically stable phases. However, their ordering was again incorrect, with ESP I being slightly more stable than ESP II by 1.5 to 5 kJ/mol. Although this energy difference is very small, the computational model should be able to rank them in the correct order if one is to use it as a prediction tool for the selection of resolving agents.

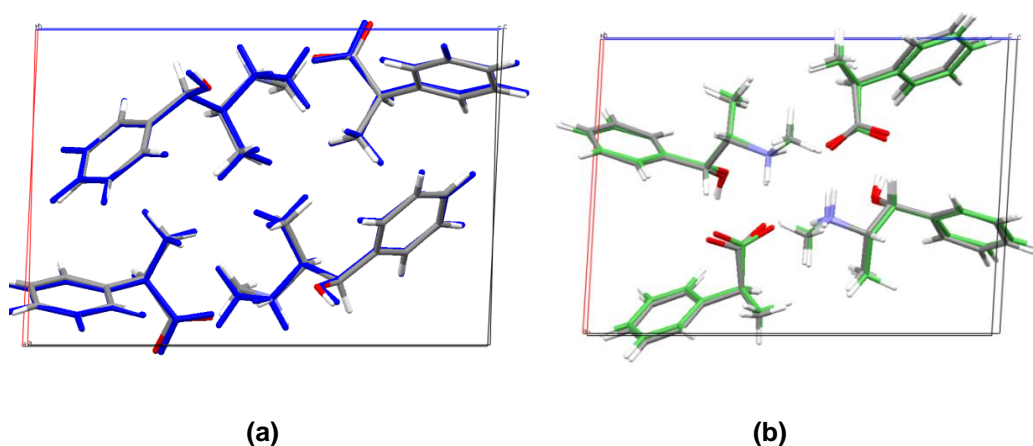


**Figure 6.8** Superposition of the experimental structure and the CrystalOptimizer minimised structures of **(a)** ERP I° (minimised structure in blue) and **(b)** ESP III° (minimised structure in green).

In order to try to improve the description of the ions' charge density and to improve the modelling of the hydrogen bonds, a basis set including a diffuse function was also tested. In this method, following the PBE1 minimisation, a further rigid-body lattice energy minimisation using the multipoles from a PBE aug-cc-pVTZ electron density calculation was performed. The results of these calculations are summarised in Table 6.4 which is found in the Appendix at the end of the chapter. The use of a more expensive basis set did not improve the prediction of the relative stability. In fact, all the polymorphs of ESP were estimated to be more stable than ERP I° with ESP III° 41 kJ/mol more stable than ERP I°.

#### 6.4.2 Effect of polarisation on the computed relative stability

One of the main limitations of the method used to compute the lattice energy is that the effect that other molecules in the crystal might have on the charge distribution of the ions is not taken into account. In order to overcome this to some extent, the charge density of

the molecules were calculated in a dielectric continuum of  $\epsilon=3$ , a value typical for organic crystals [118, 256] (Table 6.4). Lattice energy minimisations performed with the effect of the dielectric continuum on the molecule's charge distribution did not lead to improvements of the relative energies. This method once again predicted all ESP polymorphs to be more stable than the most thermodynamically stable phase, ERP I°.

The effect of polarisation on organic salts has been shown to be important, especially in the case of organic salts. In order to account for the effect of polarisation on target XIX, 1,8-Naphthyridinium fumarate, an organic salt, in the fifth blind test, van Eijk performed the charge density calculation on the supra-molecular dimer instead of the two separate molecules [184]. Performing similar *ab initio* calculations on four ion clusters cut out of the crystal structure (Figure 5.10), drastically reversed this situation, leading to the correct relative ordering of the four phases<sup>6</sup> (see Table 5.5 in the Appendix). However, the energy differences were far too large. Since the FIT empirical model potential will account for some polarisation effects, the large differences are possibly due to double-counting of polarisation effects, as well as other inaccuracies in the model. This method should therefore be refined in the future to avoid these issues.

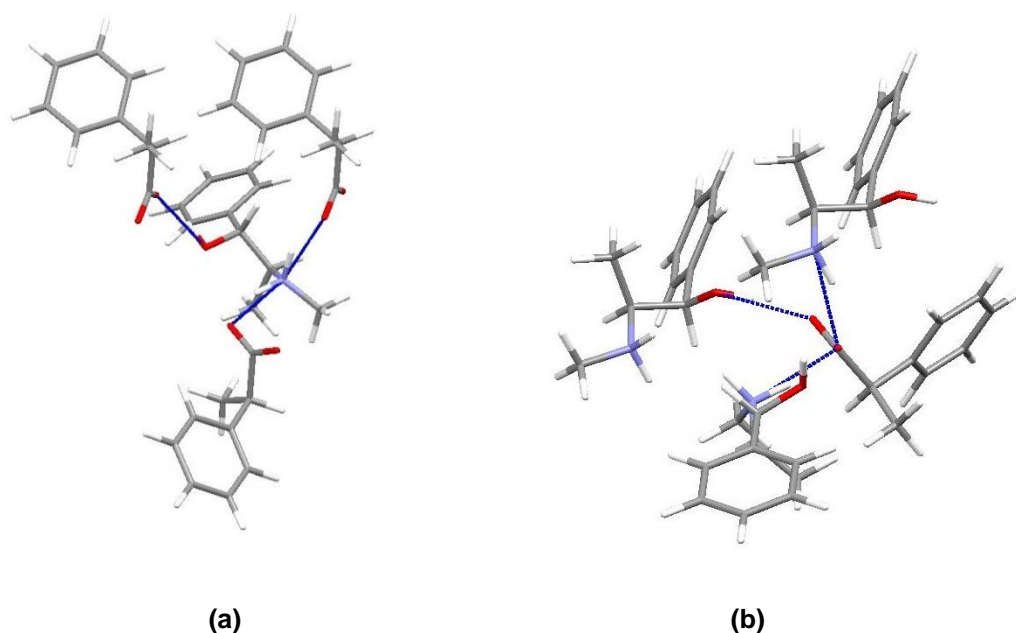


**Figure 6.9** Molecular clusters used for the charge density calculations of **(a)** Ephedrine and **(b)** 2-phenylpropionate ions. The distributed multipoles up to the hexadecapole were calculated only for the central molecule.

---

<sup>6</sup> These calculations were performed by Dr. Matthew Habgood.

### 6.4.3 Conclusion on Calculating the Lattice Energies of ERP and ESP salts

The calculations of the relative energies of the diastereomeric salts formed between ephedrine and 2-phenylpropionic acid with current methods gives totally unrealistic results compared to the experimental results and is very sensitive to the method used. It is clear that accurate modelling of the charge-transfer and polarisation of the ions within the crystal to give a realistic model for the intermolecular forces, balanced with the intramolecular forces, will be necessary for modelling these salts. Studies on octemidobenzamide and 5-formyluracil [230, 257] showed that polarisation needs to be explicitly considered to correctly model hydrogen bonding and attain the right balance between intra and inter molecular energies. The use of periodic *ab initio* dispersion corrected potentials would model these effects more accurately. However, the computational costs involved in these calculations might outweigh the benefits, and would not be possible if one has to deal with thousands of structures. Furthermore, the use of periodic *ab initio* dispersion corrected potentials for crystal structure prediction did not lead to the correct prediction of the structure of the salt target molecule in the fifth international blind test [184].

## 6.5 “Crystal structure prediction” to generate crystal structures

Crystal structure prediction techniques were employed to provide an initial survey of the type of crystal packings that might be competitive with the observed structures. Searches for plausible structures of ephedrine-2-phenylpropionate salts were performed using CrystalPredictor [121] to search for packing arrangements of low lattice energy. Four searches were carried out in the five most common non-centrosymmetric space groups ( $P2_12_12_1$ ,  $P2_1$ ,  $P1$ ,  $C2$  and  $P2_12_12$ ), to include the two conformations of ephedrine, folded and extended, and both 2-phenylpropionic acid enantiomers (i.e. 4 distinct searches). For the folded conformation,  $\theta_4$  was fixed at  $60^\circ$ , and for the extended at  $180^\circ$ , with  $\theta_3$  kept at  $180^\circ$  for both searches. The third conformation identified in the study by Alonso et al [250], and also identified in our scan as a low energy minima in the energy surface for  $\theta_3$  (Figure 6.1 (c) in Section 6.2.3) was not considered in the search, as our analysis of the CSD did not find any crystal structures containing that conformation of ephedrine, and was therefore not considered to be as relevant. If one was attempting a full prediction of the experimental crystal structures all

conformations should have probably be included. Nevertheless for our study, including only the two experimentally relevant conformers was thought to be sufficient.

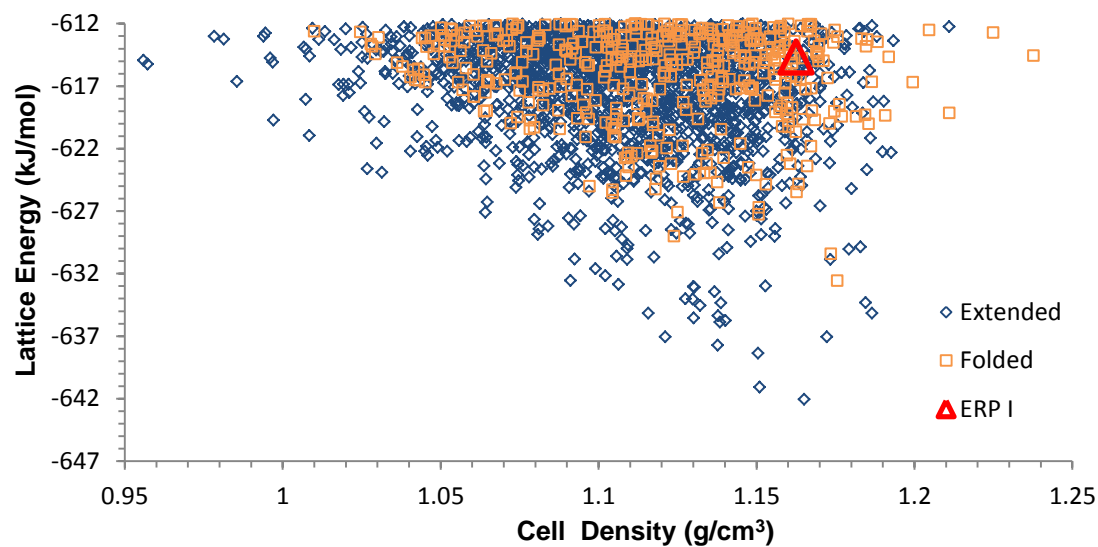
In a CrystalPredictor [121] search, the lattice energies of the cells produced are computed using crude models of the inter and intra-molecular energies. In order to calculate the intra-molecular energy contribution a grid of the  $\Delta E_{intra}$  values for the flexible torsions considered in the subsearches ( $\theta_1$  and  $\theta_2$  for ephedrine and  $\Phi_1$  and  $\Phi_2$  for 2-phenylpropionic acid) is constructed for each molecule. For ephedrine the intra-molecular energy was computed on a 6 x 15 grid, taking into account 6 points between 30° and 150° for  $\theta_1$  and 15 points between 0° and 280° for  $\theta_2$ . The intra-molecular energy for the 2-phenylpropionic ion was built on a 9 x 9 grid ranging from -50° to 190° for  $\Phi_1$  and -10° and 230° for  $\Phi_2$ . These conformational regions were considered to be the relevant ones, following the analysis conducted in Section 6.2. At each point on the grid the intra-molecular energy was calculated at the HF 6-31G(d,p) level of theory using GAMESS [258]. The value of the intra-molecular energy of the hypothetical structures is then computed by interpolation methods from the closest points on the grid.

Although the CrystalPredictor algorithm allows for the use of conformation dependent charges, the charges used were fixed to those of the optimised conformation calculated at the MP2 6-31G(d,p) level of theory, as it was found that the use of variable charges often led to interpolation errors. Given the crude model for the lattice energy used in this search, the conformation dependence of the charges is a minor error in the lattice energies. Hence the lattice energies being used to compare the structures were evaluated from the FIT potential with atomic charges. The lack of higher multipoles and the use of HF 6-31G(d,p) interpolated results means that the energy model is much cruder than that used in the preceding section (Section 6.4).

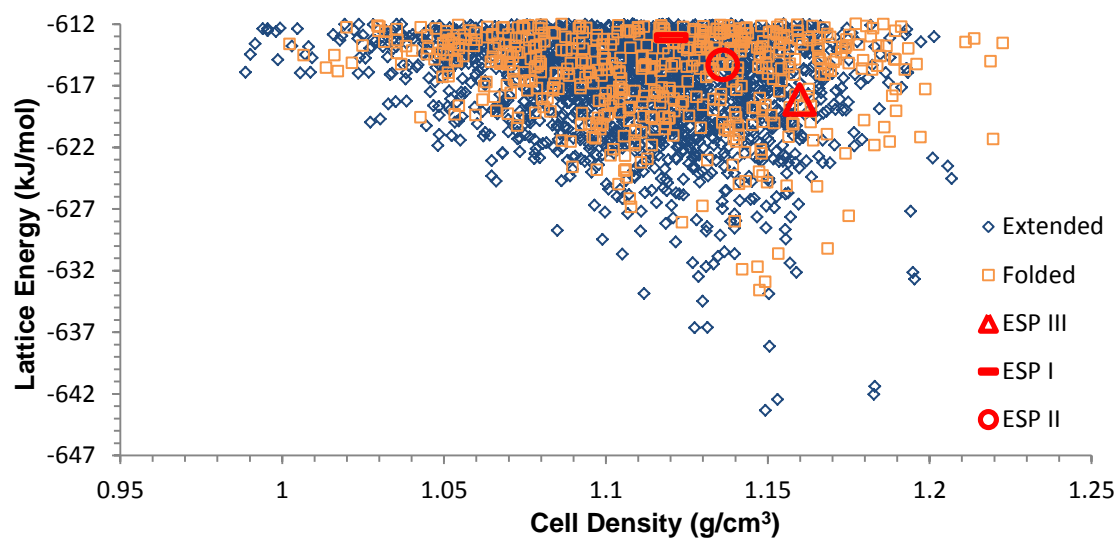
### 6.5.1 Results of the Search for Hypothetical Crystal Structures

The results of the Crystal Predictor searches for possible packing arrangements of ephedrine-2-phenylpropionate are summarised in the energy landscapes depicted in Figure 6.10. The search produced a vast number of hypothetical crystal structures, with 283 structures in the ERP search and 148 in the ESP search within the 20 kJ/mol range which is typically considered for refining with more accurate energy models to try to ensure that all potential polymorphs are refined. However, when the experimental structures were minimised using the same lattice energy model as used in the search, they were all more than 20 kJ/mol less stable than the global minima. Increasing the threshold to 40 kJ/mol increases the number of hypothetical structures to 2428 for ERP and 2520 for ESP. Hence, it is neither practical nor useful to perform further calculations, particularly since even with the most accurate models we could use, the relative

energies of the experimental structures would not be reproduced, as shown in Section 6.4.



(a)



(b)

**Figure 6.10** Energy landscapes of the search for hypothetical crystal structures of (a) ephedrine-(R)-2-phenylpropionate and (b) ephedrine-(S)-2-phenylpropionate salts. Each search was split into a sub search for structures with the extended conformation of ephedrine (blue) and a search for structures with the folded conformation (orange). Each point on the graph represents a hypothetical crystal structure. The experimental crystal structures were minimised using the same intra and intermolecular energy models as the search and are shown in red.



A packing similarity investigation of the experimental structures of ERP and ESP with hypothetical structures from the searches was performed to confirm that the experimental structures had been found in the search. A close match of ERP I° was found with the 1159<sup>th</sup> most stable of the extended conformations structures (Figure 6.11). The lattice energy of the hypothetical structure was in very close agreement with the lattice energy of the experimental structure calculated with the same model (-614.675 compared to -614.674 kJ/mol). An overlay of 15 molecules led to an RMSD<sub>15</sub> of 0.367. Matches for ESPI, ESP II and ESP III° were also found. An overlay of the experimental structure of ESP I with the computationally predicted structure led to an RMSD<sub>15</sub> of 0.27 (Figure 6.12). The overlay of the experimental structure of ESP II with its closest match from the predicted structures led to an RMSD<sub>15</sub> of 0.415 (Figure 6.13) whereas for ESP III° the overlay of 15 molecules was slightly worse with an RMSD<sub>15</sub> of 0.526 (Figure 6.14). Hence, the search was complete enough to find all known structures. However, all the structures found were very high in energy from the global minimum.

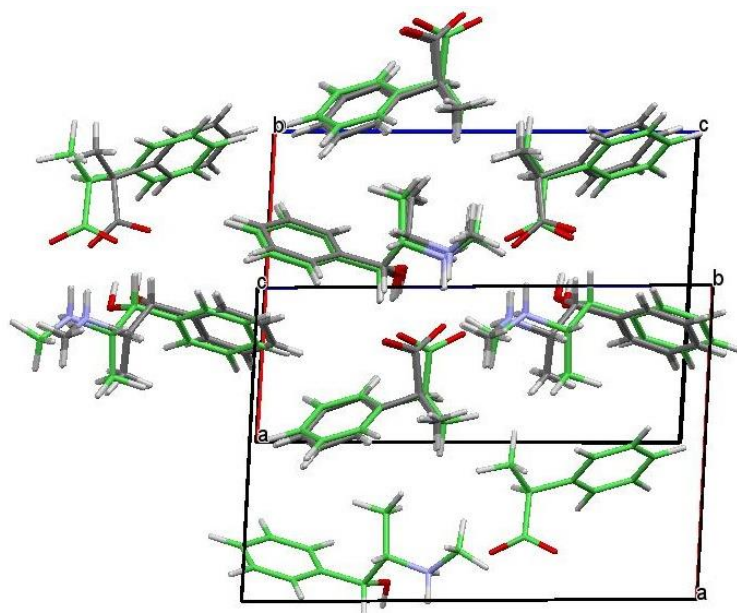


**Figure 6.11** Overlay of the experimental and predicted hypothetical (in green) structure for ERP I°.

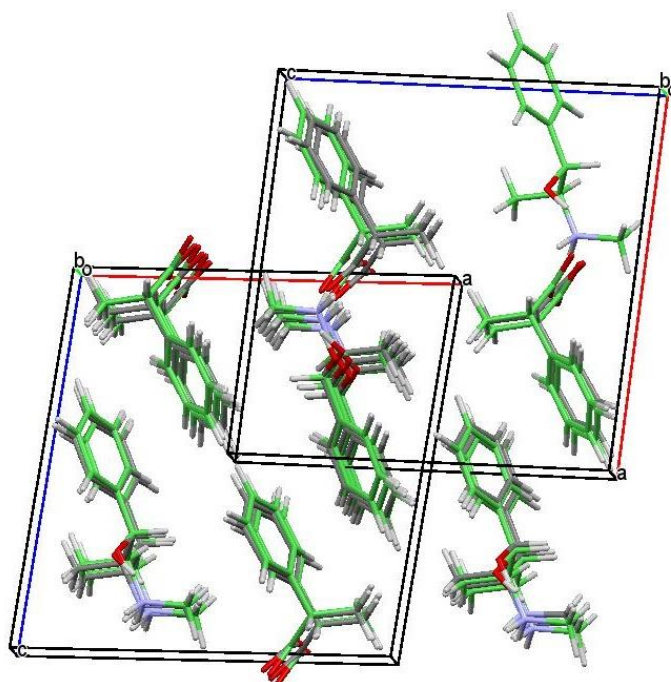


**Figure 6.12** Overlay of the experimental and predicted hypothetical (in green) structure for ESP I.

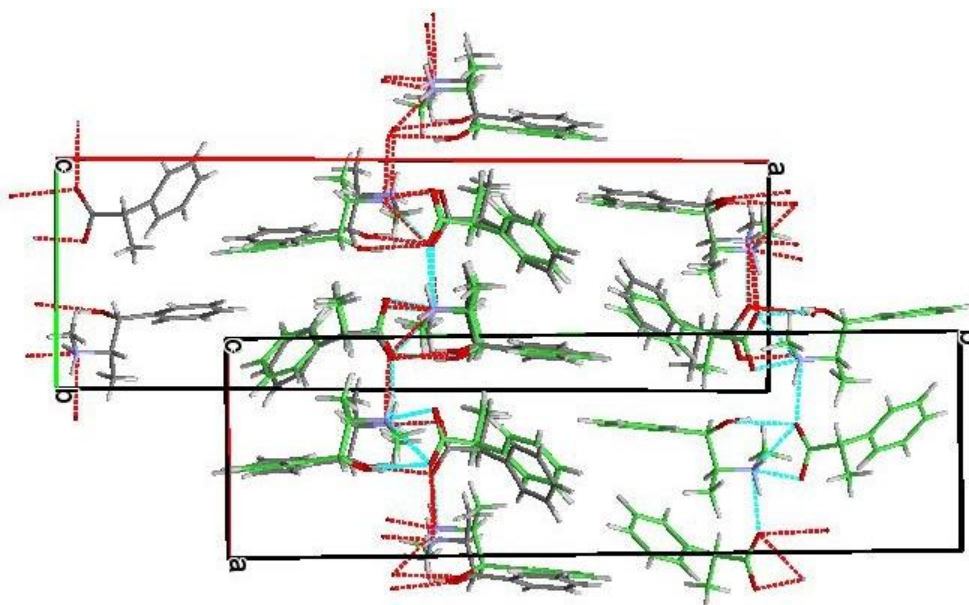


**Figure 6.13** Overlay of the experimental and predicted hypothetical (in green) structure for ESP II.

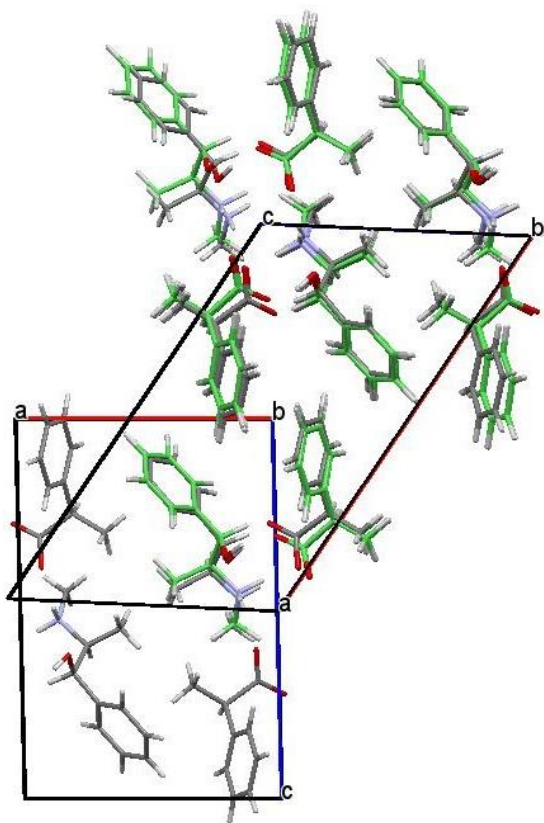


**Figure 6.14** Overlay of the experimental and predicted hypothetical (in green) structure for ESP III°.

The lowest few hundred crystal structures generated show five distinct hydrogen bonding motifs, which are mainly determined by the hydroxyl group conformation. The molecule can be in the extended or folded conformation, and there are a huge number of ways of packing these hydrogen bonded chains, corresponding to different conformations of the ions and packing of the phenyl groups. Interestingly, this analysis of the hypothetical structures in both searches shows that the ephedrine molecule in the majority of the low energy structures has the hydroxyl hydrogen in a very energetically unfavourable position, close to that seen in ESP I and ESP II. Structures containing ephedrine in such a conformation adopt a chain like hydrogen bonded pattern. Two different hydrogen bonded chain patterns arise. In the first and most common in the low energy hypothetical structures,  $R_2^1(7)$  rings link together via a hydrogen bond formed between a carboxylic acid oxygen and the free amine hydrogen as shown in Figure 6.15 (a). In the rings, one of the carboxylic acid oxygen atoms forms two hydrogen bonds with one hydrogen from the amine and the hydroxyl hydrogen in ephedrine. The second chain type, which is the one seen in ESP I and ESP II, ephedrine and 2-phenylpropionic acid form  $R_2^2(9)$  dimers which then link via a hydrogen bond formed between the free hydrogen on the amine and the oxygen in the acid (Figure 6.15 (b)). When ephedrine adopts the low energy conformation in which the hydroxyl hydrogen points away from

the amine hydrogen atoms, two distinct hydrogen bonding patterns arise, that involve the formation of interlinked rings similar to the hydrogen bonding in the thermodynamically stable forms, ERP I° and ESP III°, as shown in Figure 6.16. The two hydrogen bonding motifs are very similar and can be described using the same graph set notation,  $R_4^3(13)$ . In fact the hydrogen bonding motif depicted in Figure 6.16 (a) has been found experimentally in the structures of the pseudoephedrine diastereomeric salts investigated in Chapter 5 (see Figure 5.30)

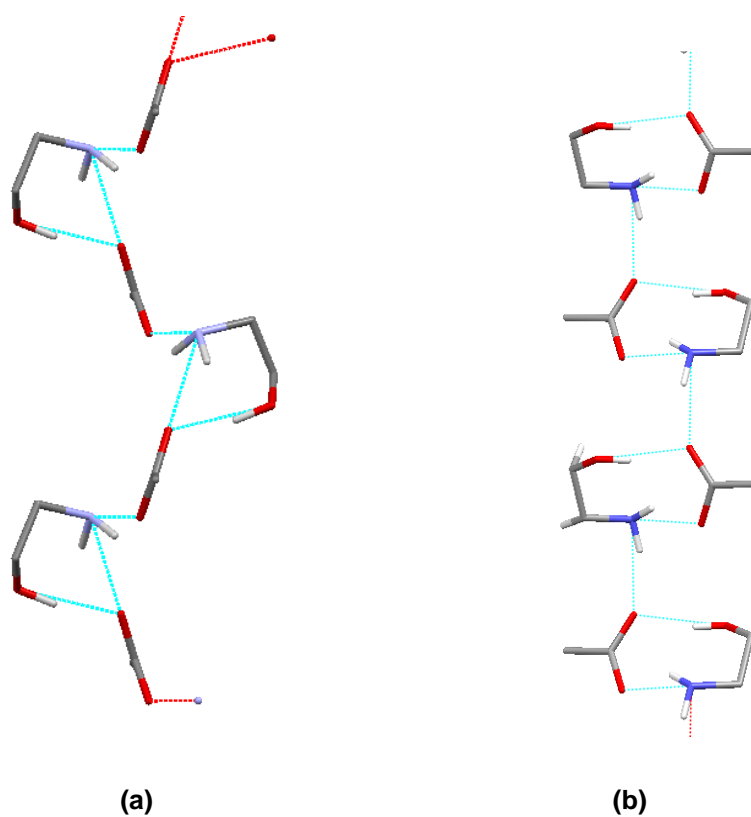


**Figure 6.15** Hydrogen bonding patterns found in the low energy hypothetical structures of ephedrine-2-phenylpropionate salts in which ephedrine is in a high energy conformation. **(a)** Chain of  $R_2^1(7)$  hydrogen bonded motifs, found in majority of low energy structures **(b)** chain of  $R_2^2(9)$  found in ESPI and ESP II

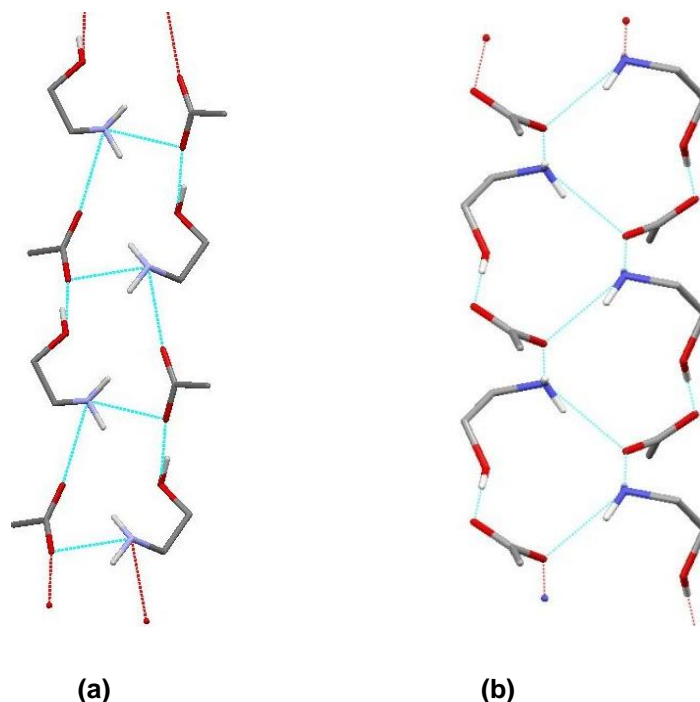


**Figure 6.16** Hydrogen bonding patterns found in the low energy hypothetical structures of ephedrine-2-phenylpropionate salts in which ephedrine is in a low energy conformation. Both **(a)** and **(b)** can be described as  $R_4^3(13)$  hydrogen bonded motifs. **(b)** is found in the thermodynamically stable ERP I° and ESP III°

## 6.6 Conclusions

Although one would intuitively think that the resolution ability of ephedrine would depend on the hydrogen bonding pattern that the salts were able to adopt, our search results show that there are a huge number of different packing arrangements containing a limited number of hydrogen bonding motifs. The most commonly occurring hydrogen bonding pattern in the energy landscapes of ephedrine-2-phenylpropionate salts (Figure 6.15 (a)) has not been seen experimentally. However, the calculations on the known forms show that the calculations are not able to reproduce the energy ordering of the two observed hydrogen bonding motifs. Hence, we cannot be confident that this new motif is thermodynamically competitive with the known forms. The simple model used in the search may be overestimating the gain in intermolecular energy that arises from the energetically unfavourable position of the hydroxyl group in the ephedrine molecule. However, future work testing the much needed improvements in the ability to rank the relative stability of diastereomeric salts should consider this new type of hydrogen bonding structure.

Furthermore, the fact that there are so many possible ways of packing the phenyl groups and that their differences lead to such small differences in lattice energies seems to suggest that it is actually the differences in the packing of the phenyl rings that lead to the big differences in solubilities. The strong fields around the ionic groups mean that the polarisation is important in the hydrogen bonding motif, but the phenyl rings will also be polarised. Accurate modelling of the conformational flexibility is also very important, as the steric interactions determine how closely the ions can pack, and the energies are very sensitive to small changes in both overall density and specific hydrogen bonding interactions. The huge numbers of structures generated show that performing more accurate CSP studies on diastereomeric salts will be very expensive, as large numbers of structures need to be evaluated by increasingly accurate energy models.

## 6.7 Appendix

| Potential       | Structure           | a<br>(Å) | b<br>(Å) | c<br>(Å) | $\alpha$<br>(°) | $\beta$<br>(°) | $\gamma$<br>(°) | $\rho$<br>(g/cm <sup>3</sup> ) | RMSD <sub>15</sub> | $U_{inter}$<br>(kJ/mol) | Diff $U_{inter}$<br>(kJ/mol) | O...O<br>(Å) | N...O<br>(Å) | N...O<br>(Å) |
|-----------------|---------------------|----------|----------|----------|-----------------|----------------|-----------------|--------------------------------|--------------------|-------------------------|------------------------------|--------------|--------------|--------------|
| <b>ERP I°</b>   |                     |          |          |          |                 |                |                 |                                |                    |                         |                              |              |              |              |
| FIT             | <i>Experimental</i> | 9.85     | 5.84     | 14.58    | 90              | 91.43          | 90              | 1.249                          | -                  | -                       | -                            | 2.628        | 2.741        | 2.842        |
|                 | <i>ExminExp</i>     | 9.84     | 5.87     | 14.47    | 90              | 92.78          | 90              | 1.255                          | 0.19               | -690.96                 | 0                            | 2.561        | 2.682        | 2.742        |
|                 | <i>Diff (%)</i>     | -0.10    | 0.51     | -0.75    | 0               | 1.48           | 0               | 0.6                            | -                  | -                       | -                            | -2.55        | -2.15        | -3.52        |
| WILL            | <i>ExminExp</i>     | 9.81     | 5.83     | 14.83    | 90              | 92.32          | 90              | 1.235                          | 0.19               | -675.08                 | 0                            | 2.514        | 2.749        | 2.793        |
|                 | <i>Diff (%)</i>     | -0.41    | -0.17    | 1.71     | 0               | 0.97           | 0               | -1.12                          | -                  | -                       | -                            | -4.34        | 0.29         | -1.72        |
| <b>ESP I</b>    |                     |          |          |          |                 |                |                 |                                |                    |                         |                              |              |              |              |
| FIT             | <i>Experimental</i> | 12.52    | 5.72     | 12.67    | 90              | 98.12          | 90              | 1.165                          | -                  | -                       | -                            | 2.691        | 2.748        | 2.668        |
|                 | <i>ExminExp</i>     | 12.71    | 5.81     | 12.58    | 90              | 96.37          | 90              | 1.135                          | 0.16               | -690.193                | 0.77                         | 2.693        | 2.695        | 2.646        |
|                 | <i>Diff (%)</i>     | 1.60     | 1.57     | -0.71    | 0               | -1.78          | 0               | -2.58                          | -                  | -                       | -                            | 0.07         | -1.93        | -0.82        |
| WILL            | <i>ExminExp</i>     | 12.54    | 5.81     | 12.55    | 90              | 96.59          | 90              | 1.153                          | 0.14               | -678.418                | -3.34                        | 2.607        | 2.710        | 2.661        |
|                 | <i>Diff (%)</i>     | 0.16     | 1.57     | -0.95    | 0               | -1.56          | 0               | -1.03                          | -                  | -                       | -                            | -3.12        | -1.38        | -0.26        |
| <b>ESP II</b>   |                     |          |          |          |                 |                |                 |                                |                    |                         |                              |              |              |              |
| FIT             | <i>Experimental</i> | 29.30    | 9.45     | 6.49     | 90              | 90             | 90              | 1.17                           | -                  | -                       | -                            | 2.708        | 2.609        | 2.880        |
|                 | <i>ExminExp</i>     | 29.35    | 9.21     | 6.61     | 90              | 90             | 90              | 1.17                           | 0.17               | -654.282                | 37.68                        | 2.751        | 2.764        | 2.839        |
|                 | <i>Diff (%)</i>     | 0.17     | -2.54    | 1.85     | 0               | 0              | 0               | 0                              | -                  | -                       | -                            | -1.56        | 5.94         | -1.42        |
| WILL            | <i>ExminExp</i>     | 29.12    | 9.13     | 6.59     | 90              | 90             | 90              | 1.19                           | 0.21               | -657.247                | 17.83                        | 2.631        | 2.768        | 2.904        |
|                 | <i>Diff (%)</i>     | -0.61    | -3.39    | 1.54     | 0               | 0              | 0               | 1.7                            | -                  | -                       | -                            | -2.843       | 6.09         | 0.83         |
| <b>ESP III°</b> |                     |          |          |          |                 |                |                 |                                |                    |                         |                              |              |              |              |
| FIT             | <i>Experimental</i> | 10.39    | 5.87     | 14.16    | 90              | 93.27          | 90              | 1.215                          | -                  | -                       | -                            | 2.710        | 2.712        | 2.909        |
|                 | <i>ExminExp</i>     | 10.34    | 5.77     | 14.44    | 90              | 91.85          | 90              | 1.216                          | 0.193              | -668.133                | 22.83                        | 2.666        | 2.743        | 2.771        |
|                 | <i>Diff (%)</i>     | -0.47    | -1.64    | 2.01     | 0               | -1.52          | 0               | 0.03                           | -                  | -                       | -                            | -1.624       | 1.143        | -4.744       |
| WILL            | <i>ExminExp</i>     | 10.26    | 5.67     | 14.55    | 90              | 93.16          | 90              | 1.24                           | 0.23               | -665.116                | 9.96                         | 2.529        | 2.749        | 2.781        |
|                 | <i>Diff (%)</i>     | -1.25    | -3.4     | 2.75     | 0               | -0.12          | 0               | 1.64                           | -                  | -                       | -                            | -6.68        | 1.36         | -4.40        |

**Table 6.1** Summary of the lattice energy minimisations with the ion conformations held rigid at the experimental structures (ExminExp), using different repulsion-dispersion models FIT and WILL performed using DMACRYS. The charge distribution was calculated using the MP2/6-31G(d,p) level of theory and represented by distributed multipoles.

| Potential           | Structure           | a     | b     | c     | $\alpha$ | $\beta$ | $\gamma$ | $\rho$               | Rmsd <sub>15</sub> | $U_{inter}$ | O...O   | N...O | N...O   |
|---------------------|---------------------|-------|-------|-------|----------|---------|----------|----------------------|--------------------|-------------|---------|-------|---------|
|                     |                     | (Å)   | (Å)   | (Å)   | (°)      | (°)     | (°)      | (g/cm <sup>3</sup> ) |                    | (kJ/mol)    | (Å)     | (Å)   | (Å)     |
| <b>ERP I°</b>       |                     |       |       |       |          |         |          |                      |                    |             |         |       |         |
| FIT +<br>DMA<br>MP2 | <i>Experimental</i> | 9.85  | 5.84  | 14.58 | 90       | 91.43   | 90       | 1.249                | -                  | -           | 2.628   | 2.741 | 2.842   |
|                     | <i>ExminExp</i>     | 9.84  | 5.87  | 14.47 | 90       | 92.78   | 90       | 1.255                | 0.19               | -690.96     | 2.561   | 2.682 | 2.742   |
|                     | <i>Diff (%)</i>     | -0.10 | 0.51  | -0.75 | 0        | 1.48    | 0        | 0.6                  | -                  | -           | -2.55   | -2.15 | -3.52   |
|                     | <i>ConOpt</i>       | 9.94  | 5.96  | 14.84 | 90       | 93.84   | 90       | 1.195                | 0.27               | -654.48     | 2.647   | 2.719 | 2.826   |
|                     | <i>Diff (%)</i>     | 0.91  | 2.05  | 1.75  | 0        | 2.64    | 0        | -4.32                | -                  | -           | 0.72    | -0.80 | -0.56   |
|                     | <i>Opt</i>          | 9.39  | 7.04  | 14.24 | 90       | 94.58   | 90       | 1.116                | -                  | -582.07     | (3.055) | 2.722 | (3.642) |
|                     | <i>Diff (%)</i>     | -4.67 | 20.72 | -2.33 | 0        | 3.45    | 0        | -10.65               | -                  | -           | 16.25   | -0.69 | 28.15   |
| <b>ESP I</b>        |                     |       |       |       |          |         |          |                      |                    |             |         |       |         |
| FIT +<br>DMA<br>MP2 | <i>Experimental</i> | 12.52 | 5.72  | 12.67 | 90       | 98.12   | 90       | 1.165                | -                  | -           | 2.691   | 2.748 | 2.668   |
|                     | <i>ExminExp</i>     | 12.71 | 5.81  | 12.58 | 90       | 96.37   | 90       | 1.135                | 0.16               | -690.193    | 2.693   | 2.695 | 2.646   |
|                     | <i>Diff (%)</i>     | 1.60  | 1.57  | -0.71 | 0        | -1.78   | 0        | -2.58                | -                  | -           | 0.07    | -1.93 | -0.82   |
|                     | <i>ConOpt</i>       | 12.81 | 5.86  | 12.55 | 90       | 95.18   | 90       | 1.117                | 0.26               | -665.158    | 2.714   | 2.716 | 2.667   |
|                     | <i>Diff (%)</i>     | 2.32  | 2.45  | -0.95 | 0        | -3.00   | 0        | -4.12                | -                  | -           | 0.85    | -1.16 | -0.04   |
|                     | <i>Opt</i>          | 12.36 | 6.40  | 12.32 | 90       | 96.89   | 90       | 1.082                | -                  | -           | (3.235) | 2.711 | (3.885) |
|                     | <i>Diff (%)</i>     | -1.28 | 11.9  | -2.76 | 0        | -1.25   | 0        | -7.12                | -                  | -           | 20.22   | -1.35 | 45.6    |

**Table 6.2** Summary of the lattice energy minimisations performed to test sensitivity to rigid ion conformations using DMACRYS[182]. ConOpt refers to minimisations in which the molecular conformations had been optimised with  $\theta$  and  $\Phi$ , the flexible torsion angles identified in Figure 6.1, fixed at the experimental values, and all other degrees of freedom optimised. *Opt* refers to minimisations in which the molecular conformations had been fully optimised for the molecule in isolation. Constrained and full optimisations of the molecular conformations were performed using the HF/6-31G(d,p) level of theory whilst the distributed multipoles were calculated using the MP2/6-31G(d,p) level of theory.



| Structure        | RMSD <sub>15</sub> | $\rho$ (g/cm <sup>3</sup> ) | $\Delta E_{intra}$ (kJ/mol) |                  | $U_{inter}$<br>(kJ/mol) | Lattice Energy<br>(kJ/mol) | Relative Energy<br>(kJ/mol) |
|------------------|--------------------|-----------------------------|-----------------------------|------------------|-------------------------|----------------------------|-----------------------------|
|                  |                    |                             | Ephedrine                   | Phenylpropionate |                         |                            |                             |
| <b>HF_MP2</b>    |                    |                             |                             |                  |                         |                            |                             |
| ERP I°           | 0.208              | 1.192                       | 5.567                       | 7.073            | -631.165                | -618.524                   | 0                           |
| ESP I            | 0.303              | 1.125                       | 55.616                      | 3.809            | -669.883                | -610.459                   | 8.065                       |
| ESP II           | 0.205              | 1.161                       | 51.503                      | 3.400            | -670.178                | -615.274                   | 3.25                        |
| ESP III°         | 0.210              | 1.211                       | 7.768                       | 15.214           | -655.387                | -632.405                   | -13.881                     |
| <b>PBE0_PBE0</b> |                    |                             |                             |                  |                         |                            |                             |
| ERP I°           | 0.227              | 1.184                       | 7.64                        | 11.48            | -622.758                | -603.63                    | 0                           |
| ESP I            | 0.383              | 1.127                       | 57.07                       | 4.25             | -659.575                | -598.26                    | 5.37                        |
| ESP II           | 0.248              | 1.156                       | 56.17                       | 3.75             | -659.758                | -599.84                    | 3.79                        |
| ESP III°         | 0.204              | 1.208                       | 10.62                       | 17.22            | -646.850                | -619.01                    | -15.38                      |

**Table 6.3** CrystalOptimizer Lattice Energy minimisations of the experimental structures of ephedrine 2-phenylpropionate. HF\_MP2 refers to calculations in which the intra-molecular energy penalty,  $\Delta E_{intra}$ , was calculated using HF/6-31G(d,p) level of theory and the intermolecular energy,  $U_{inter}$ , was calculated using the charge density from the distributed multipole from the wavefunction calculated at the MP2/6-31G(d,p) level of theory. PBE\_PBE refers to calculation in which  $\Delta E_{intra}$  and  $U_{inter}$  were calculated at the PBE1/6-31G(d,p) level of theory.

| Structure          | RMSD <sub>15</sub> | $\rho$ (g/cm <sup>3</sup> ) | $\Delta E_{\text{intra}}$ (kJ/mol) |                  | $U_{\text{inter}}$<br>(kJ/mol) | Lattice Energy<br>(kJ/mol) | Relative Energy<br>(kJ/mol) |
|--------------------|--------------------|-----------------------------|------------------------------------|------------------|--------------------------------|----------------------------|-----------------------------|
|                    |                    |                             | Ephedrine                          | Phenylpropionate |                                |                            |                             |
| <b>Aug-cc-pVTZ</b> |                    |                             |                                    |                  |                                |                            |                             |
| ERP                | 0.166              | 1.201                       | 19.812                             | 6.308            | -663.643                       | -612.237                   | 0                           |
| ESPI               | 0.302              | 1.135                       | 61.189                             | 0                | -678.310                       | -617.121                   | -4.884                      |
| ESPII              | 0.251              | 1.160                       | 59.284                             | 1.211            | -671.416                       | -610.922                   | -1.315                      |
| ESPIII             | 0.216              | 1.160                       | 0                                  | 8.664            | -663.643                       | -654.979                   | -42.742                     |
| <b>PCMe3</b>       |                    |                             |                                    |                  |                                |                            |                             |
| ERP                | 0.191              | 1.198                       | 0                                  | 2.080            | -673.951                       | -670.130                   | 0                           |
| ESPI               | 0.288              | 1.129                       | 37.790                             | 0.378            | -717.170                       | -679.183                   | -9.053                      |
| ESPII              | 0.198              | 1.159                       | 33.633                             | 0                | -711.314                       | -677.681                   | -7551                       |
| ESPIII             | 0.210              | 1.212                       | 2.697                              | 8.650            | -692.836                       | -678.388                   | -8.258                      |

**Table 6.4** CrystalOptimizer Lattice Energy minimisations of the experimental structures of ephedrine 2-phenylpropionate. Aug-cc-pVTZ refers to calculations in which, following the PBE\_PBE minimisation, a further rigid-body lattice energy minimisation using the multipoles from a PBE aug-cc-pVTZ electron density calculation was performed. PCMe3 refers to calculations in which, following the PBE\_PBE minimisation, a further lattice energy minimisation was performed using the multipoles obtained from the electron density calculated in a dielectric continuum, with  $\epsilon=3$ .

| Structure | $\Delta E_{\text{intra}}$<br>(kJ/mol) | $U_{\text{inter}}$<br>(kJ/mol) | Lattice Energy<br>(kJ/mol) | Relative Energy<br>(kJ/mol) |
|-----------|---------------------------------------|--------------------------------|----------------------------|-----------------------------|
| ERP       | 19.12                                 | -787.54                        | -768.42                    | 0                           |
| ESPI      | 61.31                                 | -736.76                        | -675.45                    | 92.97                       |
| ESPII     | 59.91                                 | -786.55                        | -726.64                    | 41.78                       |
| ESPIII    | 27.84                                 | -764.31                        | -736.47                    | 31.95                       |

**Table 6.5** CrystalOptimizer Lattice Energy minimisations of the experimental structures of ephedrine 2-phenylpropionate using the charge density distribution calculated for the central ion in a hydrogen bonded cluster.

# Chapter 7 Overall Conclusions and Recommendations for future work

The separation of mixtures of chiral molecules into pure enantiomers through crystallisation is a problem that has been troubling scientist for many years, since Pasteur recognised that a solution of tartaric acid salts produced a set of crystals that were mirror images of one another. The production of enantiomerically pure compounds in the pharmaceutical and agrochemical industries is especially relevant, given the tight regulatory guidelines in place for the production of chiral molecules. Two main crystallisation methods are usually used for production purposes of enantiomerically pure products. When equimolar mixtures of chiral molecules spontaneously separate into the constituent enantiomers, the crystallisation process can be designed so as to separate them without the need to add any additives. However, when crystals containing both enantiomers in equal quantities form, the most common method employed consists on the addition of a resolving agent that reacts with both enantiomers to form two diastereomeric adducts with different solubilities that can therefore be separated by crystallisation. Understanding the mechanisms of how mixtures of enantiomers crystallise so as to be able to control the crystallisation process is therefore not only a matter of scientific curiosity but of high industrial value too. Given the tight time constraints faced in industry, the methods employed to detect systems that spontaneously resolve and to choose resolving agents that lead to diastereomeric adducts with large solubility differences are usually based on fast screening methods. These methods however, give a limited understanding of the resolution process. The work presented in this thesis attempted to provide a more thorough and systematic study of a set of closely related systems, to obtain structural and thermodynamic data in the hope that this would help us rationalise the chiral resolution process. Extensive crystallisation screens were performed with Naproxen (Chapter 4) to understand its crystallisation behaviour, whether it would form racemic crystals or spontaneously resolve, and to look for other possible crystal phases. Chiral resolution processes by diastereomeric salt formation were investigated in Chapter 5. Chapter 5 presented an extensive crystallisation screen of the diastereomeric salt pair formed between (1R,2S)-Ephedrine and 2-Phenylpropionic acid. These results were complemented by further crystallisation experiments on a set of closely related diastereomeric salts: (1R,2S)-Ephedrine with 2-Phenylbutyric acid, (1R,2R)-Pseudoephedrine with 2-Phenylpropionic acid and (1R,2R)-Pseudoephedrine with 2-Phenylbutyric acid.

The possibility of using crystal structure prediction (CSP) methods to aid the design of resolution processes has received much attention especially given improvements seen in the field in recent years. In order to be able to use computational models as a quantitative

tool they have to be able to correctly calculate the relative stability of the different crystal forms. The experimental work provided in this thesis for Naproxen (Chapter 4) and a set of diastereomeric salts (Chapter 5) provides crystal and thermodynamic data against which any computational method based on thermodynamic controlled crystallisation could be validated.

## **7.1 Crystallisation behaviour of (1R,2S)-Ephedrine-2-phenylpropionate salts and other closely related diastereomeric salt pairs**

During the extensive crystallisation screen performed on the (1R,2S)-Ephedrine-2-phenylpropionate diastereomeric salt pair presented in Chapter 5, five new polymorphs were found, two of the less soluble salt ERP I° and ERP II, and three of the more soluble salt, ESPI, ESPII and ESPIII°. Furthermore, the more soluble salt was also found to be prone to solvation, with the formation of four solvates and a hydrate. This propensity to polymorphism and solvate formation was also observed in the crystallisation experiments performed on the set of closely related diastereomeric salts presented in Chapter 5. The most common hydrogen bonding arrangements of both (1R,2S)-Ephedrine and (1R,2R)-Pseudoephedrine diastereomeric salts were based on a  $R_4^3(13)$  graph set but with some differences in the hydrogen bonding motif. Although it was not possible to solve the structures of the solvates, the similarities in the hydrogen bonding region of their FT-IR spectra with the anhydrous phases suggested that the solvents were not participating in the hydrogen bonding and adopting the same  $R_4^3(13)$  hydrogen bonding motif as the non-solvated forms. A  $2_1$  screw axis in the middle of the hydrogen bonded rings lead to the formation of columns with a polar core and non-polar surface in which the phenyl groups point outwards. In all the crystallisation screens it became apparent that the growth of good quality single crystals was very difficult. Furthermore, single crystals were often very fine needles that were difficult to analyse using X-ray diffraction methods. This was consistent with other studies that showed that the growth was in the direction of the screw axis. These observations suggest that the packing of the columns is not easy, and so the crystals grow lengthwise instead. The fact the phenyl rings are free to rotate provides many more ways of packing the columns, as demonstrated by the CSP study in Chapter 6. The problems in finding a unique favourable packing of the phenyl groups of the hydrogen bonded columns explains not only the difficulties in growing single crystals but also the reason why the salts seem to be polymorphic and prone to solvation.

In the fast screening methods that are usually employed to assess the efficiency of different resolving agents the solid material obtained is unlikely to correspond to the most

stable crystalline form found in the crystallisation screens presented in Chapter 5. The role that polymorphism has on the resolution efficiency of the diastereomeric salts is rarely discussed. Hence the results presented in this thesis indicate that a resolution process could easily be designed based on a metastable phase, and the more stable one form later within the industrial process conditions thereby decreasing the process yield.

## 7.2 Opportunities for the design of resolution processes

The work presented in Chapter 5 shows the importance of polymorphism during the crystallisation of diastereomeric salts. Few previous studies have mentioned the occurrence of polymorphism during the crystallisation of diastereomeric salt pairs. This is probably because researchers are mainly interested in the forms that readily crystallise, whether they might be thermodynamically stable or kinetically favourable. The crystallisation behaviour of (1R,2S)-Ephedrine-2-phenylpropionate system offers the possibility of investigating a number of process conditions in order to optimise the resolution process. ERP I° and ERP II are monotropically related and so ERP I° is stable under all conditions. On the other hand, ESP I, ESP II and ESP III° are enantiotropically related and therefore each have a process window under which they are stable. The resolution efficiency of ERP I° with each of the polymorphs under different conditions could therefore be investigated. Given the differences in hydrogen bonding and packing of ESP I and ESP II with ERP I° the appearance of solid solutions might be inhibited. Similar studies could be performed looking at the effects of solvation as ERP I° does not form solvates in a number of solvents in which ESP does.

## 7.3 Computing the Relative Stabilities of Racemic and Enantiopure Naproxen and Ephedrine-2-phenylpropionate Diastereomeric salts

In chapter 4, a crystallisation screen was performed in order to try to identify all possible forms of racemic and enantiopure Naproxen. Naproxen was confirmed to be a racemic forming compound, with the racemic crystals being more stable than the homochiral phase. The relative stability of the two forms was measured experimentally at two different temperatures, ~156 °C and in the 10-45 °C range, and compared to the lattice energy difference computed at 0K. Lattice energy calculations on the idealised crystal structures were found to overestimate the stability of the racemic crystal by a few kilojoules per mole. These differences were only minor compared to the lattice energy

and sufficiently small for the energy landscape to provide a correct qualitative ordering of the different phases and predict the structure of the racemic form.

Chapter 5 described an extensive crystallisation screen to look for different forms of the diastereomeric salt pair of ephedrine-2-phenylpropionate and provided thermodynamic data for four new crystal structures. The lattice energy of the experimental crystal structures was calculated using various models for the lattice energy as described in Chapter 6. The calculations showed that the lattice energy of the salts is extremely sensitive to very small changes in the torsion angles, not only in those relevant to the hydrogen bonding motif, and also to the model of the intermolecular forces. The calculations were unable to correctly calculate the relative stability of the diastereomer salt phases overestimating the relative stability of ESP III° with respect to the most stable phase, ERP I°, by around 13 to 15 kJ/mol. This was traced to the sensitivity of the relative energies to the polarisation of the ions. Therefore, the use of specific-molecule intermolecular potentials including molecular polarisability and flexibility or the use of dispersion-corrected periodic density functional calculations may improve the reliability of the relative energies. Nevertheless, these calculations are only beginning to become feasible for a few structures. It is noted as well that DFT calculations on 1,8-naphthyridinium fumarate, target molecule XIX in the 5<sup>th</sup> international blind test, did not predict the structure of the most stable phase correctly. The CSP search showed that a particularly large number of structures would need to be considered with highly accurate methods in order to predict the relative stability at 0K. The enantiotropic relationship between the different phases of ESP shows that temperature would need to be considered to predict relative stabilities and solubilities.

## **7.4 Will Lattice Energy Minimisations ever be reliable for the prediction of resolution efficiency?**

The ability of ephedrine to resolve 2-phenylpropionic acid by measuring the ternary phase diagram of ERP I° and ESP III° in ethanol was also investigated and presented in Chapter 5. The data obtained suggested the formation of solid solutions throughout the whole composition range. Therefore, despite having a system where the solubilities of the most stable forms of the diastereomeric salts differ markedly, the resolution efficiency of the process is not dominated any more by their relative solubilities but by the level of miscibility in the solid state. Solid state miscibility could have been detected through the construction of a binary phase melting point diagram. Had our computational methods been able to accurately predict the relative stabilities of the different forms, the results would not have been able to detect the formation of solid solutions, and therefore would have still been unable to correctly predict the resolution efficiency of the process.

Another important consideration is that the current computational method cannot account for the effect of kinetics on crystallisation. The crystallisation screen showed that ESP III° was only obtained by solution mediated transformations and was not obtained in any of the evaporative or cooling crystallisation experiments. This suggests that there is an important kinetic factor affecting the outcome of the crystallisation. Furthermore both metastable phases ESP I and ESP II are kinetically stable and do not transform readily to ESP III° under ambient conditions. Hence, even if no solid solution could be formed, the outcome of the resolution experiments would have depended on whether they had been kinetically or thermodynamically driven. For example, performing fast cooling crystallisations with no stirring would have given the metastable phases ESP I and or ESP II.

## 7.5 Summary

This thesis has provided much needed experimental data to test the validity of a proposed computational method to calculate the relative stabilities of racemic and homochiral crystal and of a set of diastereomeric salts. In all cases the computational method has been shown to be inadequate in correctly calculating the differences in energies between the different phases, highlighting the need for better models of the crystal energies. The work has also highlighted the importance of other factors, such as solid solution and the role of crystallisation kinetics in determining the resolution efficiency of diastereomeric salts.



## Reference List

1. [http://www.biocheminfo.org/bnd/isomer\\_classification.jpeg](http://www.biocheminfo.org/bnd/isomer_classification.jpeg). Internet Communication Nov 9, 2005.
2. [Anon] Nomenclature and Symbolism for Amino-Acids and Peptides. *Pure and Applied Chemistry* **1984**, 56 (5), 595-624.
3. M.A.Rosanoff On Fischer's Classification of Stereo-Isomers. *Journal of the American Chemical Society* **1906**, 28 (1), 114-121.
4. Cahn, R. S.; Ingold, C. K. Specification of Configuration About Quadricovalent Asymmetric Atoms. *Journal of the Chemical Society* **1951**, (FEB), 612-622.
5. Cahn, R. S.; Ingold, C.; Prelog, V. Specification of Molecular Chirality. *Angewandte Chemie-International Edition* **1966**, 5 (4), 385-&.
6. Cahn, R. S.; Ingold, C. K.; Prelog, V. The Specification of Asymmetric Configuration in Organic Chemistry. *Experientia* **1956**, 12 (3), 81-94.
7. Hutt, A. J.; Caldwell, J. The Importance of Stereochemistry in the Clinical Pharmacokinetics of the 2-Arylpropionic Acid Non-Steroidal Anti-Inflammatory Drugs. *Clinical Pharmacokinetics* **1984**, 9 (4), 371-373.
8. Caldwell, J. Do single enantiomers have something special to offer? *Human Psychopharmacology-Clinical and Experimental* **2001**, 16, S67-S71.
9. Stinson, S. C. Chiral chemistry. *Chemical & Engineering News* **2001**, 79 (20), 45-+.
10. C.J.De Ranter Crystals, X-ray crystallography, and drugs. In *X-ray crystallography and drug action*, A.S.Horn; C.J.De Ranter, Eds.; Oxford University Press: 1984; pp 1-22.
11. Blaschke, G.; Kraft, H. P.; Fickentscher, K. Chromatographic separation of racemic thalidomide and teratogenic activity of its enantiomers. 29 ed.; 1979; pp 1640-1642.
12. Fabro, S.; Smith, R. L.; Williams, R. T. Toxicity and Teratogenicity of Optical Isomers of Thalidomide. *Nature* **1967**, 215 (5098), 296-&.
13. Eriksson, T.; Bjorkman, S.; Roth, B.; Fyge, A.; Hoglund, P. Stereospecific Determination, Chiral Inversion In-Vitro and Pharmacokinetics in Humans of the Enantiomers of Thalidomide. *Chirality* **1995**, 7 (1), 44-52.
14. [Anon] Fda Policy Statement for the Development of New Stereoisomeric Drugs. *Chirality* **1992**, 4 (5), 338-340.
15. Rekoske, J. E. Chiral separations. *Aiche Journal* **2001**, 47 (1), 2-5.
16. Caner, H.; Groner, E.; Levy, L.; Agranat, I. Trends in the development of chiral drugs. *Drug Discovery Today* **2004**, 9 (3), 105-110.
17. Crosby, J. Synthesis of Optically-Active Compounds - A Large-Scale Perspective. *Tetrahedron* **1991**, 47 (27), 4789-4846.

18. *Chirality in Industry*; John Wiley and Sons: 1998.
19. *Chirality in Industry II*; John Wiley and Sons: 2009.
20. Kotha, S. Opportunities in Asymmetric-Synthesis - An Industrial Prospect. *Tetrahedron* **1994**, *50* (12), 3639-3662.
21. Newman, D. J.; Cragg, G. M. Natural products as sources of new drugs over the last 25 years. *Journal of Natural Products* **2007**, *70* (3), 461-477.
22. Butler, M. S. Natural products to drugs: natural product-derived compounds in clinical trials. *Natural Product Reports* **2008**, *25* (3), 475-516.
23. Mori, K. Bioactive Natural Products and Chirality. *Chirality* **2011**, *23* (6), 449-462.
24. A.M.Rouhi Chiral Chemistry. *Chemical & Engineering News* **2004**, *82* (24), 47-62.
25. Stinson, S. C. Chiral drug interactions. *Chemical & Engineering News* **1999**, *77* (41), 101-+.
26. Nicoud, R. M.; Fuchs, G.; Adam, P.; Bailly, M.; Kusters, E.; Antia, F. D.; Reuille, R.; Schmid, E. Preparative-Scale Enantioseparation of A Chiral Epoxide - Comparison of Liquid-Chromatography and Simulated Moving-Bed Adsorption Technology. *Chirality* **1993**, *5* (4), 267-271.
27. Seidel-Morgenstern, A.; Kessler, L. C.; Kaspereit, M. New developments in simulated moving bed chromatography. *Chemical Engineering & Technology* **2008**, *31* (6), 826-837.
28. Rajendran, A.; Paredes, G.; Mazzotti, M. Simulated moving bed chromatography for the separation of enantiomers. *Journal of Chromatography A* **2009**, *1216* (4), 709-738.
29. Regla, I.; Luna, H.; Perez, H. I.; Demare, P.; Bustos-Jaimes, I.; Zaldivar, V.; Calcagno, M. L. Enzymatic resolution of N-acetyl-homophenylalanine with mammalian kidney acetone powders. *Tetrahedron-Asymmetry* **2004**, *15* (8), 1285-1288.
30. J H van't Hoff *The arrangement of atoms in space*; BiblioLife: 2009.
31. Levilain, G.; Coquerel, G. Pitfalls and rewards of preferential crystallization. *Crystengcomm* **2010**, *12* (7), 1983-1992.
32. Coquerel G Preferential Crystallization. In *Novel Optical Resolution Technologies*, Sakai, K.; Hirayama, N.; Tamura, R., Eds.; Springer: 2007; pp 1-51.
33. Piselli, F. L. A process for the optical resolution of 2-(6-methoxy-2-naphthyl)propionic acid. EP0298395, Jan 29, 1992.
34. Ndzie, E.; Cardinael, P.; Schoofs, A. R.; Coquerel, G. An efficient access to the enantiomers of alpha-methyl-4-carboxyphenylglycine via a hydantoin route using a practical variant of preferential crystallization AS3PC (auto seeded programmed polythermic preferential crystallization). *Tetrahedron-Asymmetry* **1997**, *8* (17), 2913-2920.
35. Pasteur, L. *C. R. Hebd Seances Acad. Sci.* **1853**, *37* (162).

36. Jean Jacques; Andre Collet; Samuel H.Wilen *Enantiomers, Racemates and Resolutions*; John Wiley and Sons: New York, 1981.
37. *CRC Handbook of Optical Resolutions via Diastereomeric Salt Formation*; CRC Press: 2002.
38. Vries, T.; Wynberg, H.; Van Echten, E.; Koek, J.; ten Hoeve, W.; Kellogg, R. M.; Broxterman, Q. B.; Minnaard, A.; Kaptein, B.; van der Sluis, S.; Hulshof, L.; Kooistra, J. The family approach to the resolution of racemates. *Angewandte Chemie-International Edition* **1998**, 37 (17), 2349-2354.
39. Broxterman, Q. B.; Van Echten, E.; Hulshof, L. A.; Kaptein, B.; Kellogg, R. M.; Minnaard, A. J.; Vries, T. R.; Wynberg, H. "Dutch resolution", a new technology in classical resolution. *Chimica Oggi-Chemistry Today* **1998**, 16 (9), 34-37.
40. Nieuwenhuijzen, J. W.; Grimbergen, R. F. P.; Koopman, C.; Kellogg, R. M.; Vries, T. R.; Pouwer, K.; Van Echten, E.; Kaptein, B.; Hulshof, L. A.; Broxterman, Q. B. The role of nucleation inhibition in optical resolutions with families of resolving agents. *Angewandte Chemie-International Edition* **2002**, 41 (22), 4281-4286.
41. Kellogg, R. M.; Nieuwenhuijzen, J. W.; Pouwer, K.; Vries, T. R.; Broxterman, Q. B.; Grimbergen, R. F. P.; Kaptein, B.; La Crois, R. M.; de Wever, E.; Zwaagstra, K.; van der Laan, A. C. Dutch resolution: Separation of enantiomers with families of resolving agents. A status report. *Synthesis-Stuttgart* **2003**, (10), 1626-1638.
42. Sakai, K.; Sakurai, R.; Nohira, H.; Tanaka, R.; Hirayama, N. Practical resolution of 1-phenyl-2-(4-methylphenyl)ethylamine using a single resolving agent controlled by the dielectric constant of the solvent. *Tetrahedron-Asymmetry* **2004**, 15 (22), 3495-3500.
43. Sakai, K.; Sakurai, R.; Nohira, H. New resolution technologies controlled by chiral discrimination mechanisms. *Novel Optical Resolution Technologies* **2007**, 269, 199-231.
44. Coquerel, G.; Petit, S. Recognition of Enantiomers Through Morphology of Single-Crystals - Application to Some 5-Alkyl-5-Aryl-Hydantoin Derivatives. *Journal of Crystal Growth* **1993**, 130 (1-2), 173-180.
45. Tobe, Y. The reexamination of Pasteur's experiment in Japan. *Mendeleev Communications* **2003**, (3), 93-94.
46. Coquerel, G. Review on the heterogeneous equilibria between condensed phases in binary systems of enantiomers. *Enantiomer* **2000**, 5 (5), 481-498.
47. Srisanga, S.; ter Horst, J. H. Racemic Compound, Conglomerate, or Solid Solution: Phase Diagram Screening of Chiral Compounds. *Crystal Growth & Design* **2010**, 10 (4), 1808-1812.
48. Galland, A.; Dupray, V.; Berton, B.; Morin-Grognet, S.; Sanselme, M.; Atmani, H.; Coquerel, G. Spotting Conglomerates by Second Harmonic Generation. *Crystal Growth & Design* **2009**, 9 (6), 2713-2718.
49. Dalhus, B.; Gorbitz, C. H. Non-centrosymmetric racemates: space-group frequencies and conformational similarities between crystallographically independent molecules. *Acta Crystallographica Section B-Structural Science* **2000**, 56, 715-719.

50. Flack, H. D. Chiral and achiral crystal structures. *Helvetica Chimica Acta* **2003**, *86* (4), 905-921.
51. Gavezzotti, A.; Filippini, G. Polymorphic Forms of Organic-Crystals at Room Conditions - Thermodynamic and Structural Implications. *Journal of the American Chemical Society* **1995**, *117* (49), 12299-12305.
52. Gourlay, M. D.; Kendrick, J.; Leusen, F. J. J. Rationalization of racemate resolution: Predicting spontaneous resolution through crystal structure prediction. *Crystal Growth & Design* **2007**, *7* (1), 56-63.
53. Gourlay, M. D.; Kendrick, J.; Leusen, F. J. J. Predicting the spontaneous chiral resolution by crystallization of a pair of flexible nitroxide radicals. *Crystal Growth & Design* **2008**, *8* (8), 2899-2905.
54. Kendrick, J.; Gourlay, M. D.; Neumann, M. A.; Leusen, F. J. J. Predicting spontaneous racemate resolution using recent developments in crystal structure prediction. *Crystengcomm* **2009**, *11* (11), 2391-2399.
55. Borghese, A.; Libert, V.; Zhang, T.; Alt, C. A. Efficient fast screening methodology for optical resolution agents: Solvent effects are used to affect the efficiency of the resolution process. *Organic Process Research & Development* **2004**, *8* (3), 532-534.
56. Leusen, F. J. J.; Noordik, J. H.; Karfunkel, H. R. Racemate Resolution Via Crystallization of Diastereomeric Salts - Thermodynamic Considerations and Molecular Mechanics Calculations. *Tetrahedron* **1993**, *49* (24), 5377-5396.
57. Karamertzanis, P. G.; Price, S. L. Challenges of crystal structure prediction of diastereomeric salt pairs. *Journal of Physical Chemistry B* **2005**, *109* (36), 17134-17150.
58. Kinbara, K. Design of resolving agents based on crystal engineering. *Synlett* **2005**, (5), 732-743.
59. Brianso, M. C. Diastereoisomer Salts of 1-Phenylethylamine and of Alpha-Substituted Phenylacetic Acids - P-Separation and N-Separation Or Syncrystallization - A Crystallographic Explanation. *Acta Crystallographica Section B-Structural Science* **1981**, *37* (MAR), 618-620.
60. Zingg, S. P.; Arnett, E. M.; Mcphail, A. T.; Bothnerby, A. A.; Gilkerson, W. R. Chiral Discrimination in the Structures and Energetics of Association of Stereoisomeric Salts of Mandelic-Acid with Alpha-Phenethylamine, Ephedrine, and Pseudoephedrine. *Journal of the American Chemical Society* **1988**, *110* (5), 1565-1580.
61. Fogassy, E.; Lopata, A.; Faigl, F.; Darvas, F.; Acs, M.; Toke, L. Quantitative Approach to Optical Resolution. *Tetrahedron Letters* **1980**, *21* (7), 647-650.
62. Marchand, P.; Lefebvre, L.; Querniard, F.; Cardinael, P.; Perez, G.; Counieux, J. J.; Coquerel, G. Diastereomeric resolution rationalized by phase diagrams under the actual conditions of the experimental process. *Tetrahedron-Asymmetry* **2004**, *15* (16), 2455-2465.
63. Kozma, D.; Pokol, G.; Acs, M. Calculation of the Efficiency of Optical Resolutions on the Basis of the Binary Phase-Diagram for the Diastereoisomeric

Salts. *Journal of the Chemical Society-Perkin Transactions 2* **1992**, (3), 435-439.

64. Ebbers, E. J.; Plum, B. J. M.; Ariaans, G. J. A.; Kaptein, B.; Broxterman, Q. B.; Bruggink, A.; Zwanenburg, B. New resolving bases for ibuprofen and mandelic acid: qualification by binary phase diagrams. *Tetrahedron-Asymmetry* **1997**, 8 (24), 4047-4057.
65. Jacques, J.; Collet, A.; Wilen, S. H. *Enantiomers, Racemates and Resolutions*; Krieger Publishing Company: Malabar, Florida, 1994.
66. Hill, A. E.; Ricci, J. E. Ternary systems. XI. Magnesium iodate, Sodium iodate and water. XII Sodium iodate, potassium iodate and water. XIII. Potassium iodate, potassium chloride and water. XIV. Potassium iodate, potassium sulfate and water. *Journal of the American Chemical Society* **1931**, 53, 4305-4315.
67. Leclercq, M.; Jacques, J. Investigation of Mixtures of Enantiomers .10. Separation of Diastereoisomeric Salts Complicated by Isomorphism. *Bulletin de la Societe Chimique de France Partie II-Chimie Moleculaire Organique et Biologique* **1975**, (9-10), 2052-2056.
68. Ebbers, E.; Ariaans, G. J. A.; Zwanenburg, B.; Bruggink, A. Controlled design of resolutions. Prediction of the efficiency of resolutions based on samples of arbitrary composition. *Tetrahedron-Asymmetry* **1998**, 9 (15), 2745-2753.
69. Gorman, A.; Gould, R. O.; Gray, A. M.; Taylor, P.; Walkinshaw, M. D. Asymmetric Resolution and Molecular Recognition .2. the X-Ray Crystal-Structures of Ephedrine-N-Benzoyloxycarbonyl-L-Leucine and Ephedrine-N-Acetyl-L-Valine. *Journal of the Chemical Society-Perkin Transactions 2* **1986**, (5), 739-746.
70. Gould, R. O.; Walkinshaw, M. D. Molecular Recognition in Model Crystal Complexes - the Resolution of D-Amino and L-Amino-Acids. *Journal of the American Chemical Society* **1984**, 106 (25), 7840-7842.
71. Fogassy, E.; Acs, M.; Faigl, F.; Simon, K.; Rohonczy, J.; Ecsery, Z. Pseudosymmetry and Chiral Discrimination in Optical Resolution Via Diastereoisomeric Salt Formation - the Crystal-Structures of (R)-N-Methylamphetamine and (S)-N-Methylamphetamine Bitartrates (Rmerta and Smerta). *Journal of the Chemical Society-Perkin Transactions 2* **1986**, (12), 1881-1886.
72. Gautam R.Desiraju *Crystal engineering: the design of organic solids*; Elsevier: Amsterdam, 1989.
73. Brianso, M. C. Atomic and Molecular-Structures of Diastereoisomeric Salts of (Para)-Alpha-Phenylethylammonium Alpha-Phenyl-Alpha-Methylacetates. *Acta Crystallographica Section B-Structural Science* **1976**, 32 (NOV15), 3040-3045.
74. Brianso, M. C.; Leclercq, M.; Jacques, J. 1-Phenylethylamine Mandelate. *Acta Crystallographica Section B-Structural Science* **1979**, 35 (NOV), 2751-2753.
75. Kinbara, K.; Sakai, K.; Hashimoto, Y.; Nohira, H.; Saigo, K. Design of resolving reagents: p-Substituted mandelic acids as resolving reagents for 1-arylalkylamines. *Tetrahedron-Asymmetry* **1996**, 7 (6), 1539-1542.

76. Kinbara, K.; Sakai, K.; Hashimoto, Y.; Nohira, H.; Saigo, K. Chiral discrimination upon crystallisation of the diastereomeric salts of 1-arylethylamines with mandelic acid or p-methoxymandelic acid: Interpretation of the resolution efficiencies on the basis of the crystal structures. *Journal of the Chemical Society-Perkin Transactions 2* **1996**, (12), 2615-2622.
77. Kinbara, K.; Harada, Y.; Saigo, K. (2-Naphthyl)glycolic acid: a tailored resolving agent for p-substituted 1-arylethylamines. *Tetrahedron-Asymmetry* **1998**, 9 (13), 2219-2222.
78. Kinbara, K.; Harada, Y.; Saigo, K. A high-performance, tailor-made resolving agent: remarkable enhancement of resolution ability by introducing a naphthyl group into the fundamental skeleton. *Journal of the Chemical Society-Perkin Transactions 2* **2000**, (7), 1339-1347.
79. Kobayashi, Y.; Kurasawa, T.; Kinbara, K.; Saigo, K. Rational design of CH/ $\pi$  interaction sites in a basic resolving agent. *Journal of Organic Chemistry* **2004**, 69 (22), 7436-7441.
80. Kinbara, K.; Hashimoto, Y.; Sukegawa, M.; Nohira, H.; Saigo, K. Crystal structures of the salts of chiral primary amines with achiral carboxylic acids: Recognition of the commonly-occurring supramolecular assemblies of hydrogen-bond networks and their role in the formation of conglomerates. *Journal of the American Chemical Society* **1996**, 118 (14), 3441-3449.
81. Etter, M. C.; Macdonald, J. C.; Bernstein, J. Graph-Set Analysis of Hydrogen-Bond Patterns in Organic-Crystals. *Acta Crystallographica Section B-Structural Science* **1990**, 46, 256-262.
82. Lemmerer, A.; Bourne, S. A.; Fernandes, M. A. Robust supramolecular heterosynthons in chiral ammonium carboxylate salts. *Crystal Growth & Design* **2008**, 8 (4), 1106-1109.
83. Lemmerer, A.; Bourne, S. A.; Fernandes, M. A. Structural and melting point characterisation of six chiral ammonium naphthalene carboxylate salts. *Crystengcomm* **2008**, 10 (11), 1605-1612.
84. D'Oria, E.; Karamertzanis, P. G.; Price, S. L. Spontaneous Resolution of Enantiomers by Crystallization: Insights from Computed Crystal Energy Landscapes. *Crystal Growth & Design* **2010**, 10 (4), 1749-1756.
85. Leusen, F. J. J. Crystal structure prediction of diastereomeric salts: A step toward rationalization of racemate resolution. *Crystal Growth & Design* **2003**, 3 (2), 189-192.
86. Karamertzanis, P. G.; Anandamanoharan, P. R.; Fernandes, P.; Cains, P. W.; Vickers, M.; Tocher, D. A.; Florence, A. J.; Price, S. L. Toward the computational design of diastereomeric resolving agents: An experimental and computational study of 1-phenylethylammonium-2-phenylacetate derivatives. *Journal of Physical Chemistry B* **2007**, 111 (19), 5326-5336.
87. Kitaigorodskii, A. I. *Organic Chemical Crystallography*; Consultants Bureau: New York, 1961.
88. Stone, A. J. *The Theory of Intermolecular Forces*; Oxford University Press: Oxford, 1996.

89. Gavezzotti, A. The chemistry of intermolecular bonding: Organic crystals, their structures and transformations. *Synlett* **2002**, (2), 201-214.
90. Hirshfeld, F. L. Bonded-Atom Fragments for Describing Molecular Charge-Densities. *Theoretica Chimica Acta* **1977**, *44* (2), 129-138.
91. Sigfridsson, E.; Ryde, U. Comparison of methods for deriving atomic charges from the electrostatic potential and moments. *Journal of Computational Chemistry* **1998**, *19* (4), 377-395.
92. Cox, S. R.; Williams, D. E. Representation of the Molecular Electrostatic Potential by A Net Atomic Charge Model. *Journal of Computational Chemistry* **1981**, *2* (3), 304-323.
93. Espinosa, E.; Lecomte, C.; Ghermani, N. E.; Devemy, J.; Rohmer, M. M.; Benard, M.; Molins, E. Hydrogen bonds: First quantitative agreement between electrostatic potential calculations from experimental X-(X+N) and theoretical ab initio SCF models. *Journal of the American Chemical Society* **1996**, *118* (10), 2501-2502.
94. Ghermani, N. E.; Bouhmaida, N.; Lecomte, C. Modeling Electrostatic Potential from Experimentally Determined Charge-Densities .1. Spherical-Atom Approximation. *Acta Crystallographica Section A* **1993**, *49*, 781-789.
95. Klooster, W. T.; Swaminathan, S.; Nanni, R.; Craven, B. M. Electrostatic Properties of 1-Methyluracil from Diffraction Data. *Acta Crystallographica Section B-Structural Science* **1992**, *48*, 217-227.
96. Williams, D. E.; Weller, R. R. Lone-Pair Electronic Effects on the Calculated Abinitio Scf-Mo Electric-Potential and the Crystal-Structures of Azabenzene. *Journal of the American Chemical Society* **1983**, *105* (13), 4143-4148.
97. Williams, D. E. Nonbonded Interatomic Potential-Energy Functions and Prediction of Crystal-Structures. *Acta Crystallographica Section A* **1984**, *40*, C95.
98. Karamertzanis, P. G.; Pantelides, C. C. Optimal site charge models for molecular electrostatic potentials. *Molecular Simulation* **2004**, *30* (7), 413-436.
99. Stone, A. J.; Alderton, M. Distributed Multipole Analysis - Methods and Applications. *Molecular Physics* **1985**, *56* (5), 1047-1064.
100. Stone, A. J. Distributed multipole analysis: Stability for large basis sets. *Journal of Chemical Theory and Computation* **2005**, *1* (6), 1128-1132.
101. Mooij, W. T. M.; van Duijneveldt, F. B.; van Duijneveldt-van de Rijdt; van Eijck, B. P. Transferable ab initio intermolecular potentials. 1. Derivation from methanol dimer and trimer calculations. *Journal of Physical Chemistry A* **1999**, *103* (48), 9872-9882.
102. Mooij, W. T. M.; Leusen, F. J. J. Multipoles versus charges in the 1999 crystal structure prediction test. *Physical Chemistry Chemical Physics* **2001**, *3* (22), 5063-5066.
103. Day, G. M.; Motherwell, W. D. S.; Jones, W. Beyond the isotropic atom model in crystal structure prediction of rigid molecules: Atomic multipoles versus point charges. *Crystal Growth & Design* **2005**, *5* (3), 1023-1033.

104. Brodersen, S.; Wilke, S.; Leusen, F. J. J.; Engel, G. A study of different approaches to the electrostatic interaction in force field methods for organic crystals. *Physical Chemistry Chemical Physics* **2003**, 5 (21), 4923-4931.
105. Lennard-Jones, J. E. On the determination of molecular fields. *Proceedings of the Royal Society of London A* **1924**, 106 (738), 463-477.
106. Buckingham, R. A. The classical equation of state of gaseous helium, neon and argon. *Proceedings of the Royal Society of London A* **1938**, 168 (933), 264-283.
107. Williams, D. E.; Starr, T. L. Calculation of Crystal-Structures of Hydrocarbons by Molecular Packing Analysis. *Computers & Chemistry* **1977**, 1 (3), 173-177.
108. Cox, S. R.; Hsu, L. Y.; Williams, D. E. Nonbonded Potential Function Models for Crystalline Oxohydrocarbons. *Acta Crystallographica Section A* **1981**, 37 (MAY), 293-301.
109. Williams, D. E.; Cox, S. R. Nonbonded Potentials for Azahydrocarbons - the Importance of the Coulombic Interaction. *Acta Crystallographica Section B-Structural Science* **1984**, 40 (AUG), 404-417.
110. Williams, D. E.; Houpt, D. J. Fluorine Nonbonded Potential Parameters Derived from Crystalline Perfluorocarbons. *Acta Crystallographica Section B-Structural Science* **1986**, 42, 286-295.
111. Hsu, L. Y.; Williams, D. E. Intermolecular Potential-Function Models for Crystalline Perchlorohydrocarbons. *Acta Crystallographica Section A* **1980**, 36 (MAR), 277-281.
112. Williams, D. E. Improved intermolecular force field for molecules containing H, C, N, and O atoms, with application to nucleoside and peptide crystals. *Journal of Computational Chemistry* **2001**, 22 (11), 1154-1166.
113. Fowler, P. W.; Stone, A. J. Induced Dipole-Moments of Vanderwaals Complexes. *Journal of Physical Chemistry* **1987**, 91 (3), 509-511.
114. Gavezzotti, A. Calculation of intermolecular interaction energies by direct numerical integration over electron densities. I. Electrostatic and polarization energies in molecular crystals. *Journal of Physical Chemistry B* **2002**, 106 (16), 4145-4154.
115. Welch, G. W. A.; Karamertzanis, P. G.; Misquitta, A. J.; Stone, A. J.; Price, S. L. Is the induction energy important for modeling organic crystals? *Journal of Chemical Theory and Computation* **2008**, 4 (3), 522-532.
116. Gavezzotti, A. Calculation of intermolecular interaction energies by direct numerical integration over electron densities. 2. An improved polarization model and the evaluation of dispersion and repulsion energies. *Journal of Physical Chemistry B* **2003**, 107 (10), 2344-2353.
117. Gavezzotti, A. Quantitative ranking of crystal packing modes by systematic calculations on potential energies and vibrational amplitudes of molecular dimers. *Journal of Chemical Theory and Computation* **2005**, 1 (5), 834-840.
118. Cooper, T. G.; Hejczyk, K. E.; Jones, W.; Day, G. M. Molecular Polarization Effects on the Relative Energies of the Real and Putative Crystal



Structures of Valine. *Journal of Chemical Theory and Computation* **2008**, 4 (10), 1795-1805.

119. Tomasi, J.; Mennucci, B.; Cammi, R. Quantum mechanical continuum solvation models. *Chemical Reviews* **2005**, 105 (8), 2999-3093.
120. Karamertzanis, P. G.; Kazantsev, A. V.; Issa, N.; Welch, G. W. A.; Adjiman, C. S.; Pantelides, C. C.; Price, S. L. Can the Formation of Pharmaceutical Cocrystals Be Computationally Predicted? 2. Crystal Structure Prediction. *Journal of Chemical Theory and Computation* **2009**, 5 (5), 1432-1448.
121. Karamertzanis, P. G.; Pantelides, C. C. Ab initio crystal structure prediction. II. Flexible molecules. *Molecular Physics* **2007**, 105 (2-3), 273-291.
122. Kazantsev, A. V.; Karamertzanis, P. G.; Adjiman, C. S.; Pantelides, C. C. Efficient Handling of Molecular Flexibility in Lattice Energy Minimization of Organic Crystals. *Journal of Chemical Theory and Computation* **2011**, 7 (6), 1998-2016.
123. Verwer, P.; Leusen, F. J. J. Computer Simulation to Predict Possible Crystal Polymorphs. Lipkowitz, K. B.; Boyd, D. B., Eds.; John Wiley and Sons: New York, 1998; pp 327-365.
124. Day, G. M. Current approaches to predicting molecular organic crystal structures. *Crystallography Reviews* **2011**, 17 (1), 3-52.
125. Karamertzanis, P. G.; Pantelides, C. C. Ab initio crystal structure prediction - I. Rigid molecules. *Journal of Computational Chemistry* **2005**, 26 (3), 304-324.
126. Holden, J. R.; Du, Z. Y.; Ammon, H. L. Prediction of Possible Crystal-Structures for C-Containing, H-Containing, N-Containing, O-Containing and F-Containing Organic-Compounds. *Journal of Computational Chemistry* **1993**, 14 (4), 422-437.
127. Sobol', I. M. On the distribution of points in a cube and the approximate evaluation of integrals. *Computational Mathematics and Mathematical Physics* **1967**, 7, 86-112.
128. Lecuyer, P. Efficient and Portable Combined Random Number Generators. *Communications of the Acm* **1988**, 31 (6), 742-&.
129. Price, S. L.; Leslie, M.; Welch, G. W. A.; Habgood, M.; Price, L. S.; Karamertzanis, P. G.; Day, G. M. Modelling organic crystal structures using distributed multipole and polarizability-based model intermolecular potentials. *Physical Chemistry Chemical Physics* **2010**, 12 (30), 8478-8490.
130. Maple, J. R.; Hwang, M. J.; Stockfisch, T. P.; Dinur, U.; Waldman, M.; Ewig, C. S.; Hagler, A. T. Derivation of Class-Ii Force-Fields .1. Methodology and Quantum Force-Field for the Alkyl Functional-Group and Alkane Molecules. *Journal of Computational Chemistry* **1994**, 15 (2), 162-182.
131. Willock, D. J.; Price, S. L.; Leslie, M.; Catlow, C. R. A. The Relaxation of Molecular-Crystal Structures Using A Distributed Multipole Electrostatic Model. *Journal of Computational Chemistry* **1995**, 16 (5), 628-647.
132. Anandamanoharan, P. R.; Cains, P. W.; Jones, A. G. Separability of diastereomer salt pairs of 1-phenylethylamine with enantiomeric 2-

substituted phenylacetic acids by fractional crystallization, and its relation to physical and phase properties. *Tetrahedron-Asymmetry* **2006**, 17 (12), 1867-1874.

133. Fernandes, P.; Florence, A. J.; Shankland, K.; Karamertzanis, P. G.; Hulme, A. T.; Anandamanoharan, R. P. Powder study of (R)-1-phenylethylammonium (R)-2-phenylbutyrate form 3. *Acta Crystallographica Section E-Structure Reports Online* **2007**, 63, O202-O204.
134. Fernandes, P.; Florence, A.; Shankland, K.; Karamertzanis, P. G.; Hulme, A. T.; Anandamanoharan, P. Powder study of (R)-1-phenylethylammonium (R)-2-phenylbutyrate form 2. *Acta Crystallographica Section E-Structure Reports Online* **2007**, 63, O247-O249.
135. Karamertzanis, P. G.; Price, S. L. Energy minimization of crystal structures containing flexible molecules. *Journal of Chemical Theory and Computation* **2006**, 2 (4), 1184-1199.
136. Antoniadis, C. D.; D'Oria, E.; Karamertzanis, P. G.; Tocher, D. A.; Florence, A. J.; Price, S. L.; Jones, A. G. A Computationally Inspired Investigation of the Solid Forms of (R)-1-Phenylethylammonium-(S)-2-phenylbutyrate. *Chirality* **2010**, 22 (4), 447-455.
137. J.W.Mullin *Crystallization*; 4th Edition ed.; 2001.
138. Kashchiev, D. Driving force for nucleation. In *Nucleation: Basic theory with applications*, Butterworth-Heinemann: 2000; pp 9-17.
139. Mullin, J. W. *Crystallization*; Butterworth-Heinemann: 2001.
140. Gerdts, C. J.; Tereshko, V.; Yadav, M. K.; Dementieva, I.; Collart, F.; Joachimiak, A.; Stevens, R. C.; Kuhn, P.; Kossiakoff, A.; Ismagilov, R. F. Time-controlled microfluidic seeding in nL-volume droplets to separate nucleation and growth stages of protein crystallization. *Angewandte Chemie-International Edition* **2006**, 45 (48), 8156-8160.
141. Galkin, O.; Vekilov, P. G. Direct determination of the nucleation rates of protein crystals. *Journal of Physical Chemistry B* **1999**, 103 (49), 10965-10971.
142. Vekilov, P. G.; Galkin, O. On the methods of determination of homogeneous nucleation rates of protein crystals. *Colloids and Surfaces A-Physicochemical and Engineering Aspects* **2003**, 215 (1-3), 125-130.
143. Ildefonso, M.; Candoni, N.; Veessler, S. Using Microfluidics for Fast, Accurate Measurement of Lysozyme Nucleation Kinetics. *Crystal Growth & Design* **2011**, 11 (5), 1527-1530.
144. Ildefonso, M.; Guidon, N.; Veessler, S. A Cheap, Easy Microfluidic Crystallization Device Ensuring Universal Solvent Compatibility. *Organic Process Research & Development* **2012**, 16 (4), 556-560.
145. Dombrowski, R. D.; Litster, J. D.; Wagner, N. J.; He, Y. Crystallization of alpha-lactose monohydrate in a drop-based microfluidic crystallizer. *Chemical Engineering Science* **2007**, 62 (17), 4802-4810.
146. Davey, R. J.; Garside, J. *From Molecules to crystallisers-An in trodution to crystallisation*; Oxford University Press: 2002.

147. Galkin, O.; Vekilov, P. G. Are nucleation kinetics of protein crystals similar to those of liquid droplets? *Journal of the American Chemical Society* **2000**, *122* (1), 156-163.
148. Vekilov, P. G. Dense liquid precursor for the nucleation of ordered solid phases from solution. *Crystal Growth & Design* **2004**, *4* (4), 671-685.
149. Groen, H.; Roberts, K. J. Nucleation, growth, and pseudo-polymorphic behavior of citric acid as monitored in situ by attenuated total reflection Fourier transform infrared spectroscopy. *Journal of Physical Chemistry B* **2001**, *105* (43), 10723-10730.
150. Mersmann, A. *Crystallization Technology Handbook*; Marcel Dekker, Inc.: 2001.
151. Hulme, A. T. Combined Experimental and Computational Studies of the Polymorphism of Small Organic Molecules. University College London, 2006.
152. Burton, W. K.; Cabrera, N.; Frank, F. C. The Growth of Crystals and the Equilibrium Structure of Their Surfaces. *Philosophical Transactions of the Royal Society of London Series A-Mathematical and Physical Sciences* **1951**, *243* (866), 299-358.
153. Hartman, P.; Perdok, W. G. On the Relations Between Structure and Morphology of Crystals .1. *Acta Crystallographica* **1955**, *8* (1), 49-52.
154. Hartman, P.; Perdok, W. G. On the Relations Between Structure and Morphology of Crystals .2. *Acta Crystallographica* **1955**, *8* (9), 521-524.
155. Hartman, P.; Perdok, W. G. On the Relations Between Structure and Morphology of Crystals .3. *Acta Crystallographica* **1955**, *8* (9), 525-529.
156. Berkovitchyellin, Z. Toward An Abinitio Derivation of Crystal Morphology. *Journal of the American Chemical Society* **1985**, *107* (26), 8239-8253.
157. Davey, R. J.; Mullin, J. W.; Whiting, M. J. L. Habit Modification of Succinic Acid Crystals Grown from Different Solvents. *Journal of Crystal Growth* **1982**, *58* (2), 304-312.
158. Davey, R. J.; Black, S. N.; Logan, D.; Maginn, S. J.; Fairbrother, J. E.; Grant, D. J. W. Structural and Kinetic Features of Crystal-Growth Inhibition - Adipic Acid Growing in the Presence of N-Alkanoic Acids. *Journal of the Chemical Society-Faraday Transactions* **1992**, *88* (23), 3461-3466.
159. Glydesdale, G.; Docherty, R.; Roberts, K. J. Habit - A Program for Predicting the Morphology of Molecular-Crystals. *Computer Physics Communications* **1991**, *64* (2), 311-328.
160. Clydesdale, G.; Roberts, K. J.; Docherty, R. HABIT95 - A program for predicting the morphology of molecular crystals as a function of the growth environment. *Journal of Crystal Growth* **1996**, *166* (1-4), 78-83.
161. Clydesdale, G.; Thomson, G. B.; Walker, E. M.; Roberts, K. J.; Meenan, P.; Docherty, R. A molecular modeling study of the crystal morphology of adipic acid and its habit modification by homologous impurities. *Crystal Growth & Design* **2005**, *5* (6), 2154-2163.
162. Walker, E. M.; Roberts, K. J.; Maginn, S. J. A molecular dynamics study of solvent and impurity interaction on the crystal habit surfaces of epsilon-caprolactam. *Langmuir* **1998**, *14* (19), 5620-5630.

163. HALEBLIA.J; Mccrone, W. Pharmaceutical Applications of Polymorphism. *Journal of Pharmaceutical Sciences* **1969**, *58* (8), 911-&.
164. Grunenberg, A.; Henck, J. O.; Siesler, H. W. Theoretical derivation and practical application of energy temperature diagrams as an instrument in preformulation studies of polymorphic drug substances. *International Journal of Pharmaceutics* **1996**, *129* (1-2), 147-158.
165. Bernstein, J.; Davey, R. J.; Henck, J. O. Concomitant polymorphs. *Angewandte Chemie-International Edition* **1999**, *38* (23), 3440-3461.
166. Allan, N. L.; Rohl, A. L.; Gay, D. H.; Catlow, C. R. A.; Davey, R. J.; Mackrodt, W. C. Calculated Bulk and Surface-Properties of Sulfates. *Faraday Discussions* **1993**, (95), 273-280.
167. ter Horst, J. H.; Kramer, H. J. M.; Jansens, P. J. A new molecular modeling approach to predict concomitant nucleation of polymorphs. *Crystal Growth & Design* **2002**, *2* (5), 351-356.
168. I.Prigogine; R.Defay *Chemical Thermodynamics*; Longmans Green and Co: 1954.
169. Li, Z. J.; Zell, M. T.; Munson, E. J.; Grant, D. J. W. Characterization of racemic species of chiral drugs using thermal analysis, thermodynamic calculation, and structural studies. *Journal of Pharmaceutical Sciences* **1999**, *88* (3), 337-346.
170. *SADABS Program for Bruker Area Detector Absorption Correction*, version 2.03; University of Gottingen: Gottingen, Germany, 2001
171. *SAINT+ version 6.45*, version 6.45; Madison, Wisconsin, USA, 2003
172. Sheldrick, G. M. A short history of SHELX. *Acta Crystallographica Section A* **2008**, *64*, 112-122.
173. Betteridge, P. W.; Carruthers, J. R.; Cooper, R. I.; Prout, K.; Watkin, D. J. CRYSTALS version 12: software for guided crystal structure analysis. *Journal of Applied Crystallography* **2003**, *36*, 1487.
174. Pflugrath, J. W. The finer things in X-ray diffraction data collection. *Acta Crystallographica Section D-Biological Crystallography* **1999**, *55*, 1718-1725.
175. Madsen, I. C.; Hill, R. J. Collection and Analysis of Powder Diffraction Data with Near-Constant Counting Statistics. *Journal of Applied Crystallography* **1994**, *27*, 385-392.
176. Shankland, K.; David, W. I. F.; Sivia, D. S. Routine ab initio structure determination of chlorothiazide by X-ray powder diffraction using optimised data collection and analysis strategies. *Journal of Materials Chemistry* **1997**, *7* (3), 569-572.
177. Markvardsen, A. J.; David, W. I. F.; Johnson, J. C.; Shankland, K. A probabilistic approach to space-group determination from powder diffraction data. *Acta Crystallographica Section A* **2001**, *57*, 47-54.
178. David, W. I. F.; Shankland, K.; van de Streek, J.; Pidcock, E.; Motherwell, W. D. S.; Cole, J. C. DASH: a program for crystal structure determination from powder diffraction data. *Journal of Applied Crystallography* **2006**, *39*, 910-915.

179. *DASH User Manual*, Cambridge Crystallographic Data Centre: Cambridge, UK, 2001
180. Bruno, I. J.; Cole, J. C.; Edgington, P. R.; Kessler, M.; Macrae, C. F.; McCabe, P.; Pearson, J.; Taylor, R. New software for searching the Cambridge Structural Database and visualizing crystal structures. *Acta Crystallographica Section B-Structural Science* **2002**, *58*, 389-397.
181. Williams, D. E. Improved intermolecular force field for molecules containing H, C, N, and O atoms, with application to nucleoside and peptide crystals. *Journal of Computational Chemistry* **2001**, *22* (11), 1154-1166.
182. Price, S. L.; Leslie, M.; Welch, G. W. A.; Habgood, M.; Price, L. S.; Karamertzanis, P. G.; Day, G. M. Modelling organic crystal structures using distributed multipole and polarizability-based model intermolecular potentials. *Physical Chemistry Chemical Physics* **2010**, *12* (30), 8478-8490.
183. Day, G. M.; Motherwell, W. D. S.; Ammon, H. L.; Boerrigter, S. X. M.; la Valle, R. G.; Venuti, E.; Dzyabchenko, A.; Dunitz, J. D.; Schweizer, B.; van Eijck, B. P.; Erk, P.; Facelli, J. C.; Bazterra, V. E.; Ferraro, M. B.; Hofmann, D. W. M.; Leusen, F. J. J.; Liang, C.; Pantelides, C. C.; Karamertzanis, P. G.; Price, S. L.; Lewis, T. C.; Nowell, H.; Torrisi, A.; Scheraga, H. A.; Arnautova, Y. A.; Schmidt, M. U.; Verwer, P. A third blind test of crystal structure prediction. *Acta Crystallographica Section B-Structural Science* **2005**, *61*, 511-527.
184. Bardwell, D. A.; Adjiman, C. S.; Arnautova, Y. A.; Bartashevich, E.; Boerrigter, S. X. M.; Braun, D. E.; Cruz-Cabeza, A. J.; Day, G. M.; la Valle, R. G.; Desiraju, G. R.; van Eijck, B. P.; Facelli, J. C.; Ferraro, M. B.; Grillo, D.; Habgood, M.; Hofmann, D. W. M.; Hofmann, F.; Jose, K. V. J.; Karamertzanis, P. G.; Kazantsev, A. V.; Kendrick, J.; Kuleshova, L. N.; Leusen, F. J. J.; Maleev, A. V.; Misquitta, A. J.; Mohamed, S.; Needs, R. J.; Neumann, M. A.; Nikylov, D.; Orendt, A. M.; Pal, R.; Pantelides, C. C.; Pickard, C. J.; Price, L. S.; Price, S. L.; Scheraga, H. A.; van de Streek, J.; Thakur, T. S.; Tiwari, S.; Venuti, E.; Zhitkov, I. K. Towards crystal structure prediction of complex organic compounds - a report on the fifth blind test. *Acta Crystallographica Section B-Structural Science* **2011**, *67*, 535-551.
185. Day, G. M.; Cooper, T. G.; Cruz-Cabeza, A. J.; Hejczyk, K. E.; Ammon, H. L.; Boerrigter, S. X. M.; Tan, J. S.; la Valle, R. G.; Venuti, E.; Jose, J.; Gadre, S. R.; Desiraju, G. R.; Thakur, T. S.; van Eijck, B. P.; Facelli, J. C.; Bazterra, V. E.; Ferraro, M. B.; Hofmann, D. W. M.; Neumann, M. A.; Leusen, F. J. J.; Kendrick, J.; Price, S. L.; Misquitta, A. J.; Karamertzanis, P. G.; Welch, G. W. A.; Scheraga, H. A.; Arnautova, Y. A.; Schmidt, M. U.; van de Streek, J.; Wolf, A. K.; Schweizer, B. Significant progress in predicting the crystal structures of small organic molecules - a report on the fourth blind test. *Acta Crystallographica Section B-Structural Science* **2009**, *65*, 107-125.
186. Li, Z. J.; Ojala, W. H.; Grant, D. J. W. Molecular modeling study of chiral drug crystals: Lattice energy calculations. *Journal of Pharmaceutical Sciences* **2001**, *90* (10), 1523-1539.
187. Kimoto, H.; Saigo, K.; Hasegawa, M. The Potential-Energy Calculation for Conglomerate Crystals. *Chemistry Letters* **1990**, (5), 711-714.
188. J.D.Dunitz; A.Gavezzotti Proteogenic Amino Acids: Chiral and Racemic Crystal Packings and Stabilities. *Journal of Physical Chemistry B* **2012**.

189. Harrington, P. J.; Lodewijk, E. Twenty years of naproxen technology. *Organic Process Research & Development* **1997**, *1* (1), 72-76.
190. Noorduyn, W. L.; Kaptein, B.; Meekes, H.; van Enckevort, W. J. P.; Kellogg, R. M.; Vlieg, E. Fast Attrition-Enhanced Deracemization of Naproxen by a Gradual In Situ Feed. *Angewandte Chemie-International Edition* **2009**, *48* (25), 4581-4583.
191. Ravikumar, K.; Rajan, S. S.; Pattabhi, V. Structure of Naproxen, C<sub>14</sub>H<sub>14</sub>O<sub>3</sub>. *Acta Crystallographica Section C-Crystal Structure Communications* **1985**, *41* (FEB), 280-282.
192. Kim, Y. B.; Song, H. J.; Park, I. Y. Refinement of the structure of naproxen, (+)-6-methoxy- $\alpha$ -methyl-2-naphthaleneacetic acid. *Archives of Pharmacal Research* **1987**, *10* (4), 232-238.
193. Mora, C. P.; Martinez, F. Solubility of naproxen in several organic solvents at different temperatures. *Fluid Phase Equilibria* **2007**, *255* (1), 70-77.
194. Yan, F. Y.; Chen, L.; Liu, D. Q.; Sima, L. F.; Chen, M. J.; Shi, H.; Zhu, J. X. Solubility of (+)-(S)-2-(6-Methoxynaphthalen-2-yl) Propanoic Acid in Acetone, Methanol, Ethanol, Propan-2-ol, and Ethyl Ethanoate at Temperatures between (278 and 320) K. *Journal of Chemical and Engineering Data* **2009**, *54* (3), 1117-1119.
195. Mora, C. P.; Martinez, F. Thermodynamic quantities relative to solution processes of Naproxen in aqueous media at pH 1.2 and 7.4. *Physics and Chemistry of Liquids* **2006**, *44* (5), 585-596.
196. Perlovich, G. L.; Kurkov, S. V.; Kinchin, A. N.; Bauer-Brandl, A. Thermodynamics of solutions III: comparison of the solvation of (+)-naproxen with other NSAIDs. *European Journal of Pharmaceutics and Biopharmaceutics* **2004**, *57* (2), 411-420.
197. Pacheco, D. P.; Martinez, F. Thermodynamic analysis of the solubility of naproxen in ethanol plus water cosolvent mixtures. *Physics and Chemistry of Liquids* **2007**, *45* (5), 581-595.
198. Pacheco, D. P.; Manrique, Y. J.; Martinez, F. Thermodynamic study of the solubility of ibuprofen and naproxen in some ethanol plus propylene glycol mixtures. *Fluid Phase Equilibria* **2007**, *262* (1-2), 23-31.
199. Neau, S. H.; Bhandarkar, S. V.; Hellmuth, E. W. Differential molar heat capacities to test ideal solubility estimations. *Pharmaceutical Research* **1997**, *14* (5), 601-605.
200. Sovizi, M. R. Thermal behavior of drugs. *Journal of Thermal Analysis and Calorimetry* **2010**, *102* (1), 285-289.
201. Manimaran, T.; Stahly, G. P. Optical Purification of Profen Drugs. *Tetrahedron-Asymmetry* **1993**, *4* (8), 1949-1954.
202. Braun, D. E.; rrid-Candel, M.; D'Oria, E.; Karamertzanis, P. G.; Arlin, J. B.; Florence, A. J.; Jones, A. G.; Price, S. L. Racemic Naproxen: A Multidisciplinary Structural and Thermodynamic Comparison with the Enantiopure Form. *Crystal Growth & Design* **2011**, *11* (12), 5659-5669.
203. Gelbrich, T.; Hursthouse, M. B. A versatile procedure for the identification, description and quantification of structural similarity in molecular crystals. *Crystengcomm* **2005**, *7*, 324-336.

204. Gelbrich, T.; Hursthouse, M. B. Systematic investigation of the relationships between 25 crystal structures containing the carbamazepine molecule or a close analogue: a case study of the XPac method. *Crystengcomm* **2006**, *8* (6), 448-460.
205. Manimaran, T.; Stahly, G. P. Optical Purification of Profen Drugs. *Tetrahedron-Asymmetry* **1993**, *4* (8), 1949-1954.
206. Neau, S. H.; Bhandarkar, S. V.; Hellmuth, E. W. Differential molar heat capacities to test ideal solubility estimations. *Pharm. Res.* **1997**, *14* (5), 601-605.
207. Sovizi, M. R. Thermal behavior of drugs. *J. Therm. Anal. Calorim.* **2010**, *102* (1), 285-289.
208. Kofler, L.; Kofler, A. *Thermo-Mikro\_Methoden zur Kennzeichnung organischer Stoffe und Stoffgemische*; Verlag Chemie GmbH, Weinheim/Bergstrasse: 1954.
209. Pacheco, D. P.; Martinez, F. Thermodynamic analysis of the solubility of naproxen in ethanol + water cosolvent mixtures. *Phys. Chem. Liq.* **2007**, *45* (5), 581-595.
210. Krug, R. R.; Hunter, W. G.; Grieger, R. A. Enthalpy-entropy compensation. 1. Some fundamental statistical problems associated with the analysis of van't Hoff and Arrhenius data. *J. Phys. Chem.* **1976**, *80* (21), 2335-2341.
211. Leclercq, M.; Collet, A.; Jacques, J. Study of optical antipode mixtures. XII. Stability of true racemates. *Tetrahedron* **1976**, *32* (7), 821-828.
212. Li, Z. J.; Ojala, W. H.; Grant, D. J. W. Molecular modeling study of chiral drug crystals: Lattice energy calculations. *J. Pharm. Sci.* **2001**, *90* (10), 1523-1539.
213. Gavezzotti, A. Molecular packing and correlations between molecular and crystal properties. *Struct. Correl.* **1994**, *2*, 509-542.
214. Chickos, J. S. A protocol for correcting experimental fusion enthalpies to 298.15 K and its application in indirect measurements of sublimation enthalpy at 298.15 K. *Thermochim. Acta* **1998**, *313* (1), 19-26.
215. Dunitz, J. D.; Gavezzotti, A. Attractions and repulsions in molecular crystals: What can be learned from the crystal structures of condensed ring aromatic hydrocarbons? *Accounts Chem. Res.* **1999**, *32* (8), 677-684.
216. Brock, C. P.; Schweizer, W. B.; Dunitz, J. D. On the Validity of Wallach Rule - on the Density and Stability of Racemic Crystals Compared with Their Chiral Counterparts. *J. Am. Chem. Soc.* **1991**, *113* (26), 9811-9820.
217. Anghel, A. T.; Day, G. M.; Price, S. L. A study of the known and hypothetical crystal structures of pyridine: why are there four molecules in the asymmetric unit cell? *CrystEngComm* **2002**, *4* (62), 348-355.
218. Day, G. M.; Price, S. L.; Leslie, M. Atomistic calculations of phonon frequencies and thermodynamic quantities for crystals of rigid organic molecules. *J. Phys. Chem. B* **2003**, *107* (39), 10919-10933.
219. Day, G. M.; Price, S. L.; Leslie, M. Elastic constant calculations for molecular organic crystals. *Cryst. Growth Des.* **2001**, *1* (1), 13-27.

220. van Eijck, B. P. Ab initio crystal structure predictions for flexible hydrogen-bonded molecules. Part III. Effect of lattice vibrations. *J. Comput. Chem.* **2001**, *22* (8), 816-826.
221. Li, Z. J.; Zell, M. T.; Munson, E. J.; Grant, D. J. W. Characterization of racemic species of chiral drugs using thermal analysis, thermodynamic calculation, and structural studies. *J. Pharm. Sci.* **1999**, *88* (3), 337-346.
222. Oliveira, M. A.; Peterson, M. L.; Davey, R. J. Relative Enthalpy of Formation for Co-Crystals of Small Organic Molecules. *Cryst. Growth Des.* **2011**, *11* (2), 449-457.
223. Yan, F. Y.; Chen, L.; Liu, D. Q.; SiMa, L. F.; Chen, M. J.; Shi, H.; Zhu, J. X. Solubility of (+)-(S)-2-(6-Methoxynaphthalen-2-yl) Propanoic Acid in Acetone, Methanol, Ethanol, Propan-2-ol, and Ethyl Ethanoate at Temperatures between (278 and 320) K. *J. Chem. Eng. Data* **2009**, *54* (3), 1117-1119.
224. Braun, D. E.; Karamertzanis, P. G.; Arlin, J. B.; Florence, A. J.; Kahlenberg, V.; Tocher, D. A.; Griesser, U. J.; Price, S. L. Solid-State Forms of beta - Resorcylic Acid: How Exhaustive Should a Polymorph Screen Be? *Cryst. Growth Des.* **2011**, *11* (1), 210-220.
225. Price, S. L. Computed crystal energy landscapes for understanding and predicting organic crystal structures and polymorphism. *Accounts Chem. Res.* **2009**, *42* (1), 117-126.
226. Lancaster, R. W.; Karamertzanis, P. G.; Hulme, A. T.; Tocher, D. A.; Lewis, T. C.; Price, S. L. The Polymorphism of Progesterone: Stabilization of a 'Disappearing' Polymorph by Co-Crystallization. *J. Pharm. Sci.* **2007**, *96* (12), 3419-3431.
227. Bond, A. D.; Boese, R.; Desiraju, G. R. On the polymorphism of aspirin: Crystalline aspirin as intergrowths of two "polymorphic" domains. *Angew. Chem., Int. Ed.* **2007**, *46* (4), 618-622.
228. Braun, D. E.; Gelbrich, T.; Kahlenberg, V.; Laus, G.; Wieser, J.; Griesser, U. J. Packing polymorphism of a conformationally flexible molecule (aprepitant). *New J. Chem.* **2008**, *32* (10), 1677-1685.
229. Misquitta, A. J.; Welch, G. W. A.; Stone, A. J.; Price, S. L. A first principles solution of the crystal structure of C<sub>6</sub>Br<sub>2</sub>C<sub>1</sub>F<sub>1</sub>H<sub>2</sub>. *Chem. Phys. Lett.* **2008**, *456* (1-3), 105-109.
230. Karamertzanis, P. G.; Day, G. M.; Welch, G. W. A.; Kendrick, J.; Leusen, F. J. J.; Neumann, M. A.; Price, S. L. Modeling the interplay of inter- and intramolecular hydrogen bonding in conformational polymorphs. *J. Chem. Phys.* **2008**, *128* (24), art-244708.
231. Price, S. L. Computational Polymorph Prediction. In *Solid State Characterisation of Pharmaceuticals*, Storey R; Ymen I, Eds.; 2010.
232. Price, S. L. Computed Crystal Energy Landscapes for Understanding and Predicting Organic Crystal Structures and Polymorphism. *Accounts of Chemical Research* **2009**, *42* (1), 117-126.
233. Valente, E. J.; Zubkowski, J.; Eggleston, D. S. Discrimination in Resolving Systems - Ephedrine-Mandelic Acid. *Chirality* **1992**, *4* (8), 494-504.



234. Valente, E. J.; Miller, C. W.; Zubkowski, J.; Eggleston, D. S.; Shui, X. Q. Discrimination in resolving systems .2. Ephedrine-substituted mandelic acids. *Chirality* **1995**, *7* (8), 652-676.
235. Leusen, F. J. J.; Slot, H. J. B.; Noordik, J. H.; Vanderhaest, A. D.; Wynberg, H.; Bruggink, A. Towards A Rational Design of Resolving Agents .3. Structural Study of 2 Pairs of Diastereomeric Salts of Ephedrine and A Cyclic Phosphoric-Acid. *Recueil des Travaux Chimiques des Pays-Bas-Journal of the Royal Netherlands Chemical Society* **1991**, *110* (1), 13-18.
236. Leusen, F. J. J.; Slot, H. J. B.; Noordik, J. H.; Vanderhaest, A. D.; Wynberg, H.; Bruggink, A. Towards A Rational Design of Resolving Agents .4. Crystal Packing Analyses and Molecular Mechanics Calculations for 5 Pairs of Diastereomeric Salts of Ephedrine and A Cyclic Phosphoric-Acid. *Recueil des Travaux Chimiques des Pays-Bas-Journal of the Royal Netherlands Chemical Society* **1992**, *111* (3), 111-118.
237. Gervais, C.; Grimbergen, R. F. P.; Markovits, I.; Ariaans, G. J. A.; Kaptein, B.; Bruggink, A.; Broxterman, Q. B. Prediction of solid solution formation in a family of diastereomeric salts. A molecular modeling study. *Journal of the American Chemical Society* **2004**, *126* (2), 655-662.
238. Wang, M.; Marriott, P. J.; Chan, W. H.; Lee, A. W. M.; Huie, C. W. Enantiomeric separation and quantification of ephedrine-type alkaloids in herbal materials by comprehensive two-dimensional gas chromatography. *Journal of Chromatography A* **2006**, *1112* (1-2), 361-368.
239. Betz, J. M.; Gay, M. L.; Mossoba, M. M.; Adams, S.; Portz, B. S. Chiral gas chromatographic determination of ephedrine-type alkaloids in dietary supplements containing Ma Huang. *Journal of Aoac International* **1997**, *80* (2), 303-315.
240. Arthur E.Hill; John E.Ricci Ternary Systems. XI Magnesium Iodate, Sodium Iodate and Water. XII Sodium Iodate, Potassium Iodate and Water. XIII Potassium Iodate, Potassium Chloride and Water. XIV Potassium Iodate, Potassium Sulfate and Water. *Journal of the American Chemical Society* **1931**, *53* (12), 4305-4315.
241. Collier, E. A.; Davey, R. J.; Black, S. N.; Roberts, R. J. 17 salts of ephedrine: crystal structures and packing analysis. *Acta Crystallographica Section B-Structural Science* **2006**, *62*, 498-505.
242. Cooke, C. L.; Davey, R. J.; Black, S.; Murny, C.; Pritchard, R. G. Binary and Ternary Phase Diagrams as Routes to Salt Discovery Ephedrine and Pimelic Acid. *Crystal Growth & Design* **2010**, *10* (12), 5270-5278.
243. McCague, R. A measure of the solid-solution extent useful for crystallisation resolution studies. *Tetrahedron Letters* **2007**, *48* (5), 869-872.
244. Lutker, K. M.; Tolstyka, Z. P.; Matzger, A. J. Investigation of a privileged polymorphic motif: A dimeric ROY derivative. *Crystal Growth & Design* **2008**, *8* (1), 136-139.
245. Rossi, D.; Gelbrich, T.; Kahlenberg, V.; Griesser, U. J. Supramolecular constructs and thermodynamic stability of four polymorphs and a co-crystal of pentobarbital (nembital). *Crystengcomm* **2012**, *14* (7), 2494-2506.
246. Lopez-Mejias, V.; Kampf, J. W.; Matzger, A. J. Polymer-Induced Heteronucleation of Tolfenamic Acid: Structural Investigation of a

Pentamorph. *Journal of the American Chemical Society* **2009**, *131* (13), 4554-+.

247. Uzoh, O. G.; Cruz-Cabeza, A. J.; Price, S. L. Is the Fenamate Group a Polymorphophore? Contrasting the Crystal Energy Landscapes of Fenamic and Tolfenamic Acids. *Crystal Growth & Design* **2012**, *12* (8), 4230-4239.
248. Larsen, S.; Dediego, H. L.; Kozma, D. Optical Resolution Through Diastereomeric Salt Formation - the Crystal-Structures of Cinchoninium (R)-Mandelate and Cinchoninium (S)-Mandelate at Low-Temperature. *Acta Crystallographica Section B-Structural Science* **1993**, *49*, 310-316.
249. Cruz-Cabeza, A. J.; Liebeschuetz, J. W.; Allen, F. H. Systematic conformational bias in small-molecule crystal structures is rare and explicable. *Crystengcomm* **2012**, *14* (20), 6797-6811.
250. Alonso, J. L.; Sanz, M. E.; Lopez, J. C.; Cortijo, V. Conformational Behavior of Norephedrine, Ephedrine, and Pseudoephedrine. *Journal of the American Chemical Society* **2009**, *131* (12), 4320-4326.
251. Portoghese, P. S. Stereochemical Studies on Medicinal Agents .4. Conformational Analysis of Ephedrine Isomers and Related Compounds. *Journal of Medicinal Chemistry* **1967**, *10* (6), 1057-1063.
252. Coombes, D. S.; Price, S. L.; Willock, D. J.; Leslie, M. Role of electrostatic interactions in determining the crystal structures of polar organic molecules. A distributed multipole study. *Journal of Physical Chemistry* **1996**, *100* (18), 7352-7360.
253. Williams, D. E. Improved intermolecular force field for molecules containing H, C, N, and O atoms, with application to nucleoside and peptide crystals. *Journal of Computational Chemistry* **2001**, *22* (11), 1154-1166.
254. Williams, D. E. Improved intermolecular force field for crystalline oxhydrocarbons including O-H...O hydrogen bonding. *Journal of Computational Chemistry* **2001**, *22* (1), 1-20.
255. Mohamed, S.; Tocher, D. A.; Vickers, M.; Karamertzanis, P. G.; Price, S. L. Salt or Cocrystal? A New Series of Crystal Structures Formed from Simple Pyridines and Carboxylic Acids. *Crystal Growth & Design* **2009**, *9* (6), 2881-2889.
256. Day, G. M.; Cooper, T. G. Crystal packing predictions of the alpha-amino acids: methods assessment and structural observations. *Crystengcomm* **2010**, *12* (8), 2443-2453.
257. Habgood, M.; Price, S. L.; Portalone, G.; Irrera, S. Testing a Variety of Electronic-Structure-Based Methods for the Relative Energies of 5-Formyluracil Crystals. *J. Chem. Theory Comput.* **2011**, *7* (9), 2685-2688.
258. Schmidt, M. W.; Baldrige, K. K.; Boatz, J. A.; Elbert, S. T.; Gordon, M. S.; Jensen, J. H.; Koseki, S.; Matsunaga, N.; Nguyen, K. A.; Su, S. J.; Windus, T. L.; Dupuis, M.; Montgomery, J. A. General Atomic and Molecular Electronic-Structure System. *Journal of Computational Chemistry* **1993**, *14* (11), 1347-1363.